NASA Contractor Report 187150

Free-Stream Turbulence and Concave Curvature Effects on Heated, Transitional Boundary Layers

Volume I–Final Report

J. Kim and T.W. Simon
University of Minnesota
Minneapolis, Minnesota

August 1991

Prepared for
Lewis Research Center
Under Grant NAG3-881

NASA
National Aeronautics and
Space Administration

ABSTRACT

An experimental investigation of the transition process on flat-plate and concave curved-wall boundary layers for various free-stream turbulence levels was performed. Where possible, sampling according to the intermittency function was made. Such sampling allowed segregation of the signal into two types of behavior--laminar-like and turbulent-like. Results show that for transition on a flat-plate, the two forms of boundary layer behavior, identified as laminar-like and turbulent-like, cannot be thought of as separate Blasius and fully-turbulent profiles, respectively. Thus, simple transition models in which the desired quantity is assumed to be an average, weighted on intermittency, of the theoretical laminar and fully turbulent values is not expected to be successful. Deviation of the flow identified as laminar-like from theoretical laminar behavior is shown to be due to recovery after the passage of a turbulent spot, while deviation of the flow identified as turbulent-like from the fully-turbulent values is thought to be due to incomplete establishment of the fully-turbulent power spectral distribution. Turbulent Prandtl numbers for the transitional flow, computed from measured shear stress, turbulent heat flux and mean velocity and temperature profiles, were less than unity. For the curved-wall case with low free-stream turbulence intensity, the existence of Görtler vortices on the concave wall within both laminar and turbulent flows was established using liquid crystal visualization and spanwise velocity and temperature traverses. Transition was found to occur via a vortex breakdown mode. The vortex wavelength was quite irregular in both the laminar and turbulent flows, but the vortices were stable in time and space. The upwash was found to be more

unstable, with higher levels of u' and u'v', and lower skin friction coefficients and shape factors. Turbulent Prandtl numbers, measured using a triple-wire probe, were found to be near unity for all post-transitional profiles, indicating no gross violation of Reynolds analogy. No evidence of streamwise vortices was seen in the high turbulence intensity case. It is not known whether this is due to the high eddy viscosity over the entire flow which reduces the turbulent Görtler number to stable values and causes the vortices to disappear, or whether it is due to an unstable vortex structure. Predictions based on two-dimensional modelling of the flow over a concave wall with high free-stream turbulence levels, as on the pressure surface of a turbine blade, would seem to be adequate. High levels of free-stream turbulence superimposed on a free-stream velocity gradient (which occurs within curved channels) was found to cause a cross-stream transport of momentum within the "potential core" of the flow. The total pressure within the "potential core" can thus rise to levels higher than that which occurs at the inlet to the test section.

Documentation is presented in two volumes. Volume I contains the text of the report including figures and supporting appendices. Volume II contains data reduction program listings and tabulated data.

ACKNOWLEDGEMENTS

The following work was sponsored by the Lewis Research Center of NASA under grant NASA/NAG3-881. The authors thank the grant monitor, Mr. Fred Simon, for his guidance.

Some additional support was provided by the Air Force Office of Scientific Research and the Graduate School of the University of Minnesota.

CONTENTS

VOLUME I

Abstract i

Acknowledgements iii

Contents iv

Nomenclature vi

List of Figures ix

List of Tables xiv

Chapter

1. Introduction

    1.1 Flat-plate Transition 1

    1.2 Transition on Concave Walls 4

2. Experimental Apparatus, Techniques and Qualification

    2.1 Experimental Apparatus 9

    2.2 Instrumentation 11

    2.3 Measurement Techniques 13

    2.4 Test-wall and Tunnel Qualification 28

3. Results and Discussion

    3.1 Case 1–Flat-wall, TI=0.45% 49

    3.2 Case 2–Flat-wall, TI=1.5% 68

    3.3 Case 3–Flat-wall, TI=8.3% 82

    3.4 Case 4–Concave curved-wall, TI=0.6% 98

    3.5 Case 5–Concave curved-wall, TI=8.3% 130

4. Conclusions 149

References 150

Appendices

A1. Measurement of wall emissivity 156

A2. Measurement of thermal conductivity of lexan/liquid crystal composite 160

A3. Measurement of autocorrelation and associated scales 162

VOLUME II

A4. Program Listings 173

A5. Data Listings

Case 1–Low TI, Flat-wall 247

Case 2–Medium TI, Flat-wall 297

Case 3–High TI, Flat-wall 353

Case 4–Low TI, Concave Curved Wall 378

Case 5–High TI, Concave Curved Wall 418

NOMENCLATURE

A	Area
b	Bar width
C_f	Skin friction coefficient
C_p	Specific heat or static pressure coefficient, depending on context
G	Görtler Number (p. 4)
Gr	Grashof number
H	Shape factor ($=\delta_1/\delta_2$)
k	Conductivity or an empirical constant, depending on context
i	Current
N	Görtler number based on boundary layer thickness
P	Production of shear stress
Pr_t	Turbulent Prandtl number
PSD	Power spectral density
$\dot{q}''$	Heat flux per unit time and area
R	Wall radius of curvature or resistance, depending on context
r	Local radius of curvature
Re	Reynolds number
St	Stanton number
T	Temperature, mean value
t	Time or instantaneous temperature, depending on context
TI	Turbulence intensity ($u'/U_\infty \times 100$)
U	Mean streamwise velocity
u	Instantaneous streamwise velocity
u't'	Streamwise turbulent transport of heat, time averaged

$u'v'$ Turbulent shear stress, time averaged

V Voltage

$v't'$ Cross-stream turbulent transport of heat, time averaged

x streamwise distance

y cross-stream distance

z cross-span distance

δ Boundary layer thickness based on 99.5% of freestream velocity

δ_1 Displacement thickness (p. 16)

δ_2 Momentum thickness (p. 16)

ε Emissivity or ratio of resistances, depending on context

γ Intermittency (p. 25)

Λ Non-dimensional wavelength (p. 104)

λ Wavelength of vortices

ν Kinematic viscosity

Π Coles wake parameter

ρ Density or autocorrelation (p. 130), depending on context

τ Shear stress or time delay, depending on context

Subscripts

c critical or computed value, depending on context

e eddy value

h heater

l laminar

p local potential flow value

pw potential value at wall

t turbulent

tr	transition
w	wall value or wall, depending on context
x	based on streamwise distance
τ	shear value
∞	free-stream value

Superscripts

'	fluctuating component, rms
+	wall coordinates
--	(overbar) mean value

LIST OF FIGURES

Fig. 1.1--Schematic of the transition process on a flat-plate boundary layer at low turbulence intensities. (From Schlichting--1979)

Fig. 1.2--Schematic diagram of Görtler vortices.

Fig. 2.1--Schematic of test facility (plan view).

Fig. 2.2--Jet-grid turbulence generator (from Russ--1989).

Fig. 2.3--Mean and fluctuating velocity measurements at the exit of the turbulence establishment section (from Russ--1989).

Fig. 2.4--Cross-section of heated test-wall (not to scale).

Fig. 2.5--Illustration of the method used to determine the distance of thermocouple probe from the heated wall.

Fig. 2.6--Schematic of triple-wire probe used to measure turbulent heat fluxes.

Fig. 2.7--Schematic of circuit used to measure cold-wire resistance.

Fig. 2.8--Comparison of Pr_t values measured using the probe to the data of Blair and Bennett (1984) and Gibson, Verriopoulos and Vlachos (1984).

Fig. 2.9--Block diagram of intermittency measuring unit.

Fig. 2.10--Method used to solve the zero-crossing problem.

Fig. 2.11--Intermittency circuit performance in a transitional boundary layer. Position in the boundary layer is as noted.

Fig. 2.12--Comparison of signals in the wake of a turbulent boundary layer using a). a hot-wire, and b). a cold-wire.

Fig. 2.13--Variation in Stanton number vs. Re_x for two wall heat fluxes.

Fig. 2.14--Comparison of the transition start location with that of other researchers and with the McDonald-Fish (1973) prediction.

Fig. 3.1.1--Power spectral density distribution of the streamwise velocity component (Case 1).

Fig. 3.1.2--Measurement of the free-stream turbulence intensity vs. streamwise distance (Case 1).

Fig. 3.1.3--Intermittency profiles along the wall (Case 1).

Fig. 3.1.4--Profiles of mean velocity sampled on intermittency (Case 1).

Fig. 3.1.5--Profiles of mean velocity sampled on intermittency and normalized on wall coordinates (Case 1).

Fig. 3.1.6--Skin friction sampled on intermittency (Case 1).

Fig. 3.1.7--Near-wall hot-wire voltage trace in transition illustrating the different mean velocities between the two regimes and the relaxation of the boundary layer after turbulent spot passage (as in "A").

Fig. 3.1.8--Shape factors sampled on intermittency (Case 1).

Fig. 3.1.9--Turbulence intensity profiles sampled on intermittency (Case 1).

Fig. 3.1.10--Shear stress profiles sampled on intermittency (Case 1).

Fig. 3.1.11--Cross-stream turbulent heat flux sampled on intermittency (Case 1).

Fig. 3.1.12--Turbulent Prandtl numbers sampled on intermittency (Case 1).

Fig. 3.2.1--Power spectral density distribution of streamwise fluctuating velocity (Case 2).

Fig. 3.2.2--Stanton number variation through transition (Case 2).

Fig. 3.2.3--Intermittency profile variation through transition (Case 2).

Fig. 3.2.4--Mean velocity profiles sampled on intermittency normalized on wall coordinates (Case 2).

Fig. 3.2.5--Skin friction sampled on intermittency (Case 2).

Fig. 3.2.6--Shape factor sampled on intermittency (Case 2).

Fig. 3.2.7--Streamwise turbulence intensity sampled on intermittency (Case 2).

Fig. 3.2.8--Mean temperature profiles through transition normalized on wall coordinates (Case 2).

Fig. 3.2.9--Shear stress sampled on intermittency through transition (Case 2).

Fig. 3.2.10--Turbulent heat flux sampled on intermittency through transition (Case 2).

Fig. 3.2.11--Turbulent Prandtl number sampled on intermittency through transition (Case 2).

Fig. 3.3.1--Hot-wire trace and its derivative in the boundary layer (Case 3).

Fig. 3.3.2--Power spectral density distribution of streamwise velocity (Case 3).

Fig. 3.3.3--Free-stream turbulence intensity variation in the tunnel (Case 3).

Fig. 3.3.4--Stanton number variation along test-wall (Case 3).

Fig. 3.3.5--Energy balance along wall (Case 3).

Fig. 3.3.6--Mean velocity profiles normalized on wall coordinates (Case 3).

Fig. 3.3.7--Skin friction values along the wall deduced from the mean velocity profiles (Case 3).

Fig. 3.3.8--Shape factors along the wall (Case 3).

Fig. 3.3.9--Turbulence intensity profiles along the test-wall (Case 3).

Fig. 3.3.10--Mean temperature profiles normalized on wall coordinates (Case 3).

Fig. 3.3.11--Shear stress profiles along the test-wall (Case 3).

Fig. 3.3.12--Turbulent Prandtl number profiles along the test-wall (Case 3).

Fig. 3.4.1--Comparison of measured velocities with potential velocity profiles at stations 3 and 4 (Case 4).

Fig. 3.4.2--Hot-wire signal and output of intermittency circuit (Case 4).

Fig. 3.4.3--Picture of heated test-wall showing spanwise variation in wall temperature (Case 4).

Fig. 3.4.4--Variation of intermittency vs. time for wall heating and wall cooling (Case 4).

Fig. 3.4.5--Spanwise variation in velocity at various normal distance from the wall (Case 4).

Fig. 3.4.6--Oscilloscope traces at upwash and downwash, station 2 (Case 4).

Fig. 3.4.7--Location on Görtler map of the late laminar (station 2) flow (Case 4).

Fig. 3.4.8--Location on Liepmann's (1943) transition diagram of the late laminar (station 2) flow (Case 4).

Fig. 3.4.9--Dimensional velocity profiles at the upwash and downwash along the wall (Case 4).

Fig. 3.4.10--Velocity profiles at the upwash and downwash normalized on wall coordinates (Case 4).

Fig. 3.4.11--Skin friction variation along the wall at upwash and downwash locations (Case 4).

Fig. 3.4.12--Shape factor variation along the wall at upwash and downwash locations (Case 4).

Fig. 3.4.13--Turbulence intensity profiles along the wall at upwash and downwash locations (Case 4).

Fig. 3.4.14--Shear stress profiles along the wall at upwash and downwash locations (Case 4).

Fig. 3.4.15--Stanton number variation vs. Re_x--comparison with the low TI flat-wall case.

Fig. 3.4.16--Stanton number variation vs. Re_x for two free-stream velocities (Case 4).

Fig. 3.4.17--Mean temperature profiles along the wall at upwash and downwash locations (Case 4).

Fig. 3.4.18--Fluctuating temperature profiles along the wall at upwash and downwash locations (Case 4).

Fig. 3.4.19--Profiles of the streamwise heat flux along the wall at upwash and downwash locations (Case 4).

Fig. 3.4.20--Profiles of the cross-stream heat flux along the wall at upwash and downwash locations (Case 4).

Fig. 3.4.21--Profiles of the turbulent Prandtl number at upwash and downwash locations (Case 4).

Fig. 3.5.1--Profiles of the mean and fluctuating velocities across the test section at the end of the turbulence establishment chamber (Case 5).

Fig. 3.5.2--Mean velocity profiles across the test section at various locations along the test wall (Case 5).

Fig. 3.5.3--Shear stress profiles across the test section at various locations along the test wall (Case 5).

Fig. 3.5.4--Mean velocity profiles normalized on wall coordinates along the test wall (Case 5).

Fig. 3.5.5--Turbulence intensity profiles along the test wall (Case 5).

Fig. 3.5.6--Comparison of the turbulence decay rate in the curved test section with the predicted decay rate of Baines and Peterson (1951) in straight channels.

Fig. 3.5.7--Comparison of the Stanton number variation along test wall between curved and straight wall cases.

Fig. 3.5.8--Energy balance for Case 5.

Fig. 3.5.9--Mean temperature profiles normalized on wall coordinates (Case 5).

Fig. 3.5.10--Profiles of the fluctuating temperature along the test wall (Case 5).

Fig. 3.5.11--Profiles of the streamwise heat flux along the test wall (Case 5).

Fig. 3.5.12--Profiles of the cross-stream heat flux along the test wall (Case 5).

Fig. 3.5.13--Profiles of the turbulent Prandtl number along the test wall (Case 5).

Fig. A.1--Emissivity measurement setup.

Fig. A.2--Composite wall construction.

LIST OF TABLES

Table 1--Summary of boundary layer parameters for Case 1.

Table 2--Summary of boundary layer parameters for Case 2.

Table 3--Summary of boundary layer parameters for Case 3.

Table 4--Summary of boundary layer parameters for Case 4.

Table 5--Summary of boundary layer parameters for Case 5.

CHAPTER 1

Introduction

Despite the attention of many investigators, understanding of the boundary layer transition process remains elusive. The sensitivity of transition to many factors (free-stream acceleration, the level of free-stream turbulence and its characteristics, surface roughness, surface curvature, surface heating, wall suction, compressibility and unsteadiness, to name a few) makes prediction of the transition process in machines such as gas turbines very difficult. Although a very few instances of direct solution of the Navier-Stokes equation have recently emerged that yield an extremely valuable window to the physics of bypass transition, much of the insight into this complex phenomenon is gained by experimentation. The transition process is sufficiently complex that observations must first be made in simple geometries with few effects. Later, as understanding builds, more effects can be added and more realistic geometries can be investigated.

1.1). Flat-plate Transition

The purpose of the first portion of the experimental program was to document the effects of three levels of free-stream turbulence on flat-plate transitional boundary layers. The experiments provide support for the testing and development of transition prediction models. Specifically, the applicability of intermittency-based transition models first proposed by Dhawan and Narasimha (1958) which assume a Blasius-type flow for the laminar portion and a fully turbulent flow for the turbulent portion were tested. Although quite a few researchers have studied the flat-plate transition process (see Wang--1984 for a good review), only a few have used conditional

sampling on intermittency to look at the laminar and turbulent portions of the transitional boundary layer separately. No previous researchers to the authors' knowledge have directly measured the turbulent heat flux and Prandtl number in the turbulent part of the intermittent boundary layer.

Transition on flat-plate boundary layers on smooth walls occurs via a T-S (Tollmien-Schlichting) path (Figure 1.1) or a bypass mode depending on the free-stream turbulence level (Morkovin--1977). For low free-stream turbulence levels, the instability is first manifested in the formation of two-dimensional Tollmien-Schlichting waves, which then become unstable in the spanwise direction and form hair-pin vortices (Klebanoff, Tidstrom and Sargent--1962, and Perry, Lim, and Teh--1981). Breakdown to turbulence occurs shortly afterwards through the formation of turbulent spots, first discovered by Emmons (1951). The bypass mode of transition occurs at higher free-stream turbulence levels, turbulent spots forming without T-S wave amplification. Spot formation is characterized by a sudden explosion of the boundary layer from laminar to turbulent flow (Suder, O'Brien and Reshotko--1988).

Dhawan and Narasimha (1958) were the first to view the transition process as being composed of a Blasius profile alternating with a fully turbulent log-law profile. They proposed calculating boundary layer parameters within transition by weighting, on the intermittency, the corresponding parameters in the fully laminar and fully turbulent flows, each at it's appropriate Reynolds number. Their measurements supported their hypothesis. A series of experiments by other researchers in which conditional sampling techniques were used to measure quantities within turbulent spots, however, generated conflicting results. Wygnanski, Sokolov and Friedman

(1976) and Blair (1991) found that the turbulent-zone mean velocity profiles along the centerline of the turbulent spot agreed with the log-law, indicating that the modelling of Dhawan and Narasimha (1958) could be used for transition. Antonia, Chambers, Sokolov, and van Atta (1981), however, found that the skin friction required to make the velocity profiles agree with the log-law were unreasonably high. Similar results were found by Cantwell, Coles and Dimotakis (1978). Mauter and van Atta (1986) found that the shear stresses in the center of turbulent spots were 10% to 15% lower than those found by Wygnanski, Sokolov, and Friedman (1976), and concluded that turbulent correlations can be used for qualitative, but not quantitative, descriptions within the spot. A flow visualization study by Gad-El-Hak, Blackwelder and Riley (1981) found that the flow in the forward overhang of the turbulent spot was relatively passive, being cut off from the bursting mechanism at the wall.

The effects of elevated free-stream turbulence on transition have been studied by van Driest and Blumer (1963), Hall and Gibbings (1972), Abu-Ghannam and Shaw (1980), Blair (1982), and Wang, Simon and Buddhavarapu (1985). The results of a large number of transition experiments were examined by McDonald and Fish (1973), who formulated a quantitative model which allowed prediction of the onset and extent of transition as a function of free-stream turbulence. Blair (1982) and Wang, Simon and Buddhavarapu (1985), who both measured the heat transfer in transitional boundary layers, found that the temperature profiles lagged the velocity profiles and that the turbulent Prandtl number was somewhat greater than unity, as deduced from mean profile measurements.

1.2). Transition on Concave Walls

In the second portion of the experimental program, the effects of concave curvature on transition were documented. The Taylor-Görtler vortices which form on the concave wall (first predicted by Görtler--1940, see Figure 1.2) hasten the transition process by producing unstable cross-span and cross-stream inflection point velocity profiles.

Clauser and Clauser (1937) and Liepmann (1943) were the first to look at curvature effects on transition. Both researchers concluded that concave curvature had a destabilizing effect on the flow, transition occurring earlier than on a flat plate. Wortmann (1969), in a flow visualization study, identified three modes of instability. The formation of Görtler vortices was the primary instability. The secondary instability manifested itself as a tilting of the vortex structure, resulting in highly unstable double inflection point velocity profiles. A third order instability in which the vortex structure oscillated was then observed. Bippes (1978) also observed a meandering of the vortex structure prior to breakdown to turbulence. The formation of vortices was found to be described by the Görtler number, G, given by

$$G = \frac{U_{pw}\theta}{\nu}\sqrt{\frac{\theta}{R}}.$$

The critical Görtler number (G_c) was found to range from 6 to 10, in agreement with other researchers, with G_c decreasing with increasing free-stream turbulence intensity. Pressure gradients in the direction of the flow had little effect on the stability. Swearingen (1985), using smoke visualization and hot-wire rakes, found that the breakdown of vortices occurs via two

modes--a horseshoe vortex mode and a sinuous mode. Breakdown to turbulence, which eventually destroyed the coherent three-dimensional structure of the vortex field, occurred shortly afterwards. Inflection points in the spanwise direction were found to be more unstable than inflection points in the cross-stream direction. McCormack, Welker and Kelleher (1970), who studied the effect of Görtler vortices on heat transfer in a duct, found Nusselt numbers 30% to 190% greater on the curved wall than the corresponding flat-plate values. This result disagreed with their conclusion, from theoretical linear stability calculations, that there should be no net heat transferred due to the vortices.

The effects of concave curvature on turbulent boundary layers is well documented. One of the first to study this was Tani (1962), who proposed replacing the molecular diffusivity in the Görtler number with the eddy diffusivity to obtain a turbulent Görtler number. So and Mellor (1975) found a system of longitudinal vortices that were unstable, and that broke up downstream, resulting in high turbulence levels. The mean flow was not homogeneous in the cross-span direction. Ramaprian and Shivaprasad (1977) found the outer region of the boundary layer to be very sensitive to wall curvature. The outer region reached a self-preserving form very soon after entry into the curve. Mean profiles were found to agree with the log-law, the extent of the turbulent core being increased by concave curvature. Shizawa and Honami (1983) found similar results. Coles profile parameter (Π) was found to decrease to zero and even become negative. In a later paper (Shizawa and Honami--1985), they suggested that the Görtler numbers may be reduced to the stable regime if the eddy viscosity becomes large enough, causing any vortex structure within the boundary layer to disappear. Barlow

and Johnston (1988 a,b) found, using LIF flow visualization, longitudinal vortices that appeared and disappeared randomly in space and time. When vortex generators were placed upstream of the curve, however, the vortex motion stabilized. Inflows were found to suppress the bursting process, outflows to enhance it. Although lower velocities near the wall at the outflows would suggest a decrease in the local skin friction, the increase in bursting seemed to compensate for the drop, resulting in a relatively constant skin friction across the span. They felt that a two-dimensional simulation of the flow would be sufficient. Similar conclusions were reached by Simonich and Moffatt (1982) in a heat transfer study in which they found that the Stanton number varied by only 15%, even under the most energetic inflows.

1.3). The Measurement Program

In the tests, a boundary layer is allowed to undergo transition naturally, becoming a fully turbulent boundary layer by the end of the test section. The effects of three levels of free-stream turbulence were investigated (nominally 0.32%, 1.79%, and 8%). The wall curvature used in the curved wall cases was R=0.97 m. The measurements consist of the following quantities:

1). Mean and fluctuating components of streamwise velocity. Mean and fluctuating velocities were measured using a horizontal hot-wire (TSI Model 1218 Boundary Layer Probe) in isothermal flows. Free-stream fluctuating components were measured using a special rotating slant wire.

2). Mean temperature profiles. A thermocouple probe consisting of butt-welded 76 μm (3 mil) dia. chromel-constantan wires held between

two hypodermic needles, as described by Wang and Simon (1987), was used.

3). Local Stanton number. Thermocouples were embedded in the test wall for this purpose.

4). Shear stress profiles and profiles of the fluctuating component of cross-stream velocity were documented in isothermal flows where the boundary layer was sufficiently thick. A cross-wire probe (TSI Model 1243 Boundary Layer Probe) was used for these measurements.

5). Intermittency. A horizontal hot-wire was used to determine whether the flow was laminar-like or turbulent-like. An analog intermittency function was generated so that processing based upon the state of the flow (laminar-like or turbulent-like) could proceed as appropriate.

6). Profiles of the turbulent heat flux $\overline{v't'}$ were made where the boundary layer was sufficiently thick. A triple-wire probe developed for this purpose is described below. Measurements of the turbulent Prandtl number were made using this probe.

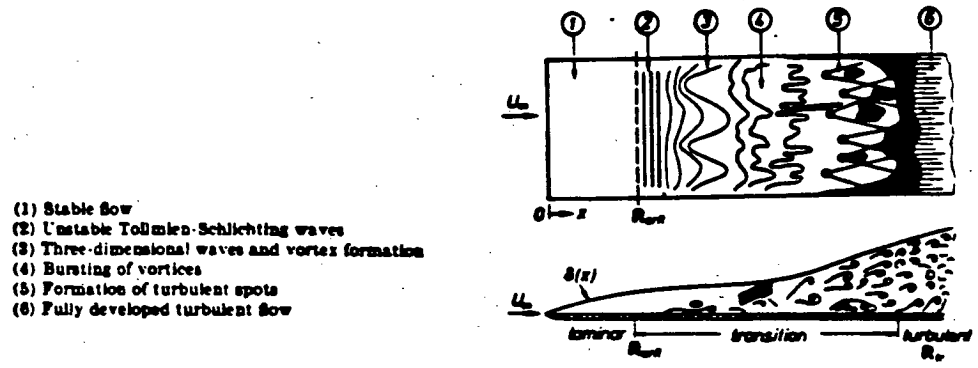

Fig. 1.1--Schematic of the transition process on a flat-plate boundary layer at low turbulence intensities. (From Schlichting--1979)

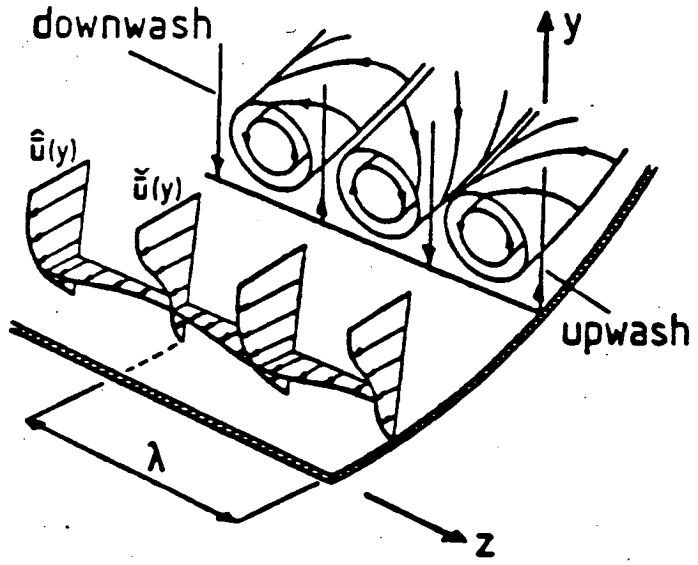

Fig. 1.2--Schematic diagram of Görtler vortices.

CHAPTER 2

Experimental Apparatus, Techniques, and Qualification

2.1). Experimental Apparatus

Wind Tunnel. A schematic of the test facility is shown on Fig. 2.1. The tunnel was originally designed and built by Wang (1984). It has since been modified by adding two settling chambers, a honeycomb pack and a motor controller. Capability of increasing the free-stream turbulence to ~9% has also been added. A brief description of the facility follows.

The wind tunnel is of the low-speed, open-return type. Air is drawn through filters capable of filtering particles larger than 5 μm which could damage the fine hot-wires downstream. A 7 hp centrifugal blower with a rated capacity of 5500 cfm and driven by a 3-phase, 230 V, 10 hp motor forces air through a series of grids and a honeycomb section. The grids provide resistance, aiding in the redistribution of the flow, while the honeycombs remove swirl and orient the flow axially. An oblique header deflects the flow into a heat exchanger used to control the flow temperature. A 3/4 hp motor-driven centrifugal pump circulates water from a 40 gallon tank which serves as a thermal capacitor. Immediately downstream of the heat exchanger is a honeycomb pack which re-orients the flow axially. Five screens downstream of the honeycomb break up the flow, after which it enters a 10.6:1 contraction nozzle. The nozzle has an exit flow aspect ratio of 6:1 to minimize secondary flow effects in the test section. The velocity at the exit of the nozzle can be continuously varied from 6 m/s to 35 m/s using a motor controller (Louis-Allis Lancer Jr. VT, 10 hp). Strong suction was applied at the exit of the contraction to re-start growth of the boundary layer. A 2 hp centrifugal fan

draws flow from the suction box and returns it to the filter box. The suction rate is controlled by a valve in the ductwork.

Two levels of higher free-stream turbulence in the test section can be achieved with the use of inserts. A removable grid designed to generate ~1.5% free-stream turbulence in the test section could be placed between the screen pack and the contraction nozzle. The grid consisted of 2.5 cm aluminum strips riveted together in a square array on 10 cm centers. Free-stream turbulence intensities of ~8% at the inlet of the test section could be achieved using an insert section after the contraction nozzle. This insert, shown on Fig. 2.2, consists of a bi-plane grid of 4.2 cm OD PVC pipes on 10.8 cm centers and a 96.5 cm long establishment region to allow for turbulence development. The grid was similar to that used by O'Brien and vanFossen (1985). Mean and fluctuating velocity measurements at the exit of the establishment region (just before the test section) shown on Fig. 2.3 measured with a hot-wire indicate velocities that are uniform to within 3%, and turbulence intensities that are uniform to within 6%. A rotating slant wire (see Russ--1989), used to measure all three components of velocity, showed that $u' \sim 1.06v'$ and $u' \sim w'$. The turbulence was, thus, quite isotropic.

A schematic of the test wall is shown in Fig. 2.4. The design is similar to that of Wang (1984), the main difference being that the stainless steel/3-M P-19 film has been replaced by a lexan/liquid crystal sheet. The lexan allows the wall to be bent into a concave configuration without the waviness that would have resulted with a stainless steel sheet. Measurement of the emissivity of the liquid crystal sheet eliminated the need for the P-19 reflective film that had been used by Wang (1984) for radiation control. The thermal conductivity of the lexan/liquid crystal was also measured so that the

temperature drop across this element could be calculated. The measurement procedures are described in the Appendix.

The liquid crystal was added so that the transition process could be visualized. Cholesteric liquid crystals change color with temperature, easily enabling the temperature field to be mapped. Also, with a constant heat flux boundary condition, isochromes correspond to lines of constant heat transfer coefficient. The transition location can thus be determined by gradually increasing the wall heat flux and seeing where the liquid crystal first changes color (this is the point of lowest heat transfer coefficient). The liquid crystal is also useful for visualizing variations in wall temperature caused by longitudinal vortices in the concave configuration. Cooler lines correspond to the downwash between vortices, with hotter lines corresponding to the upwash. The formation and growth of the vortices can be monitored, and their spacing determined.

2.2). Instrumentation

Laboratory Computer. A Hewlett Packard Series 200 Model 16 personal computer with 1.3 megabytes of memory, a math co-processor, and Basic compiler was used for data reduction and as a controller. The computer is linked via an IEEE interface with an external dual disk drive (HP9122) which utilizes 3.5 in. double sided diskettes, and an inkjet printer (HP Thinkjet). High level HP Basic is the programming language used.

Hot-Wire Anemometer and Probes. A four channel constant-temperature anemometer (TSI IFA-100) was used to drive the hot-wires. The anemometer features a built-in microprocessor with non-volatile memory which monitors and stores set-up parameters for future use. Built-in signal

conditioners enable tailoring of the output signal, maximizing digitizing resolution of the A/D converters.

Four types of hot-wire probes were used. Single wire horizontal wire probes (TSI 1218 Boundary Layer probe) were used to measure the mean and fluctuating components of streamwise velocity in isothermal flows and in near-wall situations. The probe prongs are bent at right angles to the probe holder such that prong/flow interference is minimal. Two-wire X-type probes (TSI 1243 Boundary Layer "X" probe) were used to measure the turbulent shear stress, u'v'. The prongs of this probe are also bent at right angles to the probe holder. A specially made triple-wire probe, described below, was used to measure the turbulent heat flux, v't'.

Thermocouple Probe. A thermocouple probe constructed following the design of Blackwell and Moffatt (1975) was used to measure temperature profiles within the boundary layer. Details of the design are presented in Wang (1984). A short description follows. Chromel-constantan 0.076 mm dia. (3 mil) thermocouple wire butt-welded at their junction was held between two supports which were separated by 13 mm and made of 22 gauge stainless steel hypodermic needles. The supports are electrically insulated from one another. The support/thermocouple assembly can be rotated slightly to align the probe parallel to the test wall and perpendicular to the flow. A slight bow in the wire allowed the junction to be placed very close to the test wall.

Pressure Transducer. The transducer is of the variable reluctance type (Validyne DP45), and is designed for differential measurements of extremely low pressure differences. The diaphragm has a pressure range of 0-8.9 cm (0-3.5 in. H_2O) with an accuracy of 0.5% of full scale. The response was found to

be very linear throughout the entire operating range. Calibration of the transducer was performed against a micro-manometer (Dwyer Microtector) with an accuracy of ±0.06 mm H_20. The calibration curve was obtained by a linear fit to the data.

Carrier Demodulator. The analog output of the pressure transducer is sent to a demodulator (Validyne CD-15) which provides a stable DC output. The gain and offset on the demodulator enabled tailoring the signal to maximize digitizing resolution.

A/D Convertor. The A/D converters consisted of an HP 3437A system voltmeter, a Fluke 8840A multimeter, and two Norland (now Hi-Techniques) Prowler digital oscilloscopes. The first is a 3 1/2 digit successive approximation digitizer capable of sampling up to 3600 samples per second (ASCII mode). The Fluke is a 16 bit digitizer. The Prowler is a 12 bit digitizer capable of simultaneously sampling two channels of data at speeds up to 100 kHz. Two buffers store up to 4096 data points each. The two Prowlers may also be connected as master and slave, enabling four channels of data to be taken simultaneously. Simple data processing can be done within the unit using the built-in math, calculus and signal processing routines, or the data may be sent via the IEEE-488 interface bus to a computer.

2.3). Measurement Techniques

Spectra. PSD (Power Spectral Density) distributions of the hot-wire output voltage were obtained using software provided by Jensen Transformers, Inc. The Norland Prowler was used to digitize and store the hot-wire output, then the contents of it's buffer were transferred to the computer where FFT (Fast Fourier Transform) processing was performed.

Due to storage limitations in the Prowler (4K per channel), the spectrum was calculated by averaging the FFT of ten separate waveforms. Furthermore, this was performed at three different acquisition speeds (20 kHz acquisition with low-pass filtering of the hot-wire signal at 10 kHz, 2 kHz acquisition with filtering at 1 kHz, and 200 Hz acquisition with filtering at 100 Hz) to obtain a realistic spectrum over a wide range of frequencies. A total of 30 traces was therefore required to obtain a PSD. Due to the long times required, only one PSD (taken in the free-stream at the test section entrance) was obtained for each case.

Mean and fluctuating velocity. Mean velocities were obtained by averaging the instantaneous velocities measured using a hot-wire over approximately 30 seconds and 5000 data points. Digitizing was performed using the HP 3437A single channel A/D meter. Fluctuating velocities (rms) were found according to the formula

$$u' = \sqrt{\frac{\Sigma(u-\bar{u})^2}{N-1.}} = \sqrt{\frac{\Sigma u^2}{N-1} - \frac{(\Sigma u)^2}{N(N-1)}} \qquad (2.1)$$

The resultant mean velocity and turbulence intensity profiles were smooth.

The wall position was found in two steps. First, the probe was placed close to the wall, and traversed towards the wall in 50 μm increments until the hot-wire output voltage ceased to change. This meant that the prongs of the hot-wire probe were in contact with the wall. The probe was then traversed away from the wall until an abrupt increase in the anemometer output voltage was observed. This position was taken to be the y=0 position.

Although this sounds risky, no wire ever broke during this procedure. The calibration curves were found to be very repeatable, indicating that no straining of the wire took place. The second step in finding the wall position was performed during data reduction after the raw data was acquired and stored on disc. In turbulent flows, the law-of-the-wall, given by

$$u^+=2.44\ \ln y^+ + 5.0 \tag{2.2}$$

where $$u^+ = \frac{\bar{u}/u_{pw}}{\sqrt{C_f/\rho}}, \quad y^+ = \frac{y u_{pw}\sqrt{C_f/2}}{\nu}$$

was used to find the local skin friction coefficient (C_f) as well as the correction on the y-position. This is the Clauser (1956) technique. The data was fit to the equation $u^+=y^+$ in laminar flows, upstream of transition, to find the local skin friction. The y=0 position was found by linearly extrapolating the velocity vs. position data to the wall. Within transition, no comparable technique is available, so skin friction values were determined by fitting the near-wall data points to the u^+ vs. y^+ curve, while limiting the range of the y-corrections to those obtained in the laminar and turbulent regimes (typically 50 μm). The skin friction values thus obtained were checked by a momentum balance. Agreement was typically within 20%.

Once the proper y-corrections were made, displacement thickness (δ_1) and momentum thickness (δ_2) were calculated according to their definitions:

$$\int_0^{\delta_1} u_p dy = \int_0^{\infty} (u_p - u) dy \tag{2.3}$$

$$\int_0^{\delta_2} u_p^2 dy = \int_0^{\infty} u(u_p - u)dy \tag{2.4}$$

where

$$u_p = u_\infty \tag{2.5}$$

for the flat-wall cases and

$$u_p = \frac{u_{pw}}{1 - y/R} \tag{2.6}$$

for the curved-wall cases. U_{pw} was found by fitting equation 2.6 through two points in the free-stream. R is taken to be positive for concave curvature. Substituting equations (2.5) and (2.6) into (2.3) and (2.4) yields

$$\delta_1 = \int_0^{\infty} \left(1 - \frac{u}{u_\infty}\right) dy \tag{2.7}$$

$$\delta_2 = \int_0^{\infty} \frac{u}{u_\infty}\left(1 - \frac{u}{u_\infty}\right) dy \tag{2.8}$$

for the flat-wall cases and

$$\delta_1 = \frac{1 - \exp\left[-\frac{1}{R u_{pw}} \int_0^{\infty} (u_p - u)dy\right]}{\frac{1}{R}} \tag{2.9}$$

$$\delta_2 = R\left\{1 - \left[\frac{1}{R u_{pw}^2} \int_0^{\infty} u(u_p - u)\, dy + 1\right]^{-1}\right\} \tag{2.10}$$

for the curved-wall cases, respectively. Once δ_1 and δ_2 are found, the shape factor ($H=\delta_1/\delta_2$) and momentum thickness Reynolds numbers can then be calculated.

Momentum balances were performed using the equation

$$\frac{\tau_w}{\rho u_{pw}^2} = \frac{d\delta_2}{dx} + (2\delta_2 + \delta_1)\frac{1}{u_{pw}}\frac{du_{pw}}{dx} \qquad (2.11)$$

The balance is rough, as the term $d\delta_2/dx$ cannot be accurately determined due to the sparsity of δ_2 values.

The evaluation of uncertainties in hot-wire measurements is very difficult. Even if the uncertainty in the hot-wire calibration is made arbitrarily small, there is always the doubt whether the hot-wire response inferred from a static calibration is applicable over the frequency range of interest. Perry (1982) states that errors as high as 10% in the mean square energy distribution of the turbulence are possible, but that the broad-band turbulence results are much less affected since the energy containing components of the turbulent motions are mainly weighted toward the low-frequency end. The reader is referred to Perry (1982) for further discussion of uncertainty in hot-wire measurements. The uncertainty of the hot-wire measurements in this thesis will be taken to be 5% for the single-correlation measurements (u' and v') and 10% for the cross-correlation measurements (u'v' and v't'). These values are consistent with the scatter in the measurements as observed by the author.

Shear stress. The methodology for measuring shear stress is given in Buddhavarapu (1984), and will not be repeated here. In contrast to Buddhavarapu (1984), however, where the rotating hot-wire technique was applied, the present measurements were taken with a cross-wire probe where data is available from both sensors simultaneously, It is digitized using the

Norland Prowler. Data points (4k) were taken at a 50 Hz sampling rate. Procedures for calibration and alignment of the probe with the flow are described in Kim (1986). The shear stress data was normalized by both U_{pw} and U_τ (the shear velocity). Fluctuating quantities (u' and v') were normalized on U_{pw} only.

Stanton number. Stanton numbers (St) were measured using thermocouples embedded in the wall. The thermocouples are spaced 2.54 cm (1 in) apart along the centerline of the test section. Thermocouples are also spaced 5.08 cm (2 in.) apart in the spanwise direction at stations 1, 5, and 6 within the center 30 cm (12 in.) span. At stations 2, 3, and 4, thermocouples are spaced at 2.54 cm (1 in.) intervals to provide greater resolution. Additional thermocouples were provided to measure the free-stream temperature and the temperature difference across the fiberglass insulation. An additional lead to the voltmeter was provided to check the voltmeter zero-point.

The thermocouples were routed to an isothermal box where they were soldered to copper wires. Heat shrink tubing insulated the junctions. The isothermal box consisted of two sets of aluminum blocks of nominally 20.3 cm x 30 cm x 2.54 cm dimensions which sandwiched the thermocouples. Foam was used to seal the edges. The blocks were then wrapped with fiberglass insulation. A paper cover isolated the box from room air movements. Two additional thermocouples served as ice-bath references, and a third thermocouple measured any difference in temperature between the two sets of aluminum blocks. A 150 channel scanner (Fluke 2205A) and digital multimeter (Fluke 8840A) were used to acquire the thermocouple voltages.

The Stanton number is a non-dimensional form of the heat transfer coefficient which relates the actual heat transferred to the flow to the maximum heat-carrying capacity of the flow. The quantities needed to determine St are the wall heat flux, the wall temperature, the free-stream velocity and temperature, and fluid properties. The free-stream velocity and temperature and the fluid properties are easily obtainable. The wall heat flux was computed by measuring the voltage drop across a precision resistor (~2 Ω) to find the current (i_h) and the voltage drop across the heater (V_h). The power dissipated in the heater per unit area ($\dot{q}''_h$) was computed from

$$\dot{q}''_h = \frac{i_h V_h}{A_h} \tag{2.12}$$

The power factor was measured to be very close to unity. Corrections were made for back heat loss (through the fiberglass insulation), streamwise conduction and radiation. The conductivity of the lexan/liquid crystal composite (k_w) and the emissivity of the liquid crystal (ε) were measured as described in Appendix A1 and A2. Wall temperatures were computed by measuring the thermocouple voltages and the heat flux. Since the thermocouples are located behind the lexan/liquid crystal composite, corrections must be made for the temperature drop within the composite. This correction was computed from

$$\Delta T = \frac{\dot{q}''_w \Delta x}{k_w} \tag{2.13}$$

where Δx is the composite thickness and $\dot{q}''_w$ is the heat generated in the heater minus the back heat loss and the streamwise conduction divided by

the heated area. This corrected wall temperature is also the temperature used in calculating the radiant heat transfer.

An uncertainty analysis on the Stanton number, performed with the wall in the straight-wall configuration, yielded a maximum uncertainty in St of 6%. This number was calculated using the methodology of Kline and McClintock (1953) whereby the uncertainty of the input parameters to St (δx_i), all based upon the 95% confidence level, could be combined to yield the uncertainty in St (δSt) at the same confidence level. This is the root-sum-square method given by

$$\delta St = \left\{ \sum_i \left[\left(\frac{\partial St}{\partial x_i} \right) \delta x_i \right]^2 \right\}^{1/2}$$

The partial derivatives in the above equation were evaluated by slightly perturbing the values of the input parameters one by one and observing their effect on St. The use of a computer program made the calculation very easy.

Mean Temperature Profiles. Mean temperature profiles were measured using the thermocouple probe described earlier. The local wall temperature was determined by linearly interpolating between the wall temperatures obtained from the thermocouples upstream and downstream of the probe location. The y-position correction to the temperature profiles was obtained by comparing the near-wall data points to the temperature gradient line calculated from the wall heat flux, which was measured independently. An example is given on Fig. 2.5.

Data was reduced to wall coordinates (T^+ vs. y^+) according to the equation

$$T^+ = \frac{(T_w - T)\sqrt{\frac{\tau_w}{\rho}}}{\frac{\dot{q}_w''}{\rho C_p}}, y^+ = u\sqrt{\frac{\rho}{\tau_w}} \qquad (2.14)$$

The wall shear (τ_w) is that deduced from the corresponding velocity profile measured in the unheated flow.

Energy Balance. Energy balances were performed by comparing the enthalpy thicknesses obtained by integrating the wall heat flux with that obtained from the mean velocity and temperature profile measurements at each station. The reader is referred to Appendix E of You (1986) for the numerical integration scheme employed.

Triple-wire Probe for Turbulent Heat Flux Measurements. A probe developed for this purpose (Kim and Simon--1988) is shown on Fig. 2.6. In the method used for the probe in this particular reference, two parallel hot-wires, operated at different overheat ratios, were used to deduce the instantaneous temperature in the flow. The extreme sensitivity of this probe to spatial averaging and free-stream temperature variations made operation of this probe quite inconvenient, however. The low frequency response of the probe (estimated at a few hundred hertz) did not present serious measurement problems, but a higher frequency response would have been desirable. To solve these problems, it was decided to use the same probe geometry, but operate one wire in a constant-current mode as a resistance thermometer to measure the instantaneous flow temperature, and to operate the other two wires as constant-temperature wires in a standard cross-wire configuration to obtain the instantaneous u and v velocity components. The disadvantage of this method is that a fine (~1 μm diameter), fragile platinum

wire must be used to measure the temperature and sensor survivability can pose problems. The advantages, though, are that the measurement of temperature is fairly direct, with much less sensitivity to spatial averaging effects and no sensitivity to slow ambient temperature variations. Furthermore, by using frequency compensation, the frequency response of the cold-wire can be greatly improved.

A scheme similar to that used by Hishida and Nagano (1978) for two-wire measurements was chosen as the compensation scheme. In this method, the heat transfer coefficient over a cold-wire was estimated from the parallel hot-wire signal. It was shown in their paper that

$$V_{c1} = \frac{\frac{k}{V_2^2} V_{21} \frac{dV_1}{dt} + V_1}{1 + \varepsilon \frac{k}{V_2^2} \frac{dV_1}{dt}} \qquad (2.15)$$

where V_{c1} = voltage across cold-wire if it had an infinite frequency response

V_1 = voltage across cold-wire (measured)

V_{21} = (cold-wire current)x(hot-wire resistance) (constant)

V_2 = voltage across hot-wire (measured)

ε = ratio of hot-wire and cold-wire resistance at a reference temperature (constant)

k = empirical constant determined from a frequency response test

It is to be noted that in an isothermal flow, $dV_1/dt = 0$, and eqn. (2.15) reduces to $V_{c1}=V_1$ as it should. The compensated resistance of the wire (R_c), and, thereby, the compensated flow temperature may then be obtained from

$$R_c = \frac{V_{c1}}{i} \tag{2.16}$$

where i is the current through the wire. Once the instantaneous flow temperature is known, the hot-wire signals can easily be compensated. The constant, k, in eqn. (2.15) is determined from a square-wave test in which the probe was placed in a flow and the cold-wire current stepped down from 30 mA (wire is heated) to 1 mA (wire cools to essentially room temperature). The voltage across the wire along with it's derivative is monitored on a digital oscilloscope as it cools in a characteristic exponential fashion. A compensated voltage variation is calculated from eqn. (2.15) using a guessed value of k. The k-value that yields a step drop in V_{c1} is taken to be the correct value. The frequency response of the probe, with compensation, was measured to be 4 kHz.

A circuit built for this purpose (Fig. 2.7) consists of a current source, an amplifier and a differentiator. A current source of 1 mA drives the cold-wire. The voltage across the wire is amplified 200 times then sent through a differentiator. The noise requirements on the circuit are tight. The cold-wire has a nominal resistance of 50 ohms with the variation of wire-resistance within the heated boundary layer being less than 0.05 ohms (rms). For a nominal wire-current of 1 mA, this corresponds to only a 50 μV (rms) variation. The circuit noise must be much smaller than this to get an adequate signal-to-noise ratio. The noise of the amplifier is 0.5 μV rms

referenced to input, yielding a signal-to-noise ratio of 100; the signal-to-noise ratio at the exit of the differentiator is 30. Careful attention to minimizing the potential for ground loops is essential to obtain these values.

The probe was qualified in a zero pressure gradient flat-plate, two dimensional, turbulent boundary layer, with a momentum thickness of Re_θ=1487 and a uniform wall heat flux boundary condition (q_w"=178.9 W/m2). The boundary layer thickness and free-stream velocity were 0.675 cm and 26.6 m/s, respectively. The probe was traversed across the boundary layer and measurements of u'v', t', u't' and v't' were made. Pr_t values were determined from it's definition,

$$Pr_t = \frac{\overline{u'v'}/\frac{\partial \bar{u}}{\partial y}}{\overline{v't'}/\frac{\partial \bar{t}}{\partial y}} \qquad (2.17)$$

Two dual channel digital oscilloscopes (Norland Prowler), wired as master and slave, were used to digitize the outputs of the hot-wire bridges along with the cold-wire voltage and it's time derivative. Data was sampled at 50 Hz over an 80 second period. An IEEE-488 interface bus was used to transfer the contents of the oscilloscope buffers to a computer (HP 9816) for storage on disc. Data processing occurred off-line.

Reduced data were compared with that of Blair and Bennett (1984) and Gibson, Verriopoulos and Vlachos (1984). All profiles were in excellent agreement with the data of these researchers. Measured Pr_t values are shown on Fig. 2.8. The scatter in the data, typical of direct Pr_t measurements, is larger

in the outer regions of the boundary layer where transport terms and mean gradient terms are weak.

The uncertainty in measured Pr_t values can be estimated using the methodology of Kline and McClintock (1953) discussed above. The error in u'v' is assumed to be 10%. The error in v't' is also estimated to be 10% based on scatter in the data and agreement of near-wall v't' values with measured wall heat fluxes. The uncertainties in the gradients of velocity and temperature become very large in the outer portion of the boundary layer as the gradients become small. For example, for the low TI, flat-wall, station 6 profile (the data is given in the Appendix), the error in the gradients of velocity rise from 12% at y/δ=0.395 to 53% at y/δ=0.85. Similar errors were observed for the temperature gradients. Applying the root-sum-square propagation of the uncertainty, the errors in Pr_t increase from 22% to 85% at the above y/δ locations, respectively. The uncertainty in Pr_t increases sharply for this case, at y/δ=0.71. The uncertainty of the other Pr_t profiles is expected to behave in a similar manner.

Intermittency Circuit. A circuit for determining when the flow is laminar or turbulent has been constructed. The output of the circuit, an analog signal which is high when the flow is turbulent and low when the flow is laminar, is called the intermittency function. The intermittency value (γ) can be found simply by time-averaging the intermittency function. The intermittency function can also be used to conditionally sample the signals so that data is processed only when the flow is laminar-like or turbulent-like.

The circuit takes advantage of the much larger time derivative of the turbulent-like signal as compared to the time derivative of the laminar-like signal: the hot-wire-anemometer signal is processed by a series of filters,

differentiators and rectifiers (Fig. 2.9). At the level detector, the signal is compared to an adjustable threshold value. If it is higher than the threshold, the output signal of the level detector is high (turbulent-like). It is low (laminar-like) otherwise. The analog signal, thus obtained, can be used to conditionally sample other quantities, tagging them to either laminar-like or turbulent-like behavior.

It can be seen in Fig. 2.9 that the intermittency measuring unit has two channels--the direct channel and the differentiated channel. The two channels are used to solve the problem of zero-crossing. This problem is explained in Fig. 2.10 where the time-derivative of a turbulent signal is shown. When this signal is compared to a threshold value at the level detector, the turbulent flow signal is generally higher than the threshold giving a recorded "high" signal. However, it is also seen that the signal unavoidably becomes smaller than the threshold as it crosses zero even though it is known to be from the turbulent-like flow. During this time the flow is falsely declared laminar. This is the zero-crossing problem. The circuit uses the second derivative of the signal (differentiated channel) to correct for this. This differentiated signal retains the characteristics of the first-derivative with one important difference. It is high when the zero-crossing event takes place. When the second time-derivative is compared with the threshold value there will again be regions where the flow is falsely declared laminar. However the times during which each of the two channels is at fault generally do not coincide. An "OR" gate is then used to combine the two signals. Its output is high when either of the two signals is high and is low only when both inputs are low. The number of points falsely declared laminar is thus greatly reduced. A high-pass filter at the output of the OR

gate then eliminates the remaining points falsely declared turbulent. The threshold values of the two level detectors are adjustable and are tuned for each different flow situation. A tuning procedure that has been found to work well has been established.

An example of the circuit performance in the transition region is given on Fig. 2.11. It may be seen that the circuit does a good job of discriminating between laminar and turbulent flow. The main deficiency of the circuit is that it uses a criterion based on the derivative of a hot-wire signal and not on eddy transport (u'v')--the mark of turbulence. The advantage of this technique, however, is that the wall can be approached very closely with the single-wire probe, something not possible with the bulky cross-wire probes necessary to determine u'v'.

The circuit does not perform as well in discriminating between boundary layer and free-stream flow in the boundary layer wake region (also an intermittent flow). The turbulent fluctuations in the wake decrease in intensity, while local pressure fluctuations cause unsteadiness in the free-stream, making a criterion based on velocity difficult to implement. A better way of discriminating the two regimes in this flow which are intermittent at the edge of the boundary layer is to heat the wall and use a criterion based on temperature. This technique assumes that mixing in the turbulent portion of the wake is thorough enough such that the flow temperature is higher than in the laminar region which is at the free-stream temperature. The advantage of this technique is it's insensitivity to velocity fluctuations. The disadvantage, of course, is that an additional high frequency response resistance thermometer (e.g.- a 1 μm Pt wire) is needed. Also, this technique requires heating the wall, which affects the transition start location.

A comparison of the velocity and temperature measurement schemes is shown on Fig. 2.12, where a hot-wire voltage trace and a signal from a 1 μm dia. Pt resistance thermometer are presented. The data was taken using the triple-wire probe described earlier. The wake passing seems to be more clearly indicated from the cold wire signal than with the hot-wire signal.

In conclusion, the intermittency circuit is seen to give good results in cases where there is a clear distinction between regimes (e.g. - transitional boundary layers). The circuit does not perform well in the wake region of turbulent boundary layers and, it is suspected, in the outer portion of transitional boundary layers as well.

2.4). Test-wall and Tunnel Qualification

Mean velocity and streamwise turbulence intensity measurements within the potential core of the flow exiting the nozzle showed a peak-to-peak variation in velocity of 0.2% about a nominal velocity of 27 m/s. Measurements of mean temperature within the flow exiting the nozzle showed a peak-to-peak variation of 0.02°C. The static pressure coefficient (Cp) was adjusted to within 1.79% all along the test wall for both low and high TI cases.

Qualification of the test section in a flat wall configuration with regard to the transition location was initially performed by heating the wall and visualizing transition using a liquid crystal sheet. Transition was assumed to occur at the location where the liquid crystal first changes color as the heat flux is gradually increased. This corresponds to the highest wall temperature, or, since the wall heat flux is essentially uniform, the location of lowest heat transfer coefficient. Various parameters such as the leading edge suction flow

rate and the suction slot width were optimized such that transition occurred as far downstream as possible for a given free-stream velocity and for the low free-stream turbulence intensity case. The outer flexible wall was adjusted such that there was no pressure gradient along the wall.

This method of determining the transition start location is not reliable, however, due to the destabilizing effect of heating on the boundary layer. It is well known (Schlichting--1979) that the heating of a surface in air causes an inflection in the near-wall velocity profile due to a local increase in viscosity. Transition was expected to occur earlier in a heated boundary layer, and the transition length was expected to decrease. The variation of Stanton number along the wall (low TI case) for two wall heat-fluxes taken in the test facility is shown on Fig. 2.13. It is seen that while transition occurs over a shorter length with increasing wall heat flux, as expected, the transition start location is not affected. This is due to encroachment of the side-wall influence towards the centerline of the test wall. Transition was observed to occur first at the tunnel end-walls, due to possible corner flow effects, then propagate to the tunnel centerline. The transition start location was thus fixed by the end wall effects, obscuring the influence of heating. Transition start was defined in this study as the location where the near-wall intermittency as measured in the unheated flow reached 5%.

The St values measured in the laminar flow (before the onset of transition in Fig. 2.13 do show, however, how accurately St can be measured. Except for a small unheated starting length effect (the first five points), the Stanton numbers in the laminar boundary layer are seen to be in excellent agreement with the accepted correlation for a constant wall heat flux boundary condition. The slight dip in Stanton number values below the

laminar correlation is caused by a decrease in the wall heat flux with streamwise distance due to increasing radiant heat loss. A STAN5 (Crawford and Kays--1976) simulation with the measured wall heat flux input as the wall boundary condition yielded Stanton numbers 4% lower than the constant wall heat flux correlation at the start of transition--in excellent agreement with the above trends in the data.

The Reynolds numbers based on displacement and momentum thicknesses at the beginning of transition (unheated flow) were measured to be 1920 and 737, respectively. The free-stream turbulence intensity, measured using a cross-wire (TSI Model 1243 Boundary Layer Probe) rotated into two positions to get all three velocity components, was 0.32%. A plot of the Reynolds number based on displacement thickness vs. the free-stream turbulence intensity for the present study is shown on Fig. 2.14. Transition is seen to occur slightly earlier for the present low TI case than for other researchers due to the sidewall influence.

An energy balance was performed by integrating the wall heat flux along the centerline of the test wall and comparing this with the increase in energy carried in the boundary layer flow as calculated from the mean velocity and temperature profiles. The closure was within 3%.

Further qualification of the test section and measurement techniques was performed by comparing data measured in the flat wall transitional flow with that of other researchers. Measurements of the mean velocity profiles, shape factor (H) and intermittency all were consistent with other researchers' results. For the heat transfer data, it was decided to work with the lowest wall heat-flux level which would still give reasonable wall-to-freestream temperature differences at the end of transition (the location of smallest

temperature difference). The nominal heat flux chosen was 175 W/m^2, which yielded a minimum temperature difference of about 4° C for the TI=0.32% case. As mentioned earlier, the transition process was significantly affected by the heating at this wall heat flux, the near-wall intermittency increasing from 45% with no heating to 98% with heating at a selected point within the transition zone. This unfortunately means that a precise comparison of the heated and unheated data cannot be made for the low TI case. For this reason, no heat transfer data will be presented for the low TI case, except for measurements of the turbulent heat flux and turbulent Prandtl number (Pr_t). Transition for the high TI case (TI=1.79%) was not affected by heating, the intermittency remaining invariant with the wall heat flux. All heat transfer data will therefore be presented for cases where TI=1.79% and higher.

A summary of boundary layer parameters for each of the five cases to be discussed is presented on Tables 1 through 5.

St.	x (cm)	Upw (m/s)	δ (cm)	δ1 (cm)	δ2 (cm)	Re_x x1E-5	Reδ2	C_f x1E+3
1	0.114	28.15	0.141	0.0389	0.0155	1.964	265.7	1.65
2	0.343	28.28	0.218	0.0692	0.0275	5.906	473.6	0.96
3(L)	0.572	28.17	-----	0.0951	0.0383	9.748	652.5	0.71
3(Tu)	"	"	-----	0.1757	0.0790	"	1348	2.70
3(Tr)	"	"	0.324	0.0950	0.0390	"	664.8	0.78
4A(L)	0.800	26.06	-----	0.1120	0.0481	12.55	754	0.79
4A(Tu)	"	"	-----	0.1348	0.0925	"	1450	3.15
4A(Tr)	"	"	0.894	0.1107	0.0553	"	867.4	1.40
4(L)	0.800	28.09	-----	0.1014	0.0437	13.53	739.5	0.79
4(Tu)	"	"	-----	0.1231	0.0851	"	1438	3.10
4(Tr)	"	"	1.339	0.1019	0.0577	"	975.9	1.90
5(L)	1.029	28.72	-----	0.0914	0.0449	17.78	776.6	1.10
5(Tu)	"	"	-----	0.1423	0.1044	"	1805	3.82
5(Tr)	"	"	1.010	0.1224	0.0860	"	1487	3.77
6	1.257	32.64	1.105	0.1437	0.1054	24.82	2080	3.70

Table 1--Summary of boundary layer parameters for Case 1. Values conditionally sampled on laminar, turbulent and transitional flow are denoted by (L), (Tu), and (Tr), respectively.

St.	x (cm)	U_{pw} (m/s)	δ (cm)	δ_1 (cm)	δ_2 (cm)	Re_x x1E-5	$Re_{\delta 2}$	C_f x1E+3	ΔT_w (C)	Q_w'' (W/m2)
1	0.114	16.65	0.250	0.0509	0.0212	1.174	218.1	2.26	4.52	173.4
2(L)	0.343	16.29	-----	0.0850	0.0369	3.442	370.0	1.61	-----	-----
2(Tu)	"	"	-----	0.1017	0.0645	"	647.6	4.20	-----	-----
2(Tr)	"	"	0.318	0.9852	0.0378	"	379.0	1.70	7.81	154.8
3A(L)	0.572	12.29	-----	0.1277	0.0627	4.322	473.7	1.70	-----	-----
3A(Tu)	"	"	-----	0.1685	0.1150	"	869.3	4.10	-----	-----
3A(Tr)	"	"	0.873	0.1330	0.0754	"	570.2	2.60	6.46	122.0
3(L)	0.572	16.18	-----	0.0970	0.0490	5.691	488.3	1.76	-----	-----
3(Tu)	"	"	-----	0.1420	0.1014	"	1009	4.50	-----	-----
3(Tr)	"	"	0.894	0.1152	0.0756	"	753.1	4.00	5.14	169.9
4(L)	0.800	16.38	-----	0.0922	0.0542	8.057	546.2	2.20	-----	-----
4(Tu)	"	"	-----	0.2121	0.1614	"	1625	4.25	-----	-----
4(Tr)	"	"	1.339	0.1662	0.1188	"	1196	4.20	4.44	173.9
5	1.029	16.81	1.749	0.2093	0.1538	10.62	1587	4.05	4.55	173.4

Table 2--Summary of boundary layer parameters for Case 2. Values conditionally sampled on laminar, turbulent and transitional flow are denoted by (L), (Tu), and (Tr), respectively.

St.	x (cm)	U_{pw} (m/s)	δ (cm)	δ1 (cm)	δ2 (cm)	Re_x x1E-5	$Re_{\delta 2}$	C_f x1E+3	ΔTw (C)	Qw" (W/m2)
1	0.114	9.07	0.358	0.0516	0.0319	0.649	171.4	7.00	4.17	197.8
2	0.343	9.31	1.146	0.1204	0.0832	1.985	481.6	5.75	5.44	190.7
3	0.572	9.24	1.839	0.2022	0.0143	3.273	820.8	4.85	6.14	186.7
4	0.800	9.19	2.451	0.2599	0.0191	4.549	1083	4.70	6.54	184.4

Table 3--Summary of boundary layer parameters for Case 3.

St.	x (cm)	Upw (m/s)	δ_1 (cm)	δ_2 (cm)	Re_x x1E-5	$Re_{\delta 2}$	C_f x1E+3	ΔT_w (C)	Q_w'' (W/m2)
1	0.089	16.53	0.0541	0.0213	0.917	219.2	2.23	----	-----
2(d)	0.356	17.24	0.0317	0.0164	3.760	172.9	4.60	----	-----
2(u)	0.356	17.23	0.1160	0.0531	3.757	561	2.10	----	-----
3(d)	0.610	17.08	0.1407	0.0996	6.389	1044	4.80	3.95	147.8
3(u)	0.610	17.11	0.1623	0.1124	6.403	1181	4.15	4.23	147.8
4(d)	0.876	17.14	0.1532	0.1167	9.244	1231	5.20	3.88	148.3
4(u)	0.876	17.13	0.2487	0.1820	9.234	1917	4.20	4.20	148.3
5(d)	1.130	16.76	0.2436	0.1898	11.64	1954	4.70	4.15	146.6
5(u)	1.130	16.76	0.3679	0.2718	11.65	2801	3.70	4.31	146.6

Table 4--Summary of boundary layer parameters for Case 4. Upwash and downwash are denoted by (u) and (d), respectively.

St.	x (cm)	Upw (m/s)	Re_x x1E-5	C_f x1E+3	ΔT_w (C)	Q_w'' (W/m2)
1	0.089	17.70	0.965	6.00	3.09	216.9
2	0.356	17.70	3.861	5.90	3.67	213.8
3	0.610	17.70	6.635	5.30	4.11	211.4
4	0.876	17.70	9.543	5.30	4.04	211.8
5	1.130	17.70	12.34	5.00	4.21	210.8

Table 5--Summary of boundary layer parameters for Case 5.

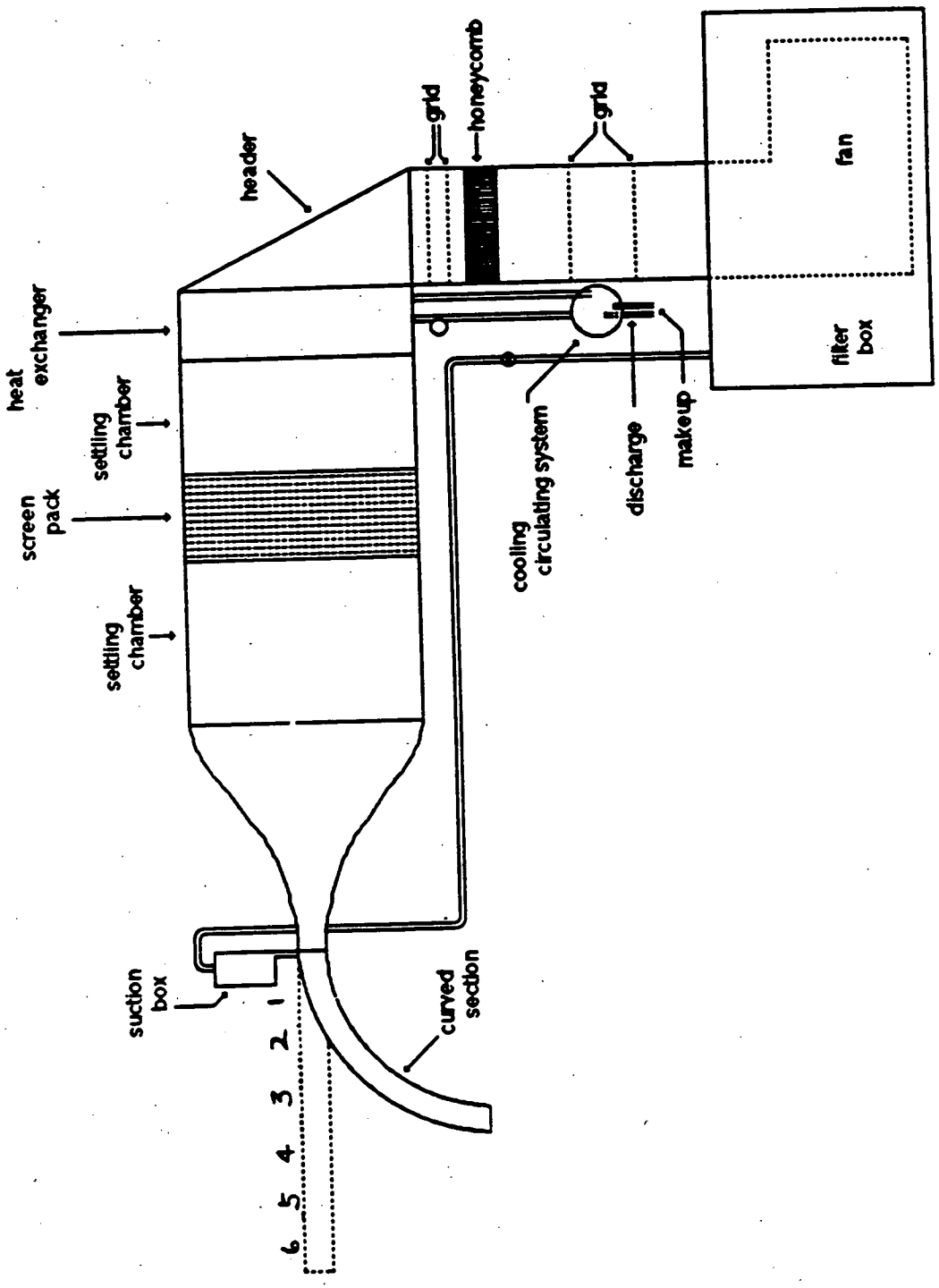

Fig. 2.1–Schematic of test facility (plan view).

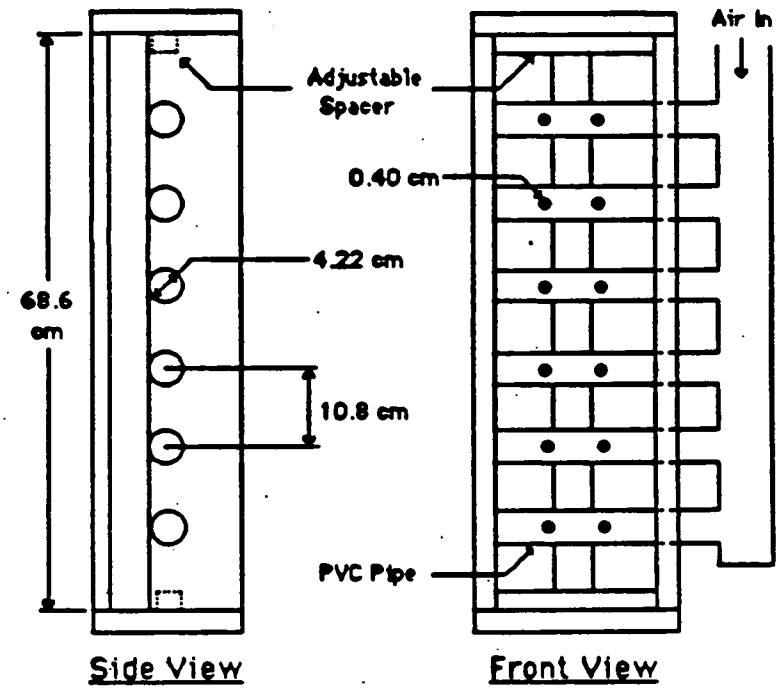

Fig. 2.2--Jet-grid turbulence generator (from Russ--1989).

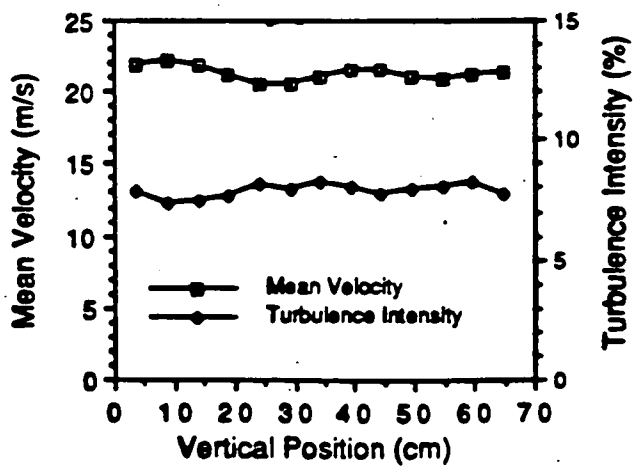

Fig. 2.3--Mean and fluctuating velocity measurements at the exit of the turbulence establishment section (from Russ--1989).

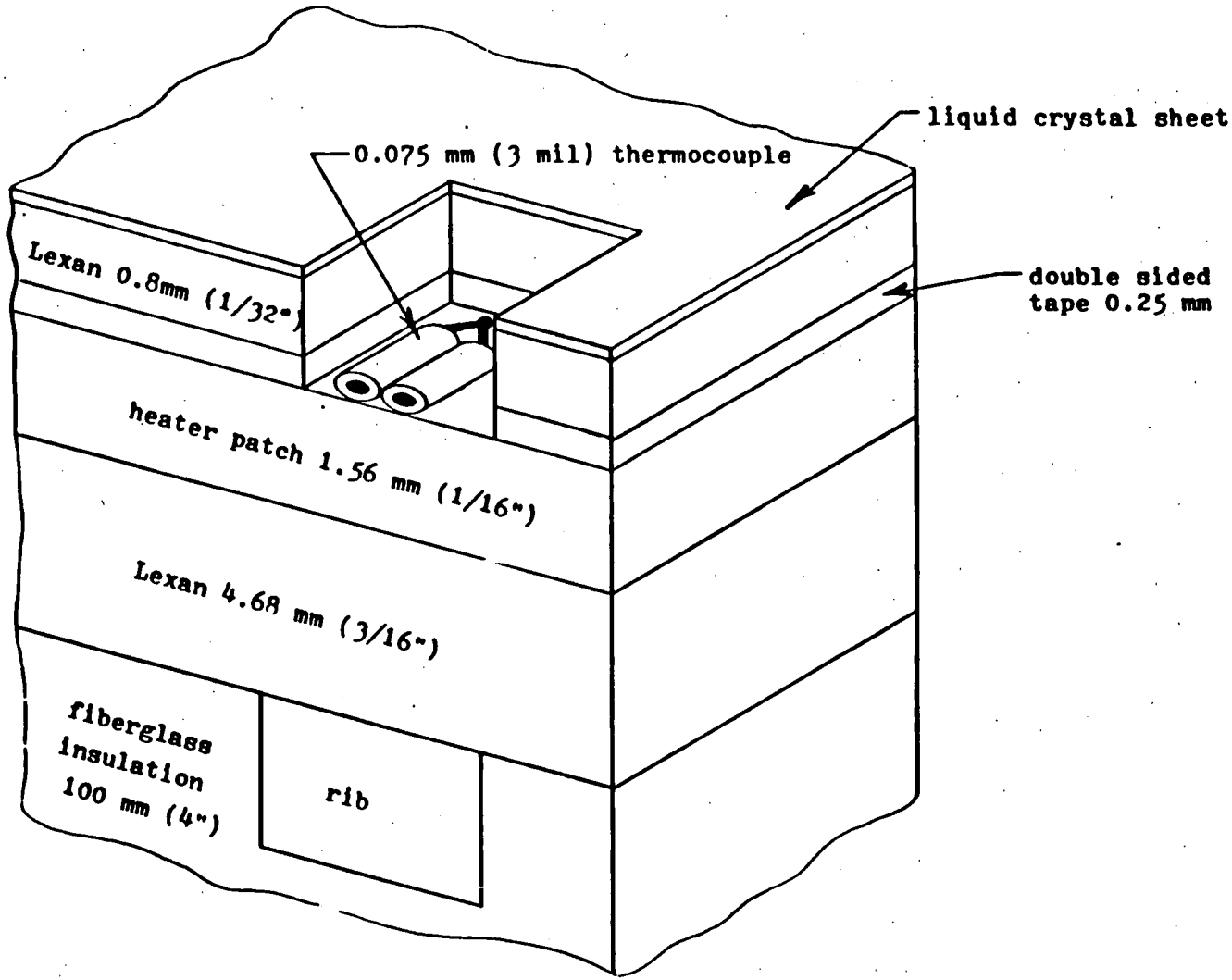

Fig. 2.4--Cross-section of heated test-wall (not to scale).

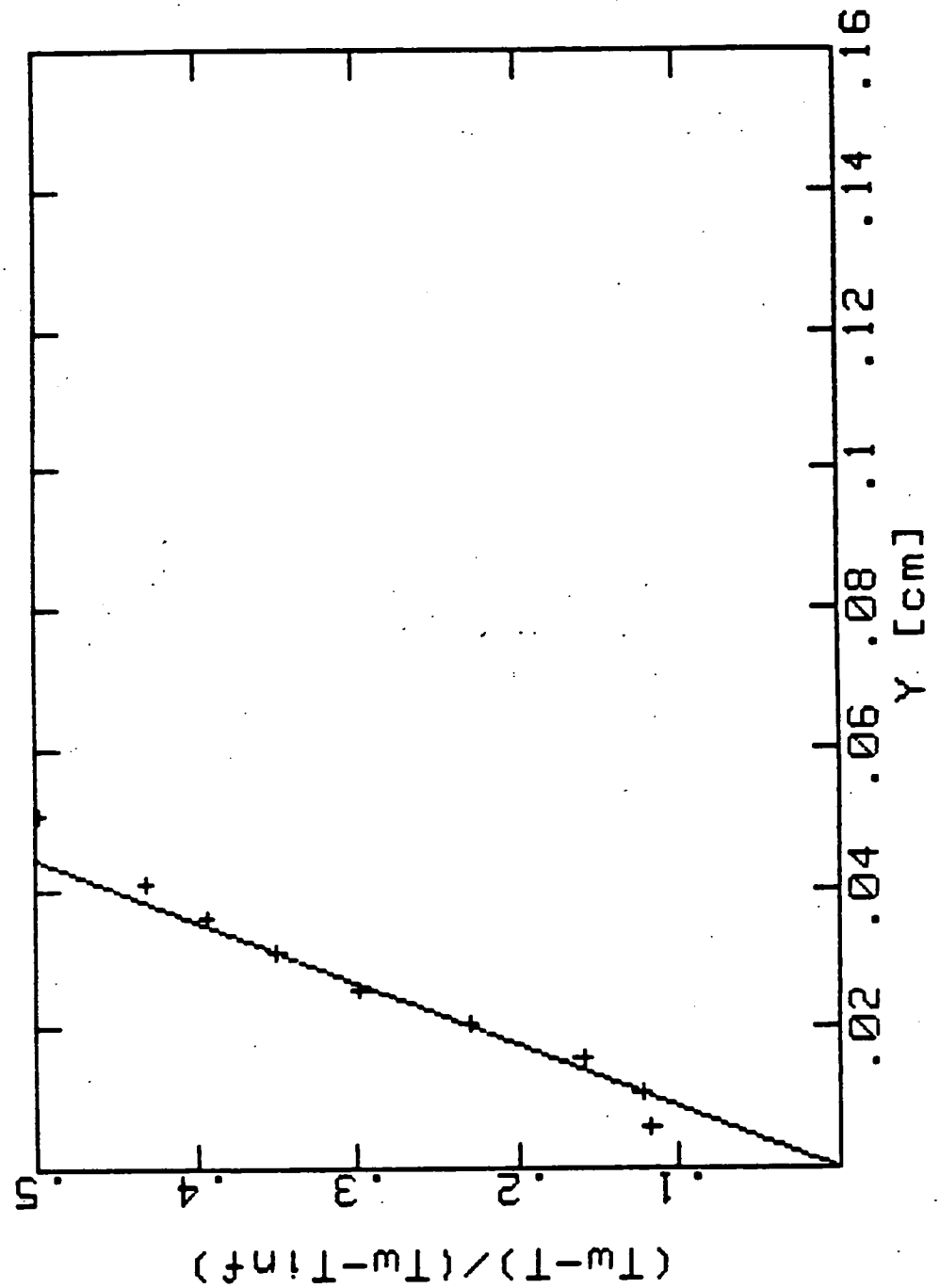

Fig. 2.5--Illustration of the method used to determine the distance of thermocouple probe from the heated wall.

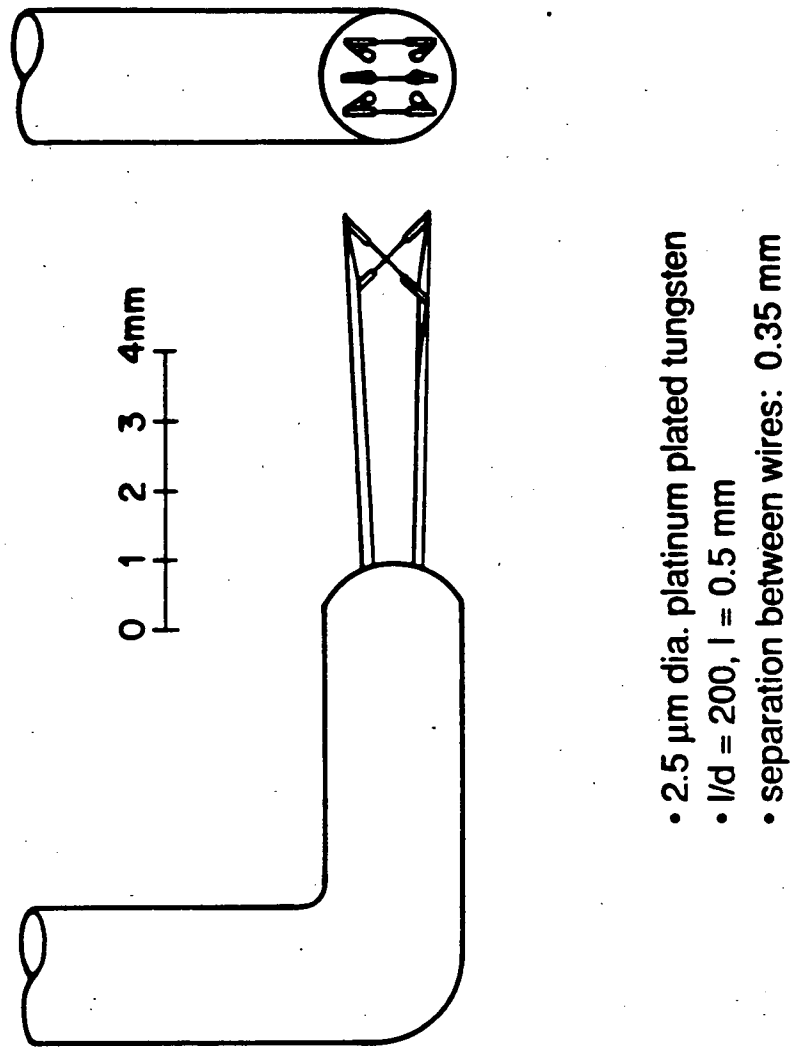

Fig. 2.6–Schematic of triple-wire probe used to measure turbulent heat fluxes.

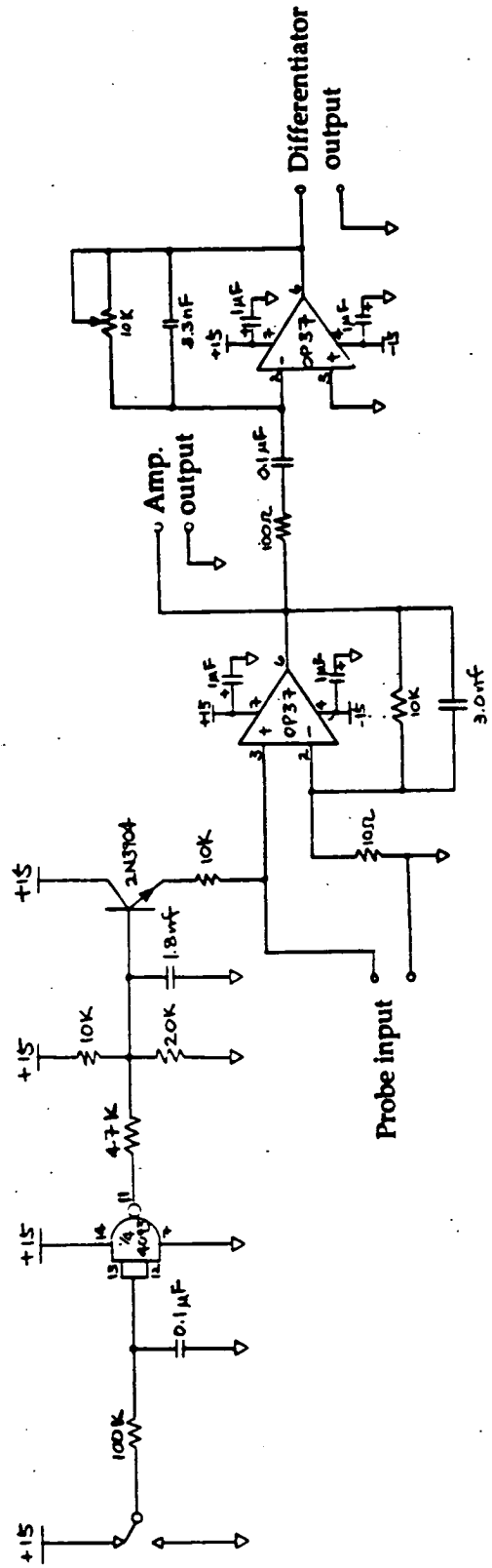

Fig. 2.7--Schematic of circuit used to measure cold-wire resistance.

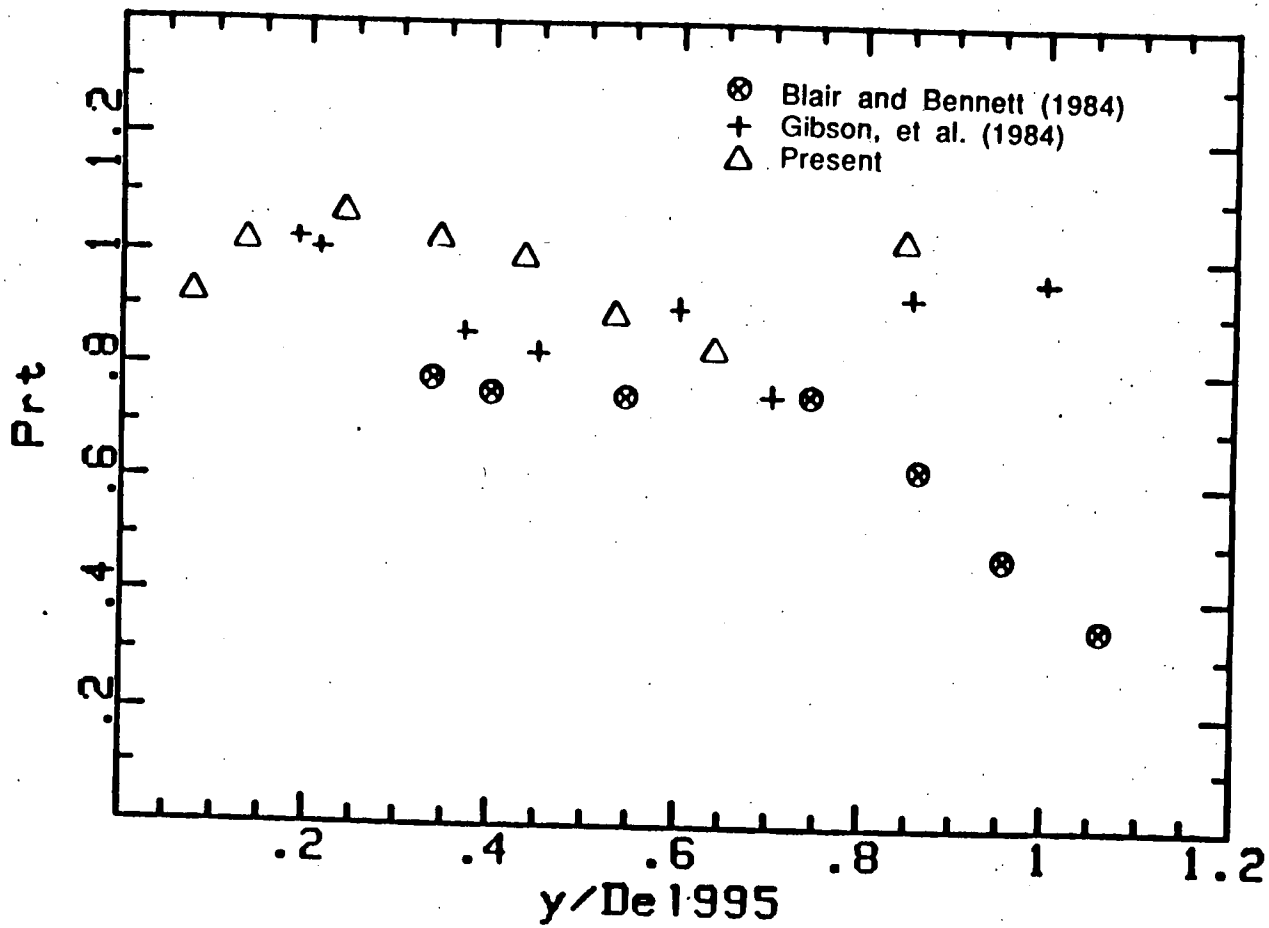

Fig. 2.8--Comparison of Pr_t values measured using the probe to the data of Blair and Bennett (1984) and Gibson, Verriopoulos and Vlachos (1984).

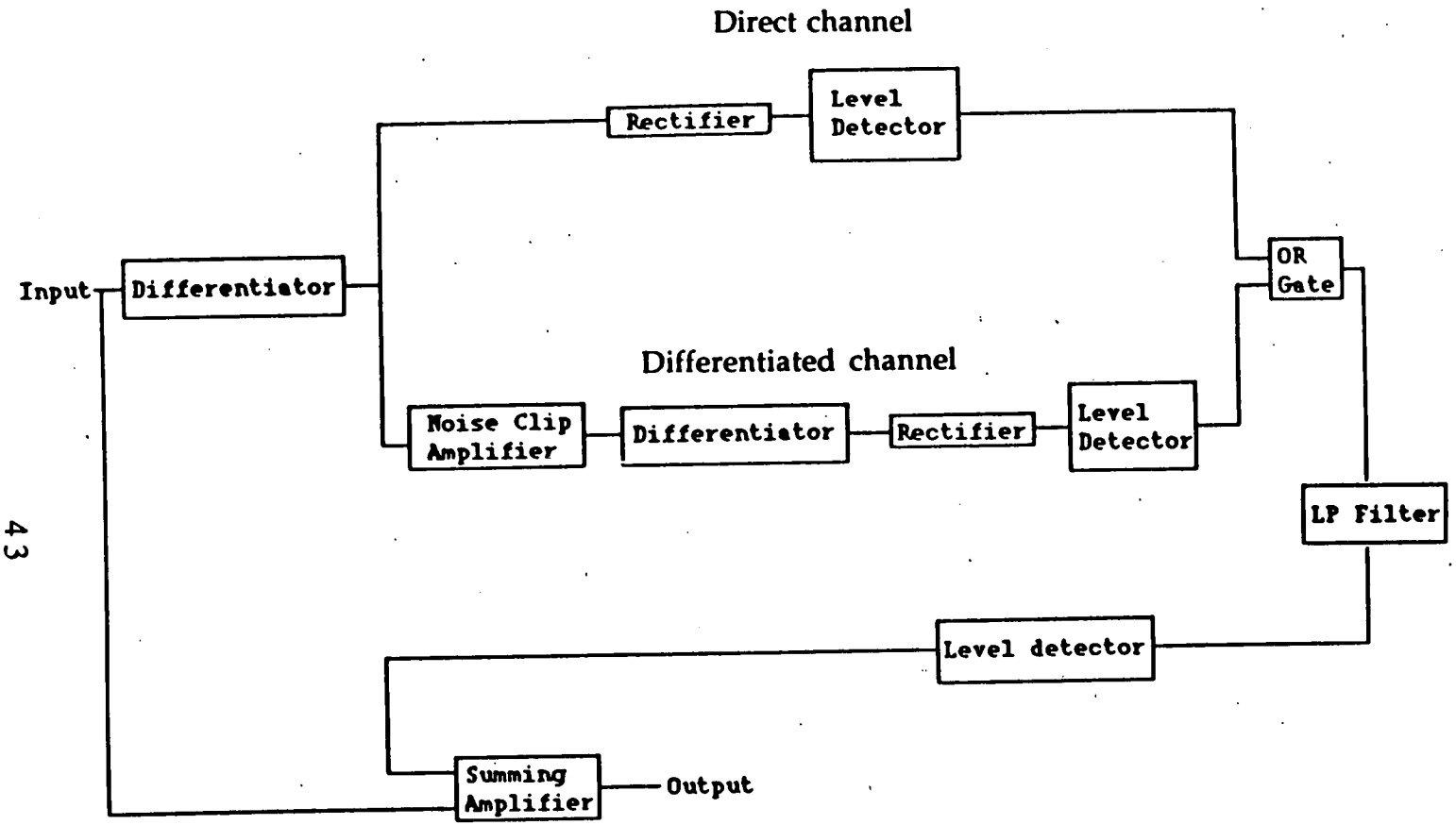

Fig. 2.9--Block diagram of intermittency measuring unit.

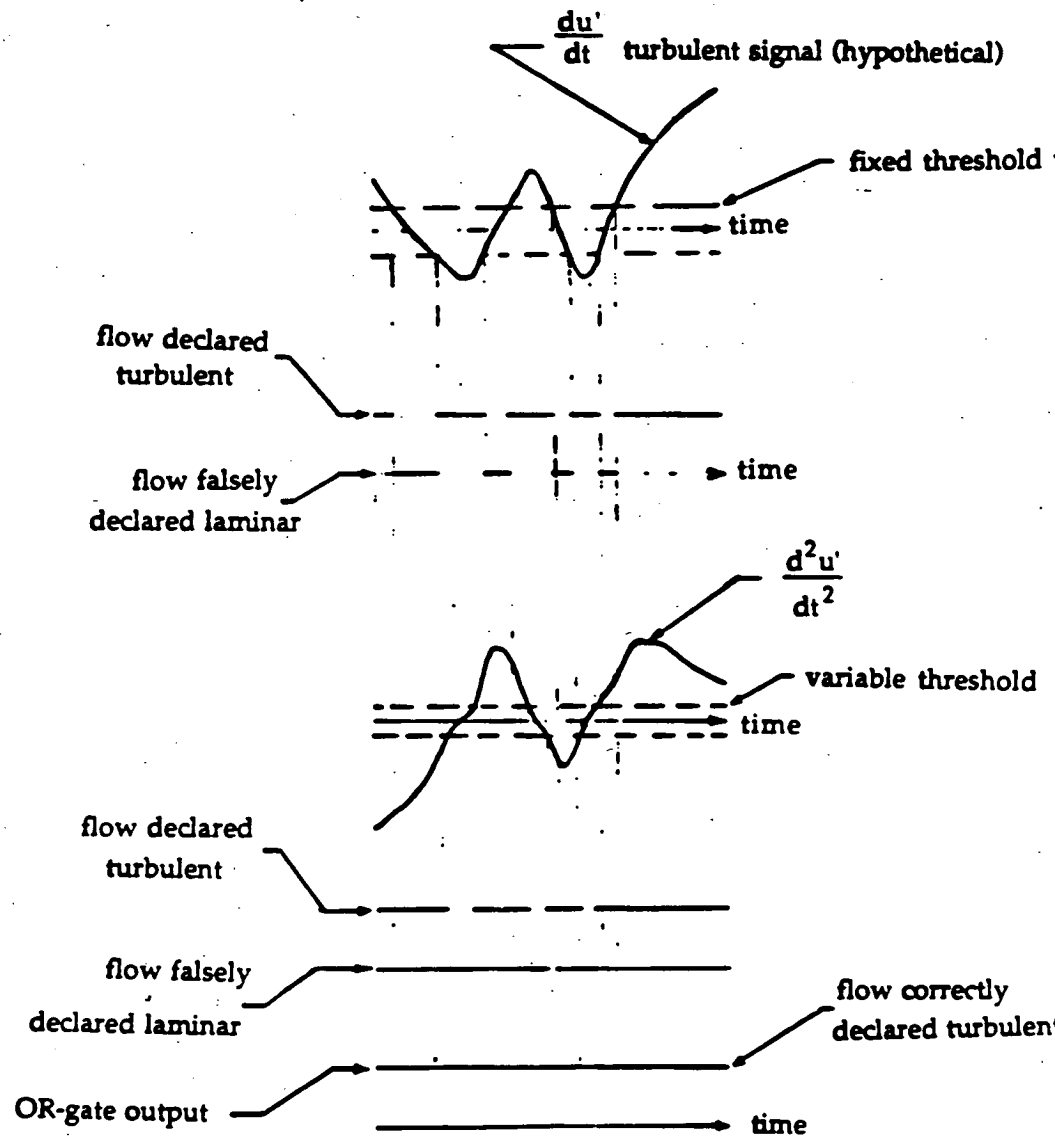

Fig. 2.10–Method used to solve the zero-crossing problem.

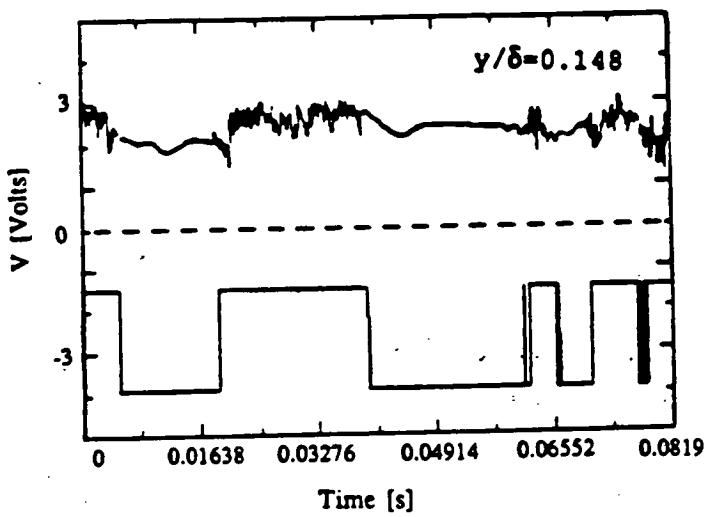

Fig. 2.11–Intermittency circuit performance in a transitional boundary layer. Position in the boundary layer is as noted.

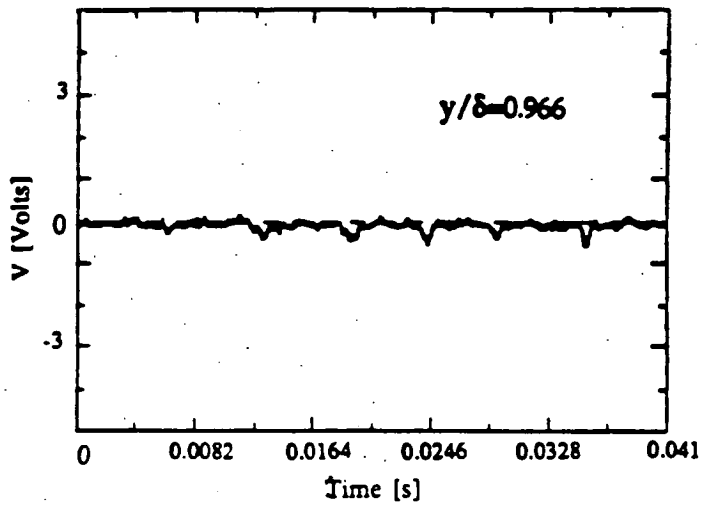

(a). Velocity signal

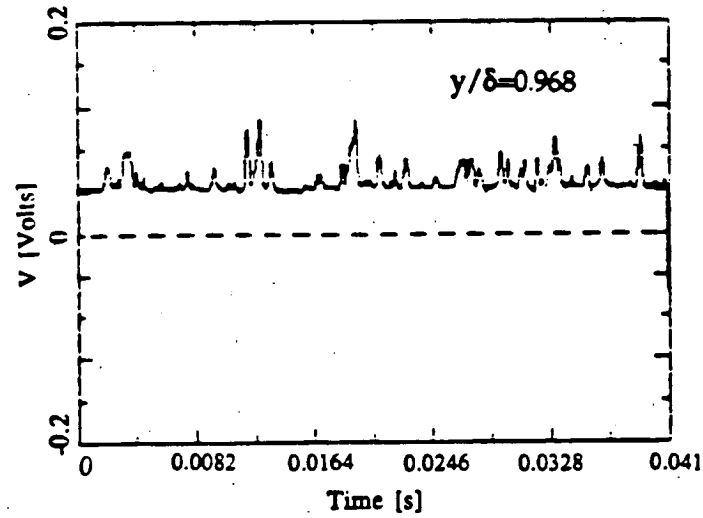

(b). Temperature signal

Fig. 2.12—Comparison of signals in the wake of a turbulent boundary layer using a). a hot-wire, and b). a cold-wire.

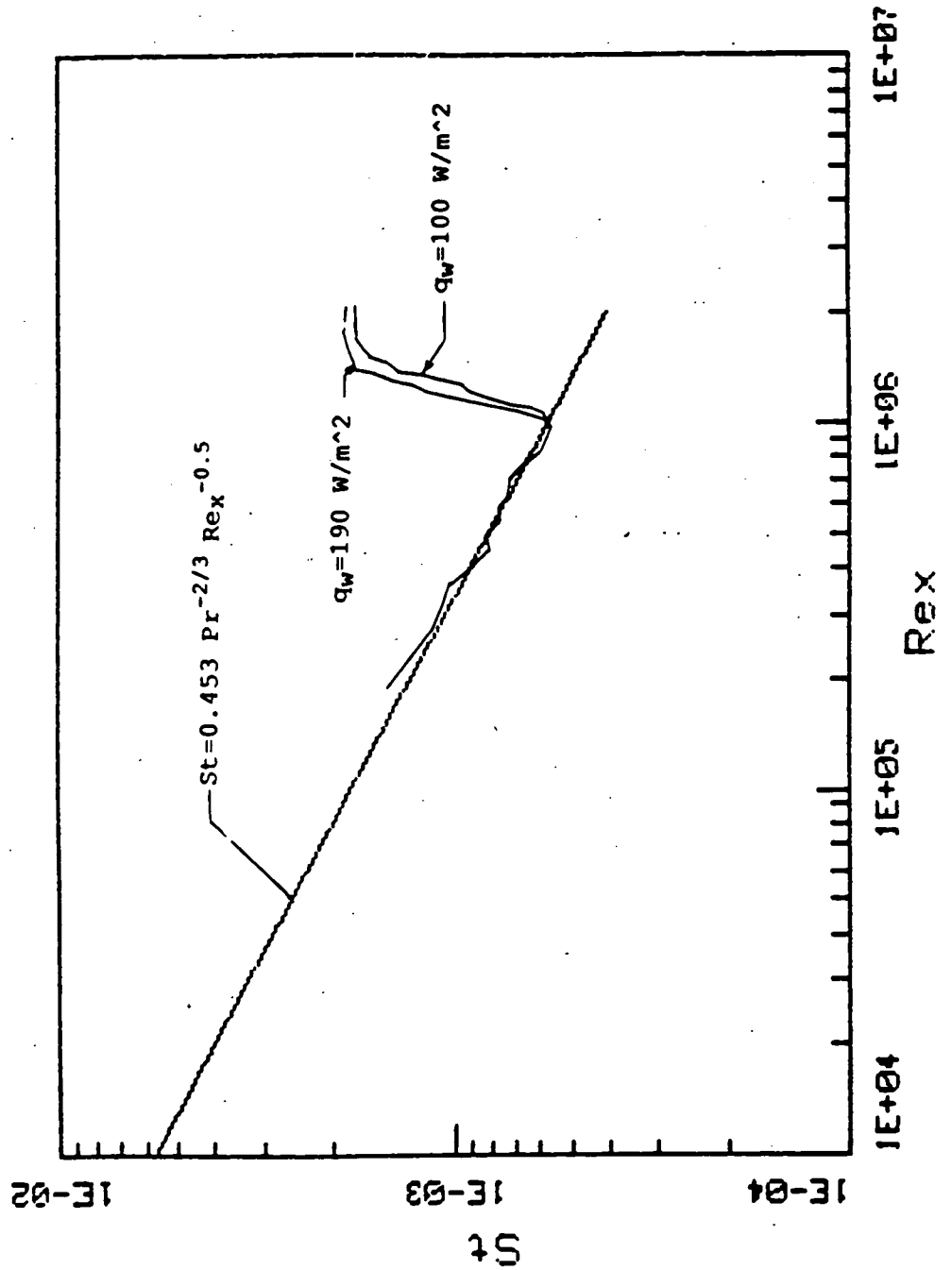

Fig. 2.13–Variation in Stanton number vs. Re_x for two wall heat fluxes.

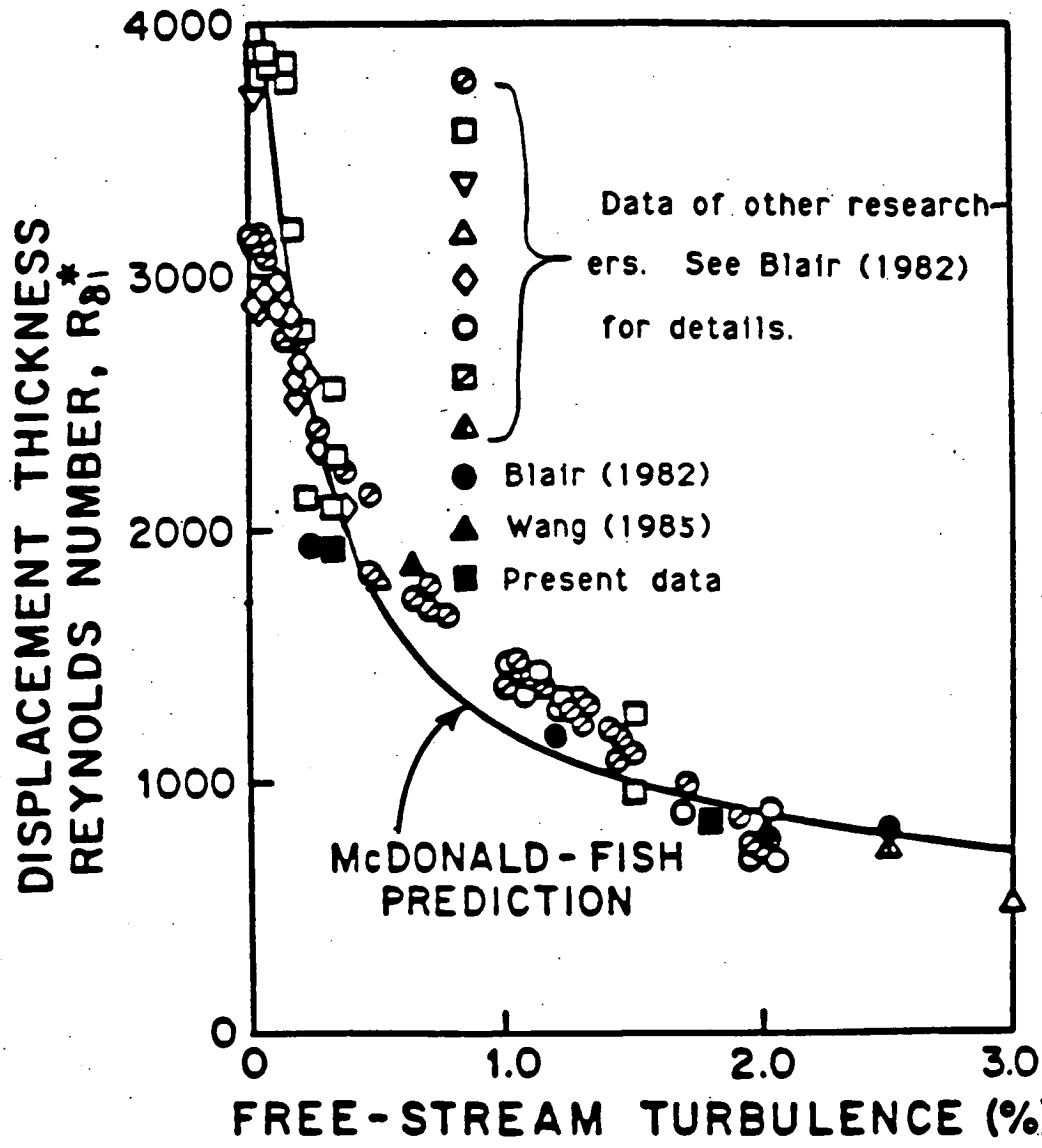

Fig. 2.14—Comparison of the transition start location with that of other researchers and with the McDonald-Fish (1973) prediction.

CHAPTER 3

Results and Discussion

3.1). Case 1 – Flat-wall, TI=0.32%

Free-stream Turbulence Intensity and Spectra. A power spectral density (PSD) distribution vs. frequency of the streamwise velocity component measured using a horizontal wire (TSI Model 1218 Boundary Layer Probe) is shown on Fig. 3.1.1. The power spectrum has a pronounced peak at 29 Hz. This peak has been traced (using an accelerometer and a vibration analyzer) to a rocking motion of the centrifugal blower on its mounts, resulting in a slight unsteadiness in free-stream velocity. All reasonable effort has been applied to minimize this fan motion. This frequency is not expected to influence the transition process as the minimum critical frequency for amp'ification of disturbances is estimated from linear stability theory to be 1600 Hz. The spectrum is seen to be relatively clean otherwise. The comparison on Fig. 2.14 supports the conclusion that the effect of this rocking motion on transition is minimal.

Results of measurements of the free-stream turbulence intensity vs. streamwise distance using a cross-wire rotated to two positions (TSI Model 1243 Boundary Layer Probe) are presented on Fig. 3.1.2. The w' component of turbulence was measured at one station only. It is seen that u' is roughly twice the value of either v' or w', with the values remaining constant all along the test section. The low-frequency unsteadiness discussed above is expected to be the source of the non-isotropy. The free-stream velocity was nominally 26.5 m/s.

Intermittency Profiles. The intermittency profiles taken at various stations are shown on Fig. 3.1.3. The intermittence is seen to decay to zero as y/δ approaches 1, as expected. The profiles at stations 4, 5, and 6 show the same qualitative behavior, namely, a relatively flat value in the region $0.05 < y/\delta < 0.15$ (the turbulent core) followed by a decay to zero for $y/\delta > 0.15$. This decay is due to both the entrainment of the free-stream flow into the boundary layer (the wake region) and intermittent turbulent spot passing. All intermittency values quoted below correspond to the intermittency values in the near-wall region where the profiles are flat.

Mean Velocity Profiles. Profiles of the mean velocity sampled on intermittency at stations 3 to 6 are shown on Fig. 3.1.4. The distance away from the wall has been normalized on the boundary layer thickness of the transitional flow profile. Two characteristics are immediately apparent in all the profiles. First, the turbulent boundary layer is thicker than the corresponding laminar boundary layer, as expected, due to bursting and subsequent turbulent spot formation. Second, the turbulent boundary layer profile is flatter than the corresponding laminar profile, resulting in a cross-over between the two. The transitional flow profile is, by definition of the intermittency, a composite of the turbulent and laminar profiles, and must lie between the two. Evolution of the transitional flow profiles is seen to be from laminar-like to turbulent-like between stations 3 and 5.

Plots of the mean velocity sampled on intermittency and normalized on wall coordinates at various locations are shown on Fig. 3.1.5. The transitional flow profile is seen to evolve from the Blasius profile to the fully turbulent log-law profile as noted above. The velocity profiles sampled on intermittency, however, do not agree with either the Blasius or log-law

profiles in the transition region. The laminar profile increasingly deviates from the Blasius profile as transition proceeds while the turbulent profile deviates most from the log-law profile early in the transition process.

A plot of the local skin friction (C_f) values deduced from the near-wall velocity gradient (in the laminar-flow case) or by fitting the near-wall data to the log-law (in the turbulent-flow case) is shown on Fig. 3.1.6. The skin friction corresponding to laminar flow increasingly deviates from the laminar correlation as transition proceeds. The higher stress at the wall is believed to be due to disturbances in the laminar flow regime as a result of nearby turbulent spot passage. A near-wall hot-wire voltage trace in the intermittent region shown on Fig. 3.1.7 illustrates this. Although the transition from laminar to turbulent flow is quite sharp at the leading interface, the laminar flow requires some time to relax back to a nominally laminar state. If the intermittency is high enough, i.e., spots pass frequently, the laminar boundary layer is continually disturbed, resulting in higher velocities near the wall (than if there were no disturbance) and, consequently, higher C_f values. Values of C_f in the turbulent flow, but at the beginning of transition (Fig. 3.1.6), are seen to be lower than the fully-turbulent correlation values. This could be due to a less than complete establishment of the full turbulence spectrum, i.e., only relatively large eddies are present at this stage of the transition process and turbulence cascading and dissipation is not fully established. This has yet to be confirmed, however.

A similar variation is seen for the shape factor (H) as shown on Fig. 3.1.8. As transition proceeds, H for the laminar boundary layer increasingly deviates from the laminar value of 2.6, indicating an increasingly non-Blasius type profile. Similarly, early in transition, H deviates substantially from the

high-Reynolds-number nominal turbulent value of 1.4. This further illustrates that the laminar and turbulent regimes in the transitional flow cannot be thought of as being composites of Blasius and mature turbulent profiles.

Velocity fluctuation. The rms of the streamwise velocity fluctuation (streamwise turbulence intensity) at stations 3 to 5 are seen in Fig. 3.1.9. The rms of the laminar profile at first increases with axial distance but then reaches a peak value of 8% at station 4, flattening out thereafter. The peaks in the profiles are seen to occur at roughly 30% of the laminar boundary layer thickness for all stations. The peak rms of the turbulent profile is initially high (16% at station 3), indicating a high production of turbulence, but then decays to a peak value of 8% as, it is assumed, the dissipation in the boundary layer increases. Equilibrium is reached by station 6. The transitional flow profile exhibits quite unexpected behavior. The profile initially follows the laminar profile due to the low intermittency (approx. 5% at station 3), but then jumps to a peak value of 17.5% at station 4, a value larger than the peak in the corresponding turbulent profile. Much of this behavior is due to intermittent "switching" of the flow between the laminar and turbulent regimes as turbulent spots pass the probe. This was first shown by Arnal, Juillen and Michel (1978). The accompanying change in the mean velocity is illustrated in the hot-wire voltage trace of Fig. 3.1.7. The differences in the mean velocities in the laminar and turbulent regimes give rise to a rms velocity fluctuation which is greater than that of either the laminar or turbulent regime. In fact, the deviation of the transitional flow profile from an average profile of u'^2 is given by

$$\overline{u_e'^2} = \gamma \overline{u_t'^2} + (1-\gamma)\overline{u_l'^2} + \gamma(1-\gamma)(\bar{u}_t - \bar{u}_l)^2 \qquad (3.1)$$

The level of turbulence as indicated by the transitional flow profile is thus not a good measure of the true turbulent activity in the transitional boundary layer.

Shear stress profiles. The variation in the shear stress u'v' through transition is shown on Fig. 3.1.10. The laminar contribution to the shear stress throughout the boundary layer is seen to be quite small for all stations except station 5 (where the number of samples is small and where cross-contamination between laminar and turbulent regimes is significant). A peak in each profile is seen to move progressively toward the wall as transition proceeds. The fully-turbulent profile is reached by station 6. Although the transitional flow profile is between the turbulent and laminar profiles for all stations, it also is affected by the intermittent "switching" from laminar to turbulent flow. The transitional flow profile is, therefore, also not indicative of the true turbulent shear stress in the boundary layer.

Turbulent Heat Flux Measurements. Measurements of the turbulent heat flux normalized on the wall heat flux and sampled on intermittency are shown on Fig. 3.1.11. This normalization is more appropriate than a normalization based on the freestream velocity and wall-to-freestream temperature difference due to the inability of assigning an appropriate temperature difference during transition for the uniform wall heat flux boundary condition. In transition, it is presumed that the wall temperature fluctuates as the flow regime switches over a given spot on the wall. A potential advantage of the present normalization is that the turbulent heat flux at the wall should vary directly with the intermittency if v't' sampled on

the laminar flow is small. Due to the destabilizing effect of heating on transition, the intermittency for these profiles corresponding to stations 3 and 4 are different than for the unheated data presented above. This heat flux data is presented not as a comparison to the hydrodynamic data, but because it provides insight into the transition process.

It is seen in Fig. 3.1.11 that a large increase in the turbulent heat flux above the wall heat flux occurs within the turbulent spot at station 3. This can occur if the cross-stream eddy diffusion of heat increases in the streamwise direction at the expense of convection of heat. The triple-wire measurements bear this out. The streamwise heat flux u't' was found to decrease almost an order of magnitude between St. 3 and 4 in the near-wall region and remain relatively constant thereafter. Whether the measurements sampled on turbulent-like flow for station 3 drops to unity in the very near-wall region (nearer the wall than can be measured) is not known. It is possible that the wall transfers more energy to the flow during the passage of a turbulent spot due to the higher heat transfer coefficient, than during the times the flow is laminar-like when the heat transfer coefficient is lower. If so, the wall heat flux would be varying with time according to the local flow regime. The time-average energy transferred must, of course, equal the time-averaged wall heat flux. A positive slope in v't' also suggests intense mixing of the flow away from the wall. It is also seen that v't' in the laminar portion of the transitional boundary layer is not zero. This does not mean that a turbulent transport of heat is present in the laminar boundary layer, but simply that v' and t' are correlated due to the unsteadiness of the flow. Because v't' in the laminar regime is not small, the value of v't' at the

wall for the transitional flow profile unfortunately does not go to the near-wall intermittency, as was anticipated.

The turbulent Prandtl number (Pr_t) sampled on intermittency through transition is shown on Fig. 3.1.12. The uncertainty in this data was estimated at 20%. The data at stations 4 and 6 show Pr_t values consistently close to unity in the inner half of the boundary layer, as would be expected of fully turbulent boundary layers. The data in the outer half of the boundary layer is not expected to be reliable due to the very shallow gradients of velocity and temperature. The data for station 3, however, show a drop in Pr_t values sampled on turbulent flow substantially below unity in the near-wall region, implying that the eddy diffusivity of heat increases faster than the eddy diffusivity of momentum as one traverses from the wall outward. This is contrary to the expectation that heat acts simply as a passive scalar and also contradicts the conclusions of other researchers (e.g.--Kuan and Wang-1990, Blair--1991, and Suder, O'Brien and Reshotko-1988). These are the first measurements in which Pr_t was directly measured, however, previous conclusions having been inferred from mean profile data.

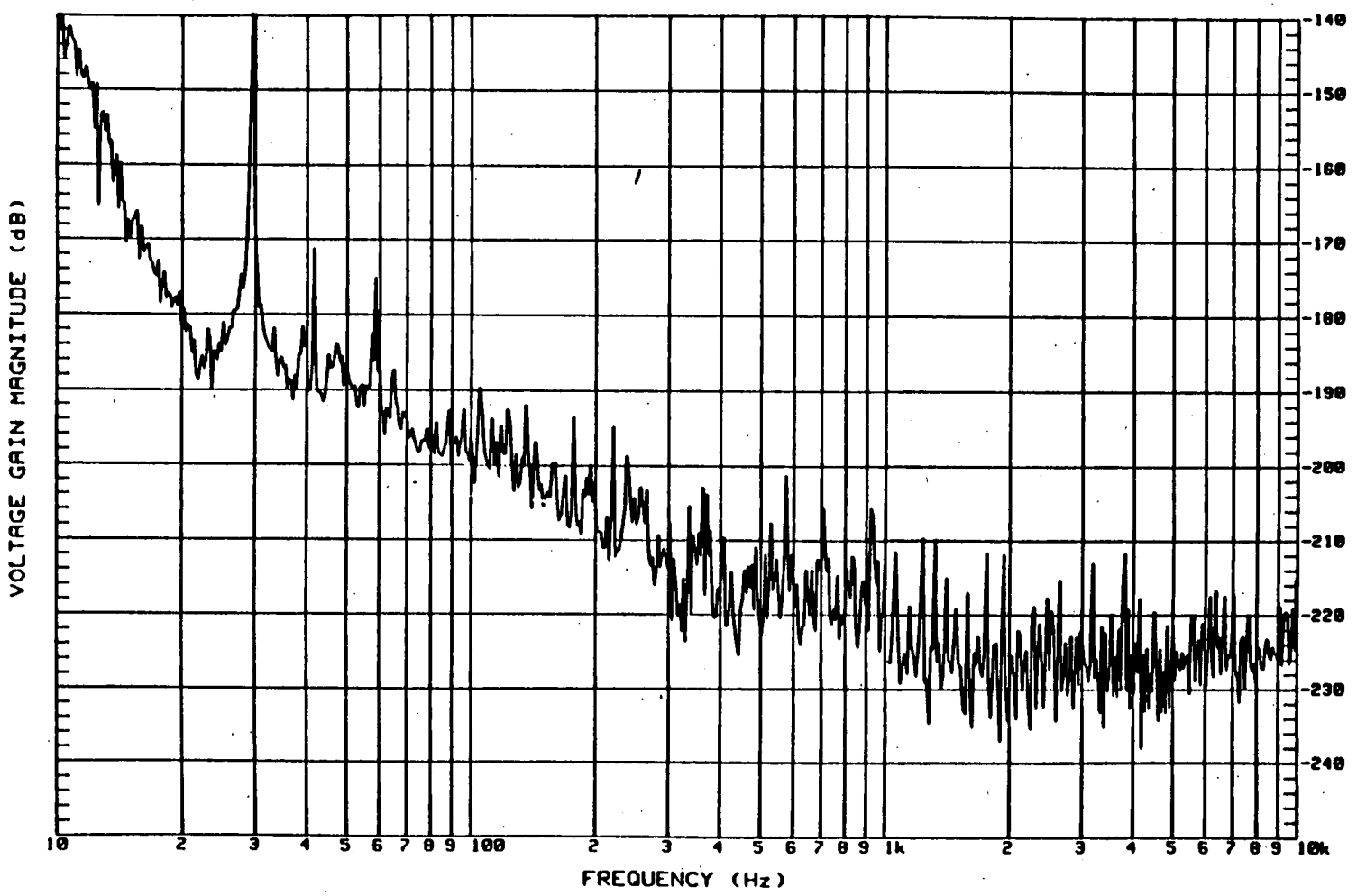

Fig. 3.1.1--Power spectral density distribution of the streamwise velocity component (Case 1).

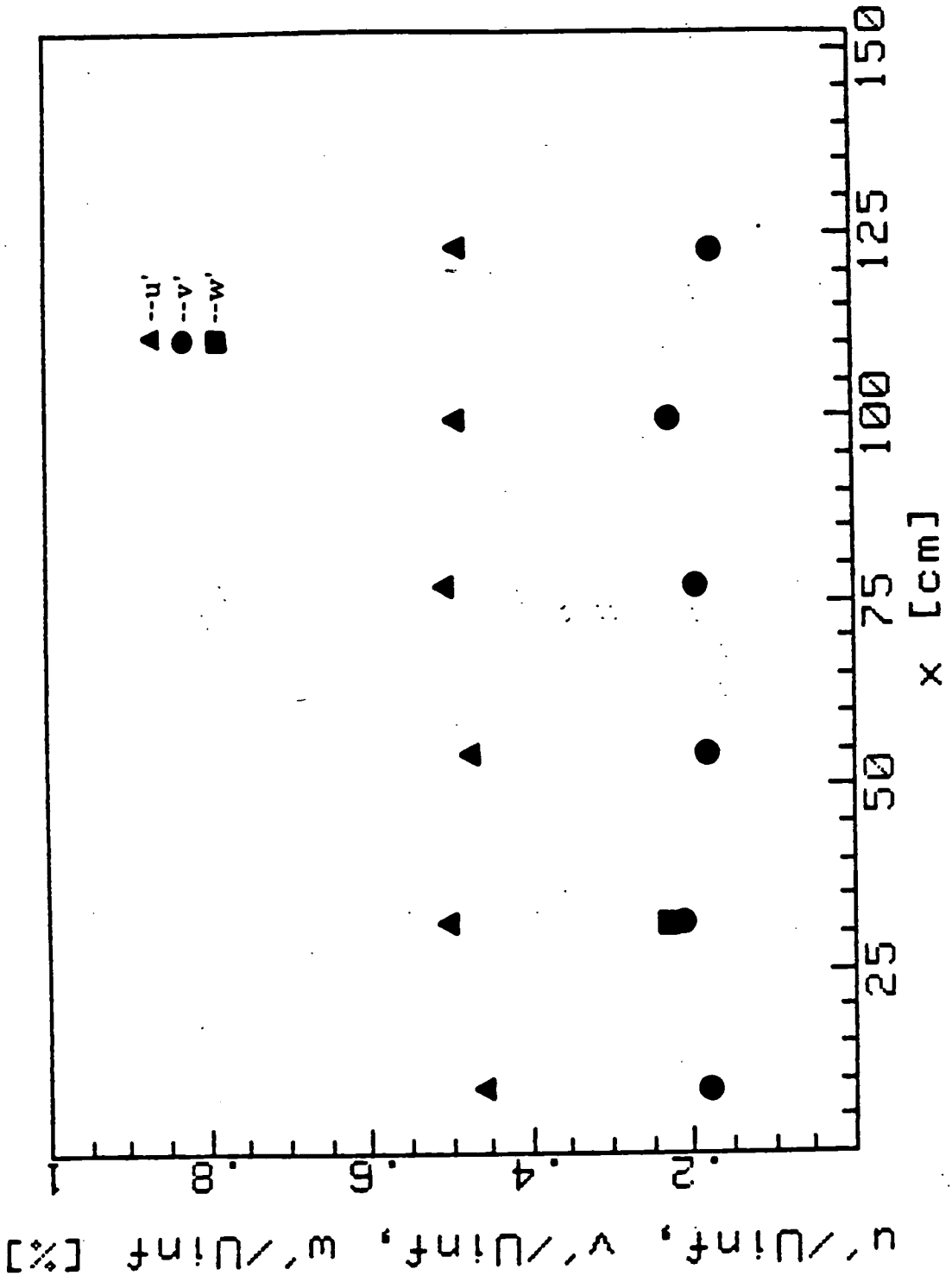

Fig. 3.1.2–Measurement of the free-stream turbulence intensity vs. streamwise distance (Case 1).

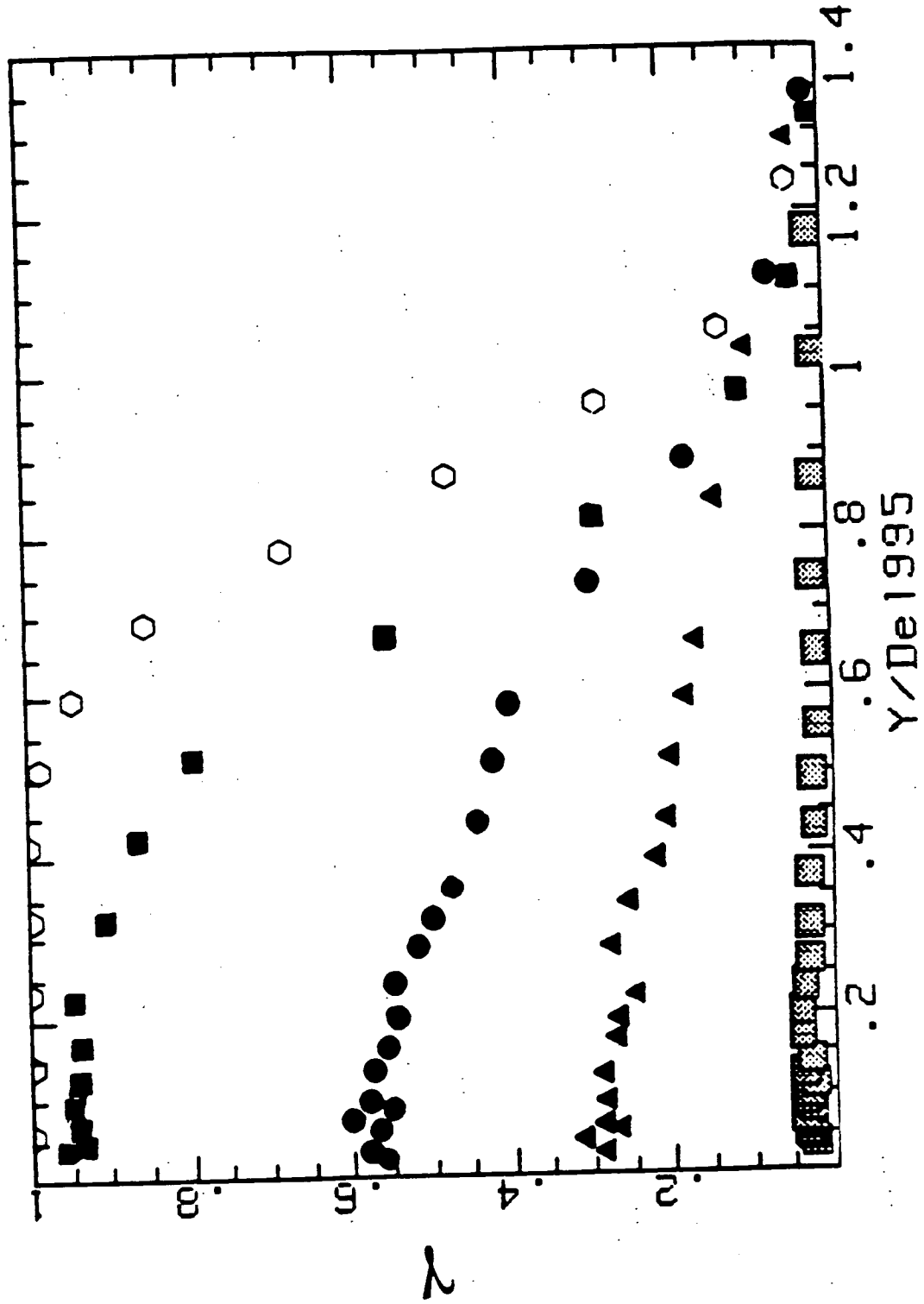

Fig. 3.1.3—Intermittency profiles along the wall (Case 1). ◘ - station 3, ▲ - station 4a, ● - station 4, ■ - station 5, ○ - station 6.

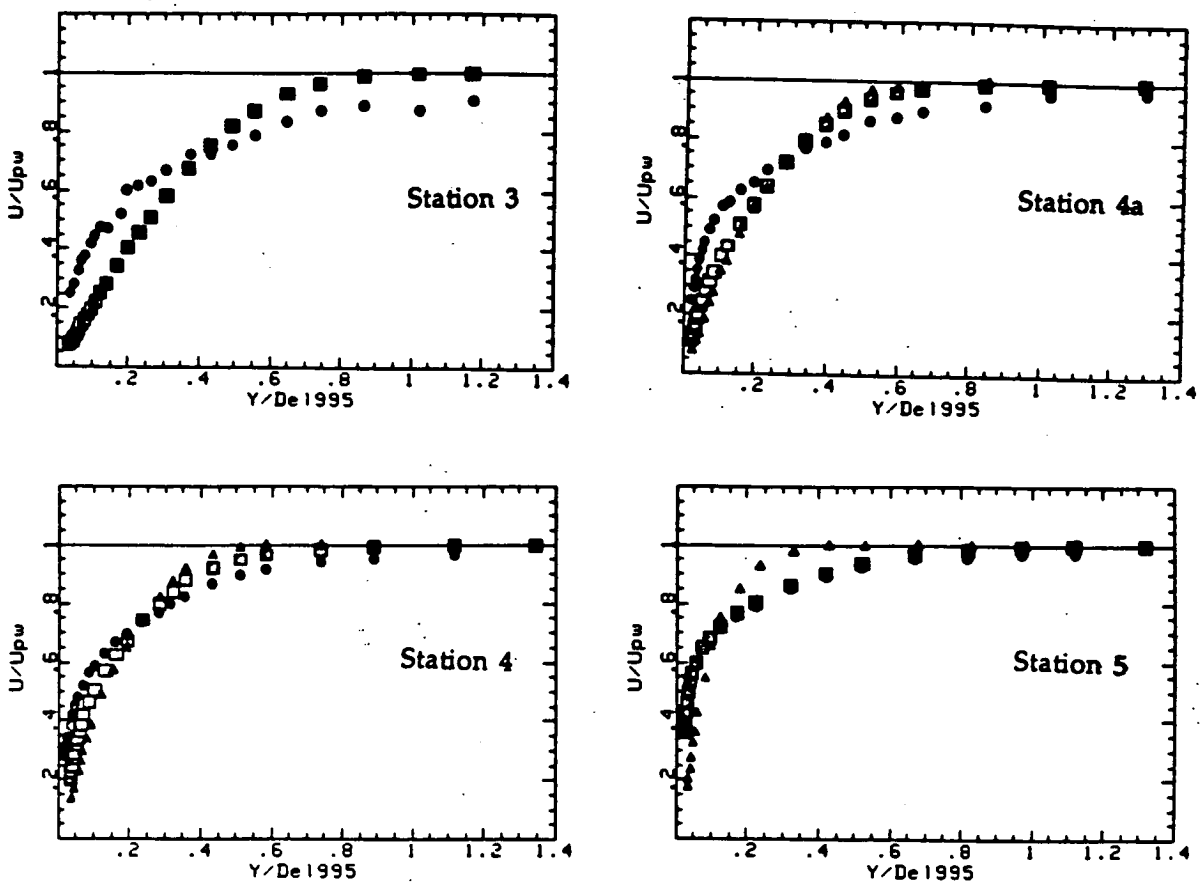

Fig. 3.1.4—Profiles of mean velocity sampled on intermittency (Case 1).
▲ - laminar, ● - turbulent, ■ - transition.

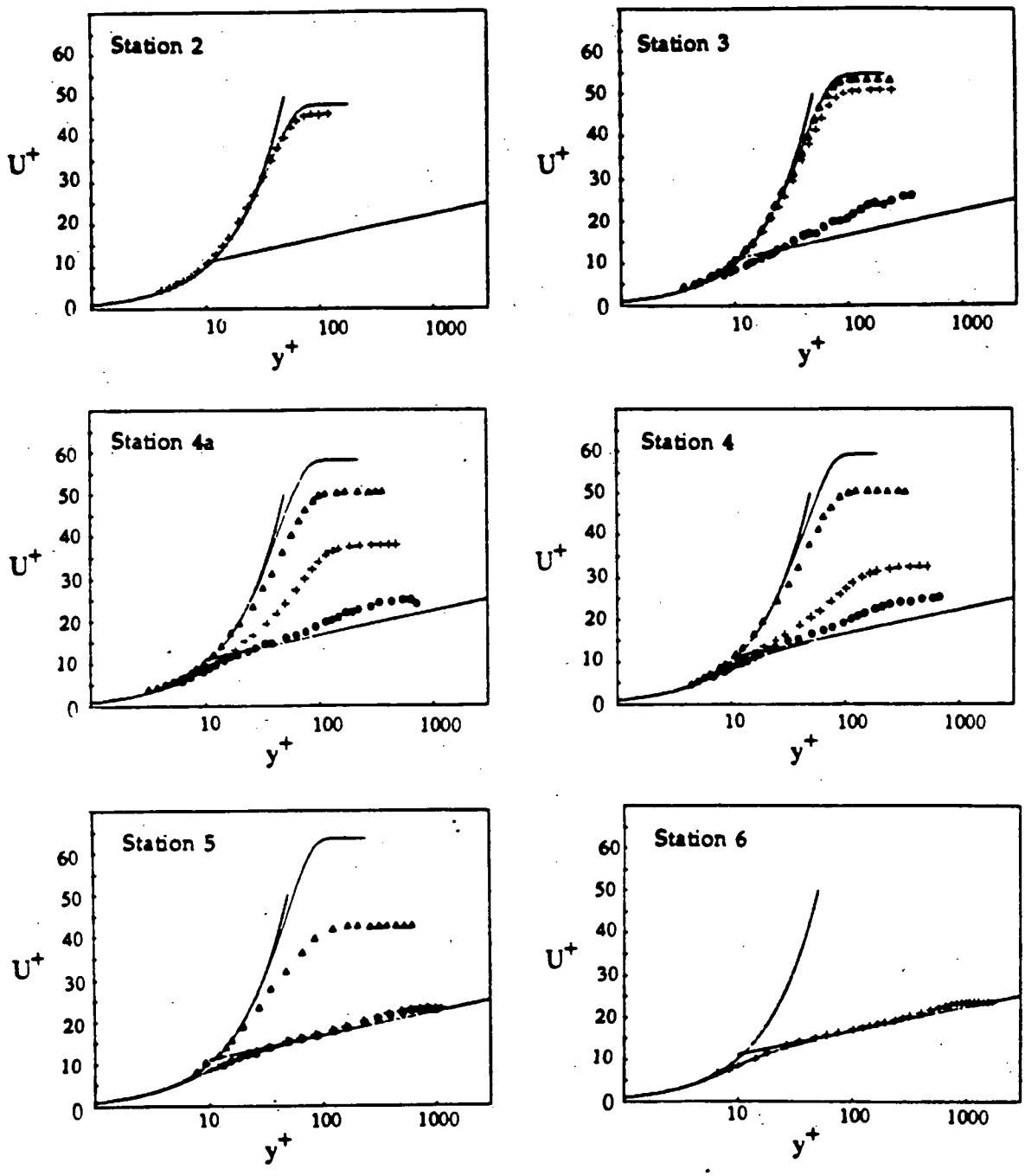

Fig. 3.1.5–Profiles of mean velocity sampled on intermittency and normalized on wall coordinates (Case 1). ▲ - laminar, ● - turbulent, + - transition.

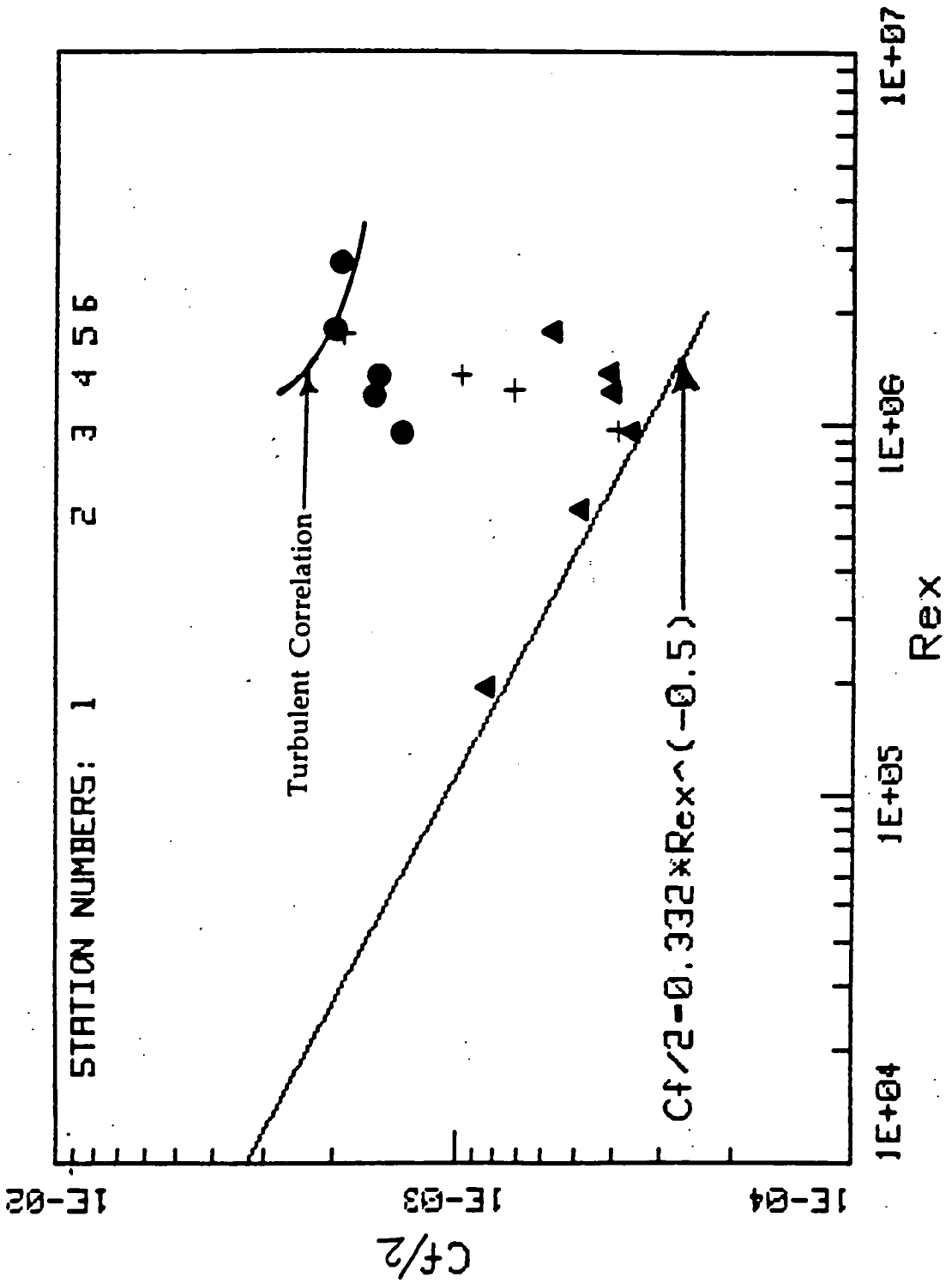

Fig. 3.1.6–Skin friction sampled on intermittency (Case 1). ▲ - laminar, ● - turbulent, + - transition.

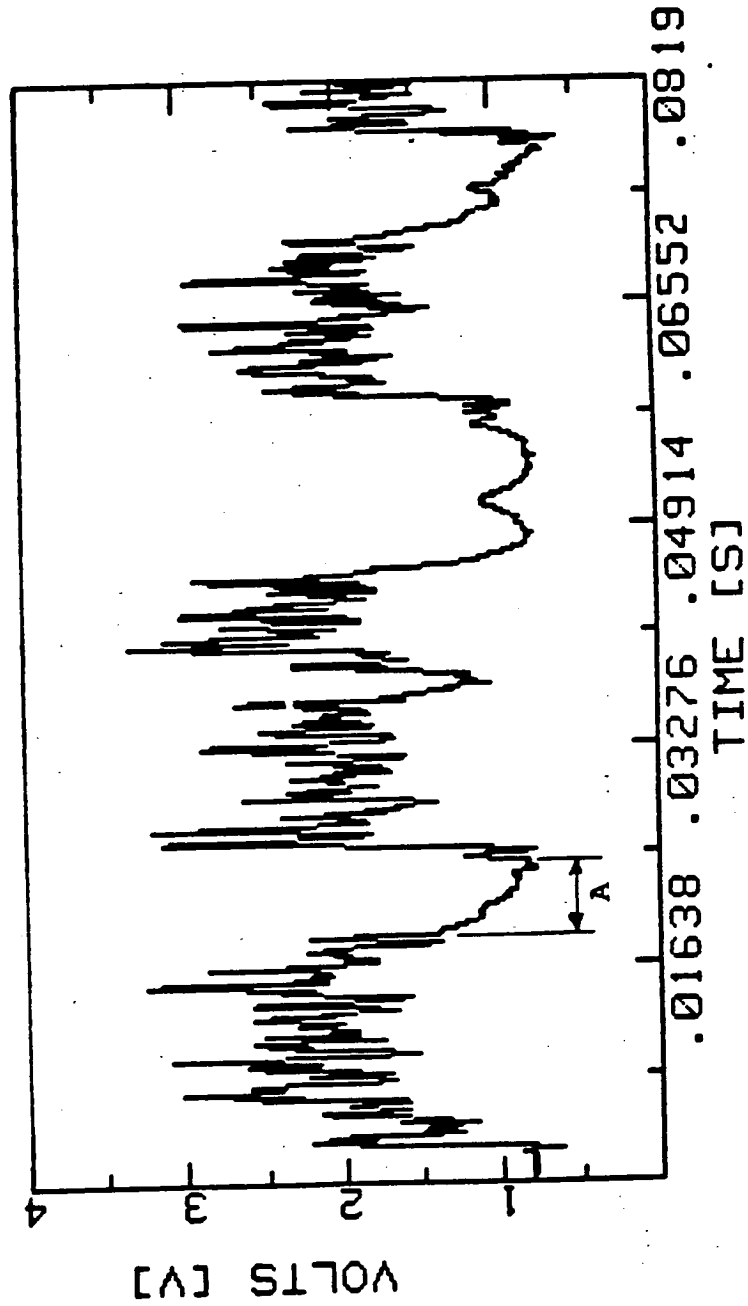

Fig. 3.1.7–Near-wall hot-wire voltage trace in transition illustrating the different mean velocities between the two regimes and the relaxation of the boundary layer after turbulent spot passage (as in "A").

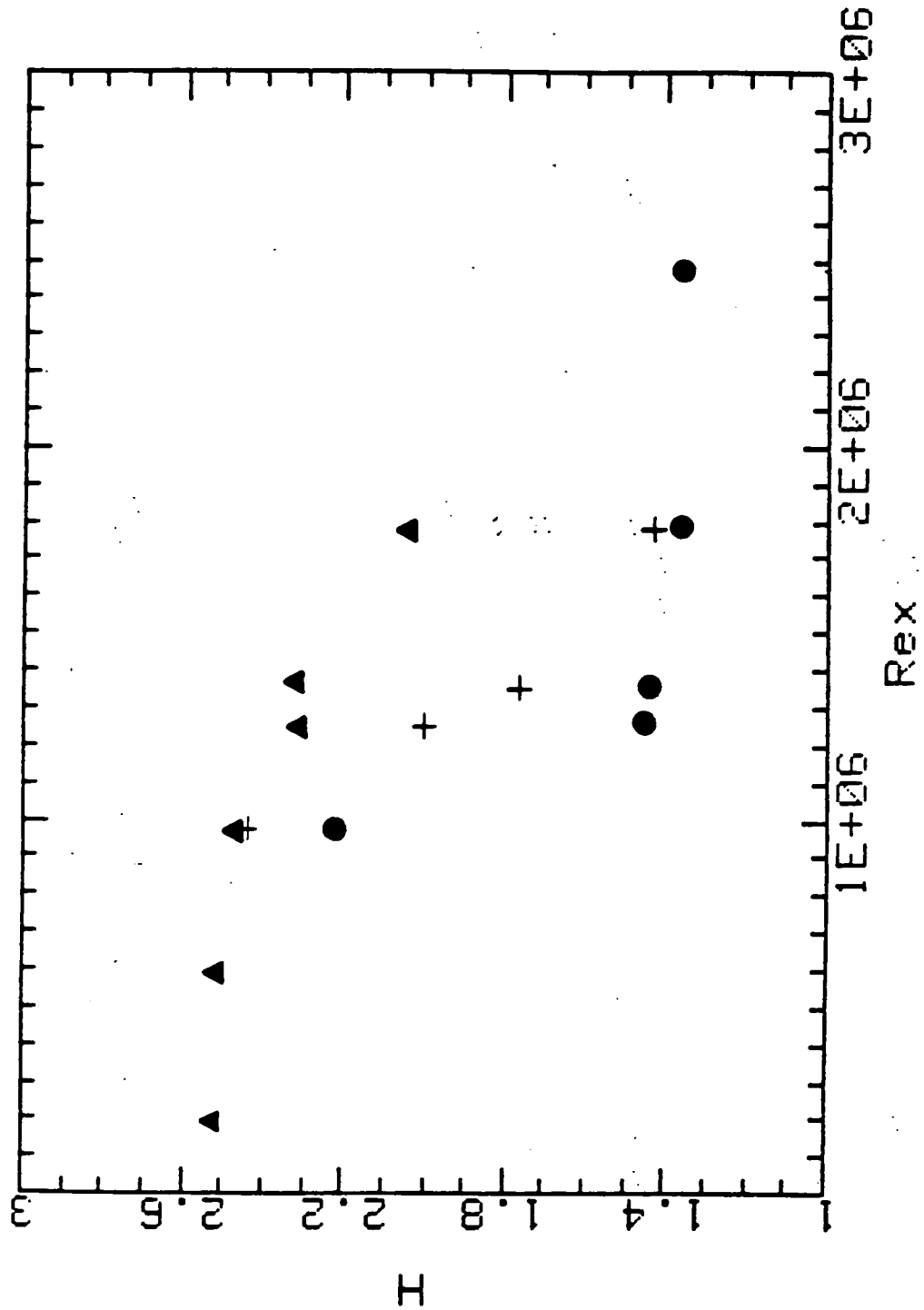

Fig. 3.1.8–Shape factors sampled on intermittency (Case 1). ▲ - laminar, ● - turbulent, + - transition.

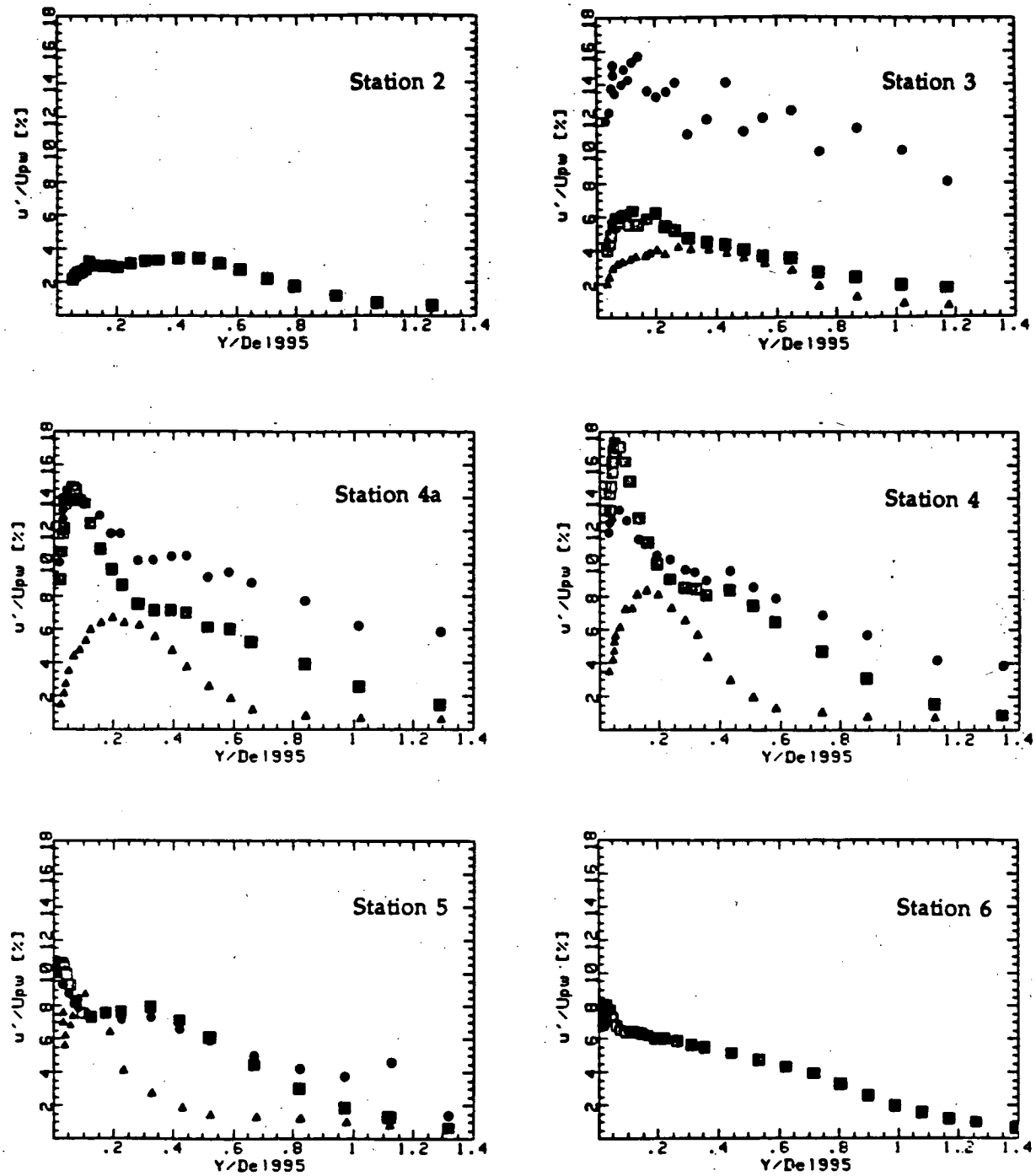

Fig. 3.1.9--Turbulence intensity profiles sampled on intermittency (Case 1).
▲ - laminar, ● - turbulent, ■ - transition.

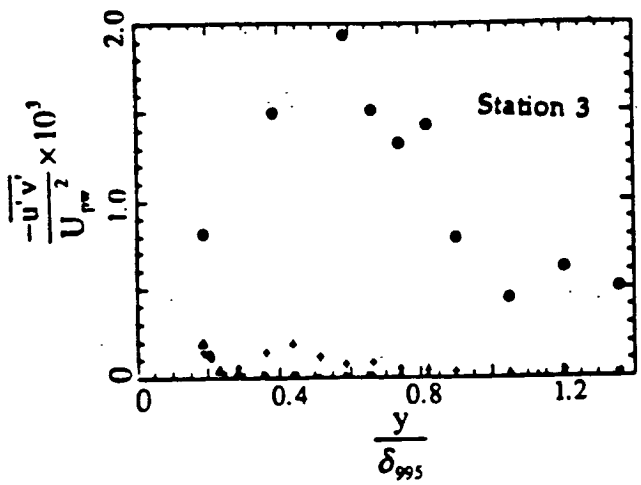

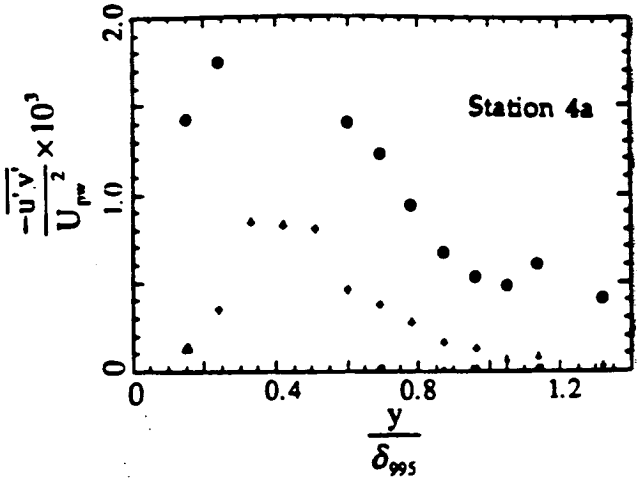

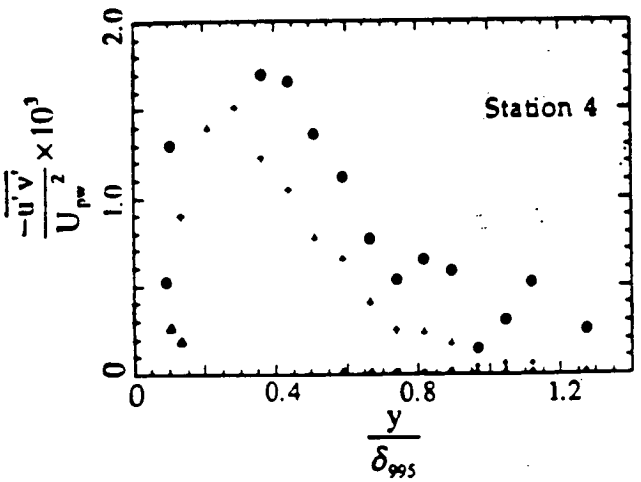

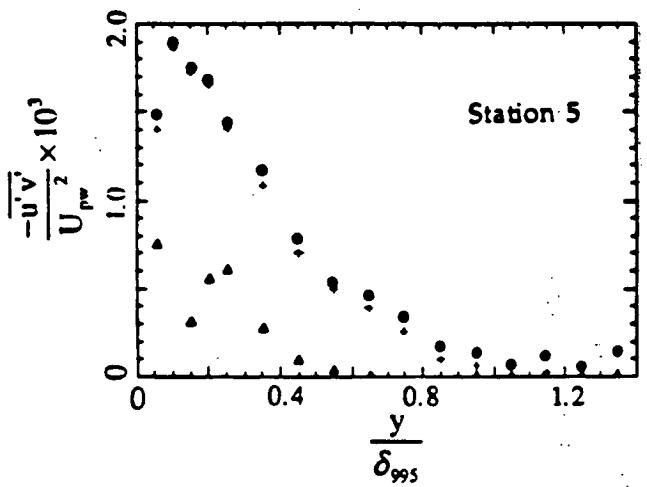

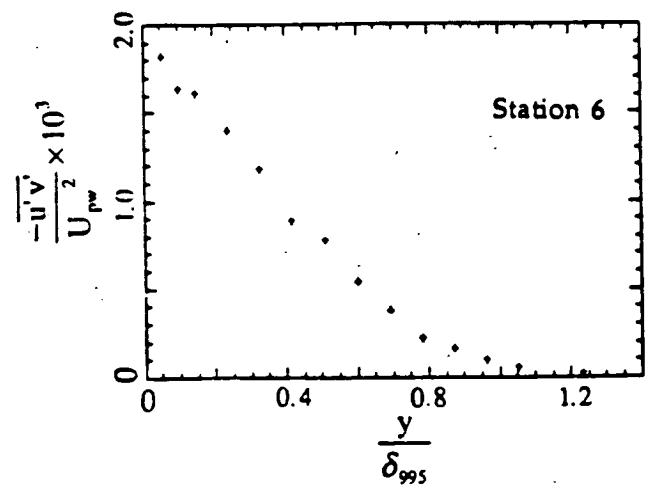

Fig. 3.1.10–Shear stress profiles sampled on intermittency (Case 1).
▲ - laminar, ● - turbulent, + - transition.

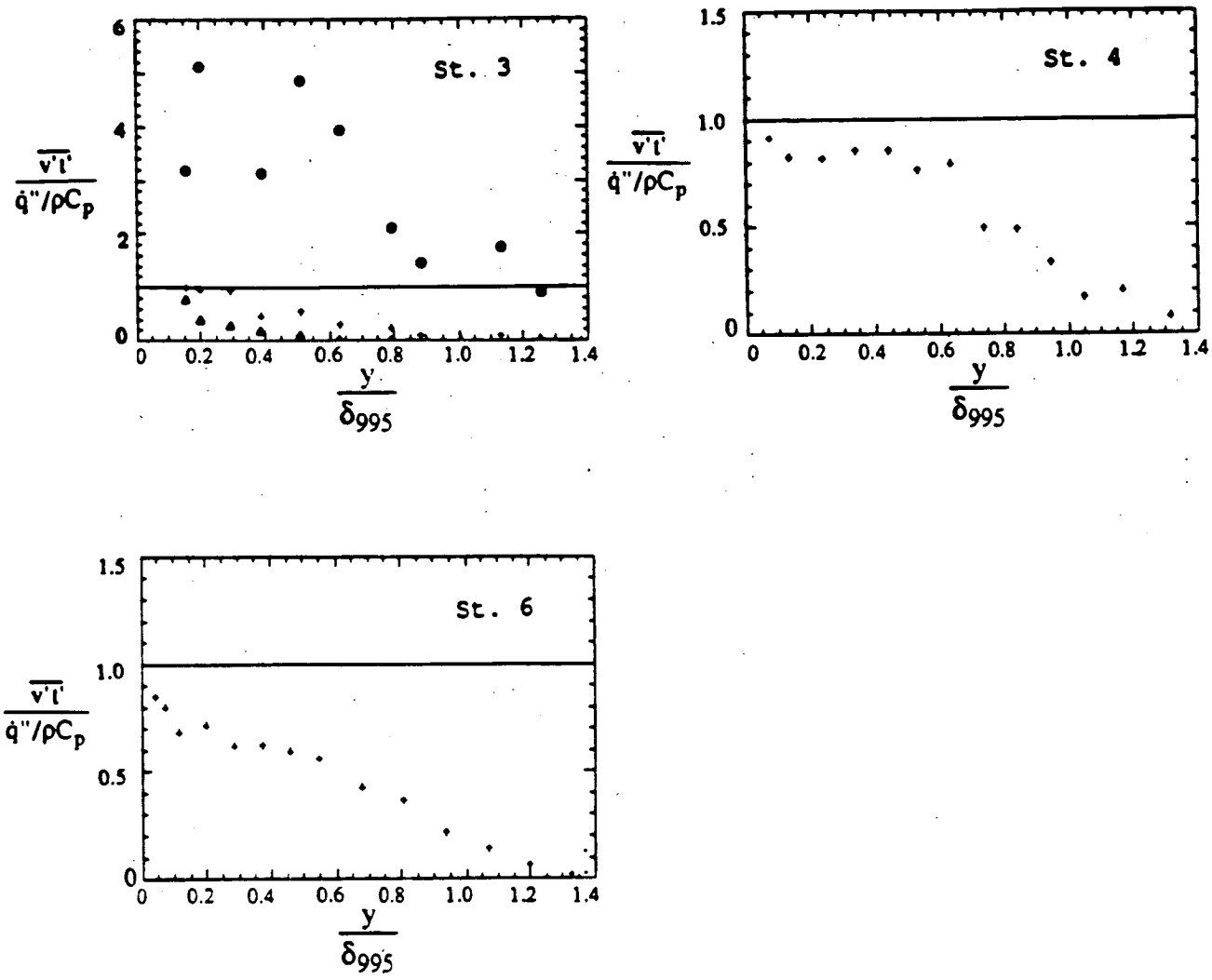

Fig. 3.1.11–Cross-stream turbulent heat flux sampled on intermittency (Case 1). Station 3 is within transition (γ=12%), stations 4 and 6 are fully turbulent. ▲ - laminar, ● - turbulent, + - transition.

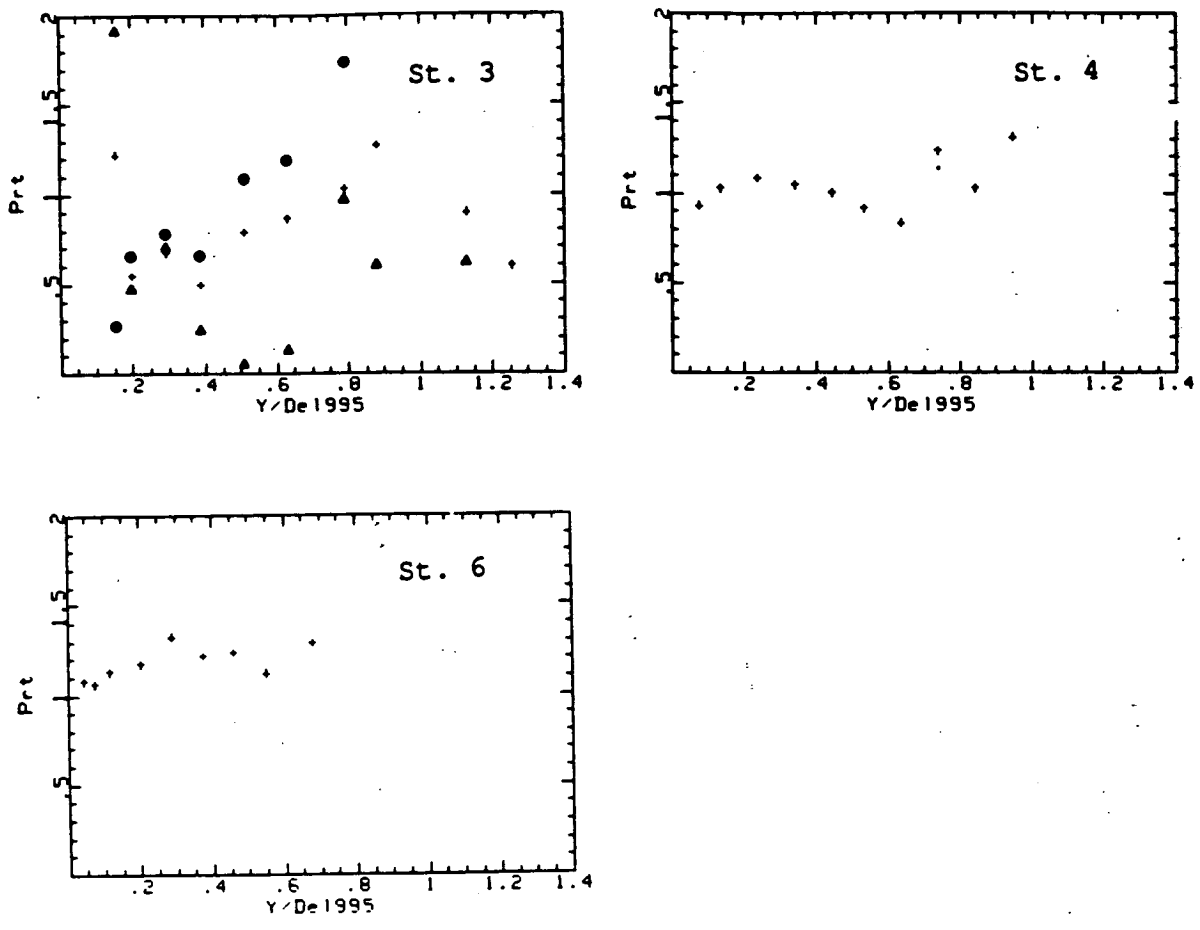

Fig. 3.1.12–Turbulent Prandtl numbers sampled on intermittency (Case 1). Station 3 is within transition (γ=12%), stations 4 and 6 are fully turbulent. ▲ - laminar, ● - turbulent, + - transition.

3.2). Case 2 -- Flat-wall, TI=1.5%

Free-stream Turbulence Intensity and Spectra. The Power Spectral Density (PSD) for this case is shown on Fig. 3.2.1. A peak, corresponding to 27 Hz, is again visible. As in the base case, this peak is caused by rocking of the fan. The frequency is slightly lower in this case, however, since the fan speed was lowered to move transition a reasonable distance from the leading edge. Another much smaller peak is seen at 3800 Hz. The source of this peak (electronic noise) was determined by computing the PSD with the hot-wire mounted in the tunnel, but in a still flow. The two dominant peaks in this PSD corresponded to 3800 Hz and 60 Hz (line noise). The free-stream velocity was nominally 16.7 m/s.

Stanton number. The Stanton number variation through transition is shown on Fig. 3.2.2. The first five points are seen (as in the lower TI case) to be higher than the laminar correlation due to the unheated starting length effect. The two data points just before transition agree with the correlation. Increasing the free-stream turbulence is seen to have a strong effect on transition onset, transition moving to $Re_x=3x10^5$, or about one third the value for the base case. A comparison of the onset location with other researchers was shown on Fig. 2.14. The agreement in this case is very good. The Stanton number variation through transition is consistent with the data of Blair (1982).

Intermittency profiles. Intermittency profiles are shown on Fig. 3.2.3. Like the profiles for the base case, the intermittency monotonically increases as transition proceeds.

Mean velocity profiles. Profiles of the mean velocity sampled on intermittency are shown on Fig. 3.2.4. The laminar profile is seen to deviate

quite strongly from the Blasius profile throughout the transition process (much more than in Case 1), indicating a large perturbation due to increased free-stream turbulence. The turbulent profile, in contrast, agrees with the log-law profile from very early in transition. The above trends are reflected in the skin friction, C_f, values plotted on Fig. 3.2.5. The laminar C_f values deviate strongly from the laminar correlation while the turbulent C_f values remain relatively unaltered. There is no drop below the turbulent correlation in the turbulent C_f values as was seen in the lower TI case. Similar trends are seen in the shape factor (H), Fig. 3.2.6.

Velocity fluctuation. The rms of the velocity fluctuations is shown on Fig. 3.2.7. The most striking feature of these profiles in comparison with those of the base case is the large increase in laminar unsteadiness, which even exceeds the turbulent profile rms values in some parts of the transitional boundary layer (station 3). The high values are consistent with the observed trends in C_f and H for the laminar regime. The turbulent profiles evolve as in the base case. The peak values of the turbulence intensity drop more or less monotonically with increasing intermittency for the two cases. A fully turbulent profile is established by station 5.

Temperature profile. The mean temperature profiles through transition plotted in T+ vs. y+ coordinates are shown on Fig. 3.2.8. A smooth variation from a laminar-like to a turbulent-like profile is seen, as was seen for the mean velocity. The temperature profiles lag the velocity profiles, however, as may be seen by comparing the two profiles at station 3 (see Fig. 3.2.4 and Fig. 3.2.8). The temperature profile is still evolving when the velocity profile has assumed a nearly log-law shape. This is consistent with the observations of Blair (1982).

Shear Stress Profiles. The variation in shear stress u'v' sampled on intermittency through transition is shown on Fig. 3.2.9. As for the low TI case, the laminar contribution to the shear stress is seen to be small everywhere except in the very near wall region. The peak in the turbulent flow profiles decreases in amplitude while moving towards the wall as transition proceeds. An equilibrium profile is reached by station 5.

Turbulent Heat Flux Measurements. Profiles of the turbulent heat flux are presented on Fig. 3.2.10. As in the lower TI case, a strong increase in the turbulent heat flux above the wall heat flux is seen. This peak is seen to decay rapidly, the profile achieving what one would expect of a fully turbulent profile by station 5.

Turbulent Prandtl numbers deduced from the measurements are presented on Fig. 3.2.11. The values are seen to all be in the vicinity of unity for the fully turbulent profiles (stations 3 to 5), while dipping below unity in the transitional flow case (station 2), as was seen previously for the low TI case.

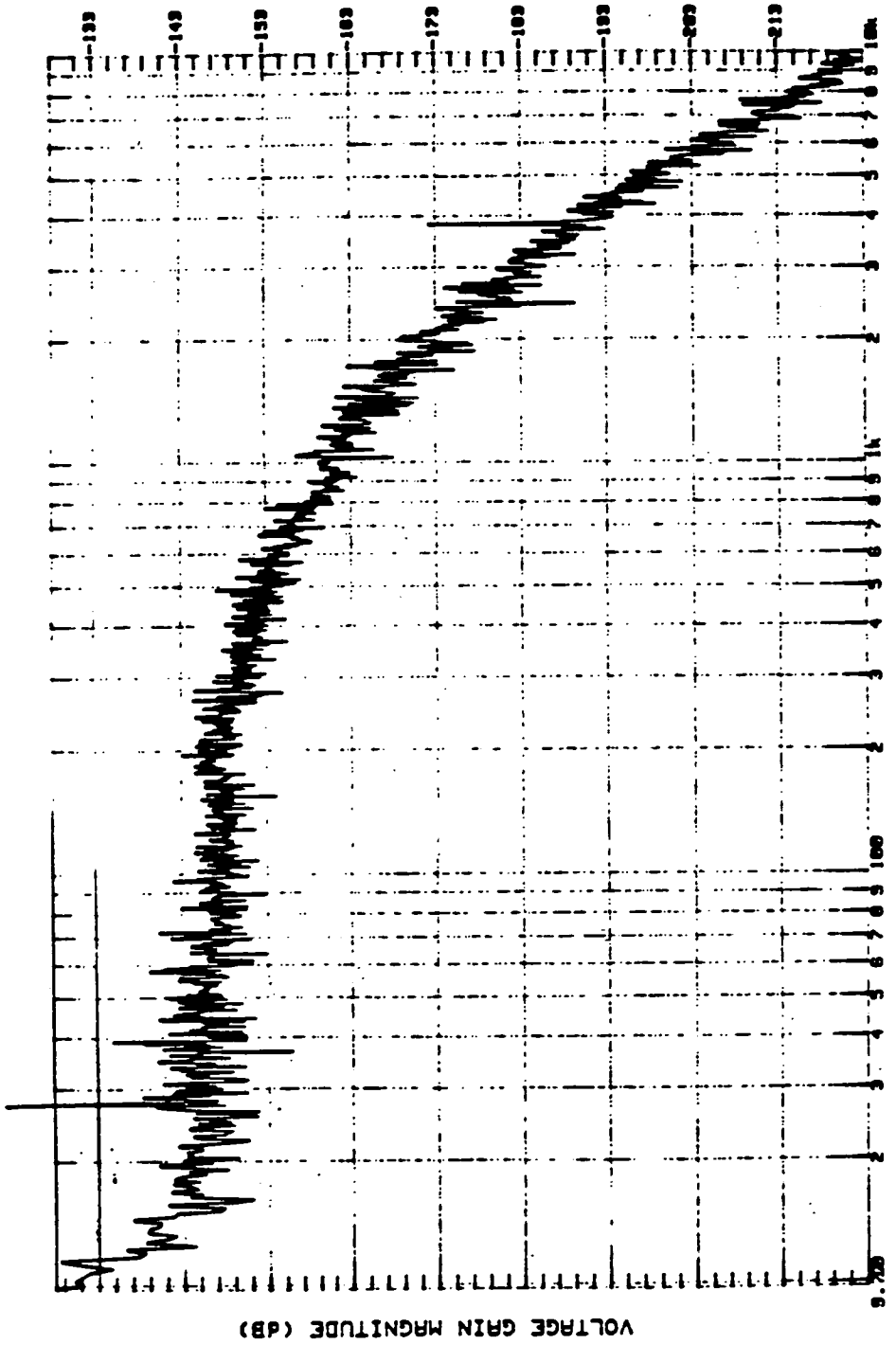

Fig. 3.2.1--Power spectral density distribution of streamwise fluctuating velocity (Case 2).

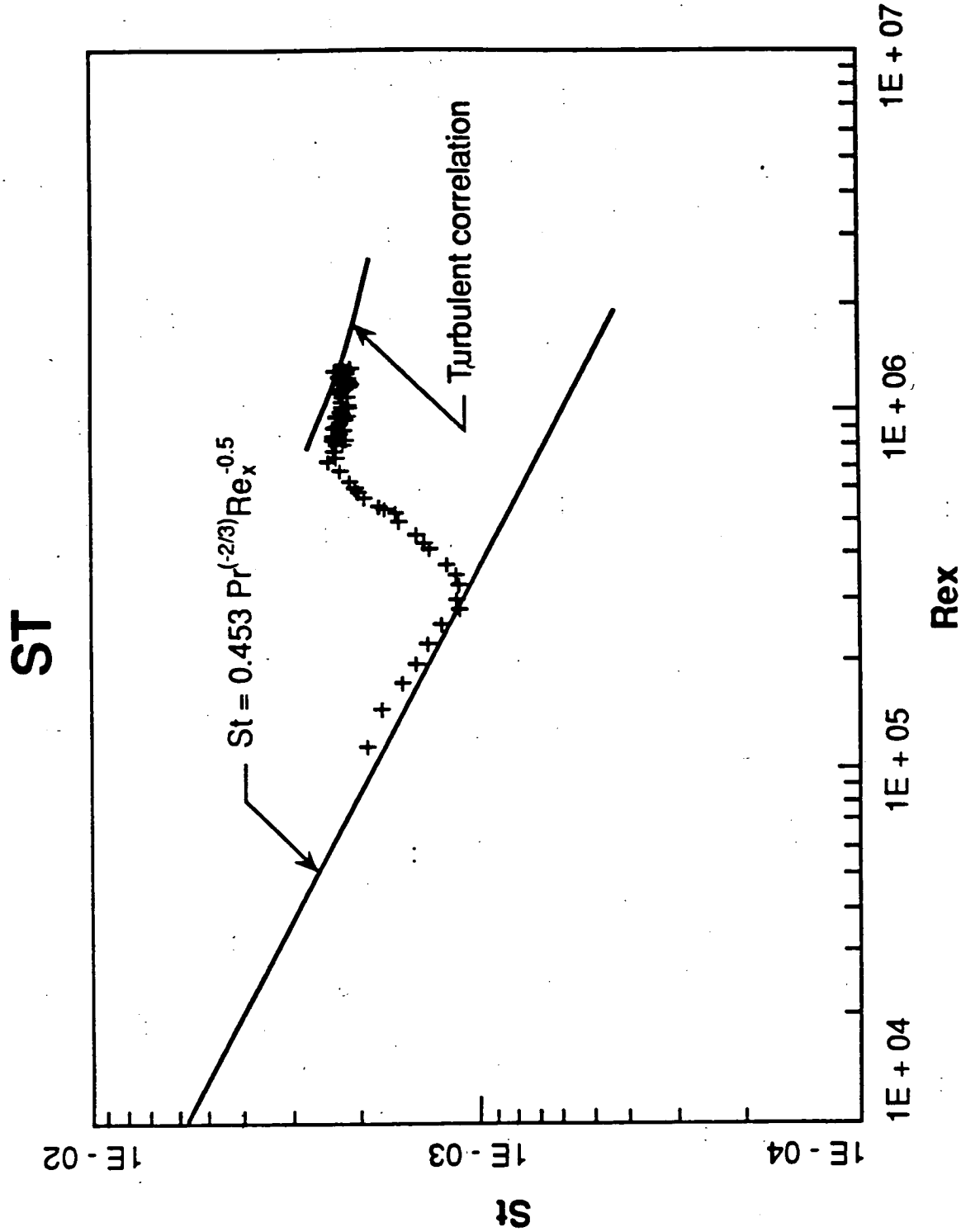

Fig. 3.2.2–Stanton number variation through transition (Case 2).

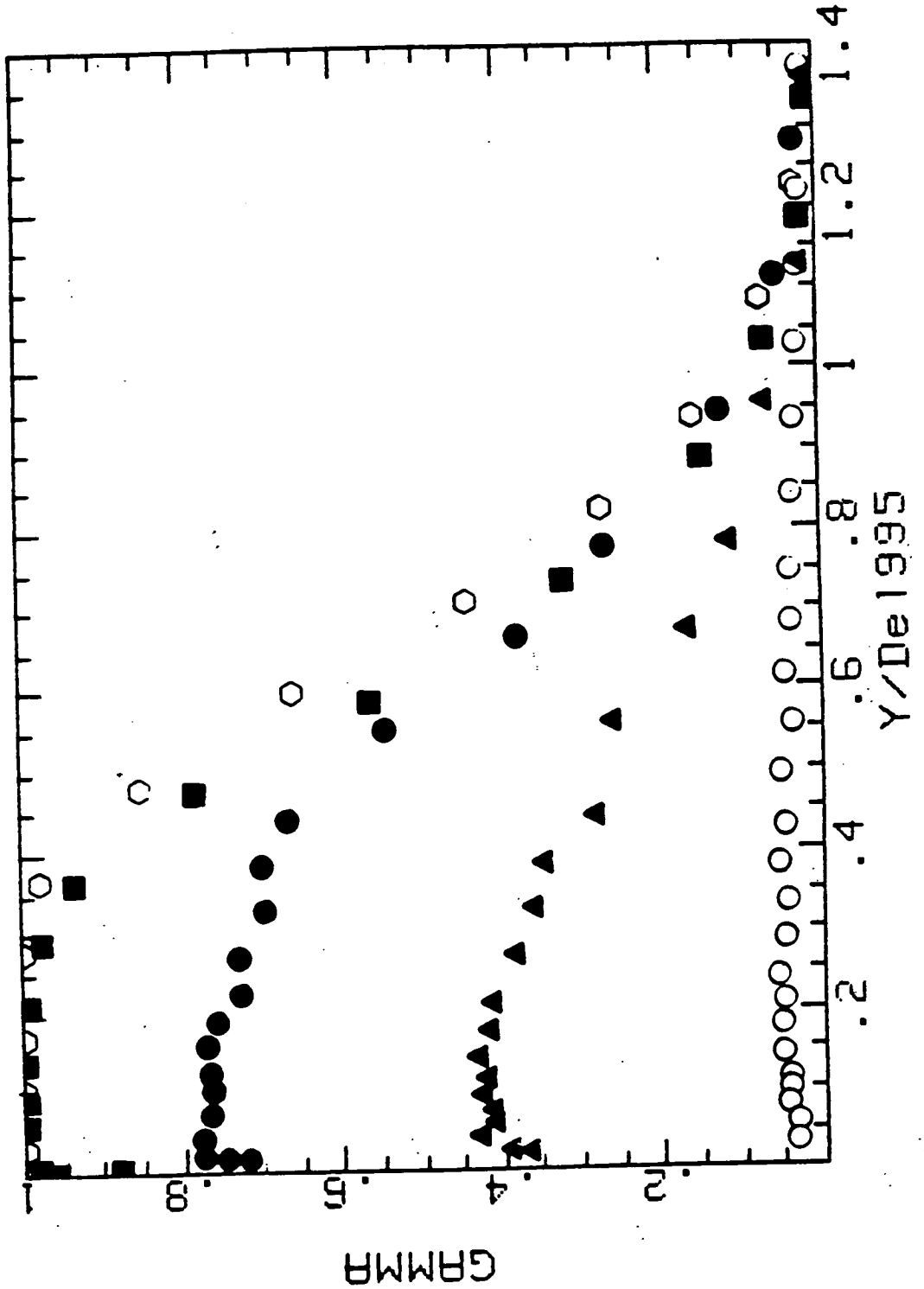

Fig. 3.2.3–Intermittency profile variation through transition (Case 2).
○ - station 2, ▲ - station 3a, ● - station 3, ■ - station 4, ⬡ - station 5.

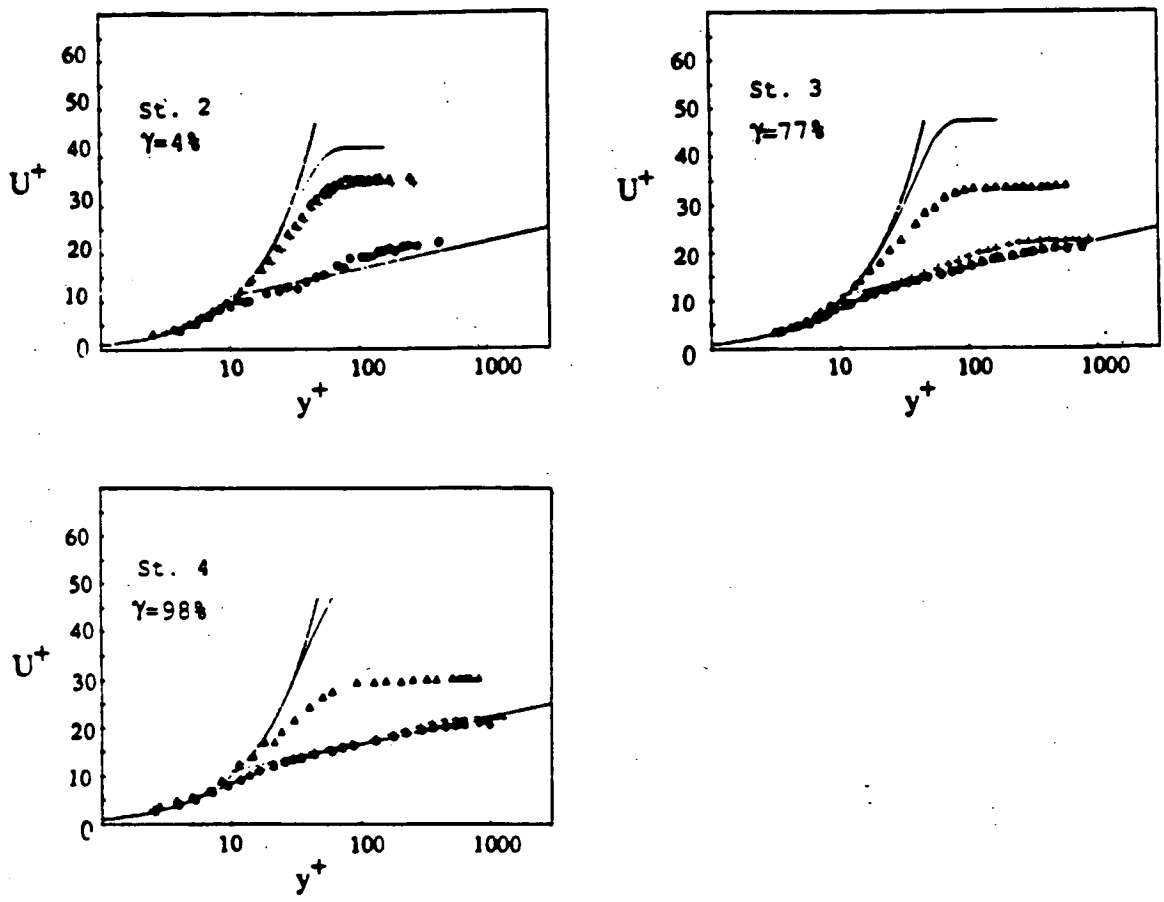

Fig. 3.2.4—Mean velocity profiles sampled on intermittency normalized on wall coordinates (Case 2). ▲ - laminar, ● - turbulent, + - transition.

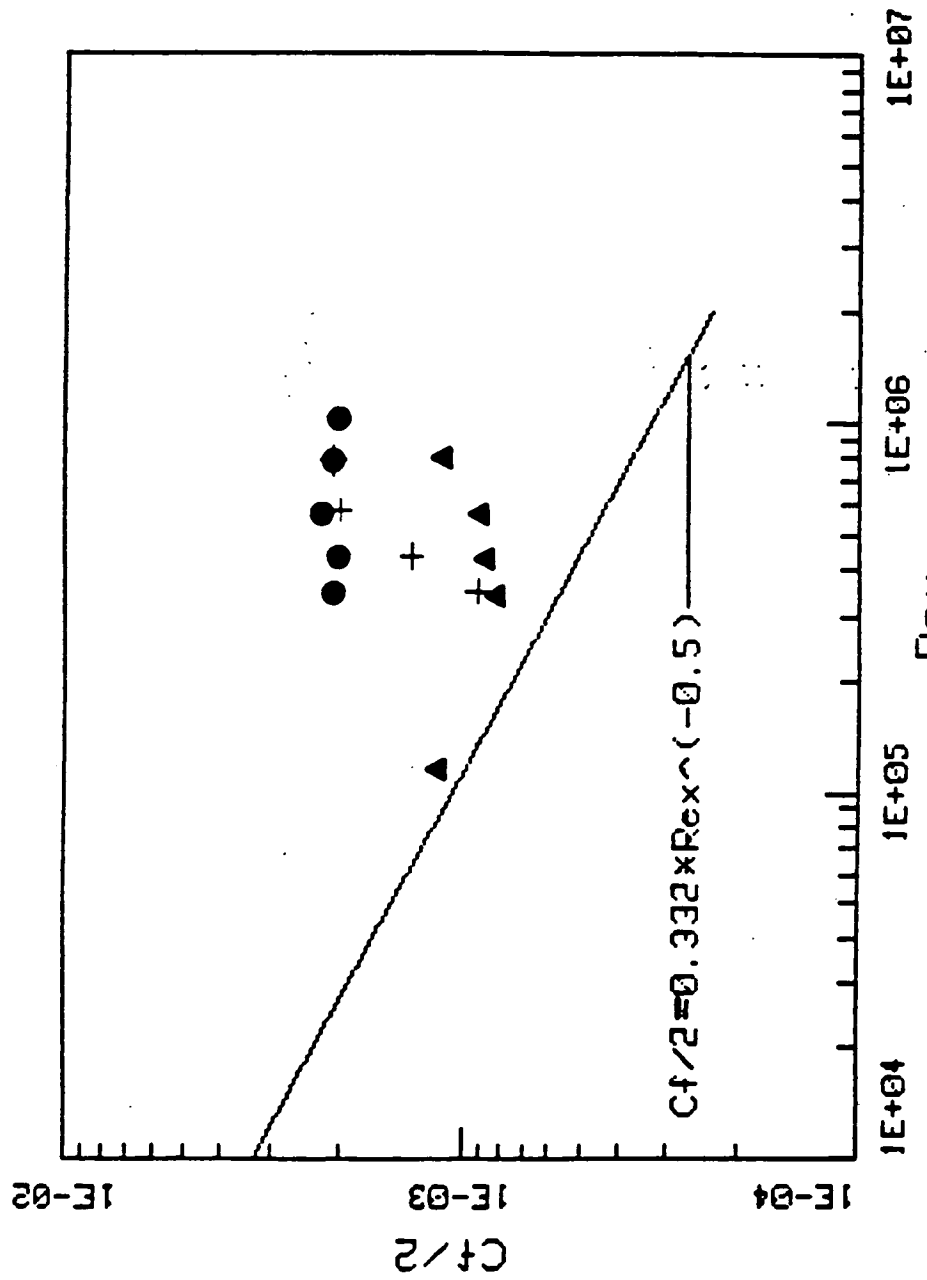

Fig. 3.2.5–Skin friction sampled on intermittency (Case 2). ▲ - laminar, ● - turbulent, + - transition.

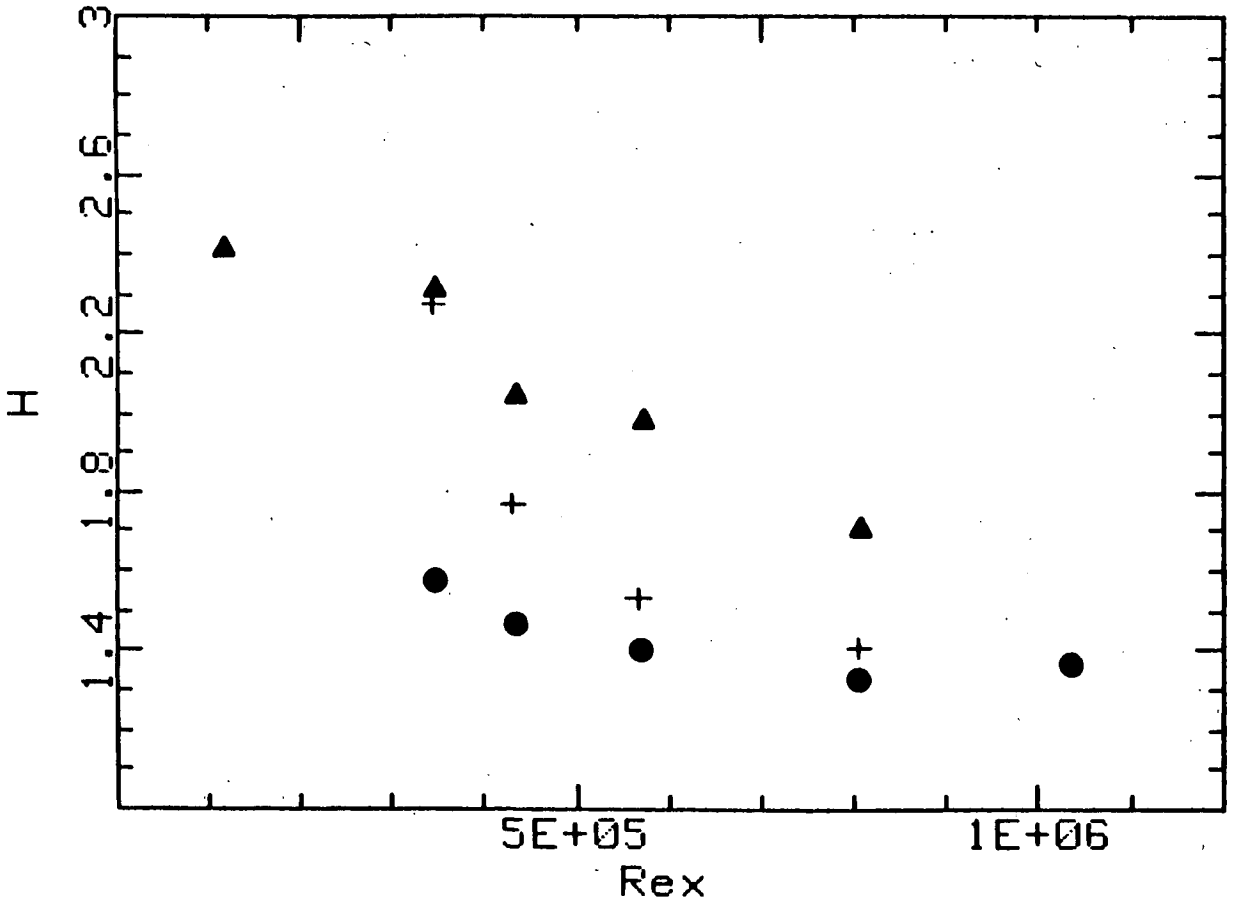

Fig. 3.2.6–Shape factor sampled on intermittency (Case 2). ▲ - laminar, ● - turbulent, + - transition.

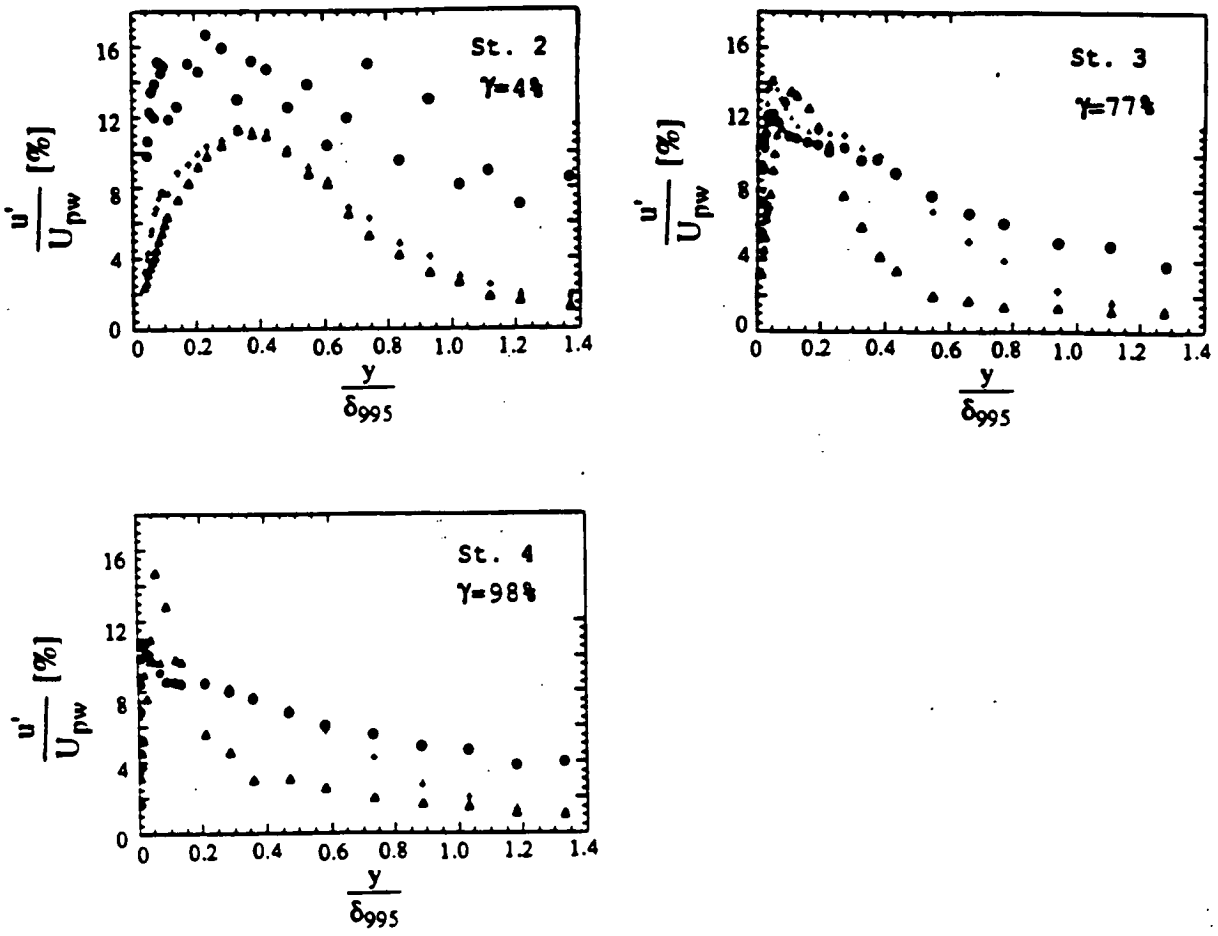

Fig. 3.2.7–Streamwise turbulence intensity sampled on intermittency (Case 2).
▲ - laminar, ● - turbulent, + - transition.

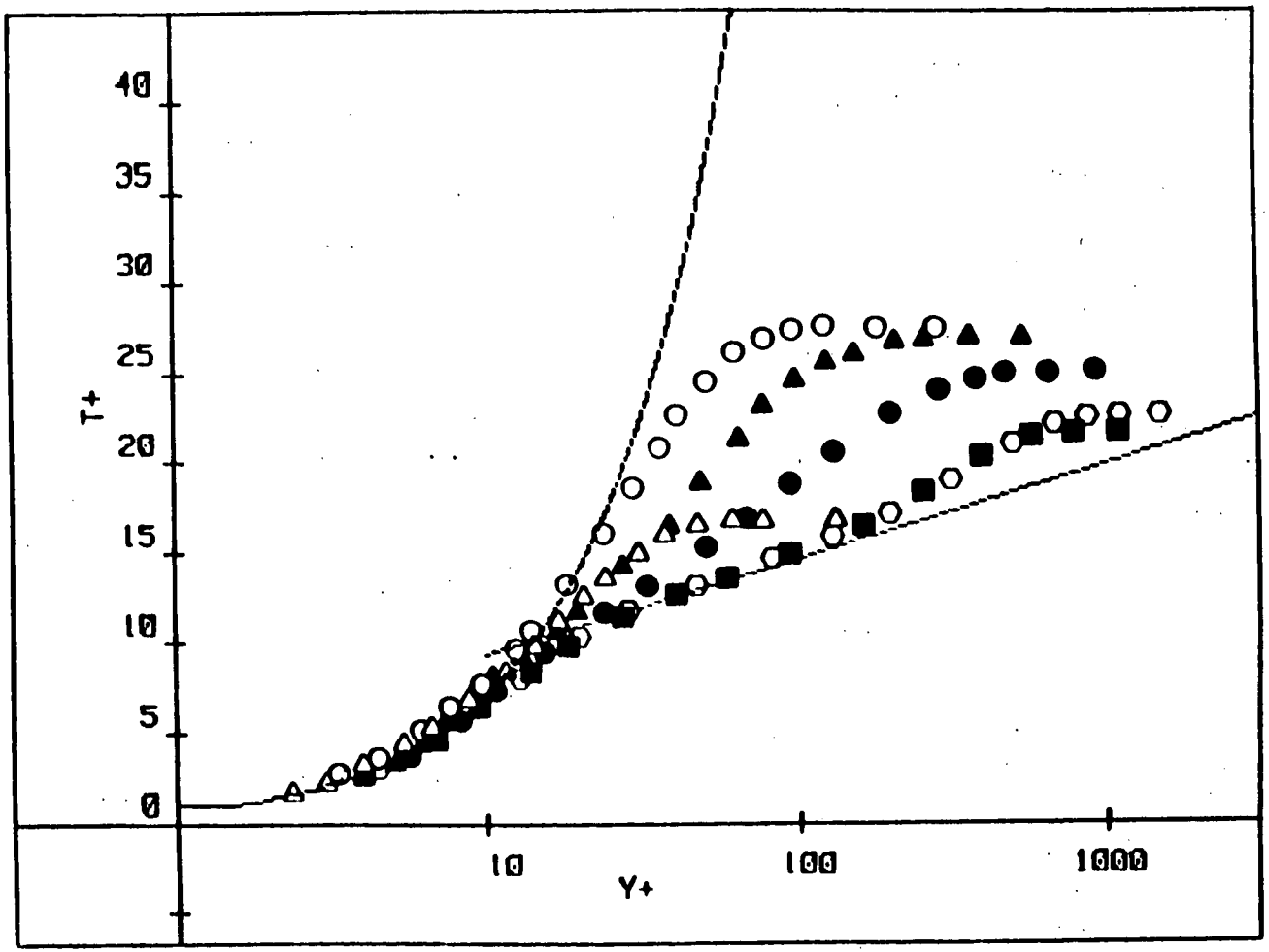

Fig. 3.2.8--Mean temperature profiles through transition normalized on wall coordinates (Case 2). △ - station 1, ○ - station 2, ▲ - station3a, ● - station 3, ■ - station 4, ⬡ - station5. Station 3a refers to data taken at station 3, but at a reduced free-stream velocity.

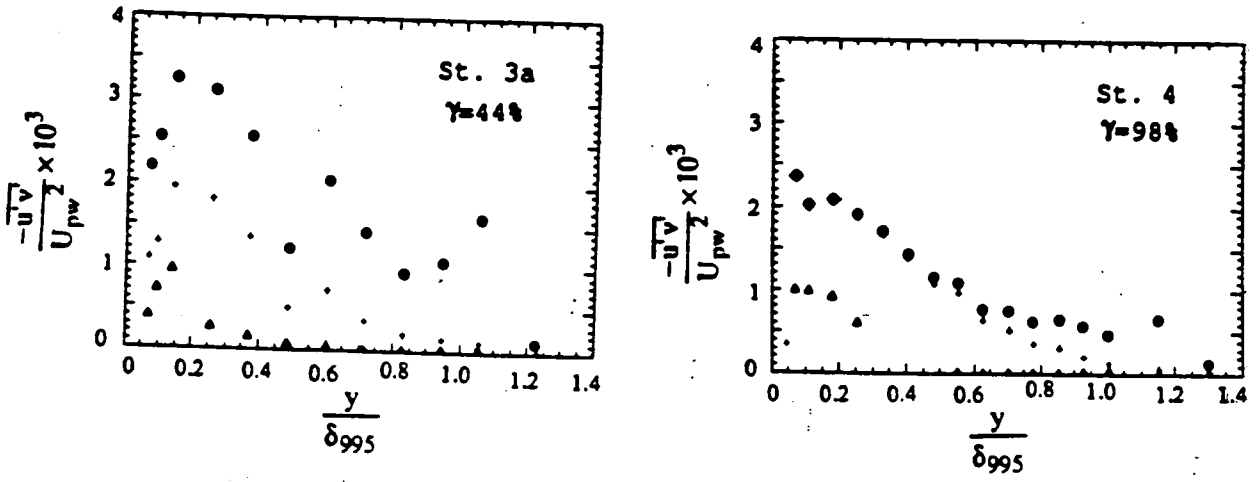

Fig. 3.2.9–Shear stress sampled on intermittency through transition (Case 2). ▲ - laminar, ● - turbulent, + - transition. Station 3a refers to data taken at station 3, but at a reduced free-stream velocity.

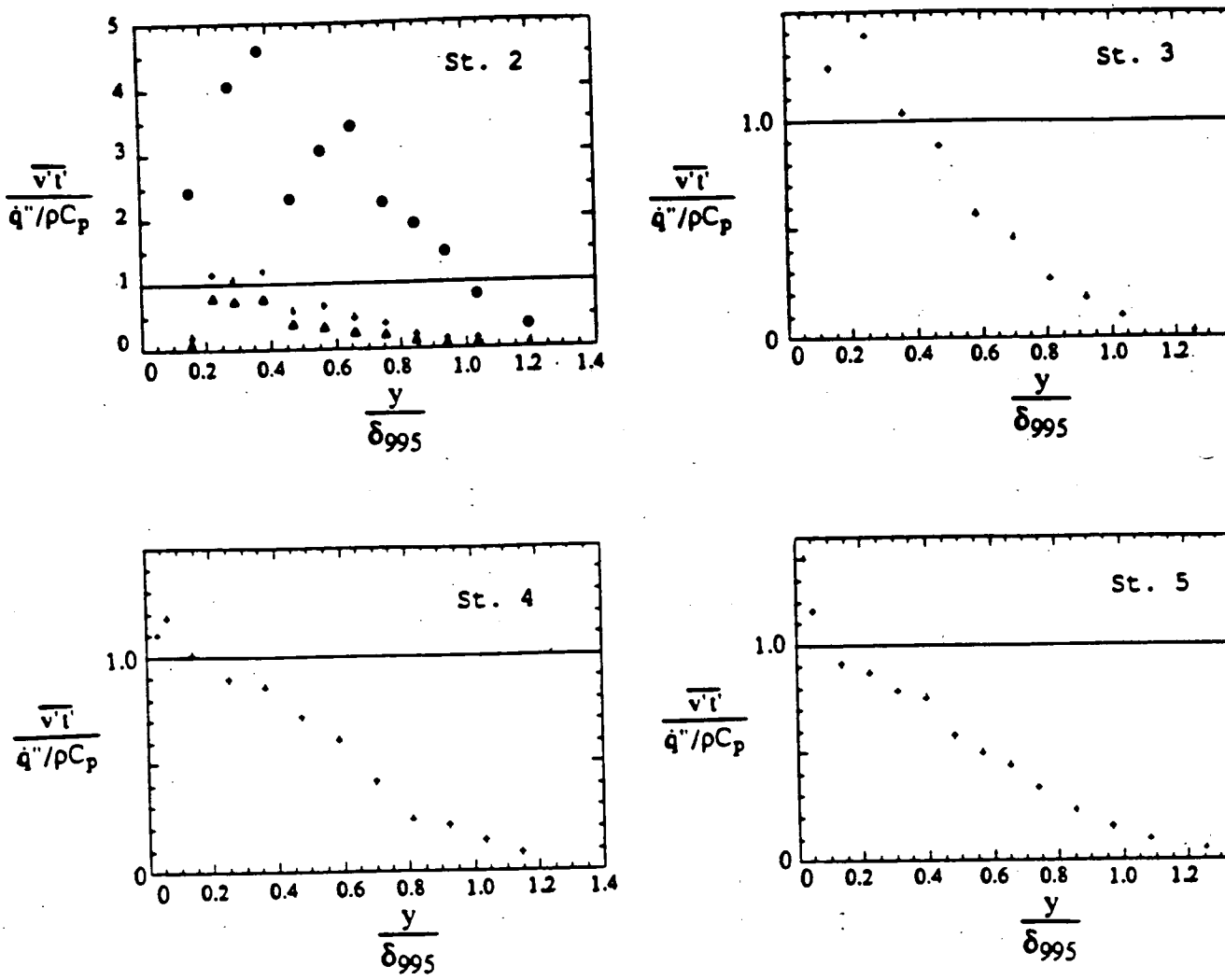

Fig. 3.2.10—Turbulent heat flux sampled on intermittency through transition (Case 2). ▲ - laminar, ● - turbulent, + - transition. The intermittency at station 2 is 9.5%. The other profiles are fully turbulent.

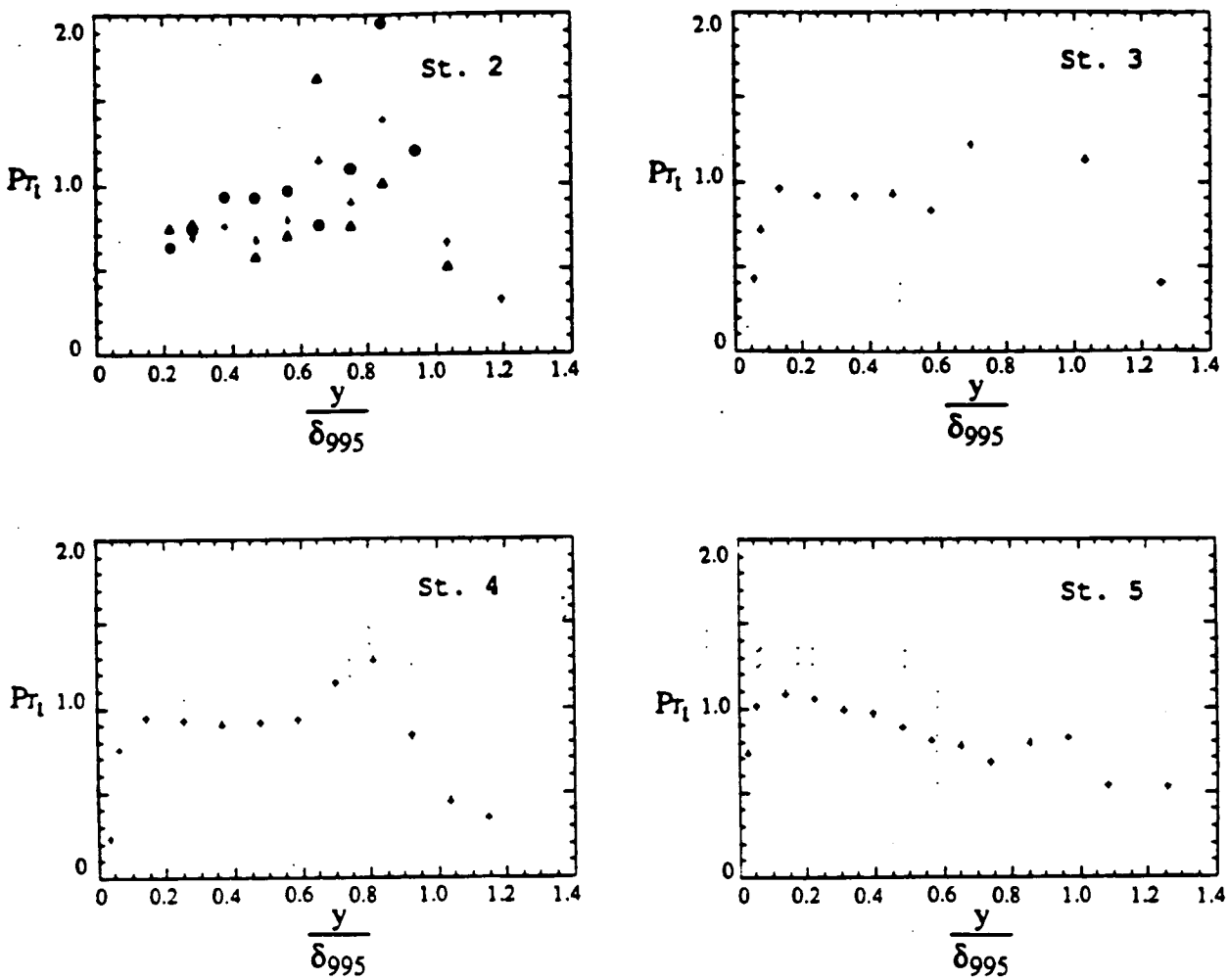

Fig. 3.2.11–Turbulent Prandtl number sampled on intermittency through transition (Case 2). ▲ - laminar, ● - turbulent, + - transition. The intermittency at station 2 is 9.5%. The other profiles are fully turbulent.

3.3). Case 3 – Flat-wall, TI=8.3%

The measurements described in this section were taken with the turbulence generating jet grid (described in Chapter 2) in place. The free-stream turbulence generated, though, was so high that it was difficult to distinguish between laminar and turbulent flow in the transition region from the hot-wire traces. The situation is illustrated on Fig. 3.3.1 where a hot-wire voltage trace in the transition region and it's first derivative are presented. The derivative of the signal seems to fall into two distinct regimes of fluctuation amplitude, suggesting that the flow is transitional, but this is difficult to verify from the direct hot-wire trace. If the velocity is increased (thereby increasing the local Reynolds number), the large-amplitude-fluctuation regime expands at the expense of the low-amplitude-fluctuation regime, further suggesting a transitional flow. The two regimes are not very distinct, however, making separation of the flow into laminar and turbulent regimes difficult (a massive number of dropouts occurs). For this reason, no intermittency based processing was performed for this case.

Free-stream Turbulence Intensity and Spectra. The power spectral density measured in the free-stream at St. 1 is shown on Fig. 3.3.2. The spectrum is seen to be clean, with no significant spikes, in contrast to the two lower TI cases. The high free-stream turbulence generated by the jet grid apparently overwhelms any tunnel unsteadiness and/or electronic noise.

The free-stream turbulence intensity at the tunnel centerline was found to be quite isotropic, as seen from Fig. 3.3.3, and decays from 8.3% at St. 1 to 5.9% at St. 4. There was a significant variation in v' in the cross-stream direction, however, with v' changing by as much as 45% from just outside the

boundary layer to the tunnel centerline. This is thought to be due to the particular jet-grid geometry used.

Stanton Number. The wall Stanton number variation is shown on Fig. 3.3.4. The data is seen to deviate from the turbulent correlation for Re_x<1x105, indicating a short "transition" region, consistent with the intermittent hot-wire signal discussed above. The laminar region (if one exists) is too short to be measured.

In contrast to the data of Blair (1983) and Simonich and Bradshaw (1978), the increase in free-stream turbulence is not seen to augment the heat transfer. This may be due to the low Reynolds number, however, as suggested by Simonich and Bradshaw (1978). An energy balance is shown in Fig. 3.3.5. The heat transfer closure is excellent.

Mean Velocity Profiles. Profiles of mean velocity plotted in wall coordinates are shown on Fig. 3.3.6. The profiles corresponding to stations 2, 3, and 4 are seen to agree very well with the log-linear law, As shown, the log-linear region expands with Re_x. A notable feature of the profiles is the absence of a wake. This is due to the high free-stream turbulence level. The profile corresponding to station 1 is seen to be transitional. As there was some difficulty in assigning an appropriate C_f value to this profile due to the absence of a log-linear region, the profile shown may not be precisely correct. Determining the local skin friction for this profile using a momentum balance was not possible since no data upstream of St. 1 was taken.

Plots of the skin friction and shape factor (H) are shown on Figs. 3.3.7 and 3.3.8, respectively. The skin friction is seen to drop monotonically with Re_x. The shape factor was measured to be 1.71 at St. 1, indicating a transitional boundary layer at this location, but one which has nearly reached

a fully-turbulent shape. The shape factor, H, equal to 1.4, the accepted value for turbulent boundary layers at stations 2, 3, and 4.

Velocity Fluctuation. Fluctuations of the streamwise turbulence intensity are shown on Fig. 3.3.9. The peak in the profile at St. 1 is relatively broad, and is indicative of a laminar or transitional flow. The peaks for the profiles at stations 2, 3, and 4 are much sharper, with the peaks dropping monotonically with Re_x and in step with the drop in free-stream turbulence level with successive downstream positions.

Mean Temperature Profile. Mean temperature profiles measured using a thermocouple probe and normalized on wall coordinates are shown on Fig. 3.3.10. The profiles at stations 2, 3, and 4 show log-linear regions. As was seen for the corresponding velocity profiles, the extent of the log-linear region increases with Re_x. No wake is seen. Turbulent Prandtl numbers deduced from the profiles were consistently near unity. The temperature profile at St. 1 does not seem to possess a log-linear region, consistent with the transitional nature of the flow at this station. This profile was obtained using the uncertain value of C_f obtained from the mean velocity profile.

Shear Stress Profiles. Profiles if u'v' are shown on Fig. 3.3.11. The profile at St. 1 with it's broad peak is indicative of a transitional flow profile, while the profiles at station 2, 3, and 4 have a turbulent flow shape. The near-wall peak is seen to decrease with Re_x.

Turbulent Prandtl Number Measurements. Profiles of the turbulent Prandtl number (Pr_t) measured using a special triple-wire probe are presented on Fig. 3.3.12. Pr_t values are greatly increased above unity for the early turbulent boundary layer (Stations 2 and 3), but are seen to decay to nominally unity by station 4. This suggests that the momentum boundary layer

establishes itself more quickly than does the thermal boundary layer in the early turbulent flow, resulting in higher values of the eddy diffusivity of momentum relative to the eddy diffusivity of heat. This view is supported by the mean velocity and temperature profiles, where similar velocity profiles were seen at stations 3 and 4 while the temperature profiles were still evolving. There is no reason to expect the momentum and thermal boundary layers to develop at the same rate, since the boundary conditions are different. The momentum boundary layer sees a non-zero fluctuation (a non-zero u') in the free-stream whereas t' in the free-stream must equal zero. It is postulated that having eddies present in the free-stream enables the momentum boundary layer to respond more quickly than if it had to grow by turbulent diffusion alone. Creating a temperature fluctuation in the free-stream (possibly by injecting heated air through the grid) may cause the thermal and momentum boundary layers to grow at comparable rates. Pr_t values are in the vicinity of unity by station 4, indicating that the momentum and thermal boundary layers have grown to comparable thicknesses.

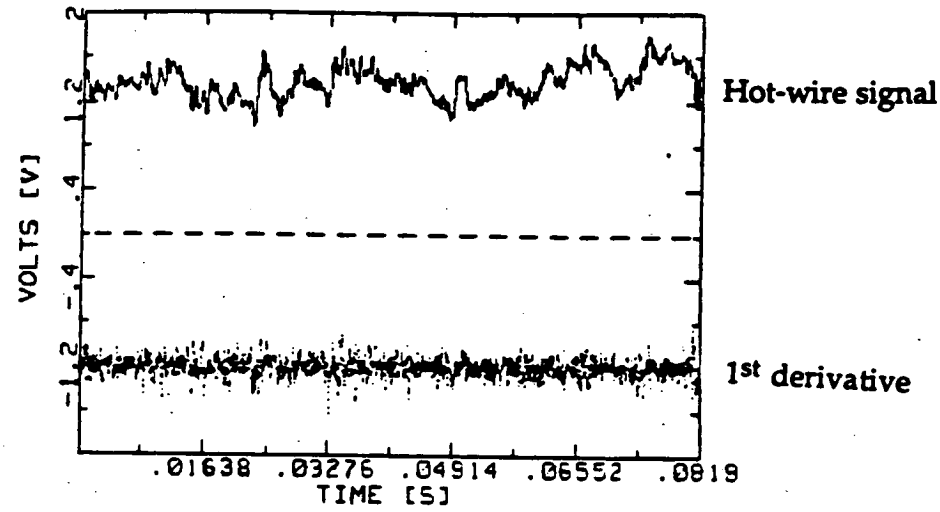

a). Near free-stream

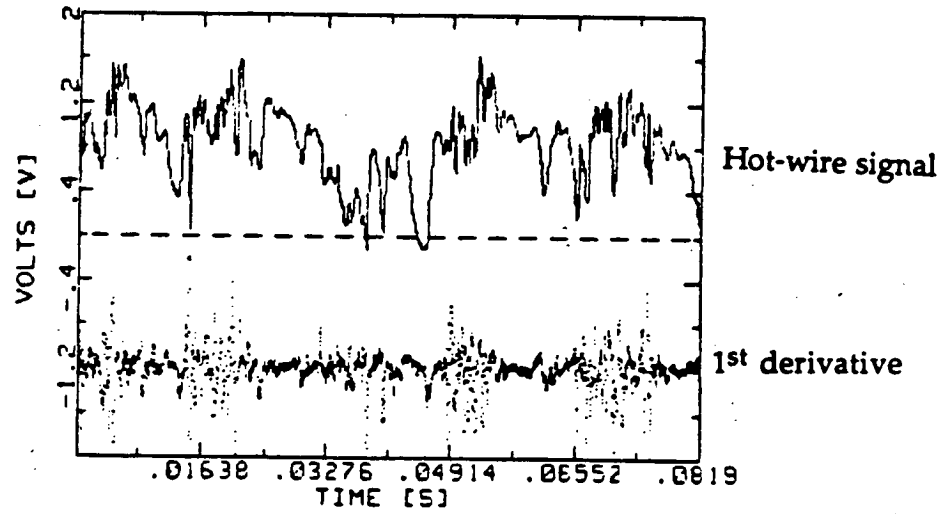

b). Near-wall flow

Fig. 3.3.1–Hot-wire trace and its derivative in the boundary layer (Case 3).

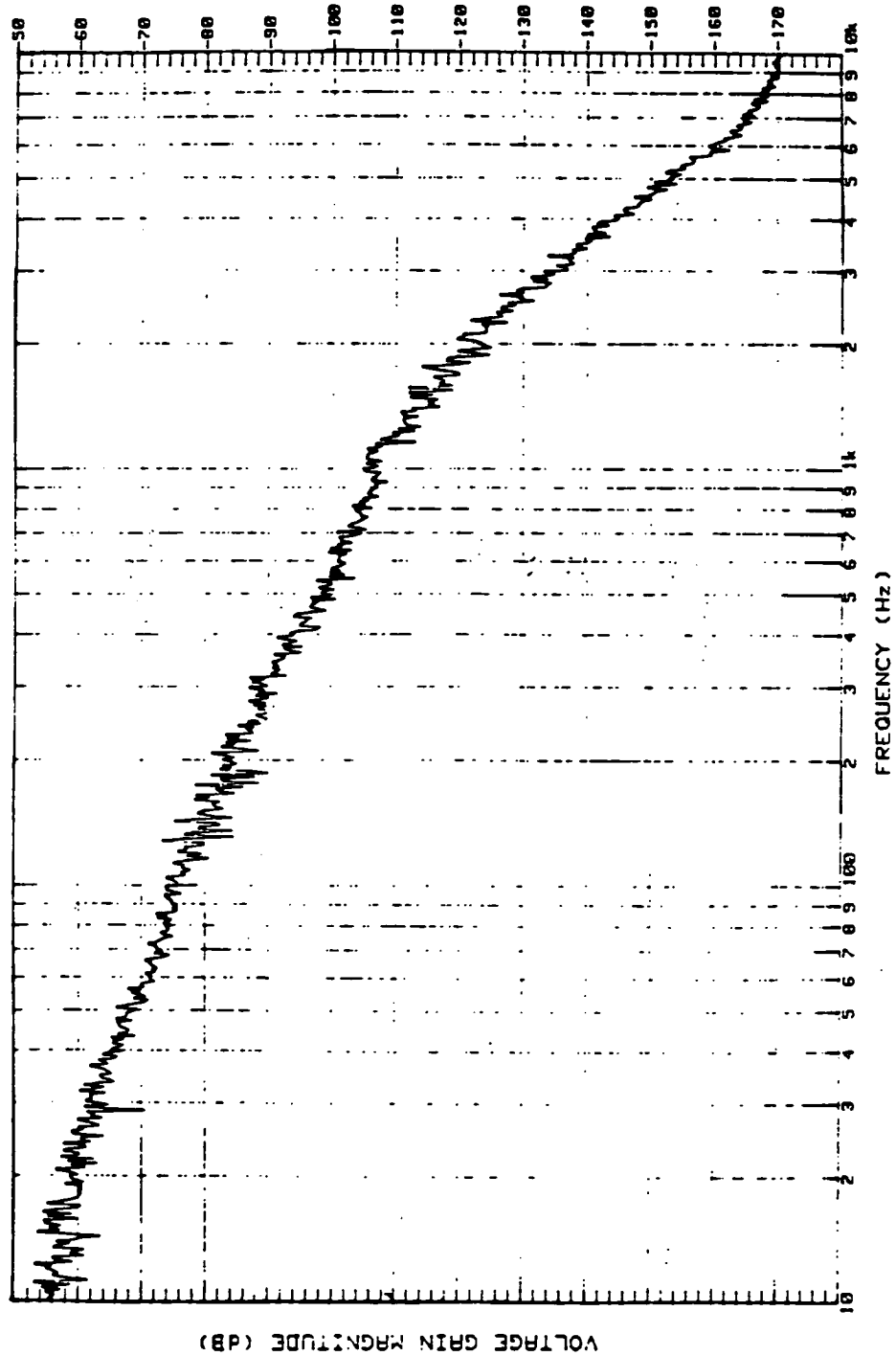

Fig. 3.3.2–Power spectral density distribution of streamwise velocity (Case 3).

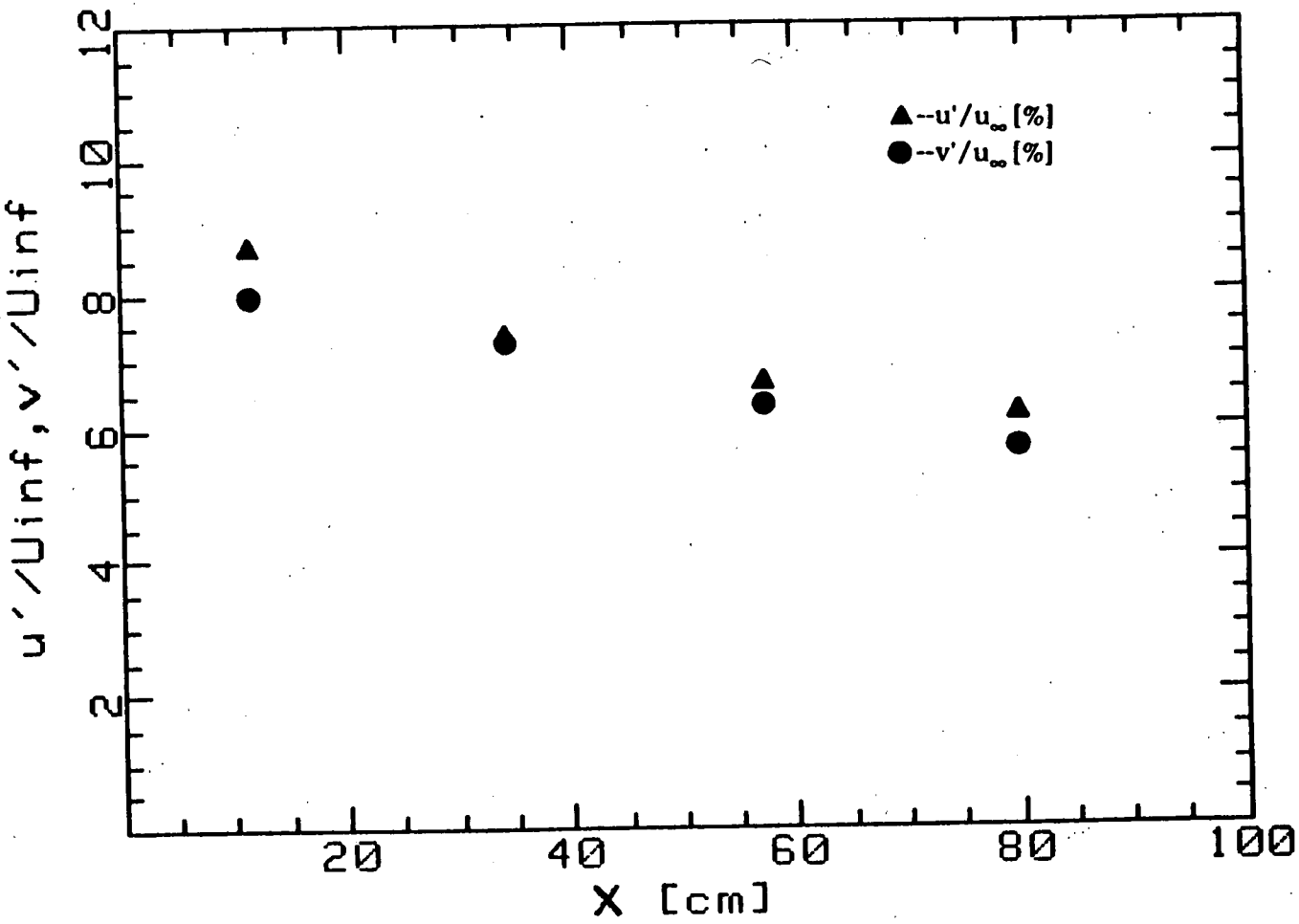

Fig. 3.3.3--Free-stream turbulence intensity variation in the tunnel (Case 3).

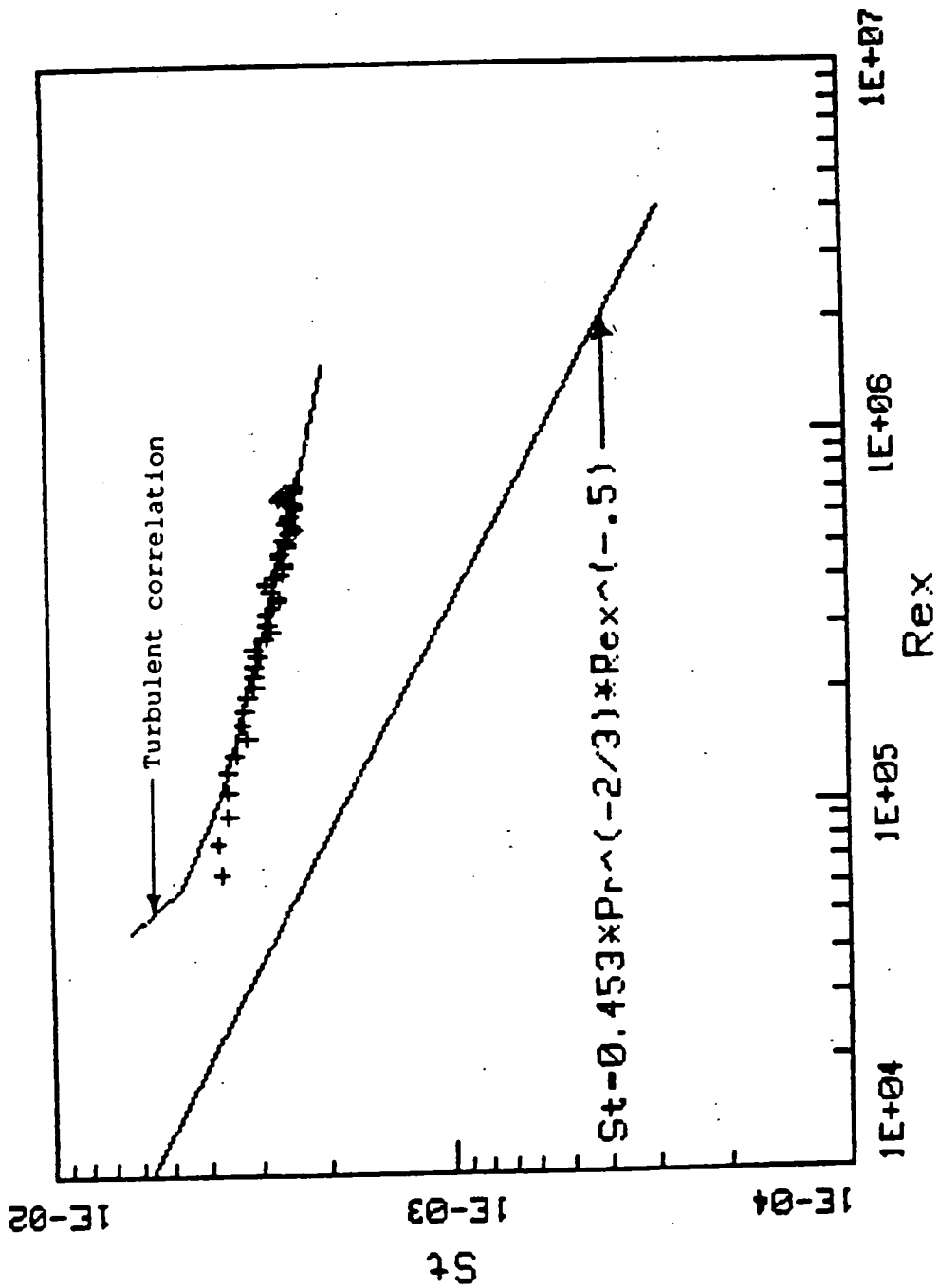

Fig. 3.3.4--Stanton number variation along test-wall (Case 3).

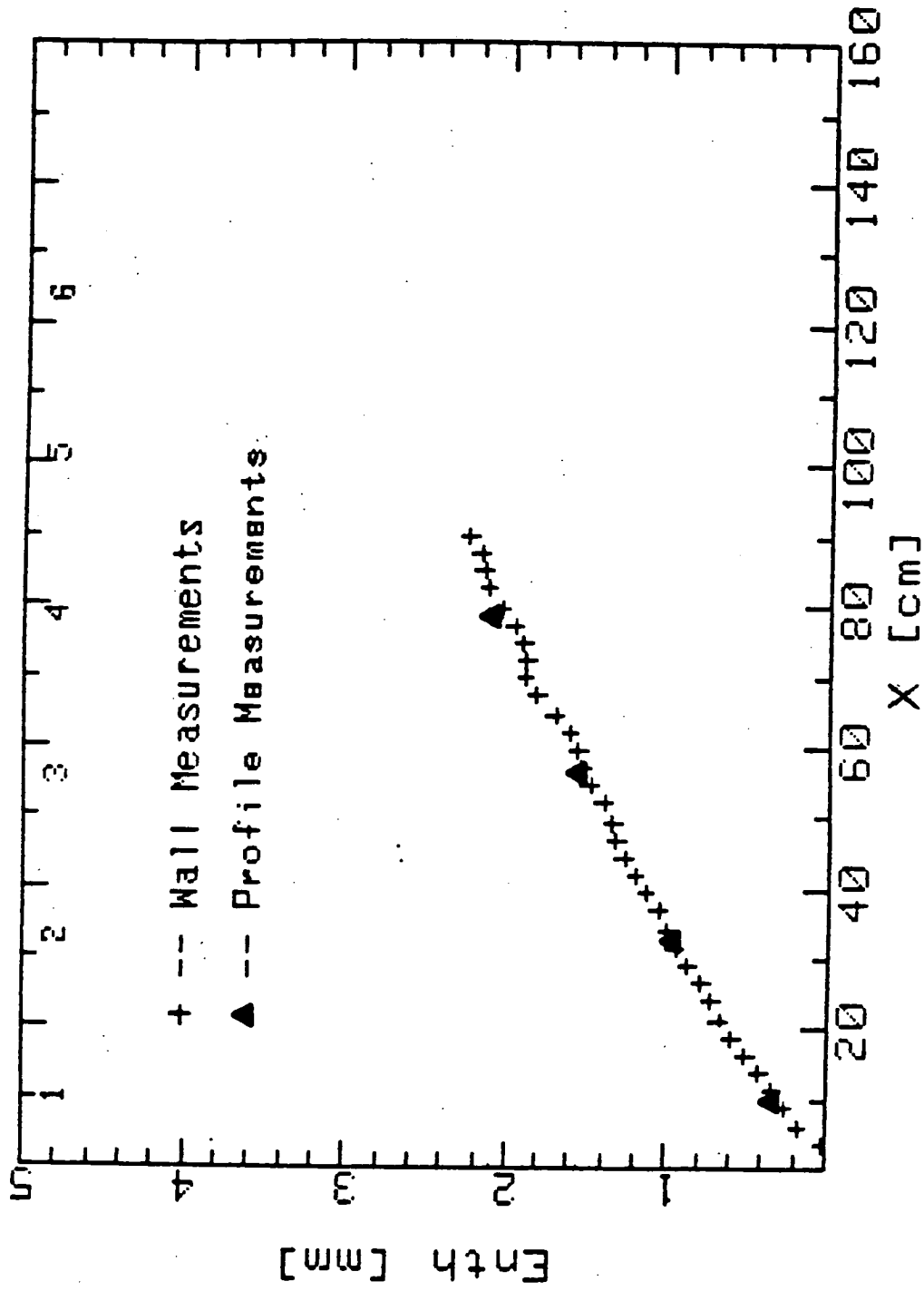

Fig. 3.3.5–Energy balance along wall (Case 3).

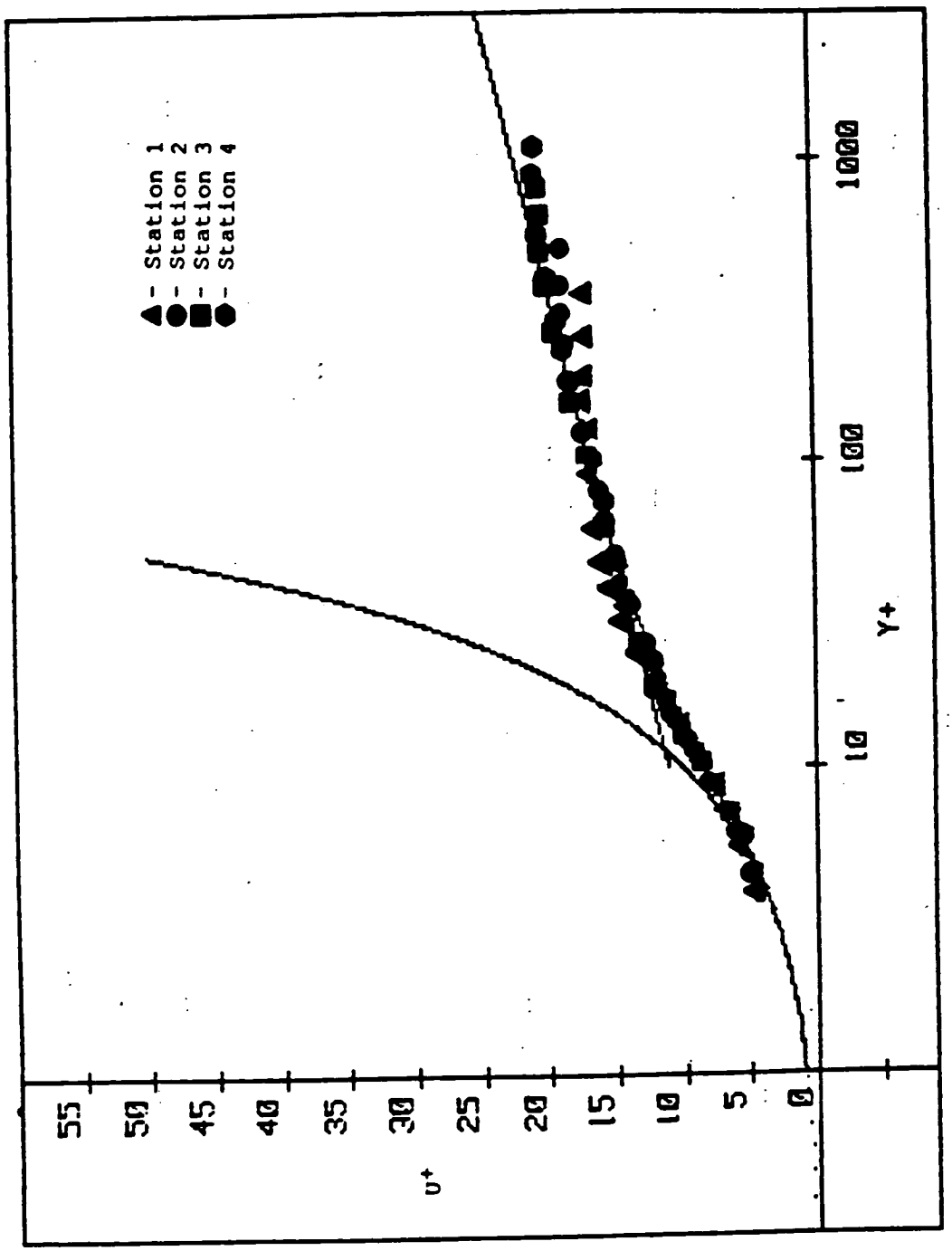

Fig. 3.3.6–Mean velocity profiles normalized on wall coordinates (Case 3).

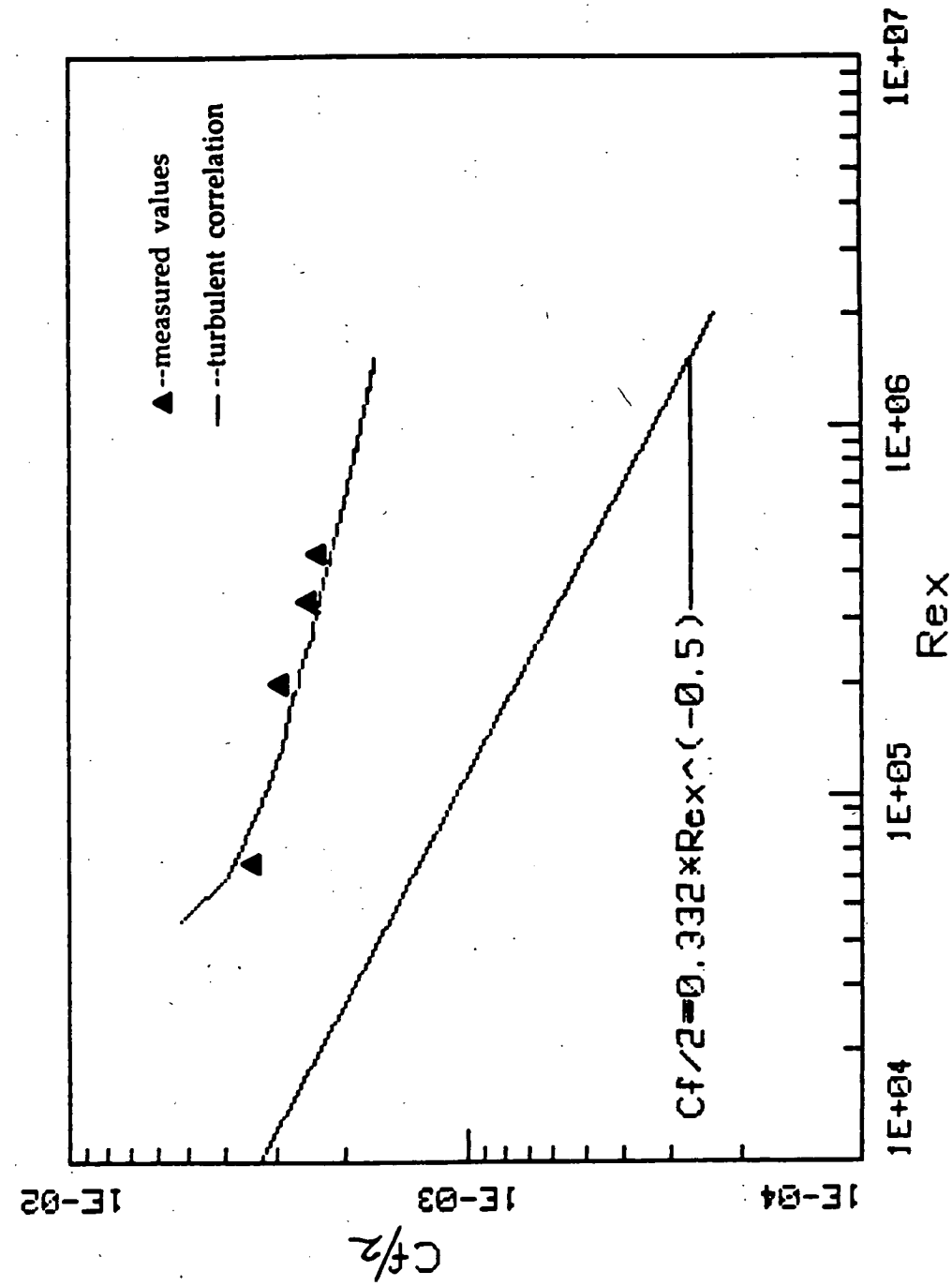

Fig. 3.3.7--Skin friction values along the wall deduced from the mean velocity profiles (Case 3).

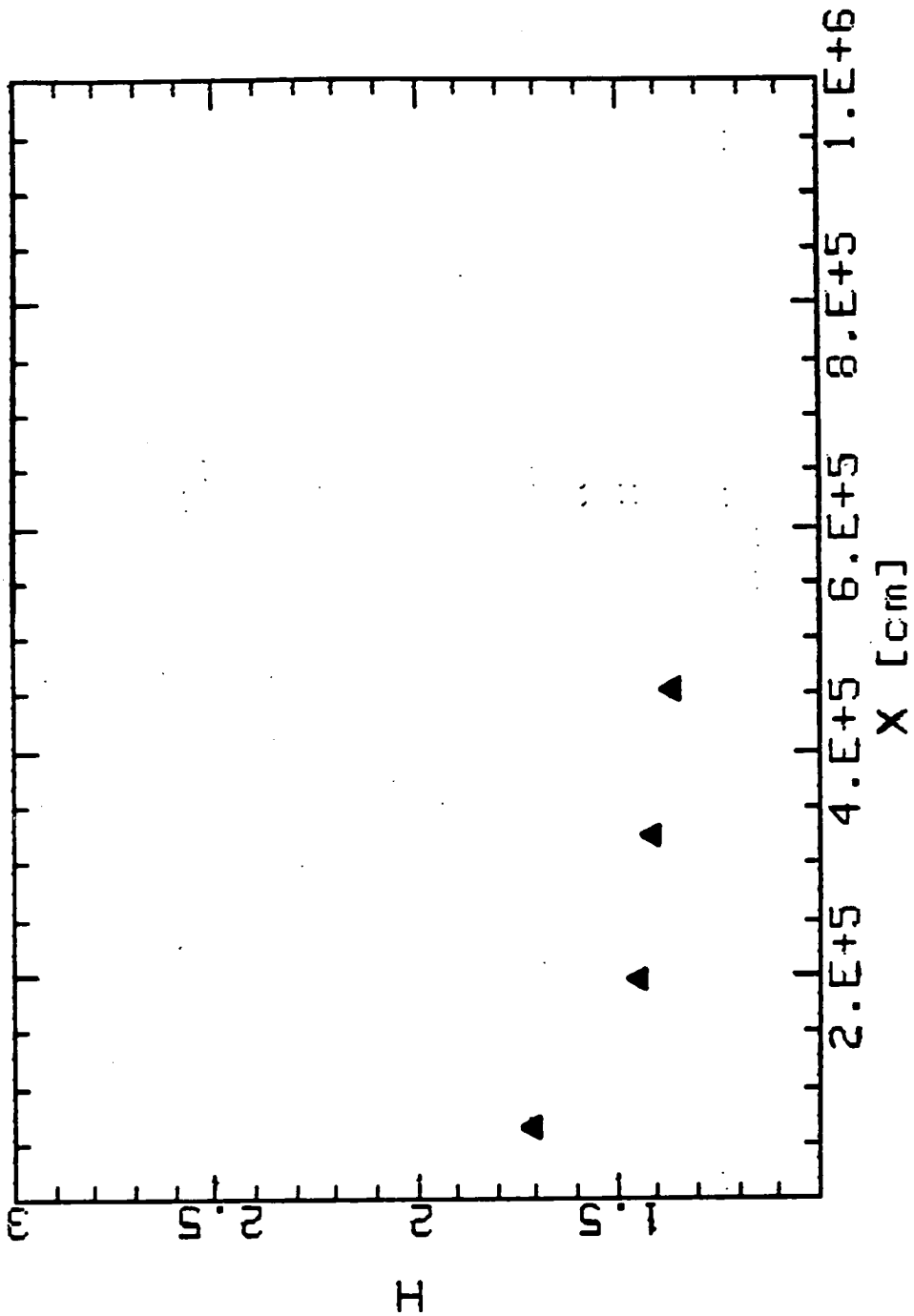

Fig. 3.3.8–Shape factors along the wall (Case 3).

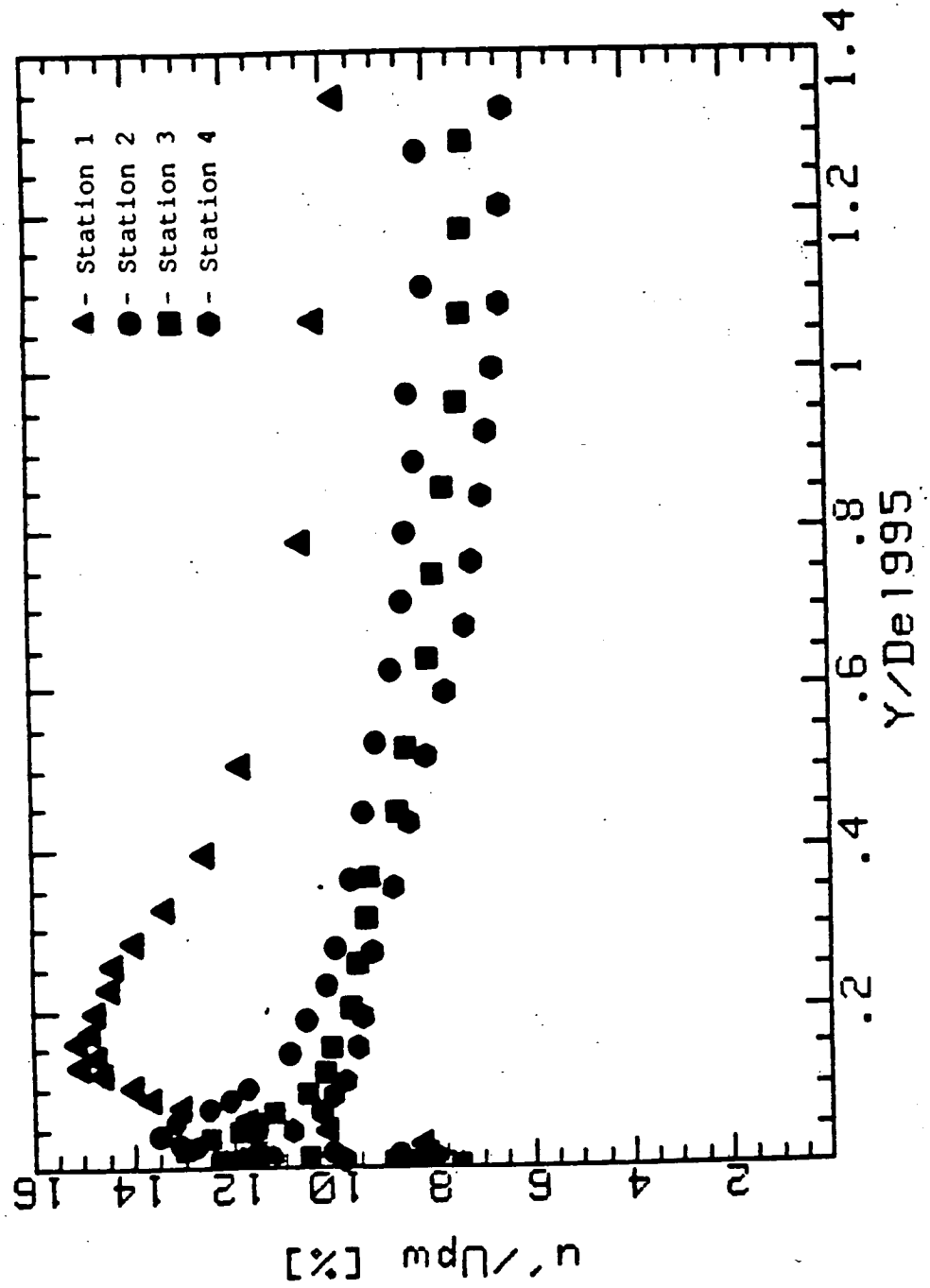

Fig. 3.3.9–Turbulence intensity profiles along the test-wall (Case 3).

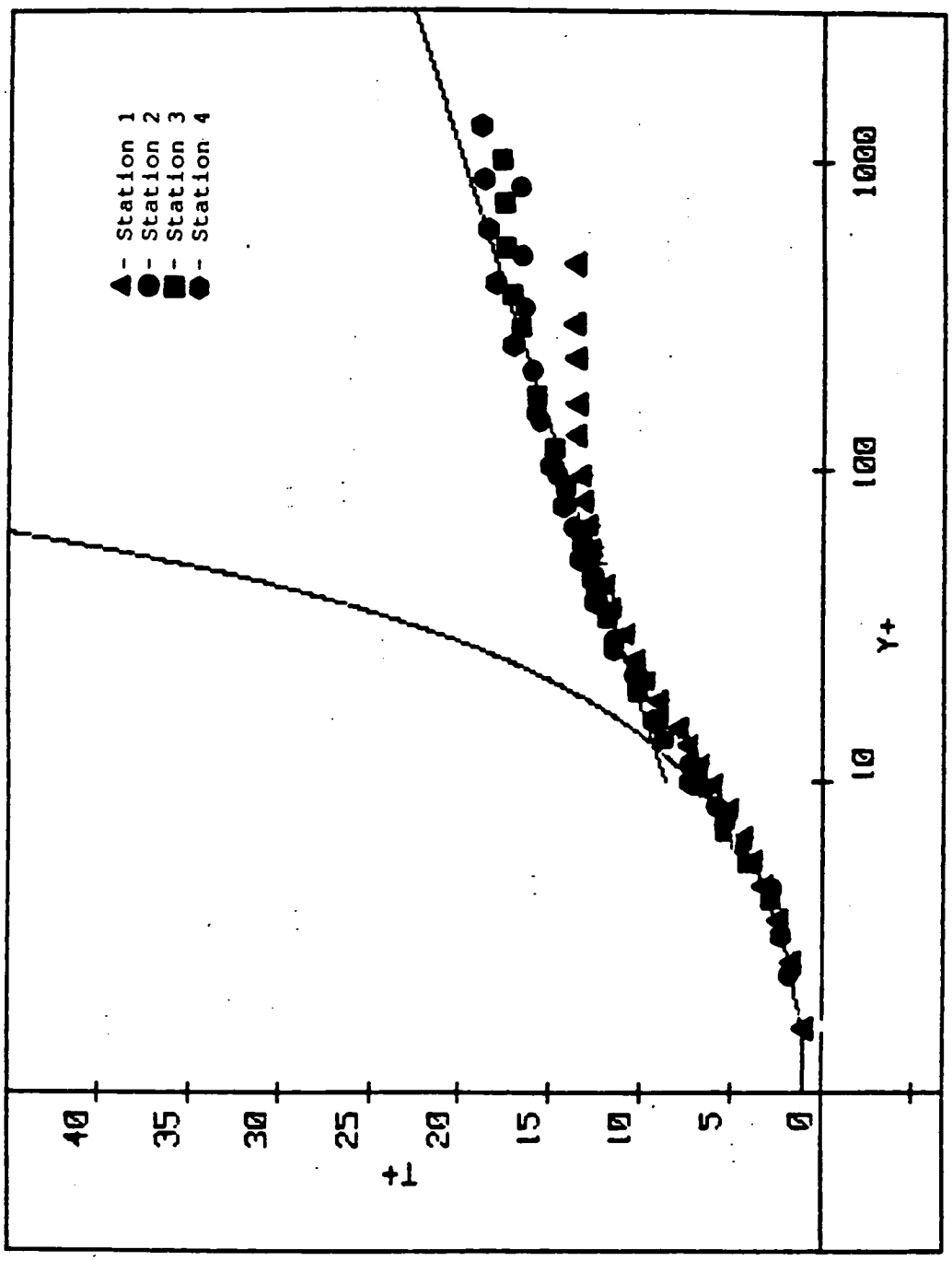

Fig. 3.3.10—Mean temperature profiles normalized on wall coordinates (Case 3).

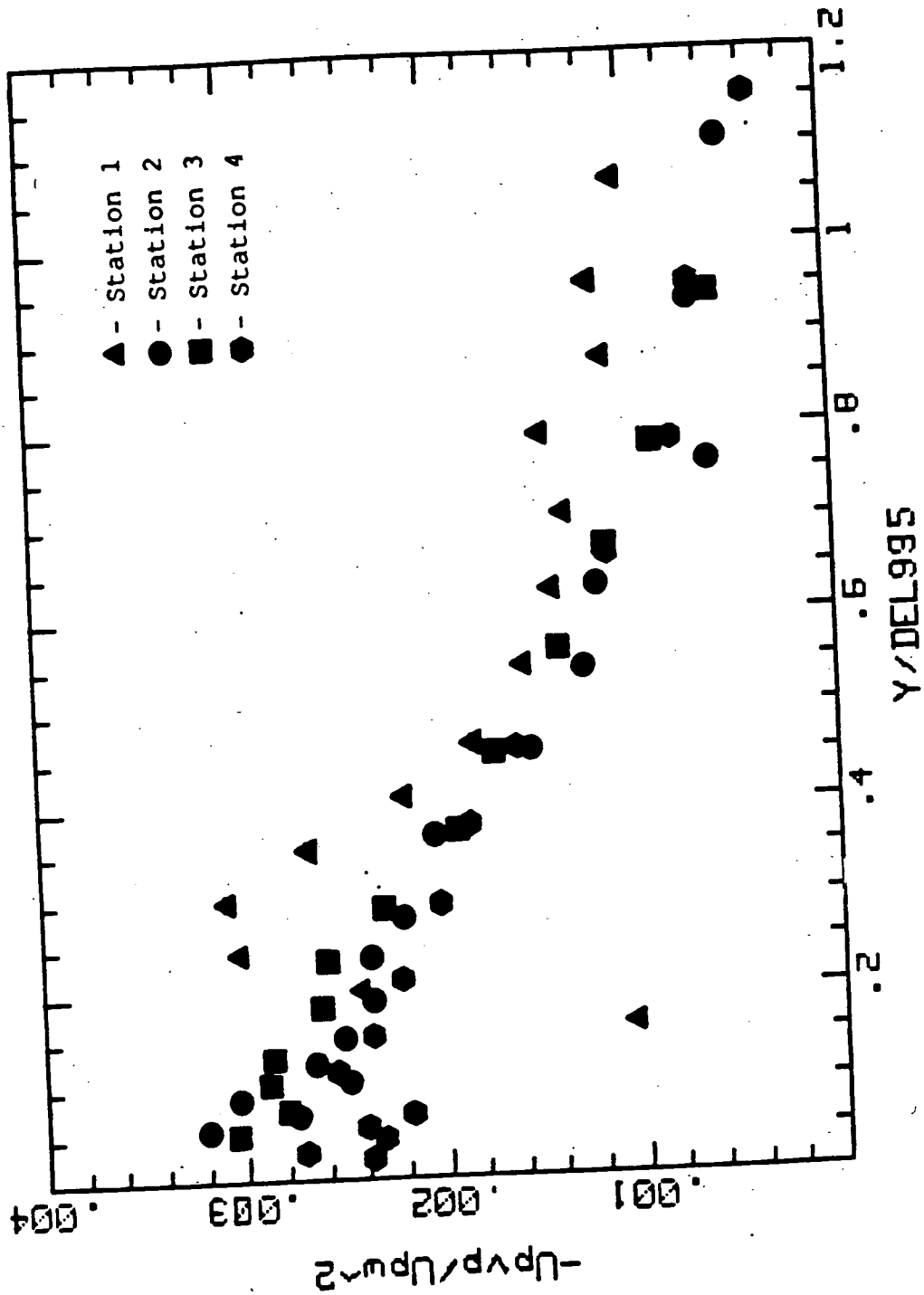

Fig. 3.3.11–Shear stress profiles along the test-wall (Case 3).

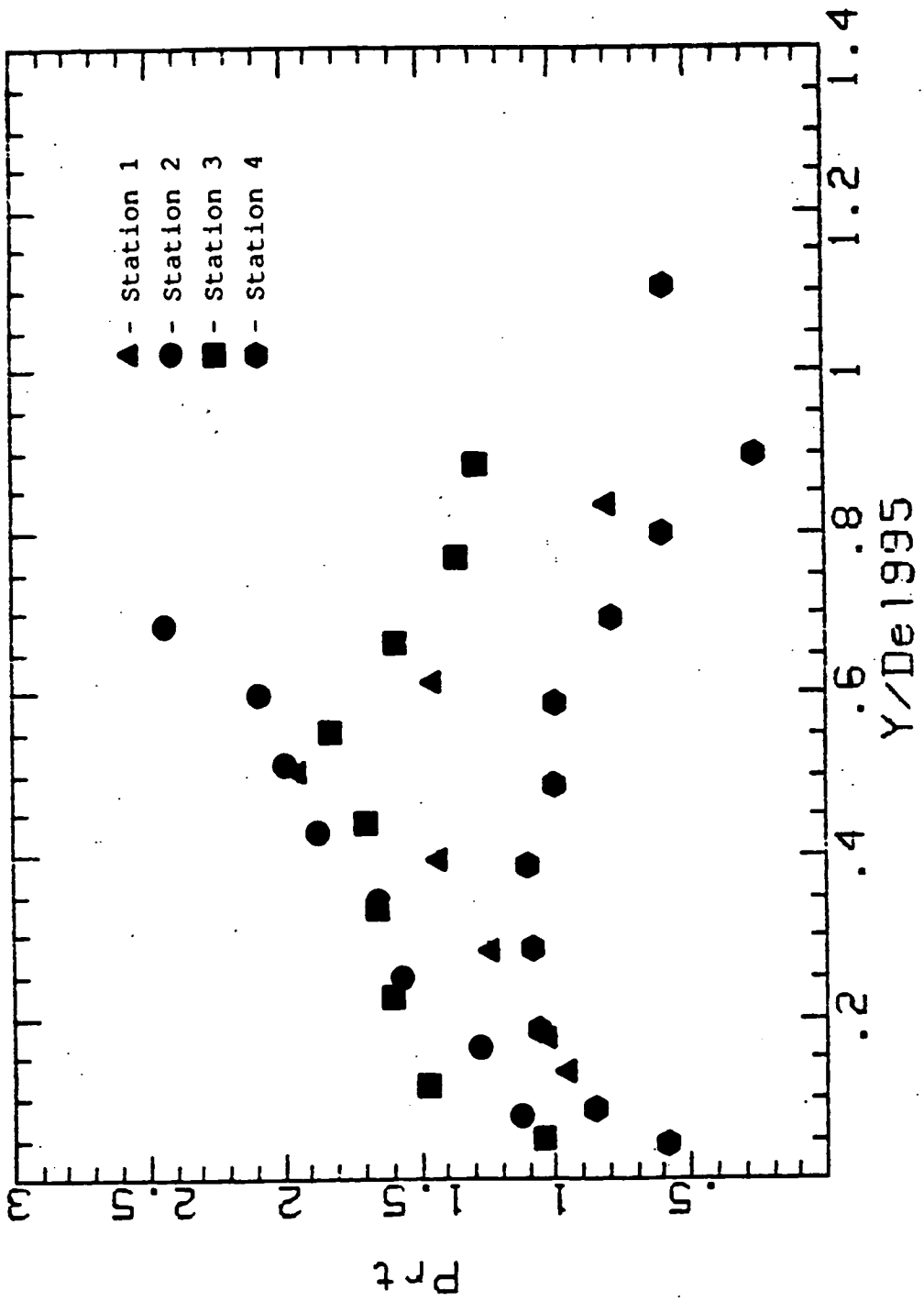

Fig. 3.3.12--Turbulent Prandtl number profiles along the test-wall (Case 3).

3.4). Case 4 -- Concave-wall, TI=0.60%

The data for this case were taken with the flexible heated wall bent to a radius of curvature of 97 cm. No turbulence generating grid was used. The outer flexible wall was adjusted such that the static pressure at the test wall was uniform within ±3% of the upstream static pressure. A comparison of the measured free-stream velocity variation within the curve at stations 3 and 4 with the theoretical velocity distribution as computed by potential theory is shown on Fig. 3.4.1. The theoretical velocity distribution was computed by fitting the equation

$$u_p(y) = \frac{u_{pw}}{1 - \frac{y}{R}} \qquad (2.6)$$

through two of the measured points. It is seen that although there is a slight discrepancy between the measured and theoretical profiles (the source of the discrepancy will be discussed in section 3.5--the curved wall, high turbulence case--where the discrepancy is much more severe), the two agree quite well. Because of the discrepancy between the two, however, the calculation of boundary layer thicknesses is not precise. For this reason, all distances normal to the wall in this section will be normalized on the wall curvature (R). This is done also to be consistent with the high-disturbance cases where integral thicknesses and the 99.5% boundary layer thickness cannot be evaluated (as will later be discussed).

A plot of the hot-wire signal in the transitional flow along with the corresponding intermittency signal is shown on Fig. 3.4.2. A large number of dropouts is observed, indicating that it is difficult for the circuit (and also the

observer) to determine which portion of the hot-wire signal represents turbulent-like flow and which portion represents laminar-like flow. Close inspection of the hot-wire signal revealed that it contained a relatively small amplitude, high frequency signal superimposed on a large amplitude, low frequency signal. It was difficult to decide whether to classify this as a turbulent flow or an unstable laminar flow. Furthermore, the derivatives in the signal were of comparable magnitudes, making it difficult for the circuit to decide whether the flow was laminar or turbulent. For these reasons, conditional sampling was not performed for this case. Since transition occurs so rapidly, it was possible to adjust the free-stream velocity such that transition occurred between stations (stations 2 and 3). This enabled data to be taken in the late laminar (station 2) and early turbulent (station 3) flows, completely bypassing the transition region.

A photograph of the liquid crystal on the test wall (with wall heating--$u_{pw} \sim 17.2$ m/s) is shown on Fig. 3.4.3. Transition occurs (for this wall heat flux) close to station 2 via, it appears, a breakdown of the vortex structure. The spanwise variation implies that the vortices break down independently of each other. This is consistent with the observations of Swearingen (1985), who used smoke to visualize the vortex breakdown. The transition pattern seen here is quite unlike that observed on the flat-wall, in which little spanwise irregularity in the transition pattern was observed. The spanwise temperature variation in the laminar flow is relatively stable in time and stationary in space, implying that the vortices are also stable. If the vortices do move, and it is quite possible they do, they move at a frequency larger than the frequency response of the liquid crystal (~1 Hz) with an amplitude smaller than the vortex wavelength. Spanwise variations in temperature are also

seen further downstream (stations 3 to 6), implying that a relatively stable vortex structure exists in the turbulent flow as well. This is at odds with the results of Simonich and Moffatt (1982) who concluded that a stable three-dimensional vortex structure did not exist on the concave wall when a turbulent boundary layer was introduced to concave curvature. Barlow and Johnston (1988), in a similar study, found that vortices existed, but were not fixed in time and space, the vortices appearing and disappearing randomly across the span. Only when vortex generators were used upstream of the curve was the vortex position fixed. It appears that in the present study, the stable vortex structure in the laminar flow serves the equivalent function to that of the vortex generators in Barlow and Johnston's (1988) study in that they provide preferred spanwise locations for the vortices. The advantage of the present study is that this "locking" is done "naturally". Lastly, the vortex wavelength is seen to be quite irregular across the span in both the laminar and turbulent flows. It was thought that the geometry of the step at the leading edge of the liquid crystal sheet might have an effect on the vortex spacing. Additional effort was expended on smoothing the joint by sanding and a picture of the vortex pattern was re-taken. Comparison of the vortex pattern before and after this sanding revealed no difference between the patterns. It was therefore concluded that the joint had little influence on the vortex spacing. The parameter controlling the vortex spacing is probably the last screen upstream of the nozzle, as was concluded by other researchers (e.g., Swearingen--1985, and Bippes--1978).

Wall heating was found to affect the transition location , as was seen in Case 1. A plot of the intermittency vs. time for wall heating and wall cooling is shown on Fig. 3.4.4. The intermittency is seen to vary from 40% with no

wall heating to approximately 90% with wall heating. As the wall cools, the intermittency returns to 40%. As in Case 1, this precludes the use of velocity profiles measured in an unheated flow to reduce the temperature profile data (such as the computation of enthalpy thickness), at least in the laminar and transitional flow cases. It is felt that this problem does not exist in the post-transitional profiles, and so the data at these stations (3, 4 and 5) will therefore be presented.

Wall heating destabilizes the flow in two ways. First, wall heating increases the viscosity near the wall, leading to inflectional velocity profiles as was discussed in Case 1. Secondly, the fluid density close to the wall decreases, causing the heated fluid to move away from the wall due to the centrifugal forces in the channel. An estimate of the effect of changes in fluid density on flow stability can be calculated using the results of Lin, Kamotani and Ostrach (1982), who investigated the effects of buoyancy on Görtler vortices in a concave-curved channel heated from below. They found that for

$$\frac{Gr}{G^2} > 2.99 \quad ,$$

where Gr is the Grashof number based on gravitational acceleration, buoyancy forces dominated the centrifugal forces and an appreciable increase in the vortex amplitude occurred. The above parameter, the ratio of buoyancy to centrifugal forces, computed for the present case using the centrifugal acceleration in place of the gravitational acceleration (the centrifugal acceleration was over 30 times greater than the gravitational acceleration) was found to be

$$\frac{Gr}{G^2} \cong 5.5 \times 10^{-3}$$

implying that the buoyancy term has little effect on the observed instability. The destabilizing effect of heating on the flow thus seems to be caused mainly by the increase in fluid viscosity near the wall.

Another potential problem with the temperature data occurs during the normalization to wall coordinates, T^+ vs. y^+, where the local wall heat flux and temperature are required. Unfortunately, the wall geometry prevents the accurate determination of these quantities when the flow is strongly three-dimensional. As shown on Fig. 2.4, the thermocouples are embedded behind a ~1 mm (40 mil) lexan/liquid crystal composite. This composite tends to smear out temporal and spatial variations in wall temperature, resulting in much smaller variations at the thermocouple locations. The temperatures recorded by the thermocouples are thus averages of the local surface temperature variation, and do not represent the true surface temperature. A similar problem occurs with the heat flux due to the conduction of heat within the composite. The heat flux is also a measure of the average and not the local value. The problem discussed above is significant only when the order of the non-uniformity (the vortex spacing in the present case) is comparable to or smaller than the composite thickness. The vortex wavelength in the late laminar flow was found to be ~4 mm, giving a disturbance wavelength to composite thickness of ~4. Though this is encouragingly large, some smearing of the temperature and wall heat flux variation is expected. Since the vortex wavelength increases from 10-25 mm after transition, however, the problem becomes much less severe and accurate values of the local wall temperature and heat flux are obtainable.

Due to the problems encountered in the laminar flow, only post-transitional profiles will be presented.

The embedded thermocouples at the centerline of the test wall were found to lie almost directly beneath a downwash. The wall temperatures beneath the downwash could thus be found. To find the wall temperatures at the upwash, two stick-on foil thermocouples 0.0127 mm (0.5 mils) thick (made by Rdf Corporation), configured to give the temperature difference between the two junctions, were taped onto the wall at the upwash and downwash locations. Knowing the wall temperature difference between the upwash and downwash and the wall temperature at the downwash, the wall temperature at the upwash could be calculated.

Mean and Fluctuating Velocity. Results of various spanwise traverses of the hot-wire at constant y-distances from the wall for stations 2 to 5 are shown on Fig. 3.4.5. The spanwise variation of the mean (Fig. 3.4.5) and fluctuating velocities (not shown) in the laminar flow (St. 2) is especially pronounced, with a peak in velocity corresponding to a dip in fluctuating velocity, and vice versa, illustrating the unstable nature of the inflection point velocity profile in the upwash. Oscilloscope traces of the hot-wire output at a constant y-distance from the wall in the upwash and downwash, shown on Fig. 3.4.6, illustrates the difference in fluctuation level between the two flows. It is further seen from Fig. 3.4.5 that the vortex spacing in the late laminar flow (station 2) is quite irregular, as was also seen in the liquid crystal visualization, and that the upwash and downwash do not line up from one y-distance to another, indicating a tilted vortex structure. Also, close inspection of the fluctuating velocity revealed a double peak in u' within the vortex, consistent with the observations of Swearingen (1985).

The location of the state of the flow at station 2 on the Görtler map, shown on Fig. 3.4.7, was determined from calculated values of G and $k\delta_2$. The momentum thickness corresponding to the average between the upwash and downwash values was used in the calculations. The location on the map is well within the unstable range. Also plotted on Fig. 3.4.7 are lines of non-dimensional wavelength, Λ, given by

$$\Lambda = \frac{u_\infty R}{\nu}\left(\frac{\lambda}{R}\right)^{3/2} \tag{3.2}$$

which were calculated from stability theory. From the spanwise measurements, an estimate of the wavelength (λ) was made from which the nondimensional wavelength, Λ, was calculated to be 281. This is in good agreement with the map values.

Shown on Fig. 3.4.8 is a plot of the transition Reynolds number vs. a non-dimensional radius (R/δ_2) from Liepmann (1943). The flat plate transition Reynolds number is shown by a horizontal line, while Liepmann's criterion is shown by the sloped line marked N=240 (N is the Görtler number, G, calculated using the boundary layer thickness in place of the momentum thickness). Note that for smaller radii, i.e., smaller $R/\delta_{2,tr}$, the data fit Liepmann's stability criterion. However, for larger radii, the data approach the flat plate transition criteria. It can therefore be concluded that transition to turbulence on highly concave surfaces is dominated by the Görtler vortices. Also marked on Fig. 3.4.8 is the state of the present flow. It is seen to fall near Liepmann's stability criterion, implying that the Görtler vortices dominate the transition process.

The difference in the spanwise profiles between the upwash and downwash (Fig. 3.4.5) becomes much less pronounced after transition, due to the increased mixing in the boundary layer. The vortex wavelength becomes much larger, and no double peak in u', as was observed in the laminar flow, is seen. The crests and troughs also align.

The growth of the boundary layer and the effect of the vortices on the mean velocity profiles are illustrated on Fig. 3.4.9. Large differences between the upwash and downwash profiles are seen in the late-laminar flow (station 2) with a clearly inflectional upwash velocity profile. The profiles become quite similar just after transition, then again deviate at the later stations. An explanation for this remarkable behavior will be discussed later. The mean velocity normalized on wall coordinates at the upwash and downwash locations near the tunnel centerline are shown on Fig. 3.4.10. The upwash profile at station 2 is distinctly inflectional and a dramatic difference between the upwash and downwash profiles is seen. Again, much of this difference disappears after transition. Although it appears that the upwash profiles have a fuller shape than the downwash profiles, this is an artifact of the normalization (the skin frictions for the upwash are smaller than for the downwash, resulting in higher u^+ values in the upwash).

Plots of the skin friction and shape factor vs. Re_x are shown on Figures 3.4.11 and 3.4.12, respectively. In both plots, large differences in values in the late-laminar region, followed by closer values in the turbulent flow are seen, supporting the trends seen in both the spanwise and normal profiles of streamwise velocity. It is interesting to observe, however, that the upwash and downwash values approach one another just downstream of transition, then increasingly deviate downstream, implying that the vortices again

become stronger. This led the authors to speculate that this behavior may be reflected in the "turbulent" Görtler number (G_t) (the Görtler number with the eddy viscosity replacing the molecular viscosity). This value decreases to a low value immediately after transition due to the sudden increase in eddy viscosity, then slowly increases in value as the turbulent boundary layer grows. Measurements of G_t using a cross-wire probe to measure the shear stress and the mean velocity gradient to obtain the eddy viscosity (ν_e) are shown below.

Station	δ_2x1000 [m]	ν_e [m^2/s]	ν [m^2/s]	G_t
2 (upwash)	.530	------	.000016	13.06
2 (downwash)	.164	------	.000016	2.230
3 (upwash)	.998	0.000425	------	1.288
3 (downwash)	1.124	0.00043	------	1.522
4 (upwash)	1.167	0.000894	------	0.592
4 (downwash)	1.820	0.000882	------	1.531
5 (upwash)	1.898	0.001046	------	1.345
5 (downwash)	2.718	0.001329	------	1.814

The eddy viscosity used is the average value across the boundary layer. It was computed by numerically integrating the values then dividing by the boundary layer thickness. The measurements show that G_t does decrease to ~1.3 immediately after transition, but remains fairly constant thereafter. G_t values computed using the maximum value of eddy viscosity within the boundary layer decrease the magnitude of G_t, but show a similar trend.

Profiles of u' are shown on Fig. 3.4.13. The large variation in u' in the late laminar flow between the upwash and downwash is seen to completely disappear after transition (station 3), where similar profiles are seen. The differences re-emerge at the later stations (stations 4 and 5) in the outer part of the flow, consistent with the observed trends in mean velocity, C_f and H. The

near-wall peak in u' is consistently near 11% for all the post-transitional profiles indicating a near-wall curved-asymptotic situation.

Shear Stress Profiles. Profiles of the shear stress u'v' are shown on Fig. 3.4.14. The data at station 2 is not considered reliable since the spacing between the wires of the X-wire probe is comparable to the vortex wavelength. When the probe was placed in the boundary layer and traversed in the spanwise direction, it was clearly seen that both wires were not in a upwash or downwash simultaneously. The data at this station was taken by centering the probe at the upwash or downwash as best the author could.

The shear stresses at the wall plotted on these figures are not measured values of u'v' but computed values obtained from the skin friction values deduced from the mean velocity profiles. Generally good agreement between the wall values and the profile values are seen. A reversal in shear stress in the upwash at station 2 is observed due to the inflection point velocity profile. The shear stresses in the upwash are greater than the shear stresses in the downwash in the turbulent flow, at odds with what the skin friction values would suggest (C_f in the upwash is smaller than in the downwash). A distinction must be made between the near-wall flow and the wake flows, however. The wake flow is significantly affected by the large vortical motion which convects turbulent fluid towards the upwash. The near-wall flow is less affected, depending more on the local velocity profile.

Stanton Number. The Stanton number variation along the wall under an upwash is plotted on Fig. 3.4.15 along with the corresponding flat-plate results. Concave curvature is seen to be highly destabilizing, causing transition to occur about five times earlier than on the flat plate. It was noted that the transition start, path and length varied depending on whether the

centerline thermocouples were beneath a downwash or an upwash, however. An example is given on Fig. 3.4.16 where Stanton number measurements at two free-stream velocities were made. The change in the boundary layer thickness causes the vortex wavelength to change, enabling the embedded thermocouples along the centerline to lie under an upwash for the 6.74 m/s case or a downwash for the 17.2 m/s case. Transition is seen to occur over a shorter length under an upwash than under a downwash. Stanton number values for the upwash locations in the laminar flow are seen to lie below the laminar correlation. It is not known whether the downwash values lie slightly above the correlation due to unheated starting length effects.

Mean and Fluctuating Temperature Profiles. Mean temperature profiles normalized on wall coordinates are plotted on Fig. 3.4.17. The striking feature of these profiles is their deviation from the thermal law-of-the-wall. Pauley and Eaton (1988) found that for a pair of spanwise-separated vortices embedded in a boundary layer where the common flow of the vortices is toward the wall, a strong increase in T^+ was observed for all locations within the vortex except in the upwash at the edge of the vortex pair where a decrease in T^+ was observed. The increase in T^+ values in both the present case and in the study by Pauley and Eaton (1988) is thought to be due to dilution of the heated boundary layer flow by the free-stream flow, resulting in an overall lowering of the temperature in the boundary layer. The difference between the wall temperature and the temperatures in the boundary layer increases, resulting in higher values of T^+. The present results and those of Pauley and Eaton (1988) indicate that the thermal law-of-the-wall is not valid in boundary layers which have such large, streamwise vortices embedded within them.

Profiles of the fluctuating temperature are shown for the post-transitional stations on Fig. 3.4.18. The data was obtained using the triple-wire probe described earlier. Values of t' in the upwash and downwash are similar for station 3, then deviate for stations 4 and 5, similar to the behavior observed for the corresponding u' profiles. Peak values of t' are ~12% of the wall to free-stream temperature difference for all stations. The temperature fluctuations in the upwash are greater than those in the downwash, reflecting the relatively unstable nature of the flow and the convection of heated flow (and thus larger fluctuation magnitudes) toward the upwash.

Turbulent Heat Flux and Turbulent Prandtl Number. Profiles of the streamwise and normal cross-stream heat fluxes normalized on the wall heat flux are shown on Figs. 3.4.19 and 3.4.20, respectively. The streamwise heat flux is roughly twice the cross-stream heat flux for all profiles at both the upwash and downwash locations. The cross-stream heat flux profiles approach unity near the wall, as expected. The cross-stream diffusion of heat is greater in the upwash than in the downwash, similar to the behavior observed in the shear stress profiles. Again, this occurs due to spanwise convection of heat to the upwash locations. Values of v't' in the upwash are greater than those in the downwash even though Stanton numbers in the upwash are lower than those in the downwash.

Profiles of the turbulent Prandtl number deduced from u'v', v't', and the gradients in velocity and temperature are shown on Fig. 3.4.21. All profiles are seen to be near unity in the vicinity of the wall, indicating no gross violation of Reynolds analogy. The data in the outer part of the boundary layer is not reliable due to the weak values of u'v' and v't' and the very shallow gradients in velocity and temperature.

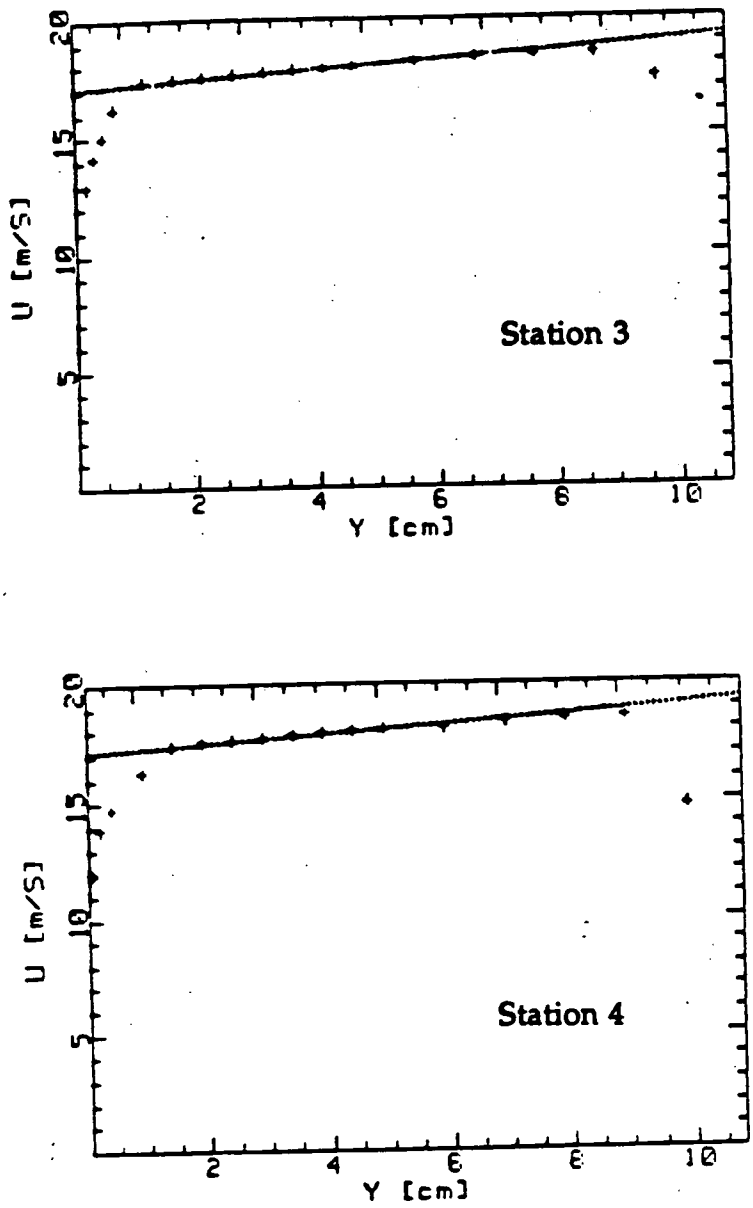

Fig. 3.4.1—Comparison of measured velocities with potential velocity profiles at stations 3 and 4 (Case 4).

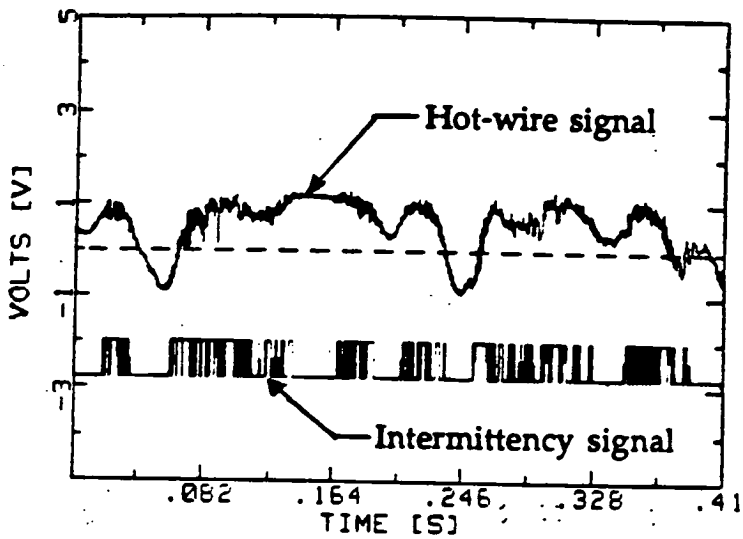

Fig. 3.4.2--Hot-wire signal and output of intermittency circuit (Case 4).

Fig. 3.4.3--Picture of heated test-wall showing spanwise variation in wall temperature (Case 4).

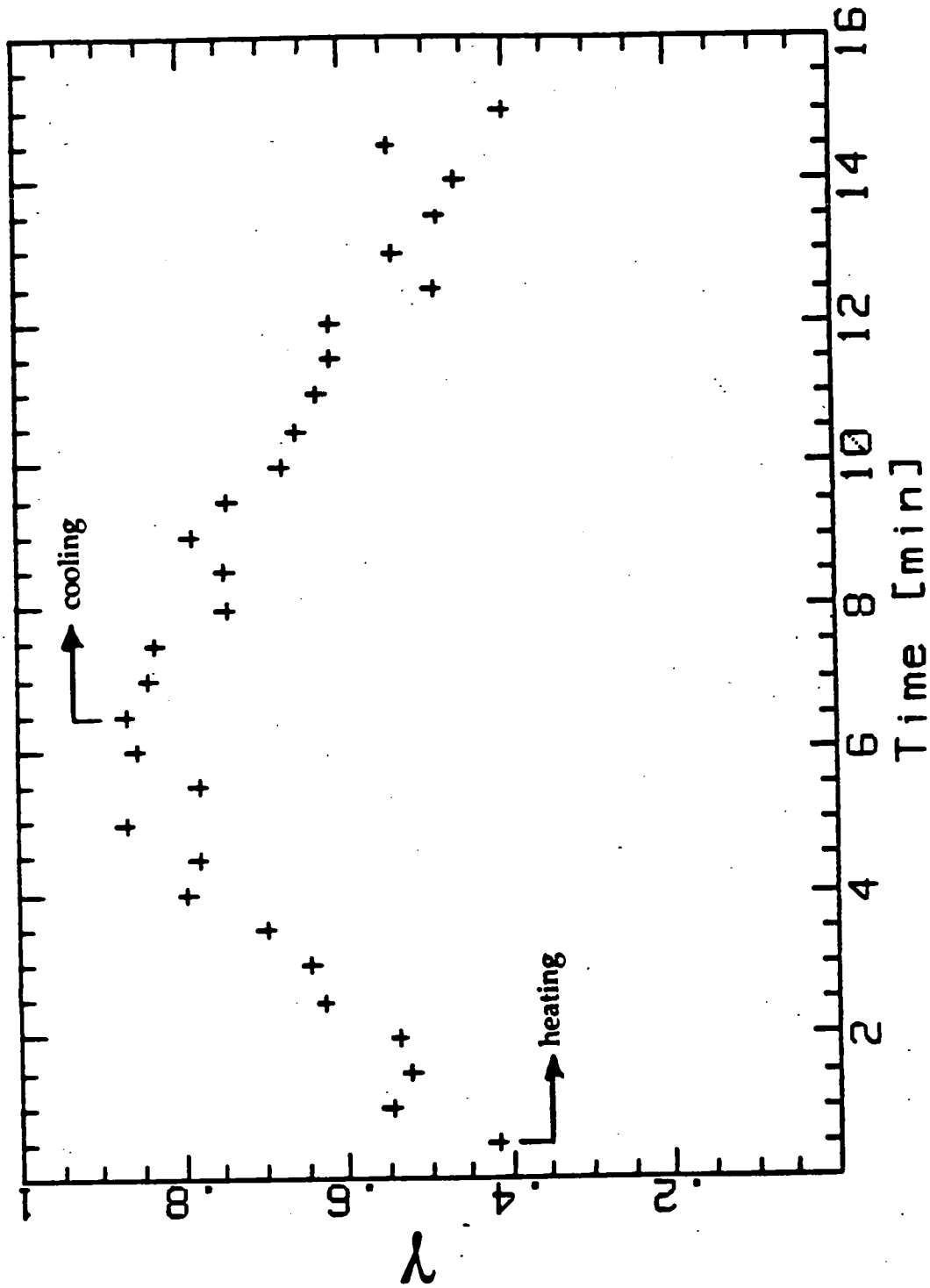

Fig. 3.4.4—Variation of intermittency vs. time for wall heating and wall cooling (Case 4).

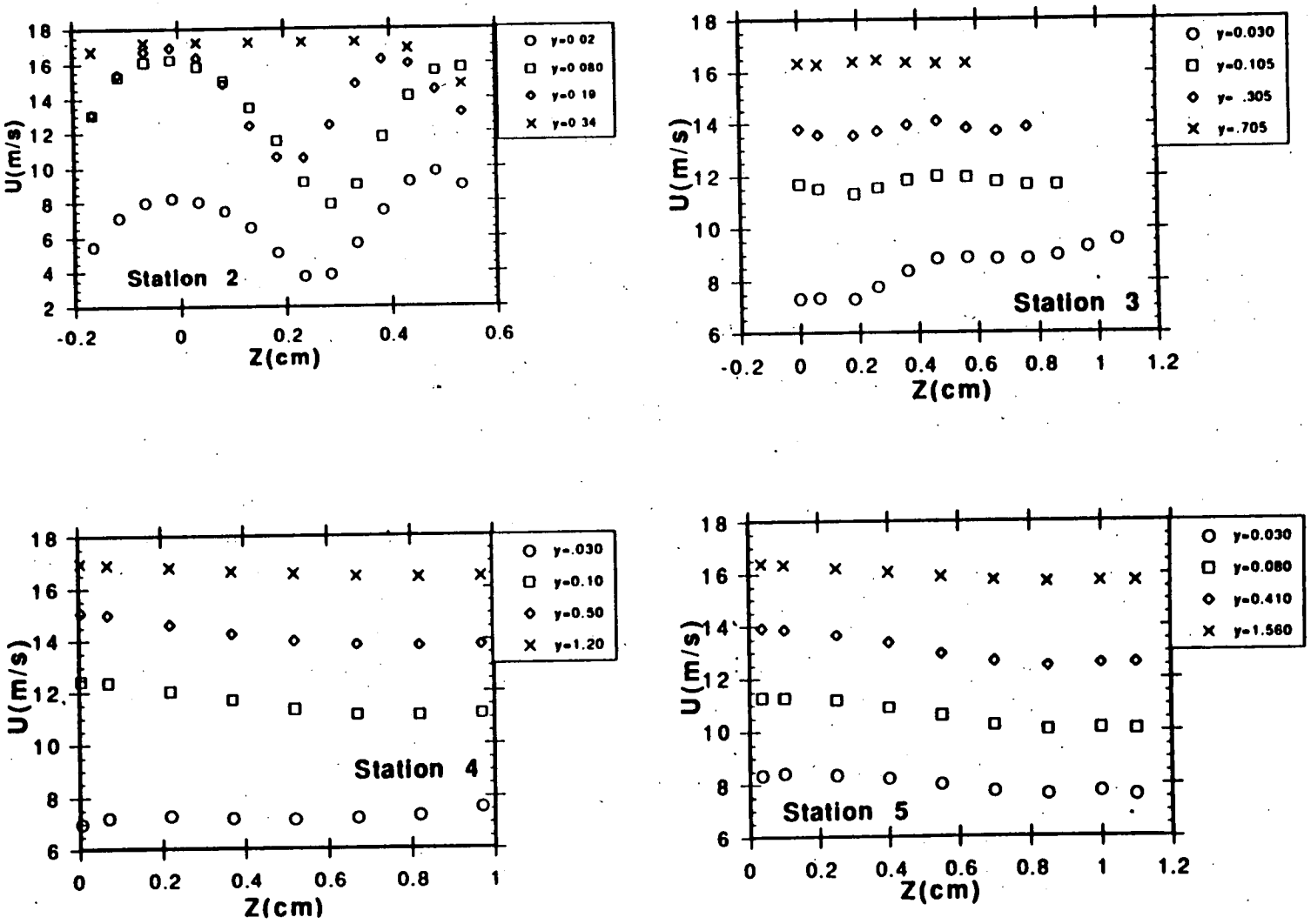

Fig. 3.4.5--Spanwise variation in velocity at various normal distance from the wall (Case 4)

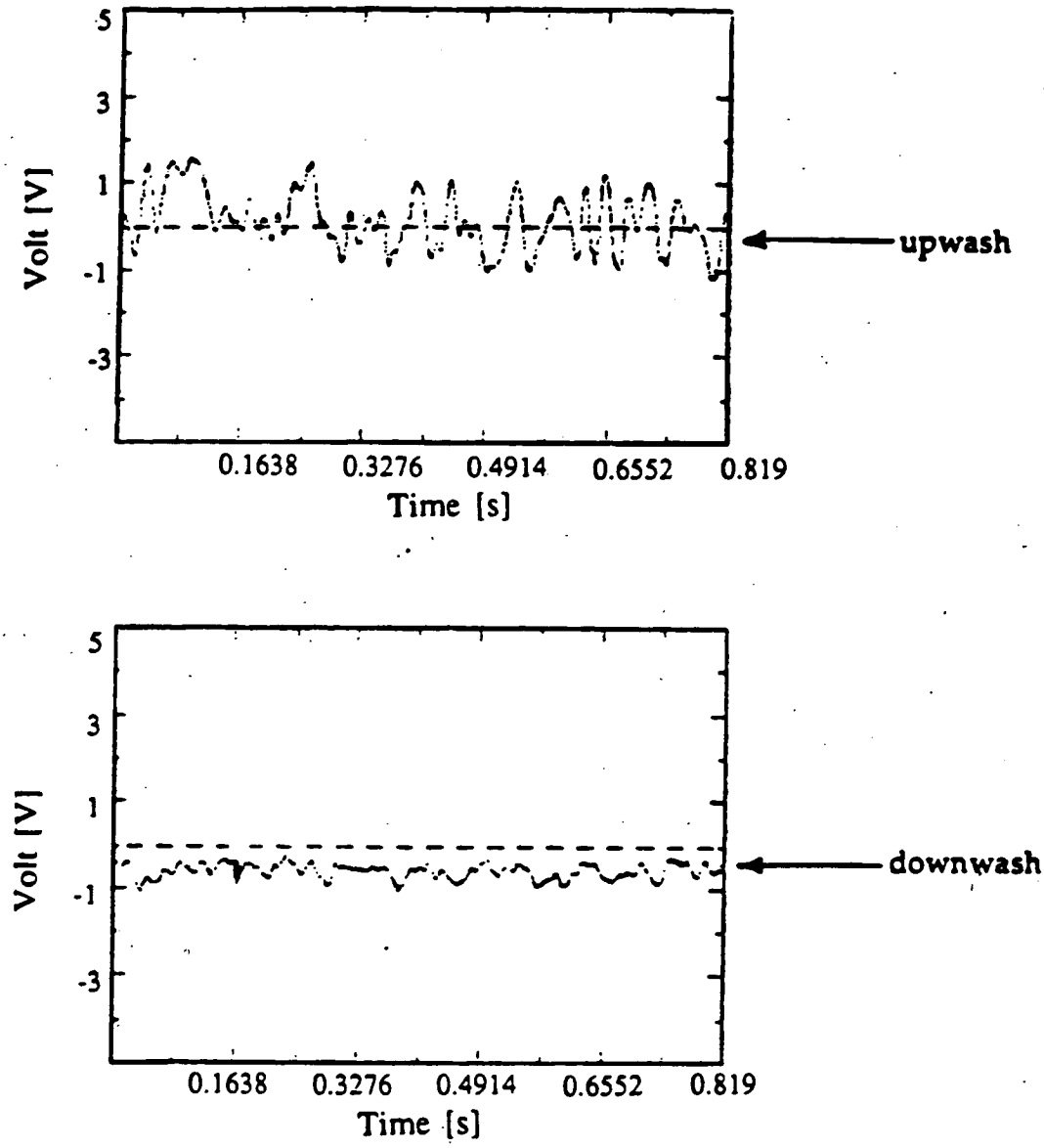

Fig. 3.4.6—Oscilloscope traces at upwash and downwash, station 2 (Case 4).

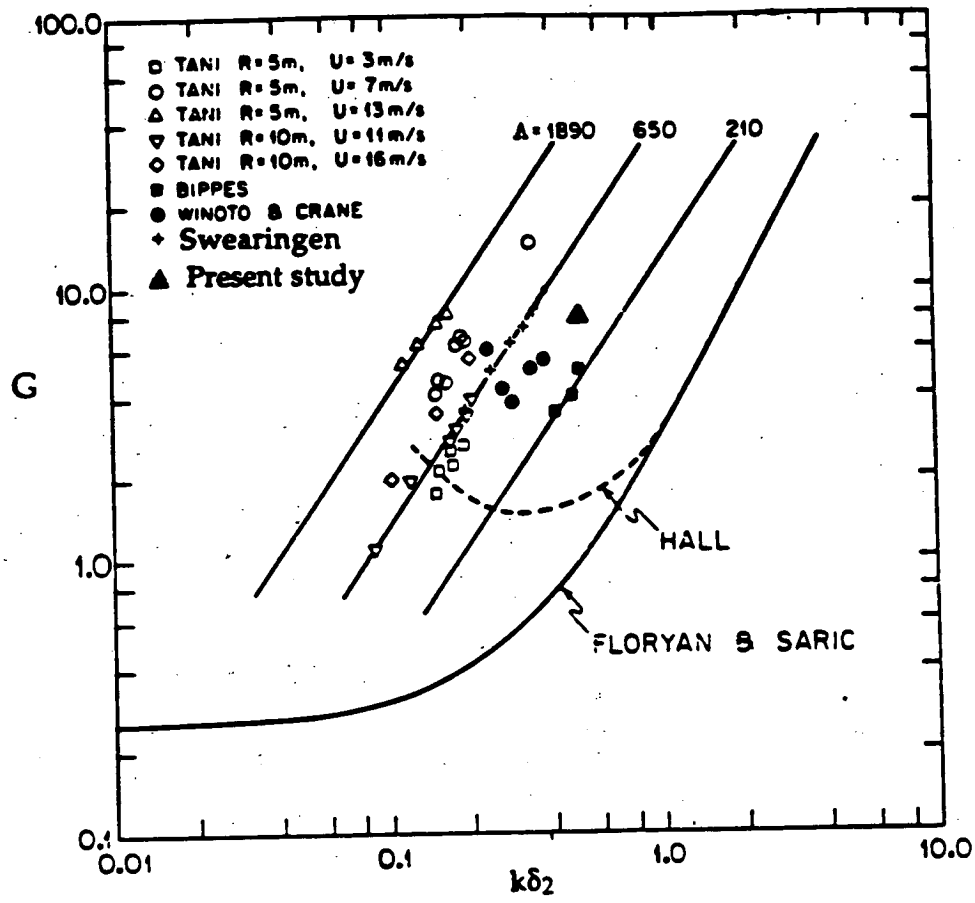

Fig. 3.4.7--Location on Görtler map of the late laminar (station 2) flow (Case 4).

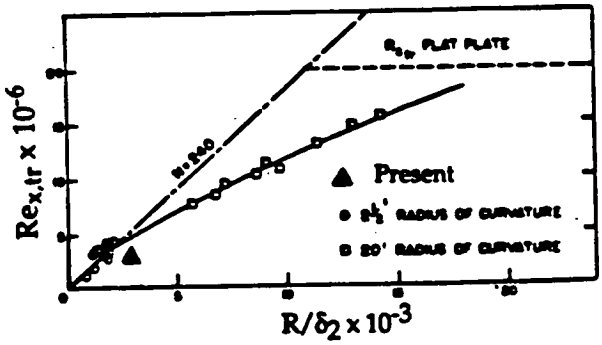

Fig. 3.4.8--Location on Liepmann's (1943) transition diagram of the late laminar (station 2) flow (Case 4).

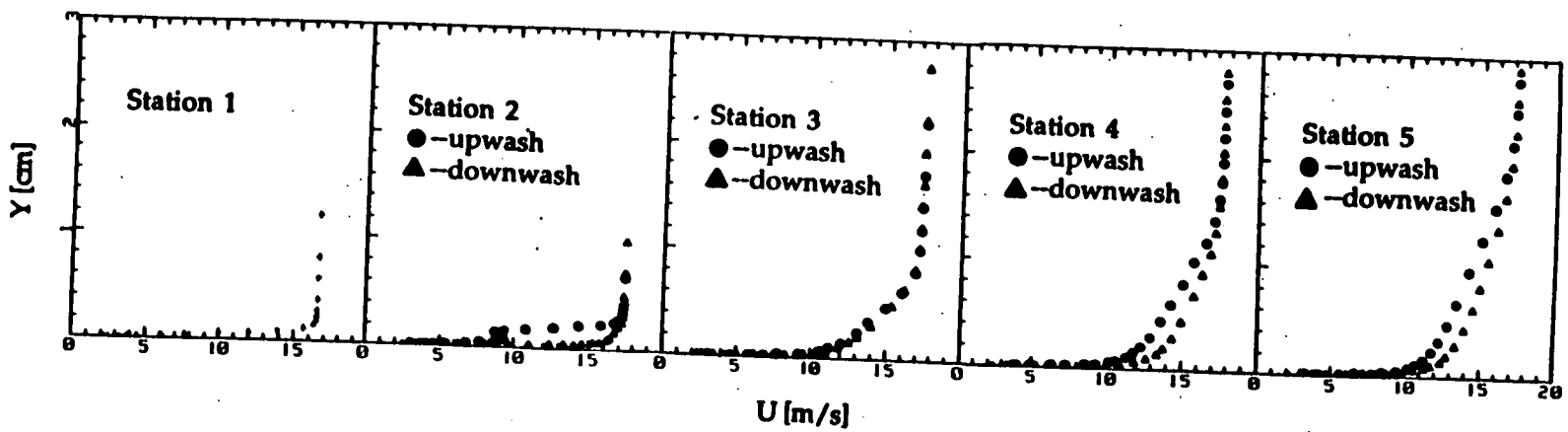

Fig. 3.4.9--Dimensional velocity profiles at the upwash and downwash along the wall (Case 4).

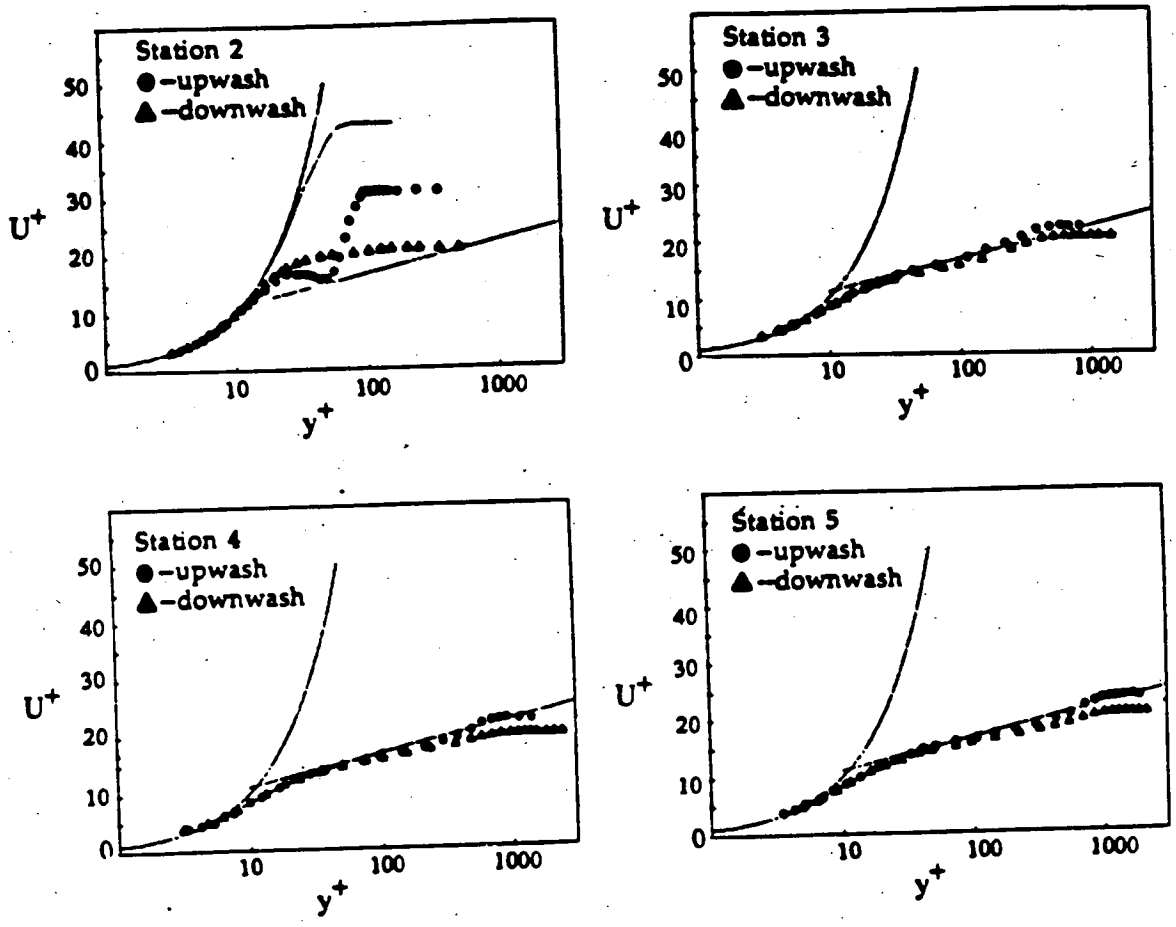

Fig. 3.4.10–Velocity profiles at the upwash and downwash normalized on wall coordinates (Case 4).

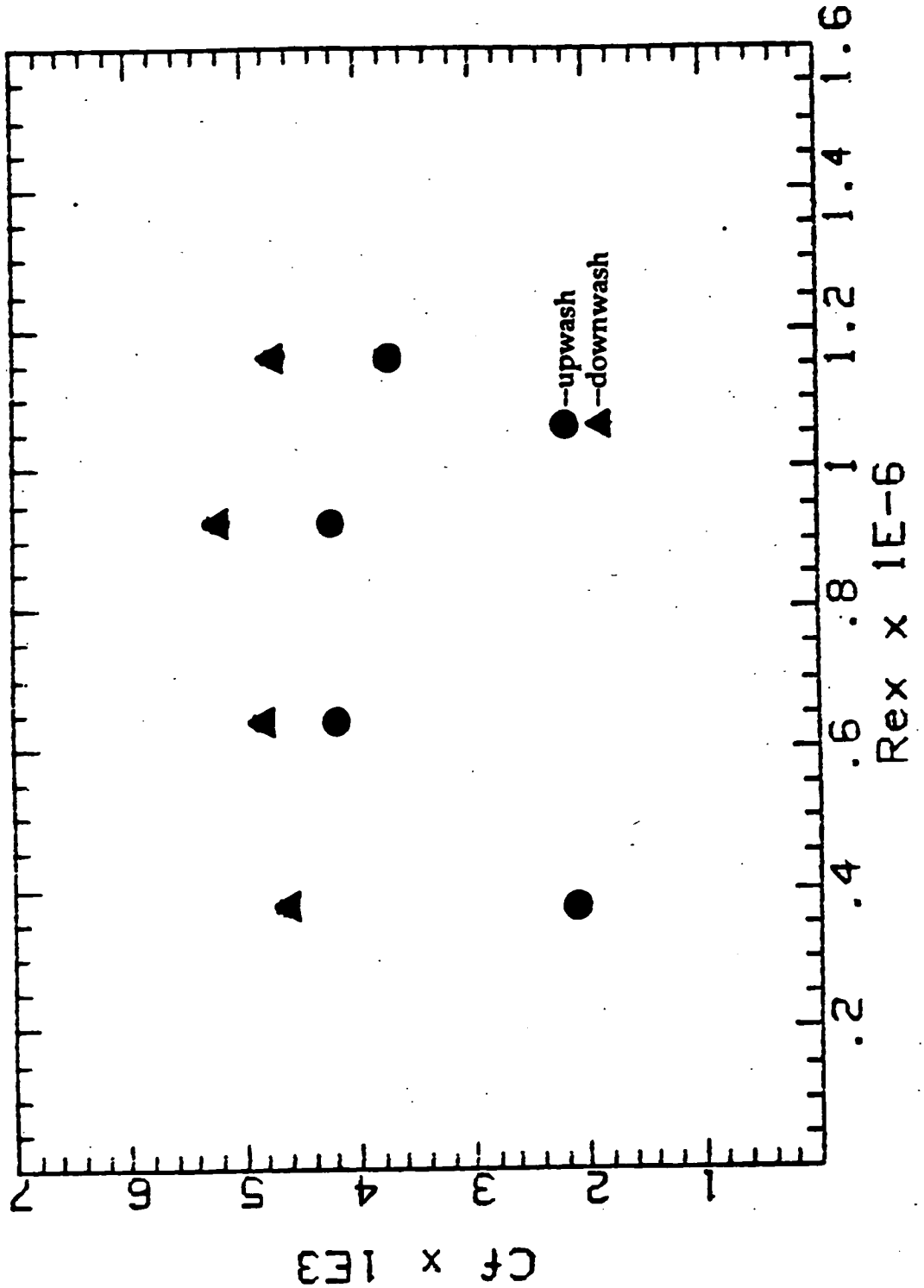

Fig. 3.4.11–Skin friction variation along the wall at upwash and downwash locations (Case 4).

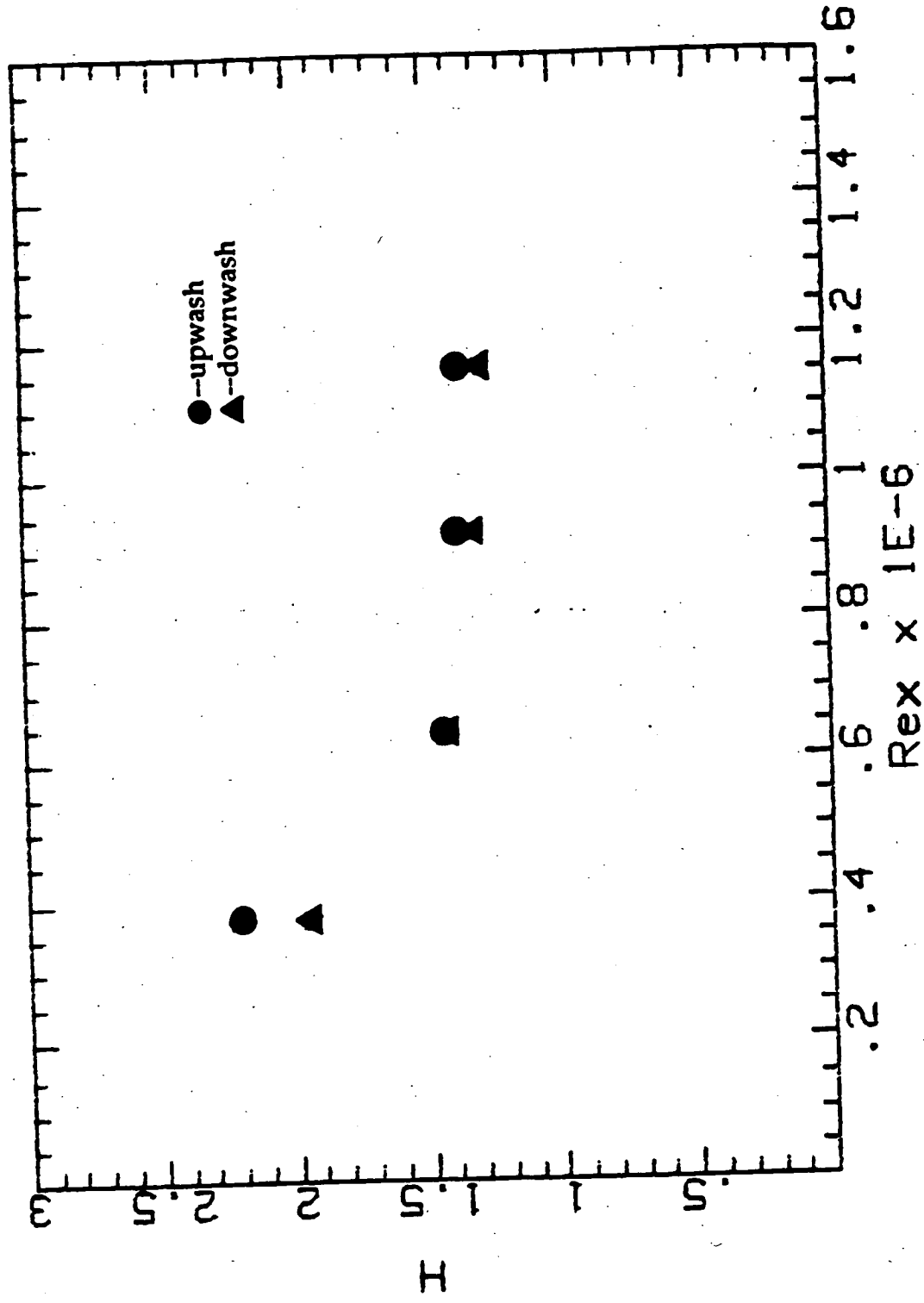

Fig. 3.4.12–Shape factor variation along the wall at upwash and downwash locations (Case 4).

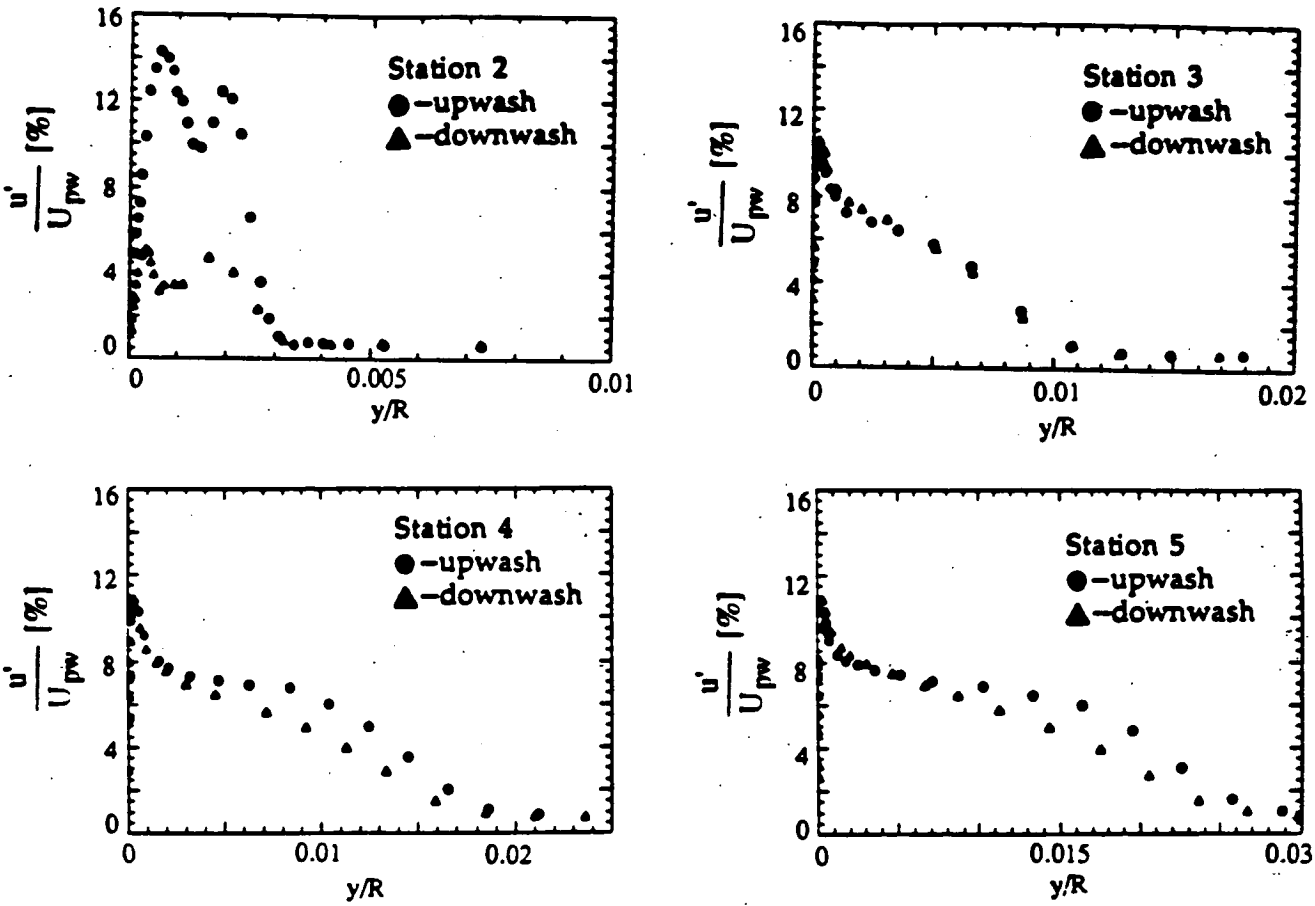

Fig. 3.4.13–Turbulence intensity profiles along the wall at upwash and downwash locations (Case 4).

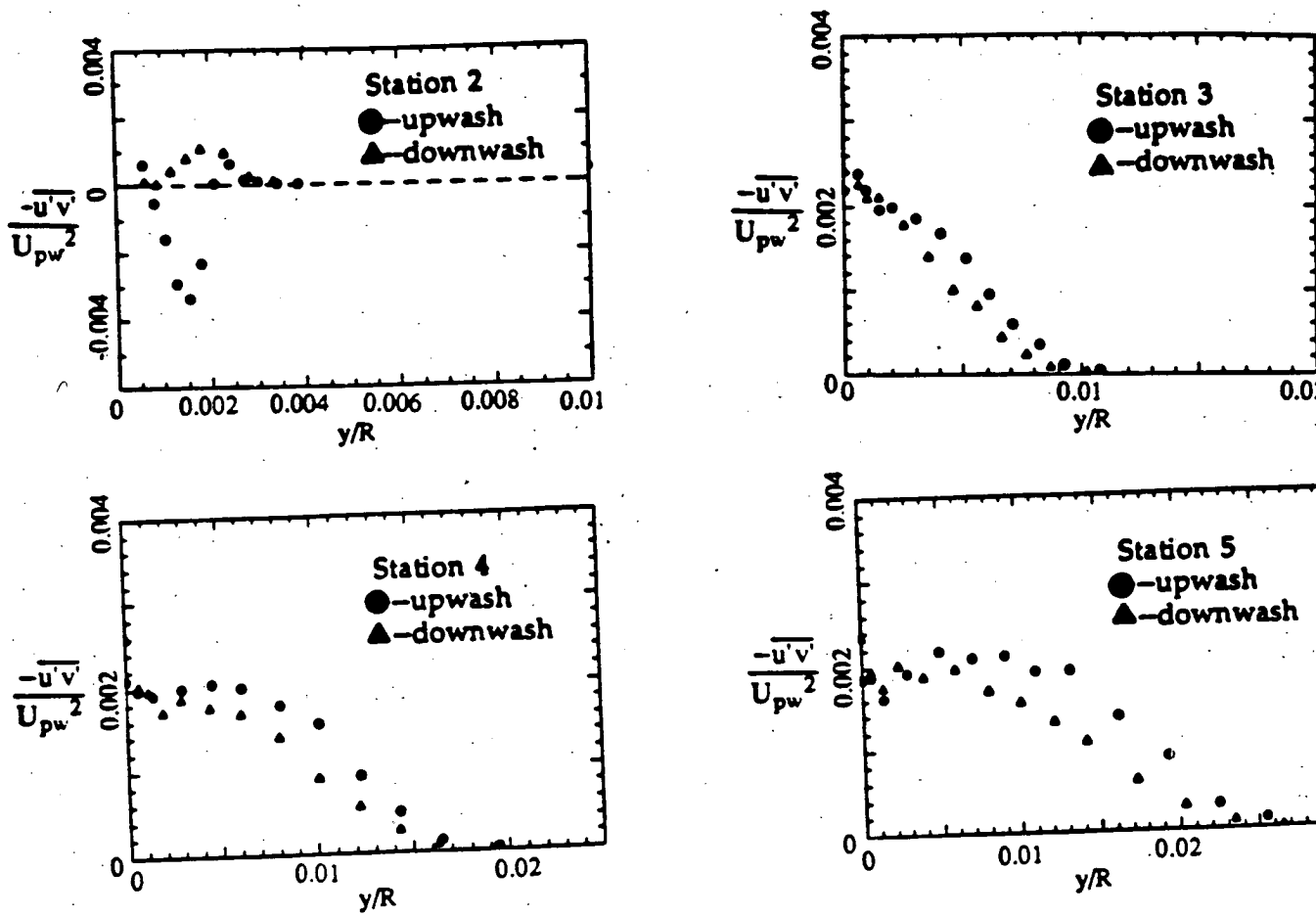

Fig. 3.4.14–Shear stress profiles along the wall at upwash and downwash locations (Case 4).

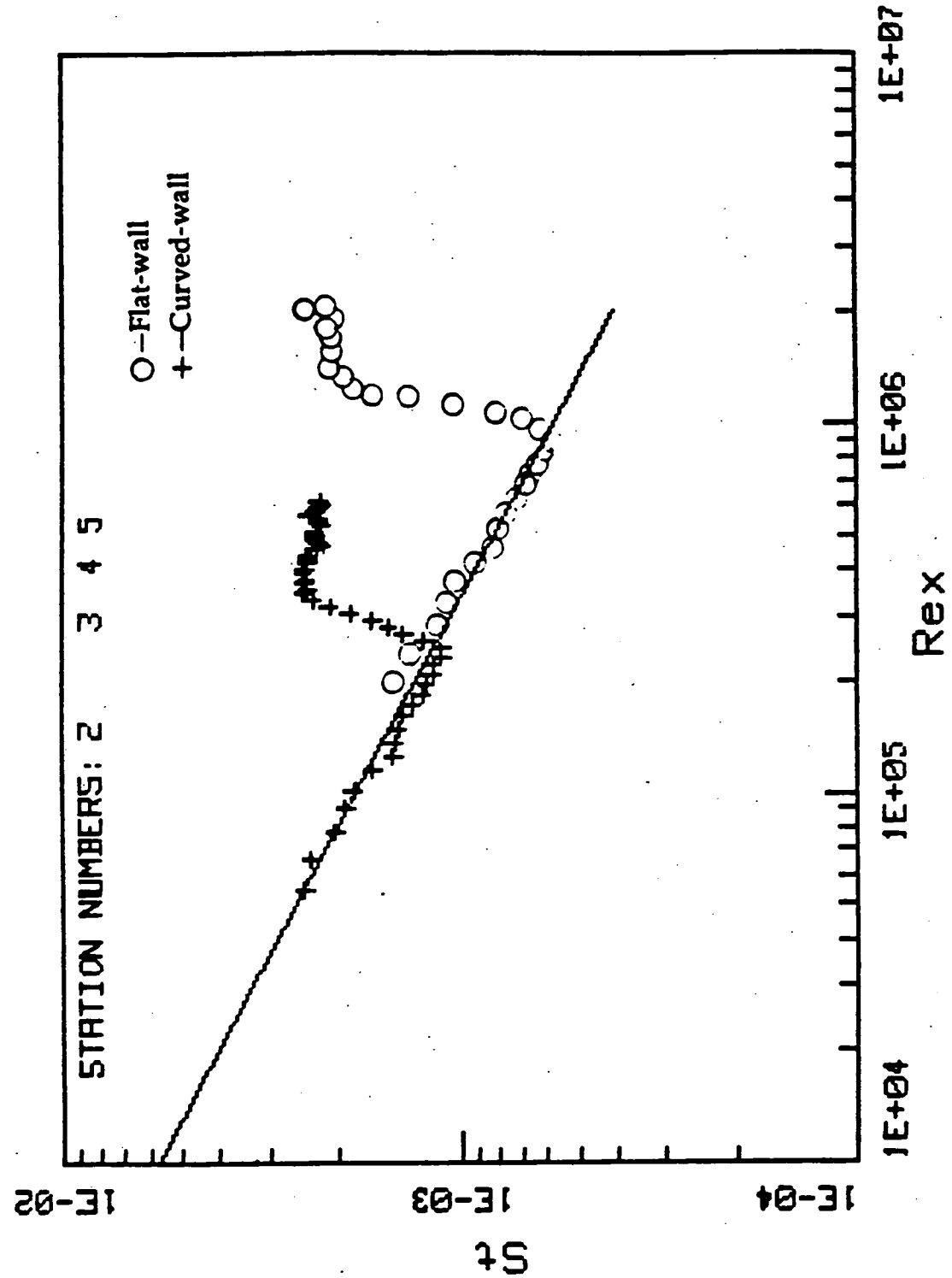

Fig. 3.4.15--Stanton number variation vs. Rex--comparison with the low TI flat-wall case.

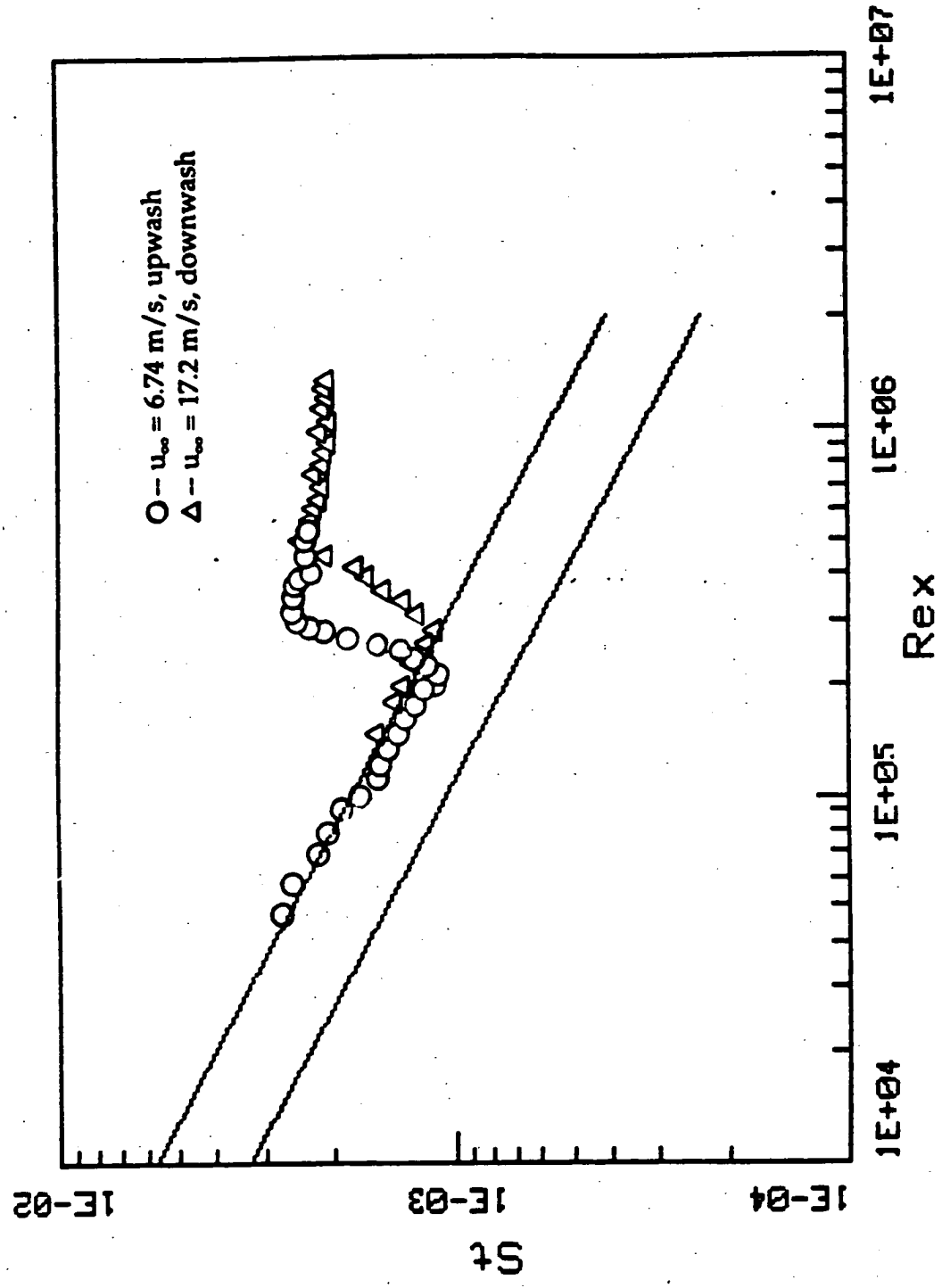

Fig. 3.4.16–Stanton number variation vs. Rex for two free-stream velocities (Case 4).

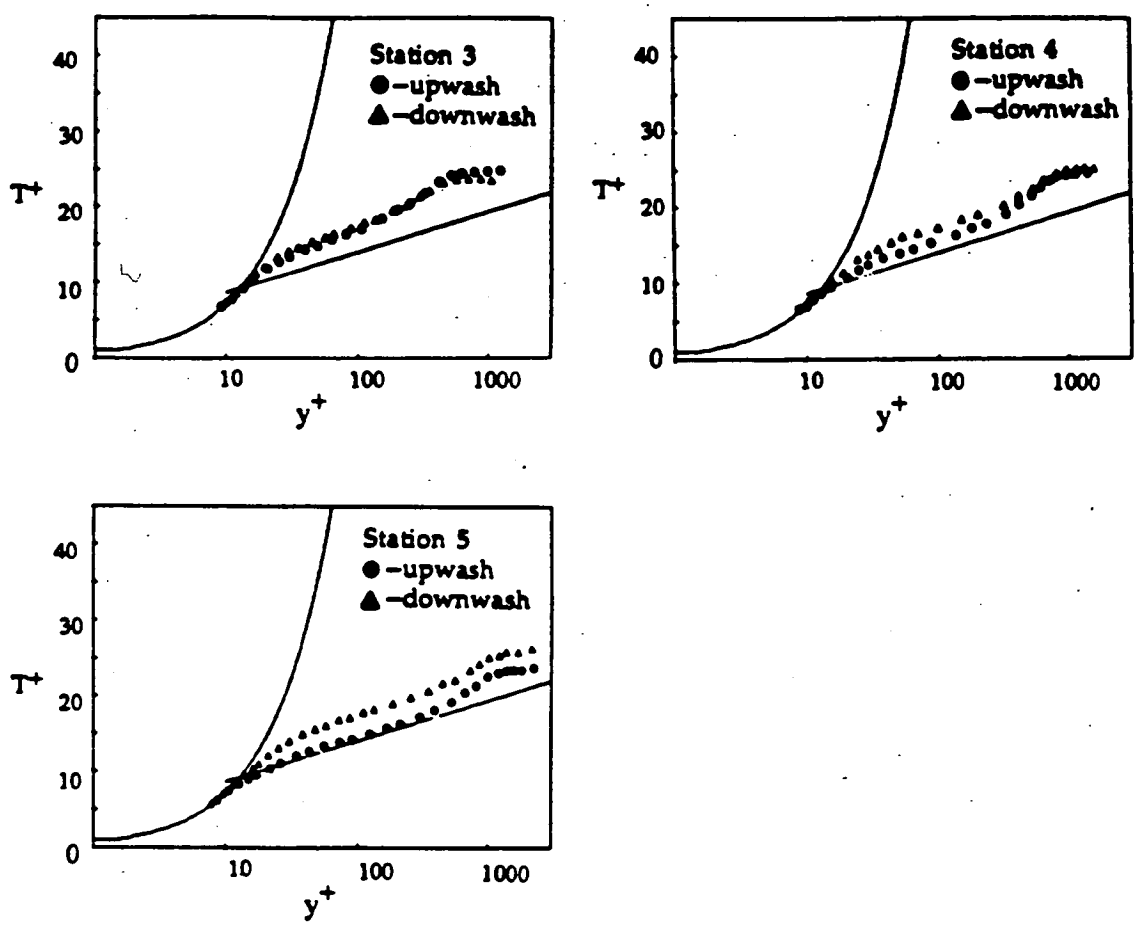

Fig. 3.4.17–Mean temperature profiles along the wall at upwash and downwash locations (Case 4).

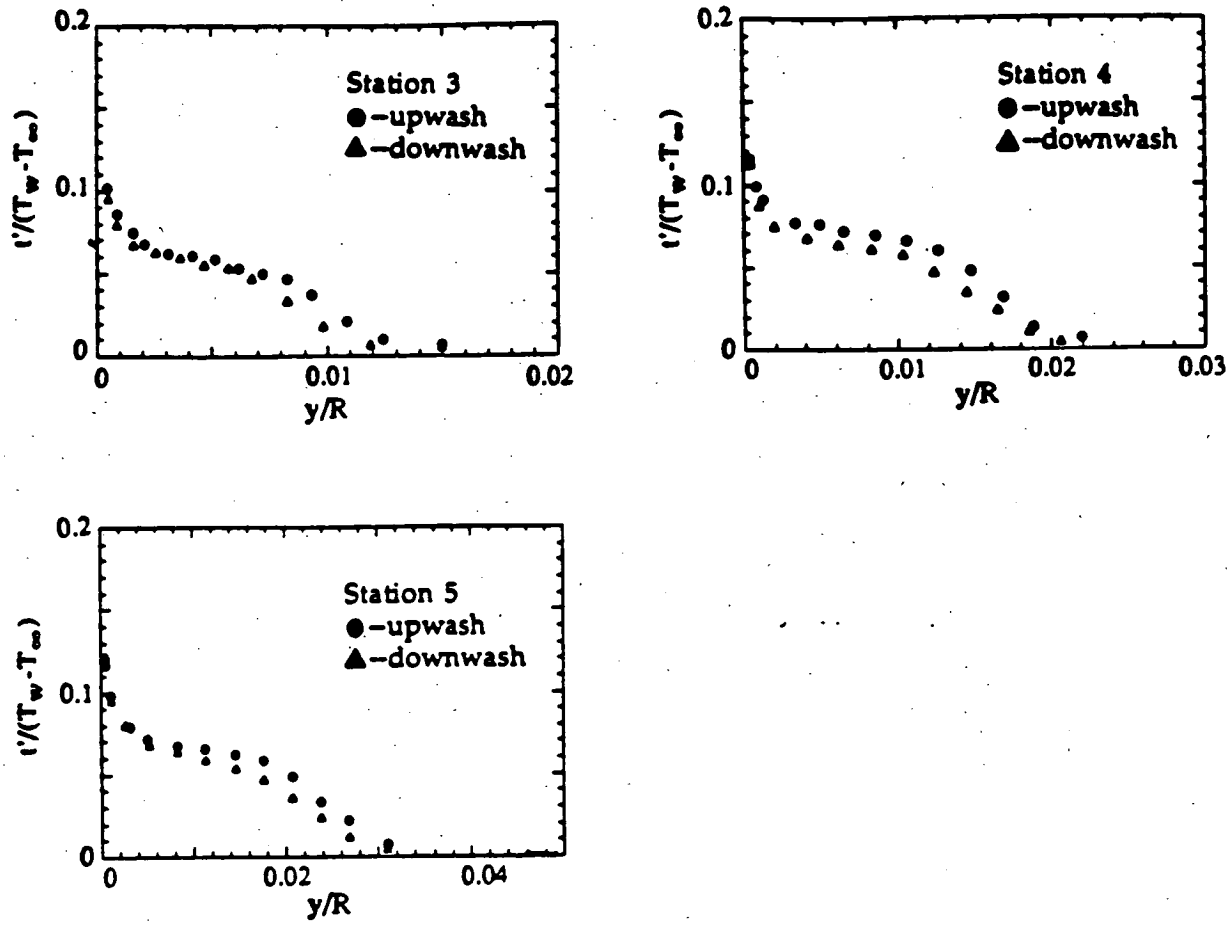

Fig. 3.4.18–Fluctuating temperature profiles along the wall at upwash and downwash locations (Case 4).

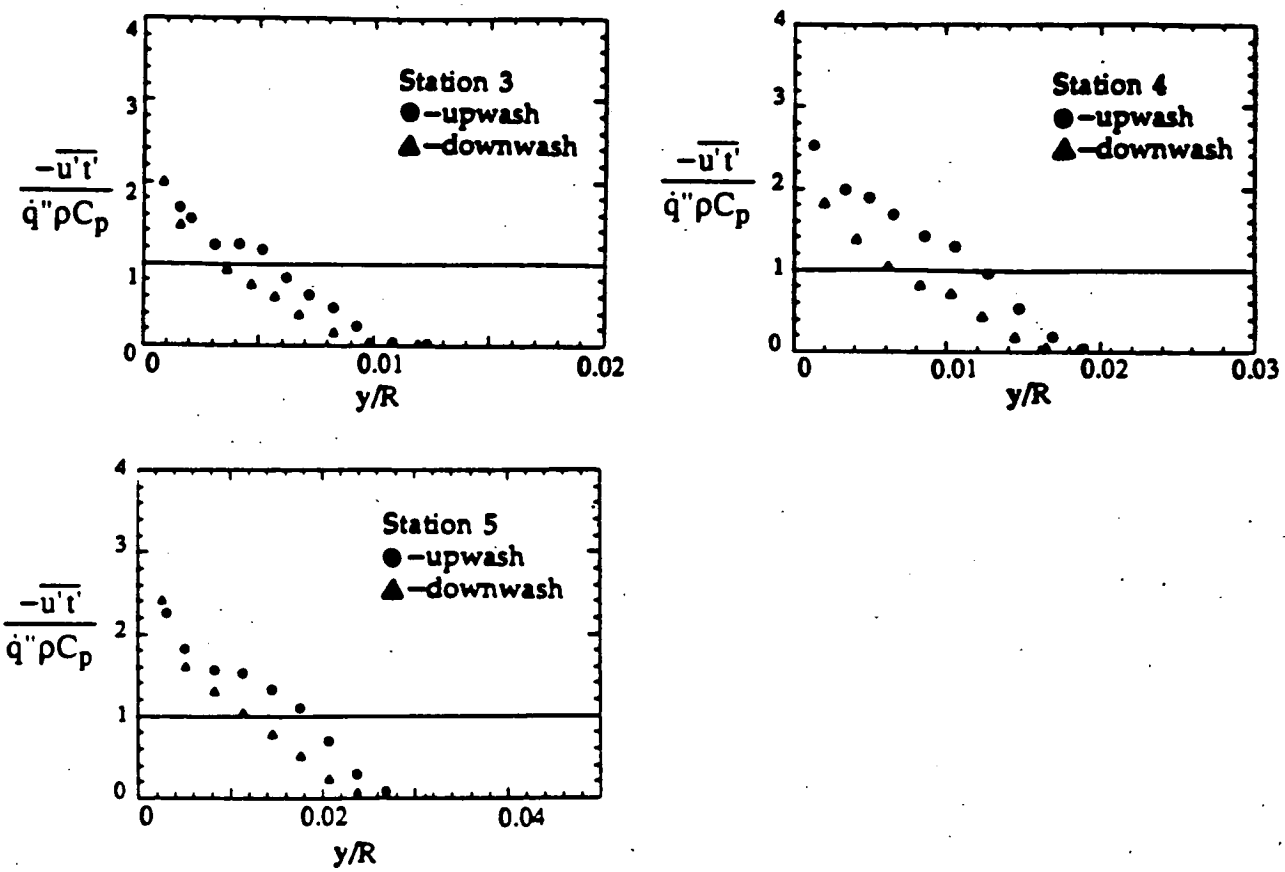

Fig. 3.4.19--Profiles of the streamwise heat flux along the wall at upwash and downwash locations (Case 4).

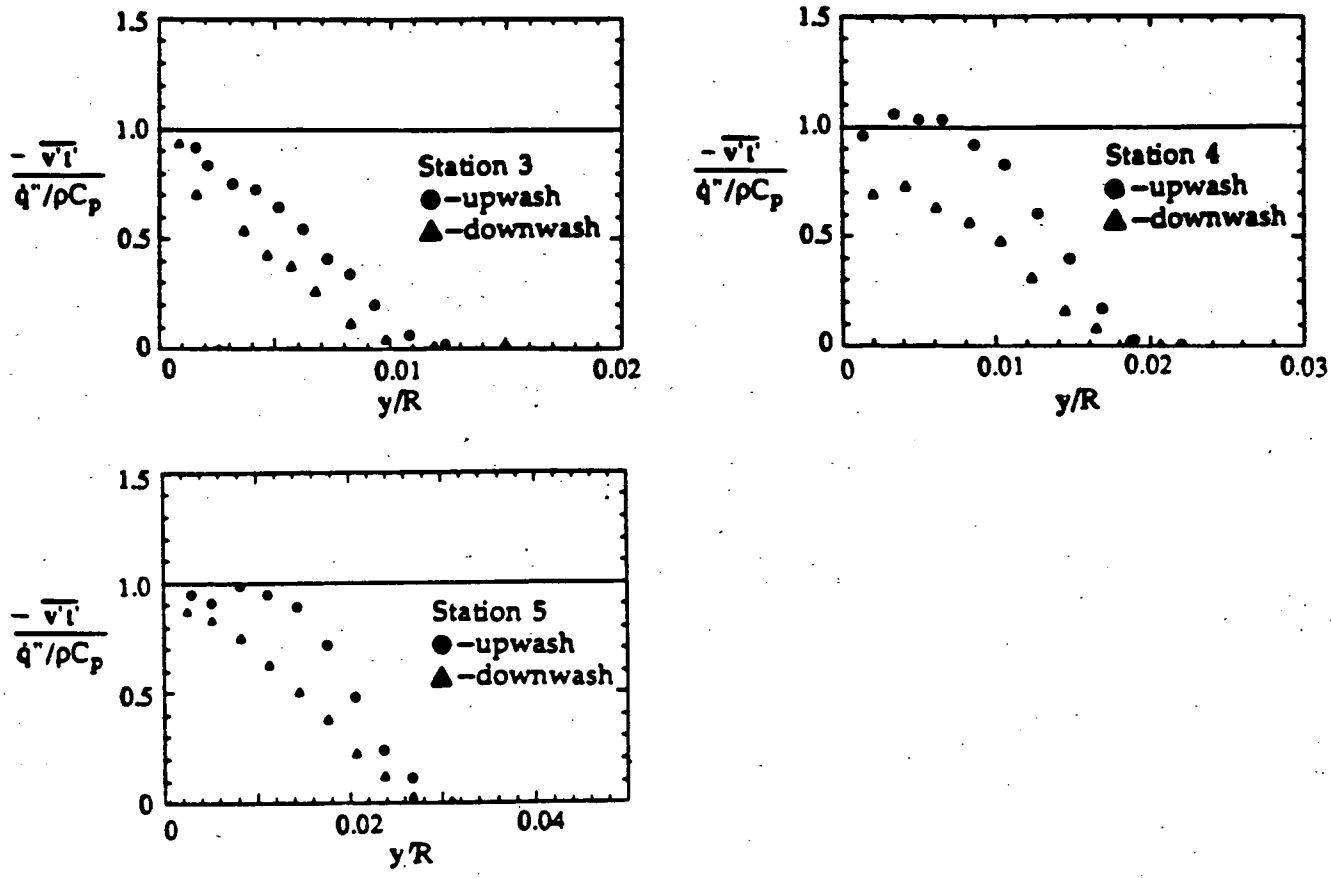

Fig. 3.4.20–Profiles of the cross-stream heat flux along the wall at upwash and downwash locations (Case 4).

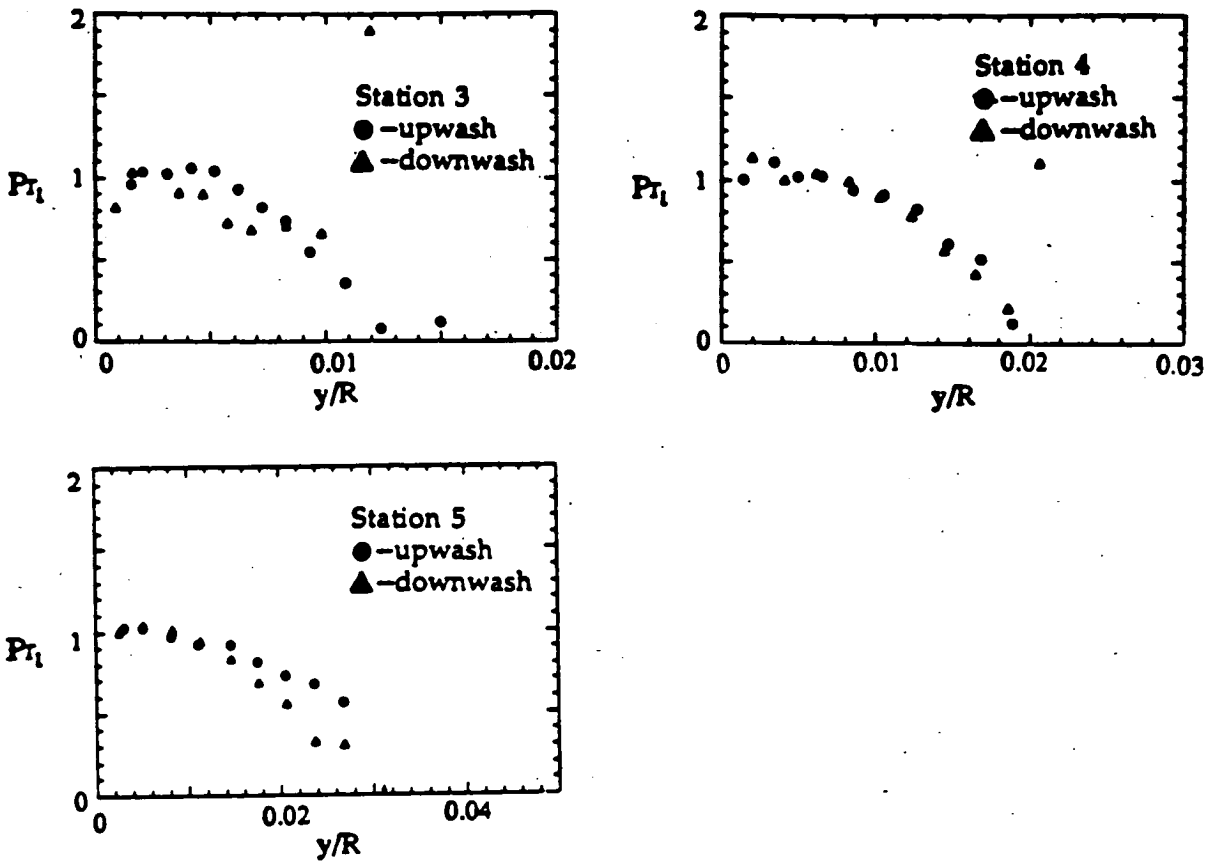

Fig. 3.4.21–Profiles of the turbulent Prandtl number at upwash and downwash locations (Case 4).

3.5). Case 5 -- Concave-wall, TI=8.3%

This case deals with the effects of concave curvature on transitional boundary layers under high free-stream turbulence conditions. The free-stream turbulence at the test section entrance, generated using the bi-plane grid generator described earlier, was measured to be 8.6%, similar to the corresponding flat-wall, high turbulence intensity case (Case 3). The PSD distribution was smooth, with no significant spikes over the range from 10 Hz to 10 kHz. Velocity and turbulence intensity profiles at the end of the turbulence establishment chamber and just before the test section entrance (see Fig. 3.5.1) showed a mean velocity variation across the span of 2% and a variation in turbulence intensity of 6%. The autocorrelation, given by

$$\rho(\tau) = \frac{\overline{u'(t)u'(t+\tau)}}{u'^2(t)}$$

can be used to find two turbulence scales. The area under the autocorrelation curve, called the integral scale, represents the average size of the turbulent eddies. The Taylor microscale, which is related to the turbulent dissipation, is determined from the curvature of the autocorrelation curve at the origin (τ=0). A description of this measurement, written by Mr. Steve Russ, is given as an appendix. The integral scale and Taylor microscale at the test section entrance were measured to be 3.3 cm and 0.61 cm respectively at the center of the channel.

Perhaps the most startling find of this case was the phenomenon of cross-stream transport of momentum within a flow that was thought to be a potential core. Apparently, the combination of a high free-stream turbulence

intensity superimposed on a free-stream velocity gradient (due to conservation of angular momentum within the curve) causes a transport of momentum within the "potential core", as manifested in high levels of shear stress (u'v') . As a result, there exists a velocity profile in the core that is flatter than the profile predicted by potential theory (given by U(y)r(y)=constant) due to the increased mixing. Mean velocity profiles, measured across the test section normal to the test wall at each station (Fig. 3.5.2) increasingly deviate from the potential flow distribution with downstream distance. The deviation is seen as early as station 2, where one would expect the boundary layer to still be thin. The profiles are seen to be flatter than the potential flow profile. It is hypothesized that this is due to a large momentum transport in the "core" flow. This seems to be supported by the shear stress profiles (Fig. 3.5.3) where large values of shear stress are seen even at the channel centerline. It seems that the high turbulence intensity in the core, when superimposed on a velocity gradient, causes transport of momentum from the flow near the convex wall (higher velocities) towards the flow near the concave wall (lower velocities). The production term in the shear stress budget equation, given by

$$P = \overline{v'^2}\frac{\partial U}{\partial y} - \left(2\overline{u'^2} - \overline{v'^2}\right)\frac{U}{R}$$

shows that the production of shear stress can be positive for non-zero free-stream turbulence when streamline curvature is present (note that for concave curvature, R<0). The parameters thought to govern this phenomenon are the free-stream mean velocity gradient and turbulence level, the wall curvature and the channel width.

A consequence of this was that the usual normalizing techniques were not applicable since neither a potential velocity at the wall nor a boundary layer thickness (there was no boundary layer) existed. The quantity selected to normalize velocities was the potential velocity at the wall as determined by the upstream total pressure and the radius of curvature of the wall, i.e., a velocity profile in the free-stream was inferred using the measured total pressure upstream of the curve, and the velocity at the wall was the quantity chosen. Normal distances from the wall were normalized on the wall curvature, R. Momentum balances were not possible in this case, due to the cross-transport of momentum, unless detailed profiles were taken near both the convex and concave walls for evaluation of wall shear at both locations. The present facility did not allow such measurement. Energy balances, however, could be made if velocity and temperature profiles were measured beyond the thermal 'boundary layer" thickness.

Another interesting result is that no evidence of streamwise vortices were seen. The turbulent Görtler number (G_t) could not be calculated for this case as no momentum thickness could be obtained. The values of the eddy viscosity in the high turbulence intensity case flow were, however, anywhere from 10 to 100 times that of the lower turbulence intensity case, suggesting that if G_t could have been calculated, they would have been much lower than the values computed for the low turbulence intensity case. Possibly, G_t would have been reduced to the stable region on the Görtler map, and no vortices would would be expected. Alternatively, it could be that vortices exist, but that they meander or appear and disappear randomly in time and space at a rate faster than the frequency response of the liquid crystal. Clearly, the flow appears two-dimensional.

Mean and Fluctuating Velocity. Measurements of the mean velocity normalized on wall coordinates are shown on Fig. 3.5.4. As in the corresponding flat-wall case, no wake, and a very short log-linear region is observed. Both concave curvature and high free-stream turbulence reduce the size of the wake. Both effects are visible in these profiles. Station 1 is thought to be transitional. Skin friction (C_f) values deduced from the law-of-the-wall showed a monotonic decrease with Re_x.

The variation in turbulence intensity profiles along the test wall is shown on Fig. 3.5.5. The near-wall peak decays slowly with distance. The turbulence intensity in the outer part of the flow decays rapidly at first, and essentially stops decaying beyond station 3. Baines and Peterson (1951), who studied the decay of turbulence behind screens, found that the decay of free-stream turbulence behind lattice type grids was governed by the equation

$$\frac{u'}{u_\infty} = 1.12\left(\frac{x}{b}\right)^{-5/7}$$

where x is the distance from the grid generator and b is the bar width. The above equation was used to find the effective bar width for the present flow (note that cylinders instead of bars were used in the turbulence generator) by solving for the bar width which yielded the measured u'/u_∞ at station 1. The effective bar width was found to be 2.78 cm compared to the actual cylinder diameter of 4.45 cm. The equation was then used to predict what the turbulence decay rate would have been if the channel had been straight. Results are plotted on Fig. 3.5.6. It is seen that the turbulence in the straight section would have continued to decay if it were not for the cross-stream transport of momentum in the curved-wall flow. In contrast to the curved-

wall flow, the high free-stream turbulence levels in the flat-wall flow (Fig. 3.3.9) showed a continuous decay.

Stanton Numbers. Stanton numbers along the wall centerline are shown on Fig. 3.5.7. A line representing the data obtained for the high turbulence intensity, flat-wall case is also shown. Concave curvature is seen to increase the heat transfer from the wall significantly, suggesting increased mixing of the near-wall flow. Vortex motion may be responsible for this increase, although the high eddy viscosity discourages the formation of coherent vortices. If vortex motion does exist, it must be quite disorganized as no evidence of a spanwise variation in heat transfer was observed on the liquid crystal. Alternatively, the concave curvature may lead to increased instability and more frequent turbulence bursting, but not coherent cellular structures. Thus, this concave-wall flow is two-dimensional. An energy balance for this flow (Fig. 3.5.8) shows exce'lent closure.

Mean and Fluctuating Temperature Profiles. Mean temperature profiles normalized on wall coordinates are shown on Fig. 3.5.9. As in the lower turbulence intensity case, a discrepancy between the measured values of T^+ and the thermal law of the wall is seen. The discrepancy is much smaller in the present case, however, illustrating the effects of increased turbulence intensity.

The variation in fluctuating temperature, measured using the triple-wire, is shown on Fig. 3.5.10. Unlike the turbulence intensity profiles, the t' profiles are seen to approach zero in the outer portion of the flow since the "core" flow is isothermal. This illustrates a fundamental difference between the momentum and heat transfer processes. The boundary conditions for the two processes are different (similarity in boundary conditions in the high

turbulence intensity case could be achieved if the outer wall were heated and heated air were injected into the free-stream). Due to this non-similarity, the turbulent Prandtl number is not expected to equal unity.

Turbulent Heat Flux and Turbulent Prandtl Numbers. Profiles of the streamwise and cross-stream transport of heat are shown on Figs. 3.5.11 and 3.5.12, respectively. Both profiles show an evolution with downstream distance as heat diffuses away from the wall. The v't' profiles approach unity near the wall, as expected. In contrast to the shear stress profiles, which remained high across the test section, the turbulent heat flux profiles approach zero in the outer part of the flow. The difference in boundary conditions between the heat and momentum transfer processes is again illustrated.

Turbulent Prandtl numbers deduced from the triple-wire measurements are shown on Fig. 3.5.13. All the near-wall values are seen to be slightly higher than unity. This increase in Pr_t is not surprising given the difference in boundary conditions discussed above.

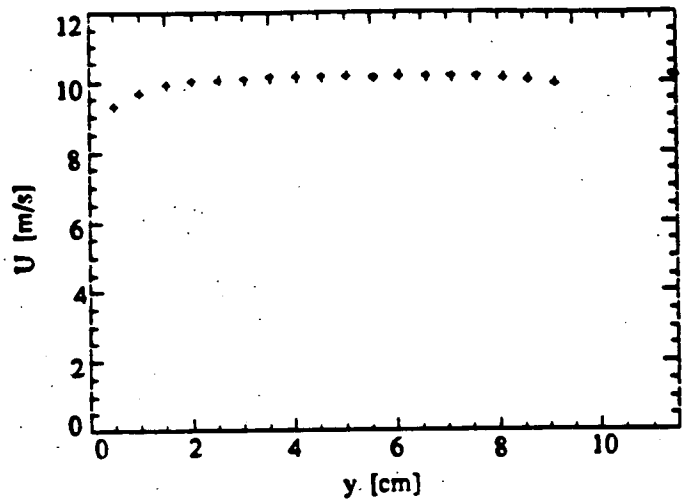

a). Mean velocity

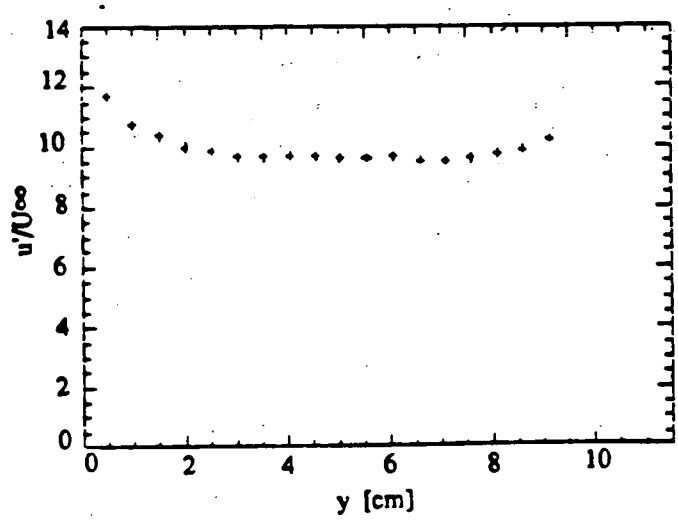

b). Turbulence intensity

Fig. 3.5.1–Profiles of the mean and fluctuating velocities across the test section at the end of the turbulence establishment chamber (Case 5).

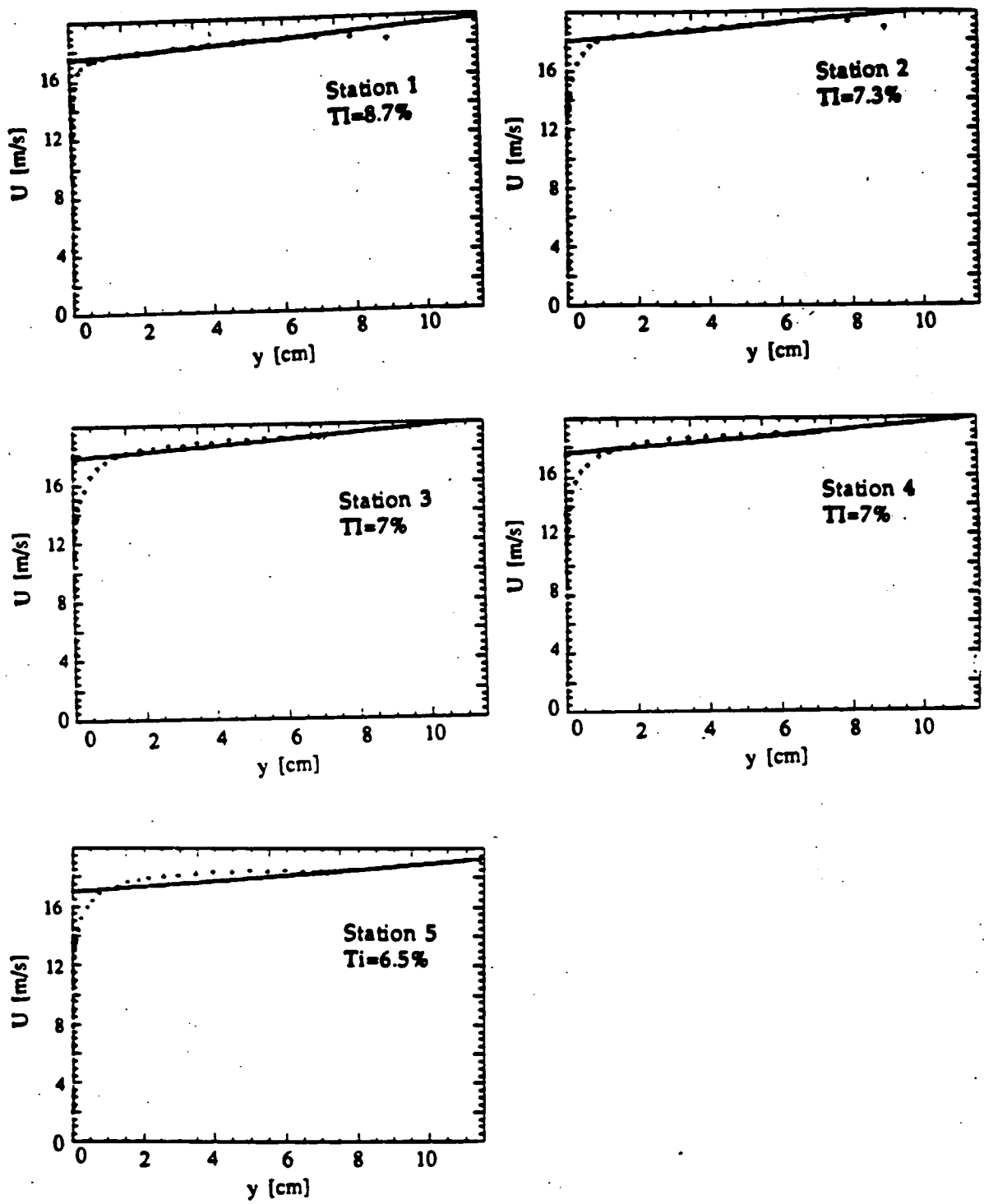

Fig. 3.5.2--Mean velocity profiles across the test section at various locations along the test wall (Case 5). The test section is approximately 11.5 cm wide.

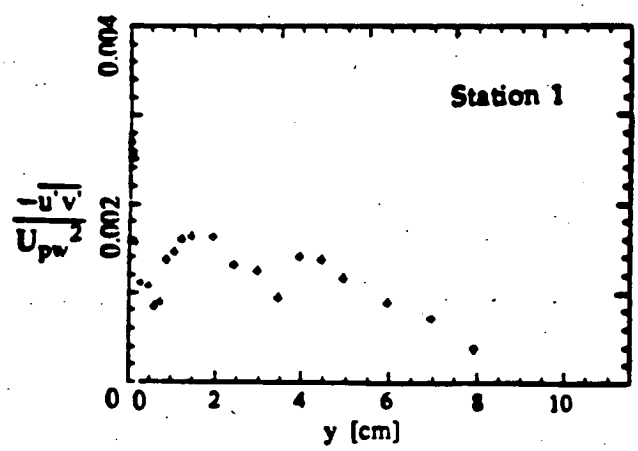

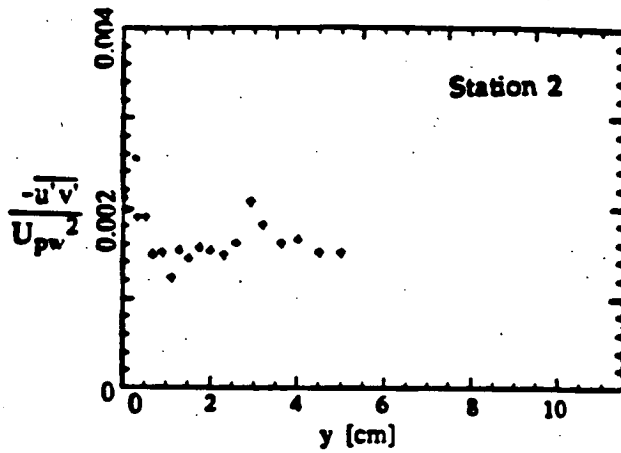

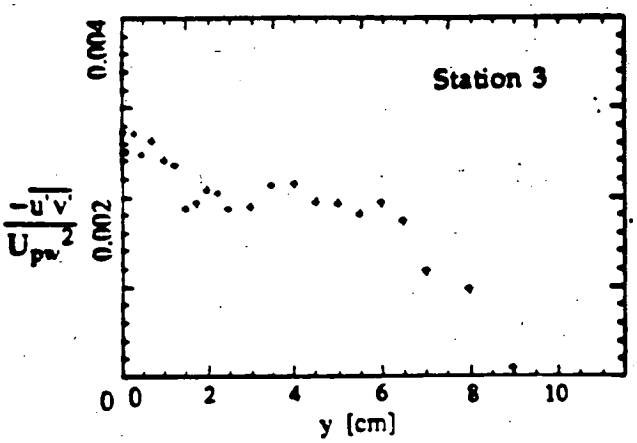

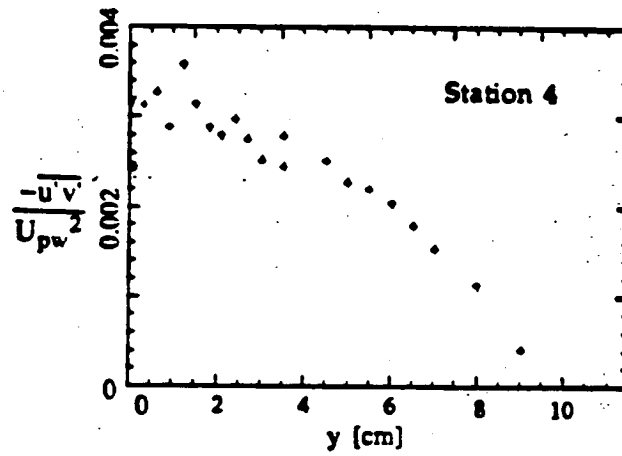

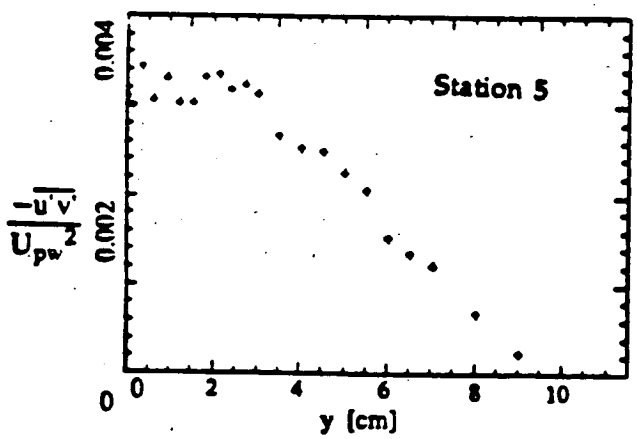

Fig. 3.5.3--Shear stress profiles across the test section at various locations along the test wall (Case 5). The test section is approximately 11.5 cm wide.

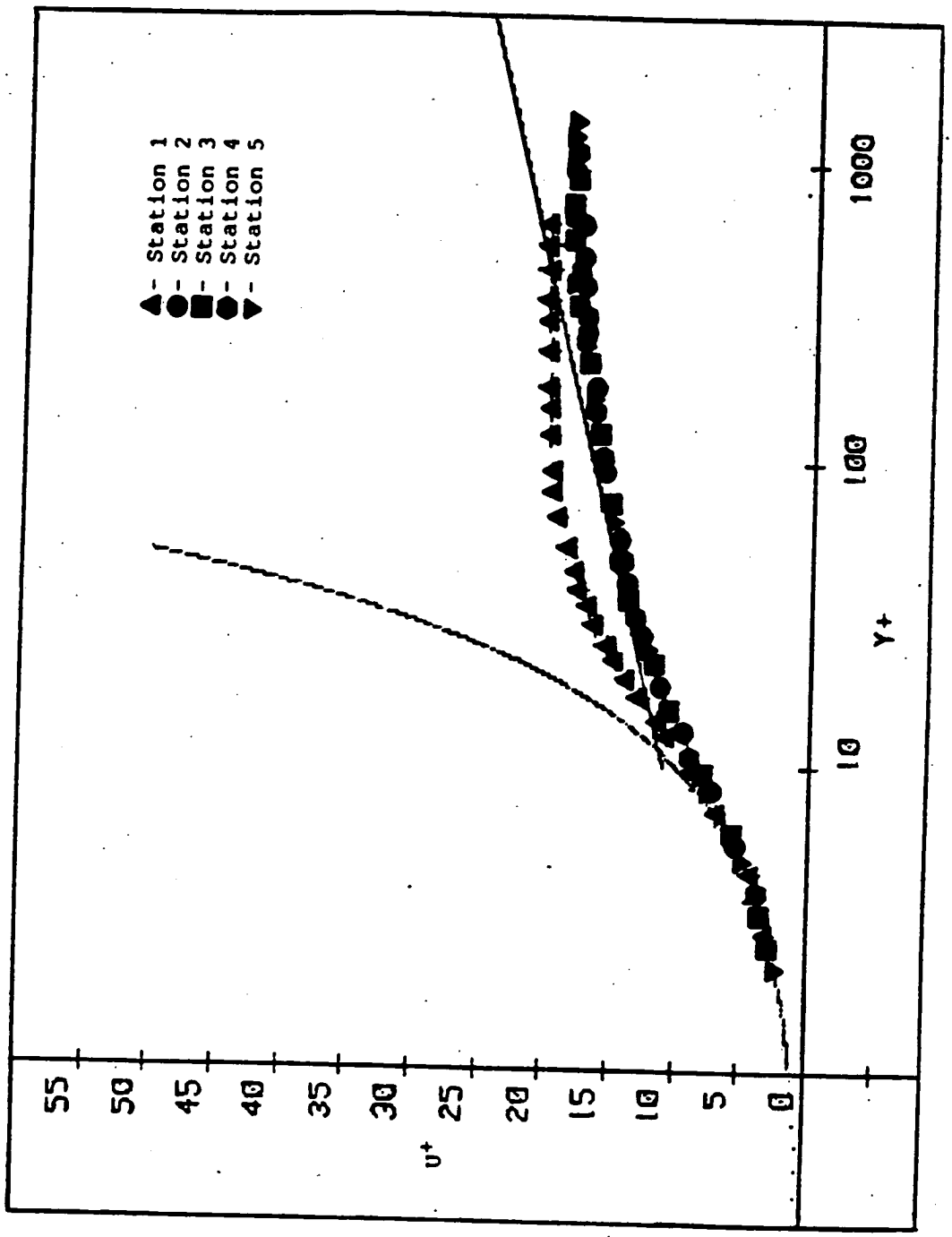

Fig. 3.5.4–Mean velocity profiles normalized on wall coordinates along the test wall (Case 5).

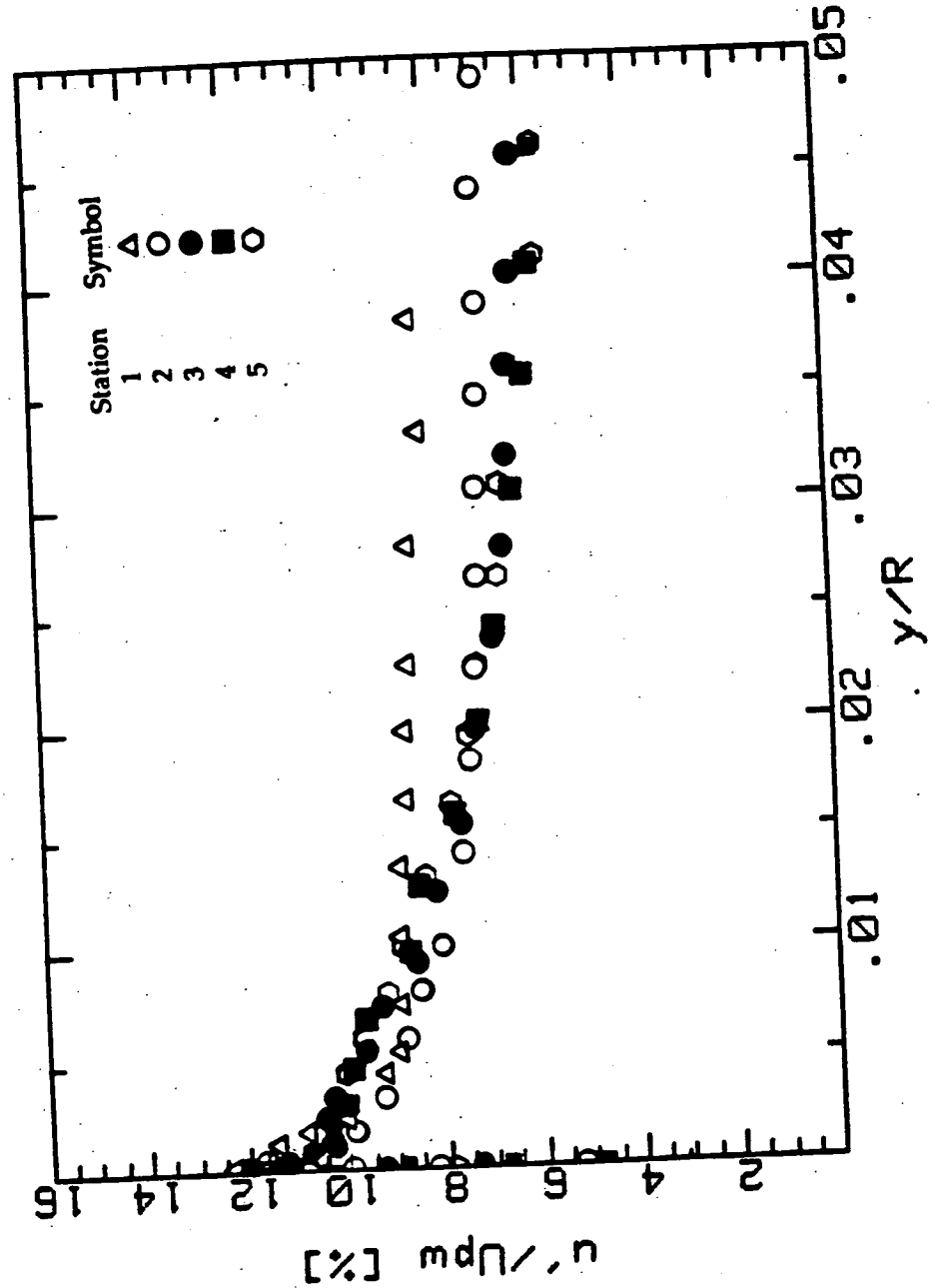

Fig. 3.5.5–Turbulence intensity profiles along the test wall (Case 5).

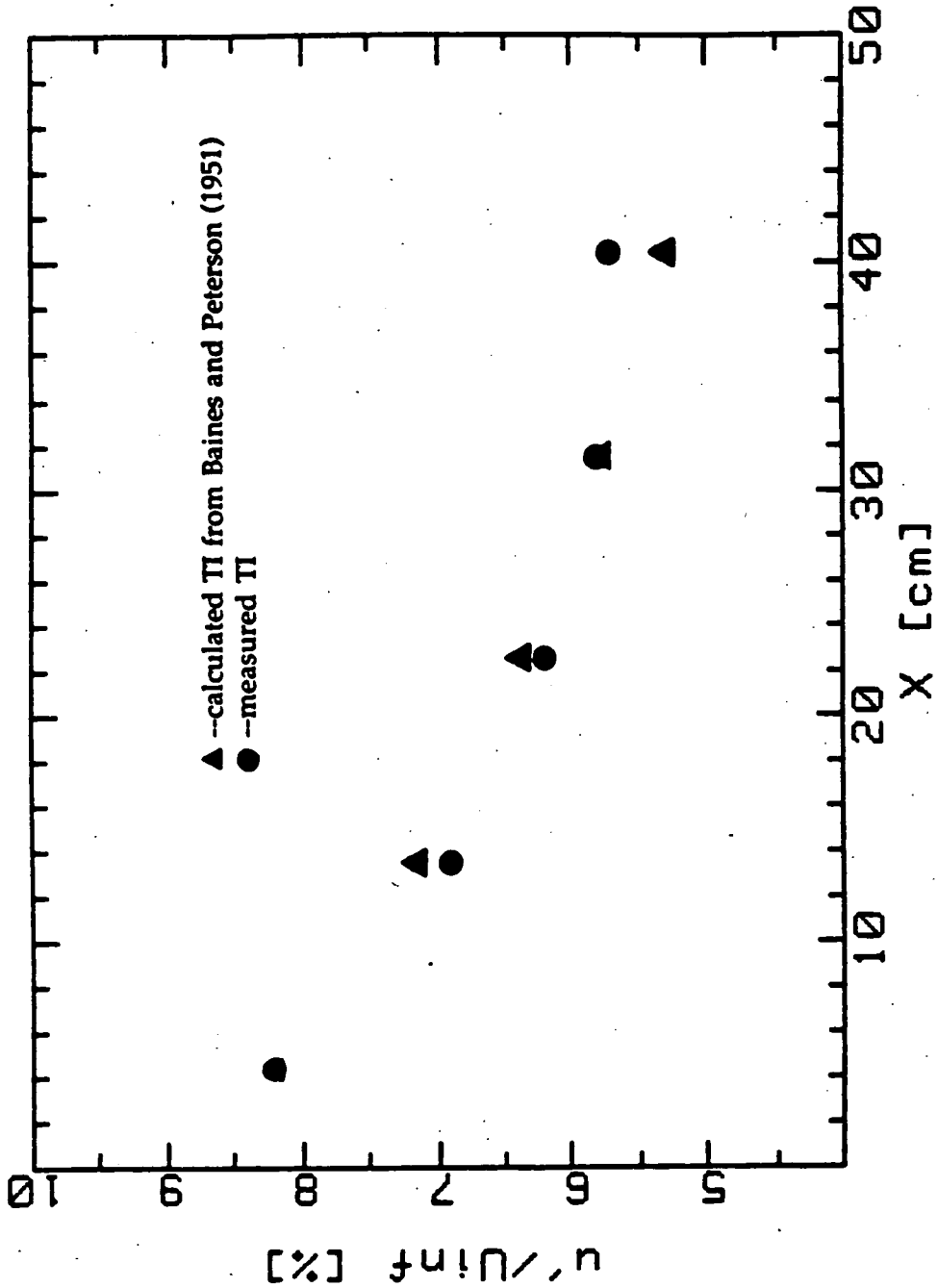

Fig. 3.5.6—Comparison of the turbulence decay rate in the curved test section with the predicted decay rate of Baines and Peterson (1951) in straight channels.

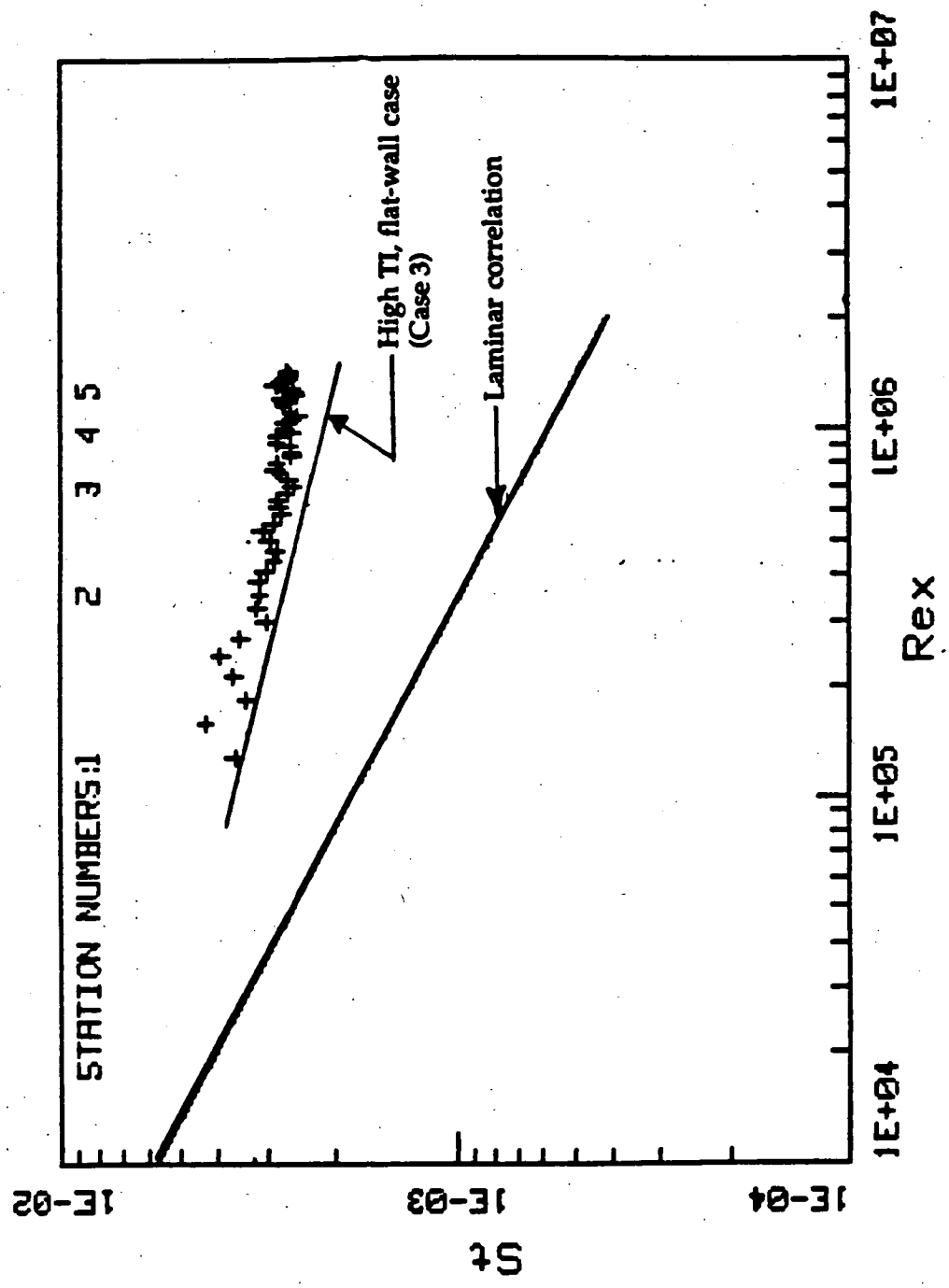

Fig. 3.5.7—Comparison of the Stanton number variation along test wall between curved and straight wall cases.

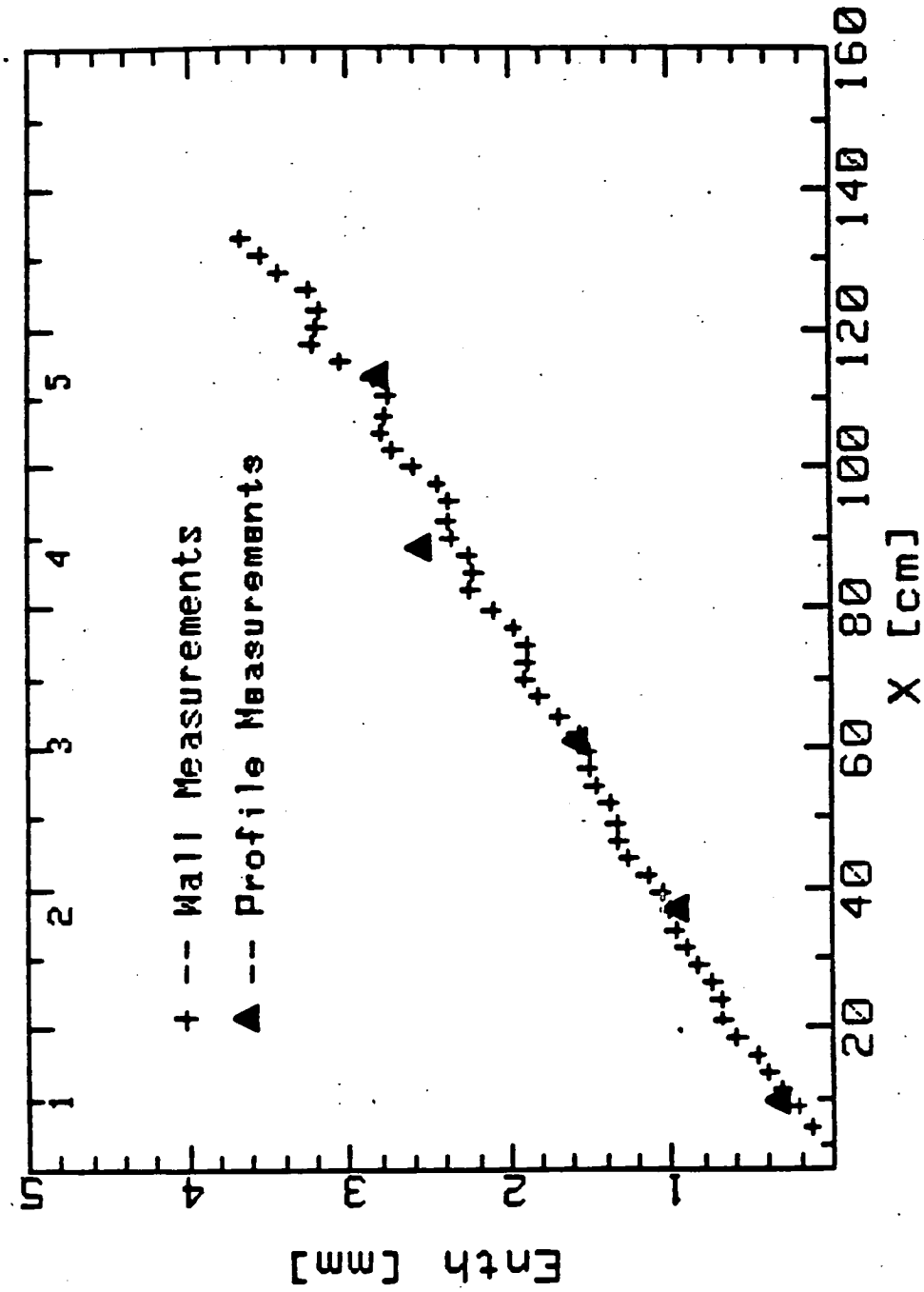

Fig. 3.5.8–Energy balance for Case 5.

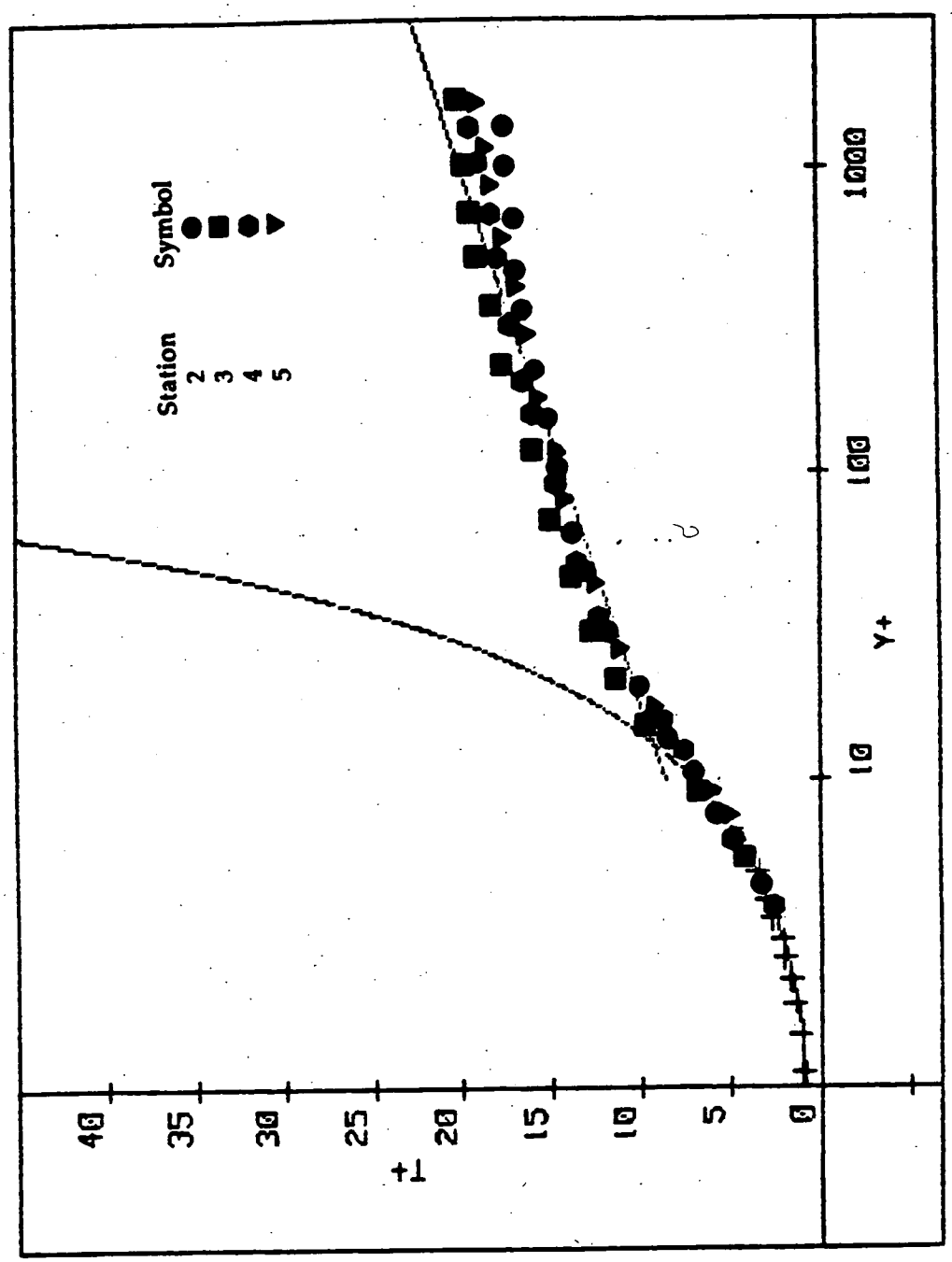

Fig. 3.5.9--Mean temperature profiles normalized on wall coordinates (Case 5).

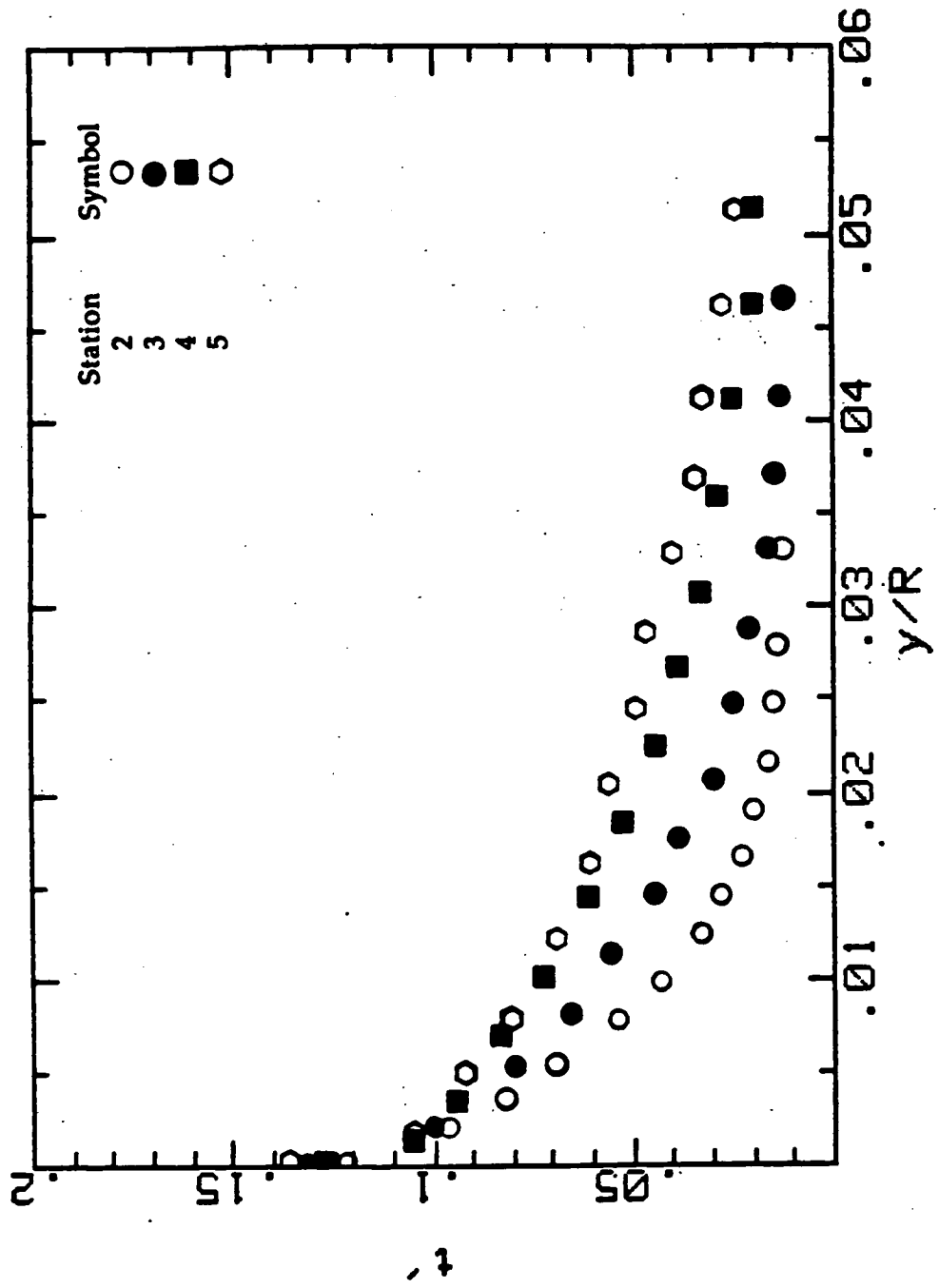

Fig. 3.5.10—Profiles of the fluctuating temperature along the test wall (Case 5).

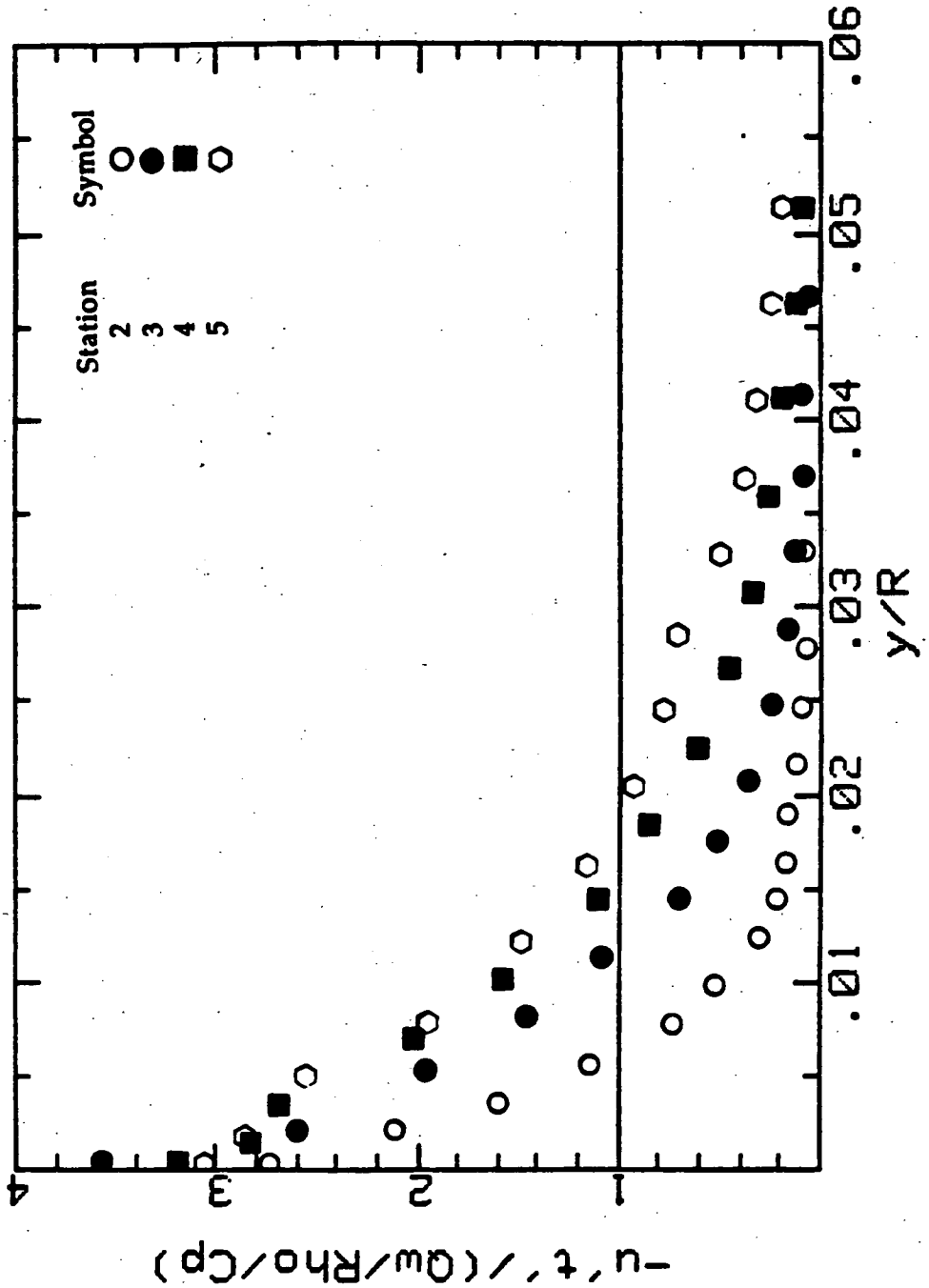

Fig. 3.5.11–Profiles of the streamwise heat flux along the test wall (Case 5).

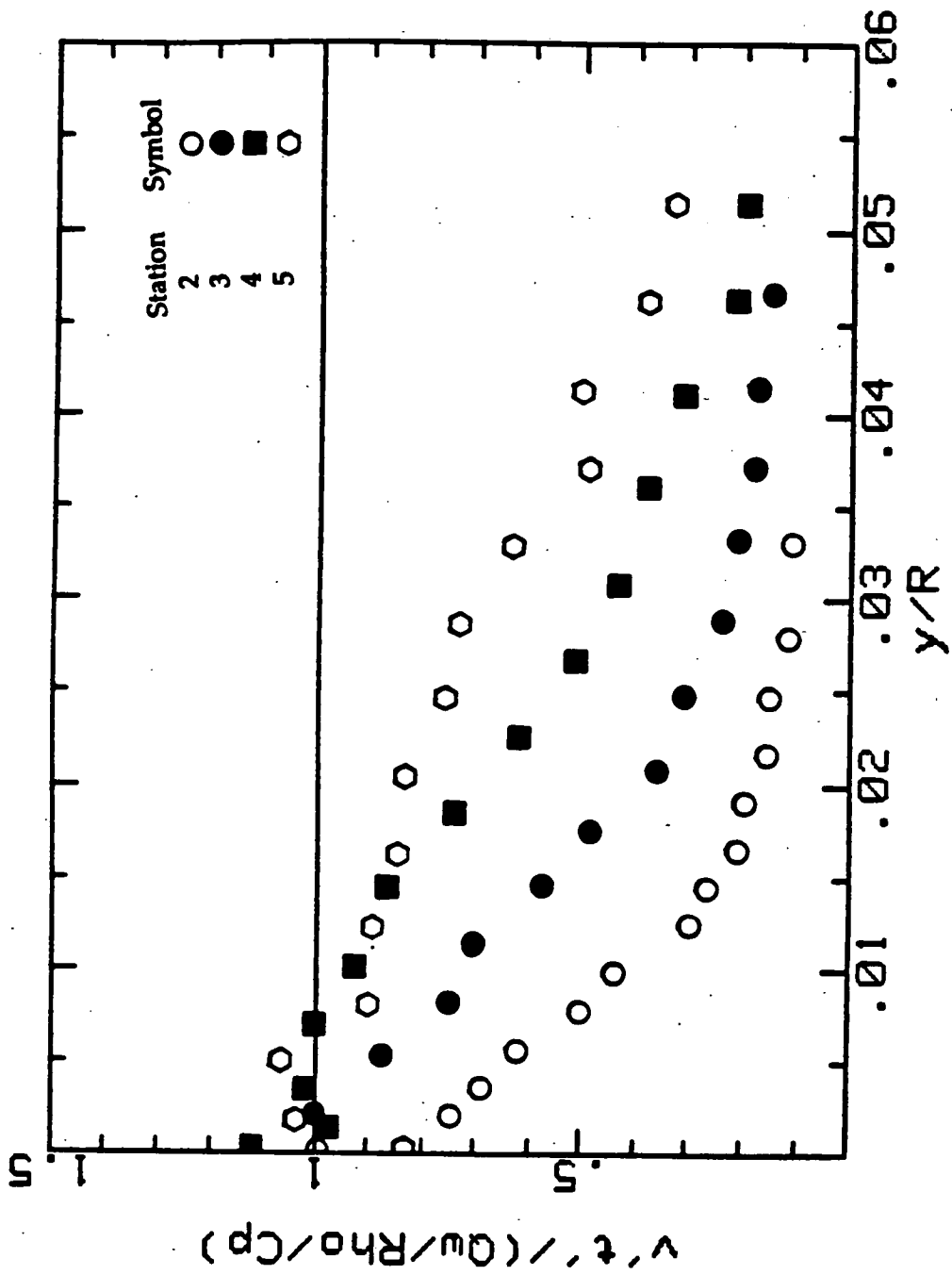

Fig. 3.5.12–Profiles of the cross-stream heat flux along the test wall (Case 5).

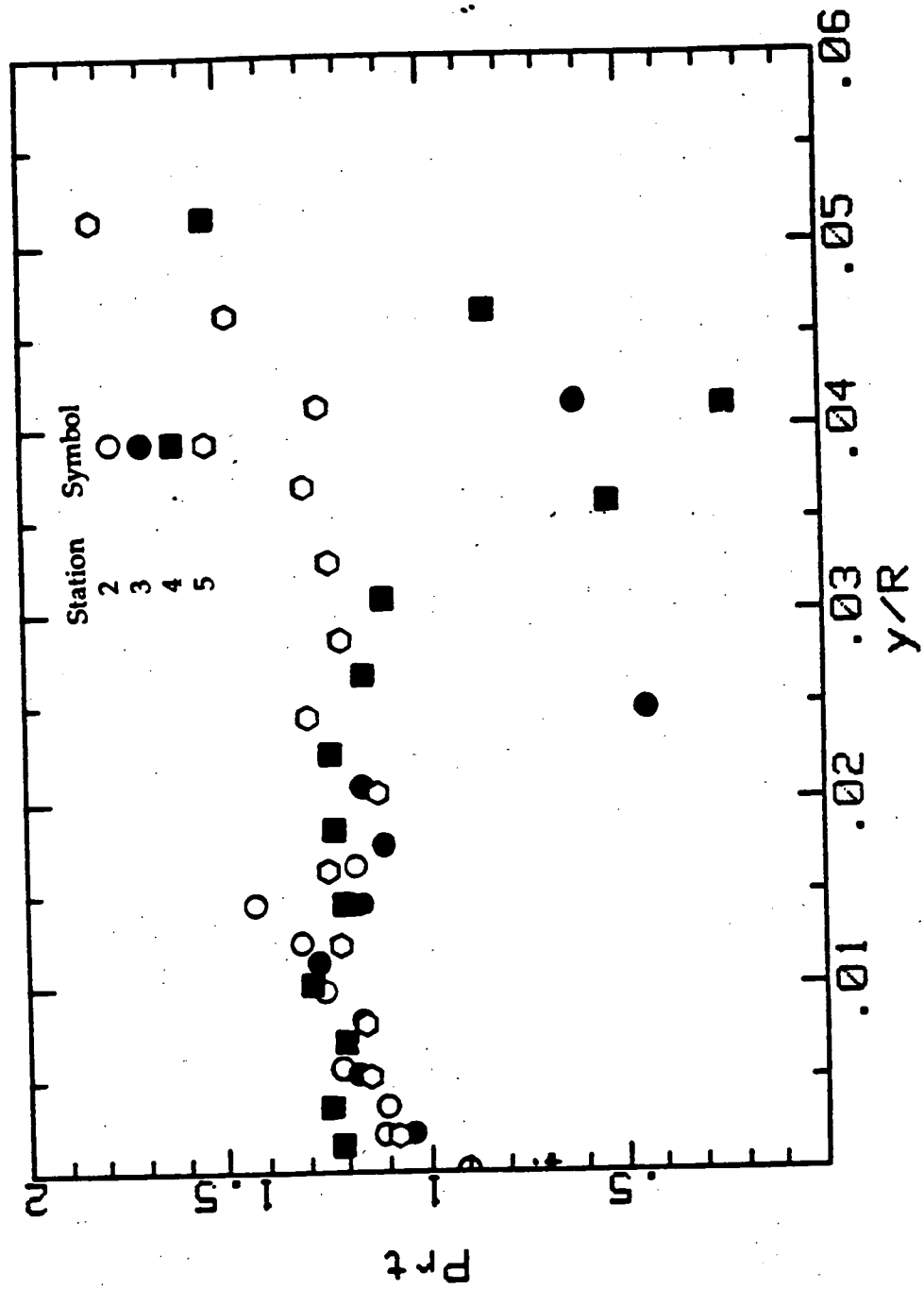

Fig. 3.5.13--Profiles of the turbulent Prandtl number along the test wall (Case 5).

CHAPTER 5

Conclusions

The effects of free-stream turbulence and concave curvature on transitional boundary layers were studied. The main conclusions of this study are :

1). The flat-plate transitional boundary layer cannot be thought of as being a simple composite of a Blasius and a fully-turbulent flow. Transition modelling based on the intermittency function weighting of pure laminar and turbulent flows may be in error.

2). Conditional sampling of turbulence quantities on the intermittency function must be made during transition. Measurements of time-averaged quantities may not give an accurate view of the transition process.

3). The turbulent Prandtl numbers in the turbulent core region of the transitional flow are somewhat smaller than unity.

4). The existence of stable vortices on the concave-curved wall in both the laminar and turbulent boundary layers was established for low free-stream turbulence intensities. No coherent vortices were found for the higher turbulence intensity case.

5). Concave curvature destabilizes the flow, causing transition to occur earlier than on the flat-wall. This is a confirmation of earlier findings.

6). No gross violation of Reynolds analogy was found for the post-transitional profiles in both the low and high turbulence intensity cases although small deviations from an exact analogy were noted.

7). High levels of free-stream turbulence superimposed on a free-stream velocity gradient were found to cause a cross-stream transport of momentum within the "potential core" of the flow.

REFERENCES

Abu-Ghannam, B.J. and Shaw, R. (1980) "Natural Transition of Boundary Layers--The Effects of Turbulence, Pressure Gradient, and Flow History", J. of Mech. Engin. Sci., Vol. 22, No. 5, pp. 213-228.

Antonia, R.A., Chambers, A.J., Sokolov, M. and Van Atta, C.W. (1981) "Simultaneous Temperature and Velocity Measurements in the Plane of Symmetry of a Transitional Turbulent Spot", JFM, Vol. 108, pp. 317-343.

Arnal, D., Juillen, J.C., and Michel, R. (1978) "Experimental Analysis and Computation of the Onset and Development of the Boundary Layer Transition", NASA TM-75325.

Baines, W.D. and Peterson, E.G. (1951) "An Investigation of Flow through Screens", Trans. of ASME, Vol. 73, pp. 467-480.

Barlow, R.S. and Johnston, J.P. (1988) "Structure of a Turbulent Boundary Layer on a Concave Surface", JFM, Vol. 191, pp. 137-176.

Barlow, R.S. and Johnston, J.P. (1988) "Local Effects of Large-Scale Eddies on Bursting in a Concave Boundary Layer", JFM, Vol. 191, pp. 177-195.

Bippes, H. (1978) "Experimental Study of the Laminar-Turbulent Transition of a Concave Wall in a Parallel Flow", NASA TM-75243.

Blackwell, B.F. and Moffatt, R.J. (1975) "Design and Construction of a Low-Velocity Boundary Layer Temperature Probe", J. Heat Transfer, Vol. 97, pp. 313-315.

Blair, M.F. (1982) "Influence of Free-Stream Turbulence on Boundary Layer Transition in Favorable Pressure Gradients", Journal of Engineering for Power, Vol. 104, pp. 743-750.

Blair, M.F. (1983) "Influence of Free-Stream Turbulence on Turbulent Boundary Layer Heat Transfer and Mean Profile Development, Part I - Experimental Data", J. Heat Transfer, Vol. 105, pp. 33-39.

Blair, M.F. (1991) "Bypass-mode Boundary Layer Transition in Accelerating Flows", manuscript in preparation.

Blair, M.F., and Bennett, J.C. (1984) "Hot-wire measurements of velocity and temperature fluctuations in a heated turbulent boundary layer", 29th ASME

International Gas Turbine Conference, Amsterdam. (Also J. Physics E, Vol. 20, pp. 209-216, 1987).

Buddhavarapu, J. (1984), "An Experimental Study of Transitional Boundary Layers on a Flat Plate", MSME Thesis, Dept. of Mech. Engin., U. of Minnesota.

Cantwell, B., Coles, D. and Dimotakis, P. (1978) "Structure and Entrainment in the Plane of Symmetry of a Turbulent Spot", JFM, Vol. 78, part 4, pp. 641-672.

Clauser, F.H. (1956) "The Turbulent Boundary Layer", Advances in Applied Mechanics, Vol. IV, Academic Press, New York, pp. 1-51.

Clauser, M. and Clauser, F. (1937) " The Effect of Curvature on the Transition from Laminar to Turbulent Boundary Layer", NACA TN-613.

Crane, R.I., and Sabzvari, J. (1982) "Laser-Doppler Measurements of Görtler Vortices in Laminar and Low Reynolds Number Turbulent Boundary Layers", Proc. Int. Symp. on Application of Laser Doppler Anemometry to Fluid Mechanics, Lisbon, June 1982; also in: Laser Anemometry in Fluid Mechanics, R.J. Adrian et al., eds., LADOAN-Instituto Superior Téchnico, Lisbon, 1984, pp. 19-35.

Crawford, M. E., and Kays, W. M. (1976) "STAN5--A Program for Numerical Computation of Two-Dimensional Internal and External Boundary Layer Flows", NASA CR-2742.

Dhawan, S. and Narasimha, R. (1958) "Some Properties of Boundary Layer Flow During the Transition from Laminar to Turbulent Motion", JFM, Vol. 3, pp 418-436.

Emmons, H.W. (1951) "The Laminar-Turbulent Transition in a Boundary Layer", J. Aero. Sci., Vol 18, pp. 490-498.

Gad-El-Hak, M., Blackwelder, R.F. and Riley, J.J. (1981) "On the Growth of Turbulent Regions in Laminar Boundary Layers", JFM, Vol. 110, pp. 73-95.

Gibson, M. M., Verriopoulos, C. A. and Vlachos, N.S. (1984) "Turbulent Boundary Layer on a Mildly Curved Convex Surface, Part 2: Temperature field measurements", Experiments in Fluids, Vol. 2, pp. 73-80.

Görtler, H. (1940) "Uber eine dreidimensionale Instabilität laminarer Grenzschichten an konkaven Wänden", Ges. d. Wiss. Göttingen, Nachr. a.d. Math.-Phys. Bd.2, Nr 1. (Also: "On the Three-Dimensional Instability of Laminar Boundary Layers on Concave Walls", NACA TM-1375, 1954).

Hall, D.J. and Gibbings, J.C. (1972) "Influence of Stream Turbulence and Pressure Gradient upon Boundary Layer Transition", J. Mech. Engin. Sci., Vol. 14, No. 2, pp. 134-146.

Hishida, M., and Nagano, Y. (1978) "Simultaneous Measurements of Velocity and Temperature in Non-isothermal Flows", Journal of Heat Transfer, Vol. 100, pp. 340-345.

Kays, W. M., and Crawford, M. E. (1980) Convective Heat and Mass Transfer, Second Edition, McGraw-Hill, New York.

Kim, J. (1986) "The Development of a Turbulent Heat Flux Probe and its Use in a 2-D Boundary Layer over a Convex Surface", MSME Thesis, Dept. of Mech. Engin., U. of Minnesota.

Kim, J. , and Simon, T. W. (1988) "Measurements of the Turbulent Transport of Heat and Momentum in Convexly Curved Boundary Layers: Effects of Curvature, Recovery, and Free-Stream Turbulence", Journal of Turbomachinery, Vol. 110, No. 1, pp. 80-87.

Klebanoff, P.S., Tidstrom, K.D. and Sargent, L.M. (1962) "The Three-Dimensional Nature of Boundary-Layer Instability", JFM, Vol. 12, pp. 1-34.

Kline, S.J. and McClintock (1953) "Describing Uncertainties in Single-Sample Experiments", Mechanical Engineering, Vol. 75, pp. 3-8.

Kuan, C.L. and Wang, T.W. (1990) "Investigation of the Intermittent Behavior of Transitional Boundary Layer Using a Conditional Averaging Technique", Experimental Thermal and Fluid Science, Vol. 3, pp. 157-173.

Liepmann, H.W. (1943) "Investigations on Laminar Boundary-Layer Stability and Transition on Curved Surfaces", NACA Wartime Report W-107, (originally issued as NACA ACR No. 3H30, 1943).

Lin, J.K., Kamotani, Y. and Ostrach, S. (1982) "Effect of Heating on Görtler Instability", Department of Mechanical and Aerospace Engineering, Case Western Reserve University, Report FTAS/TR-82-162.

Mauter, T.S. and van Atta, C.W. (1986) "Wall Shear Stress Measurements in the Plane of Symmetry of a Turbulent Spot", Experiments in Fluids, Vol. 4, pp. 153-162.

McCormack, P.D., Welker, H. and Kelleher, M. (1970) "Taylor-Görtler Vortices and their Effect of Heat Transfer", J.Heat Transfer, Vol. 92, pp. 101-112.

McDonald, H., and Fish, R. W. (1973) "Practical Calculations of Transitional Boundary Layers", International Journal of Heat and Mass Transfer, Vol. 16, No. 9, pp. 1729-1744.

Morkovin, M.V. (1977) "Instability, Transition to Turbulence, and Predictability", AGARD-AG-236.

O'Brien, J.E. and vanFossen, G.J. (1985) "The Influence of Jet Grid Turbulence on Heat Transfer from the Stagnation Region of a Cylinder in Crossflow", ASME 85-HT-58.

Pauley, W.R. and Eaton, J.K. (1988) "The Fluid Dynamics and Heat Transfer Effects of Streamwise Vortices Embedded in a Turbulent Boundary Layer", Thermosciences Division, Dept. of Mechanical Engineering, Stanford University, Report MD-51.

Perry, A.E. (1982) Hot-wire Anemometry, Clarendon Press, Oxford.

Perry, A.E., Lim, T.T. and Teh, E.W. (1981) "A Visual Study of Turbulent Spots", JFM, Vol. 104, pp. 387-405.

Ramaprian, B.R. and Shivaprasad, B.G. (1977), "Mean Flow Measurements in Turbulent Boundary Layers along Mildly Curved Surfaces", AIAA Journal, Vol. 15, No. 2, pp. 189-196.

Russ, S.G. (1989) "The Generation and Measurement of Turbulent Flow Fields", MSME Thesis, Dept of Mech. Engin., U. of Minnesota.

Schlichting, H. (1979), Boundary Layer Theory, Seventh Edition, McGraw-Hill, New York.

Simonich, J.C. and Bradshaw, P. (1978) "Effect of Free-Stream Turbulence on Heat Transfer through a Turbulent Boundary Layer", J. of Heat Transfer, Vol. 100, pp. 671-677.

Simonich, J.C. and Moffatt, R.J. (1982) "Local Measurements of Turbulent Boundary Layer Heat Transfer on a Concave Surface using Liquid Crystals", Rept. HMT-35, Thermosciences Division, Dept. of Mechanical Engineering, Stanford University.

Shizawa, T. and Honami, S. (1983) "Experiment on Turbulent Boundary Layers over a Concave Surface--Effects of Introduction of Curvature", 4th Symposium on Turbulent Shear Flows.

Shizawa, T. and Honami, S. (1985) "Experiments on Turbulent Boundary Layers over a Concave Surface--Response of Turbulence to Curvature", 5th Symposium on Turbulent Shear Flows, Cornell University, Ithaca, NY.

So, R.M. and Mellor, G.L. (1975) "Experiment on Turbulent Boundary Layers on a Concave Wall", The Aeronautical Quarterly, Vol. 26, pp. 25-40.

Suder, K.L., O'Brien, J.E. and Reshotko, E. (1988) "Experimental Study of Bypass Transition in a Boundary Layer", NASA TM-100913.

Swearingen, J.D. (1985) "The Growth and Breakdown of Streamwise Vortices in the Presence of a Wall", Ph.D. Thesis, University of Southern California.

Tani, I. (1962) "Production of Longitudinal Vortices in the Boundary Layer along a Concave Wall", J. of Geophysical Research, Vol. 67, pp. 3075.

Tennekes and Lumley (1972) A First Course in Turbulence, MIT Press, Cambridge, Mass.

van Driest, E.R. and Blumer, C.B. (1963) "Boundary Layer Transition: Free-stream Turbulence and Pressure Gradient Effects", AIAA Journal, Vol. 1, No. 6, pp. 1303-1306.

Wang, T. (1984) " An Experimental Investigation of Curvature and Free-stream Turbulence Effects on Heat Transfer and Fluid Mechanics in Transitional Boundary Layer Flows", Ph.D. Thesis, University of Minnesota.

Wang, T., and Simon, T. W. (1987) "Heat Transfer and Fluid Mechanics Measurements in a Boundary Layer Undergoing Transition on a Convex-Curved Wall", Journal of Turbomachinery, Vol. 109, No. 3, pp. 443-452.

Wang, T., Simon, T.W. and Buddhavarapu J. (1985) "Heat Transfer and Fluid Mechanics Measurements in Transitional Boundary Layer Flows", ASME 85-GT-113, J. of Eng. for Gas Turbines and Power, Vol. 107, No. 4, pp. 1007-1015.

Wortmann, F.X. (1969) "Visualization of Transition", JFM, Vol. 38, part 3, pp. 473-480.

Wygnanski, I., Sokolov, M. and Friedman, D. (1976) "On a Turbulent 'Spot' in a Laminar Boundary Layer", JFM, Vol. 78, part 4, pp. 785-819.

You, S.M. (1986) "Turbulent Boundary Layer Heat Transfer and Fluid Mechanics Measurements on a Curved Convex Wall", MSME Thesis, Dept. of Mech. Engin., U. of Minnesota.

APPENDICES

A1). Measurement of Emissivity

The emissive power of a surface is defined as the radiant energy emitted by a surface per unit time and unit surface area. A blackbody absorbs all the radiation incident upon it and is the most efficient emitter of radiation. The emissive power of a blackbody is given by the Stephan-Boltzmann law

$$q_b = \sigma T^4 \qquad \text{(A.1.1)}$$

where q_b = emissive power [W/m^2]

σ = Stephan-Boltzmann constant

T = absolute temperature [K]

Most surfaces emit less radiation than that emitted by a blackbody at the same temperature. The ratio of the emissive power of a non-blackbody to that of a blackbody is called the emissivity of the surface:

$$\varepsilon = q/q_b \qquad \text{(A.1.2)}$$

where q = emissive power of the non-black surface

q_b = emissive power of the black surface measured at the same temperature

The emissivity of the liquid crystal surface is measured using the setup shown in Fig. A-1. The blackbody is an aluminum plate with Fresnel rings machined into the surface and covered with a black coating. The energy radiated from this surface is within 1% of that predicted by Eq. (A.1.1). The "radiation thermopile" consists of thirty thermocouples connected in series. The hot junctions of the thermocouples are coated with carbon black to absorb

the radiation falling upon them and are positioned at the focal point of a polished, parabolic reflector. The reference junctions of the "radiation thermopiles" are shielded from the incoming radiation and remain at room temperature. The EMF produced by the thermopile depends on the difference in temperature between the hot and reference junctions, and is a linear function of the emissive power of the surface radiating into the thermopile:

$$EMF = A + (B)(q) \qquad (A.1.3)$$

The intercept, A, depends on the surface, while the slope, B, should be constant as long as the distance between the surface and the thermopile remains the same.

The emissivity of the liquid crystal surface is measured by making simultaneous measurements of the EMF produced by the thermopile and the surface temperature as the surface is heated from room temperature to 100 °C. Radiation from the blackbody is used to calibrate the thermopile. For a blackbody,

$$EMF_b = A_b + (B)(\sigma T^4) \qquad (A.1.4)$$

The blackbody is then replaced by a liquid crystal surface. For the liquid crystal surface,

$$EMF_{lc} = A_{lc} + (B)(\varepsilon_{lc}\sigma T^4) \qquad (A.1.5)$$

or $$EMF_{lc} = A_{lc} + (B\varepsilon_{lc})\ (\sigma T^4)$$

The derivative of EMF_b with respect to σT^4 is B, while the derivative of EMF_{lc} with respect to σT^4 is $B\varepsilon_{lc}$. The emissivity of the liquid crystal surface can thus be determined by generating curves of EMF vs. σT^4 for both the black and liquid crystal surfaces, and taking the ratio of their slopes.

The value of ε_{lc} calculated by averaging the results from the data sets was found to be 0.846. The uncertainty in the above is estimated to be 5%. Independent measurements of the emissivity made using an emissometer (a device for measuring emissivity) yielded readings of 0.85-0.90.

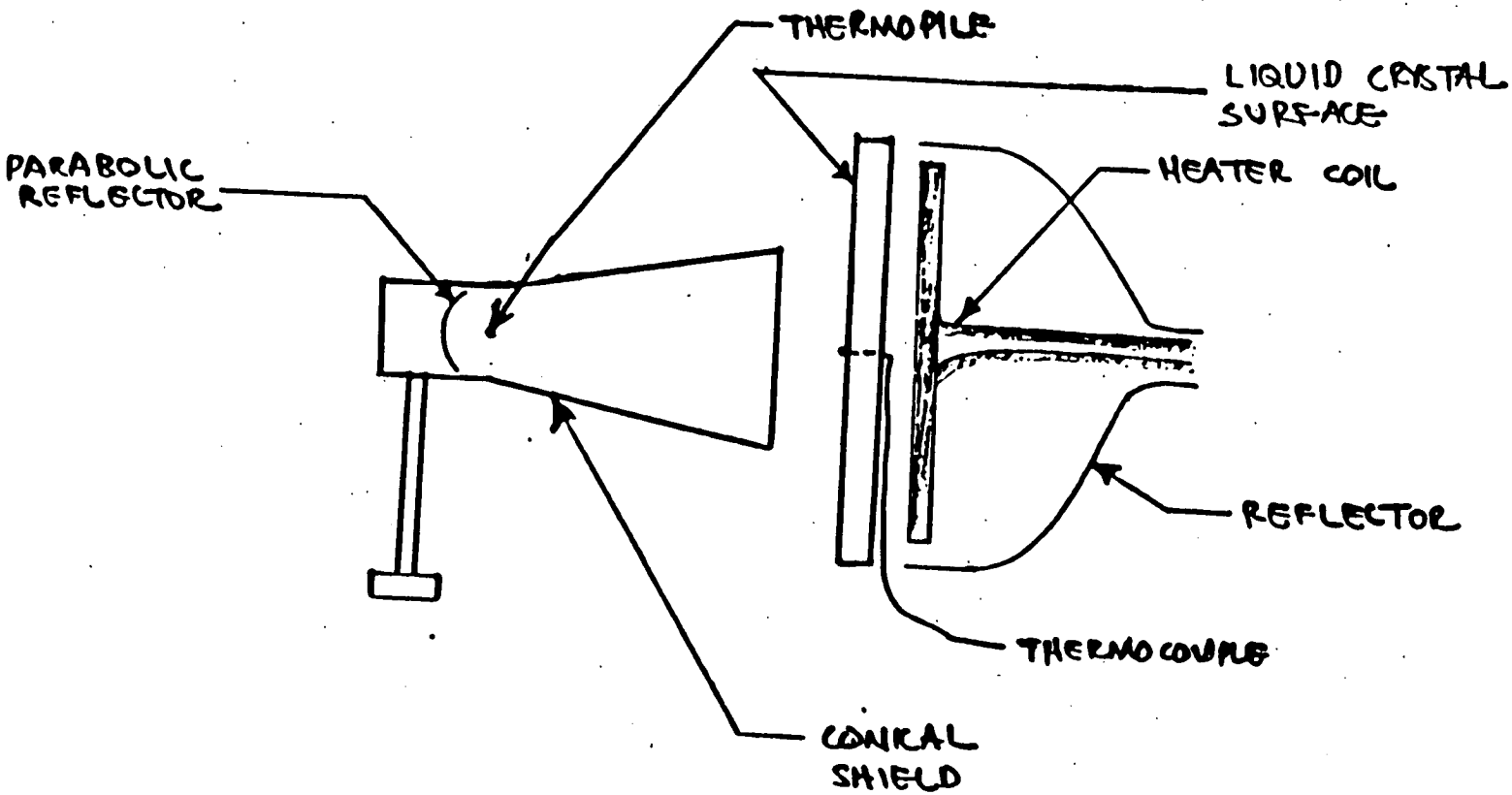

Figure A.1--Emissivity measurement setup.

A2). Measurement of the thermal conductivity of the lexan/liquid crystal Composite

The thermal conductivity of the lexan/liquid crystal composite is measured using the composite wall shown on Fig. A-2. The wall is constructed in a symmetrical manner about a resistance heater patch similar to that used by Wang (1984) as a source of constant heat flux. The copper plates have grooves cut into them, allowing thermocouples to be placed on either side of the composite. The composite is then sealed with epoxy around the edges and placed in a water bath.

The thermal conductivity of the composite is determined by measuring the power to the patch heater and the temperature difference across the composite. An energy balance on the composite yields

$$q_1 + q_2 = q_T \tag{A.2.1}$$

where q_1 and q_2 represent the heat leaving from either side of the composite and q_T represents the power supplied to the heater. An expression for the conductivity may be obtained by substituting $q_1 = k\Delta T_1/\Delta x_1$, $q_2 = k\Delta T_2/\Delta x_2$ into Eq. (A.2.1) and solving for the conductivity, k. The conductivity may thus be found if the power supplied to the patch (q_T), the temperature differences across the composite and their thicknesses are known. The results of the measurements yielded a thermal conductivity of k=0.1495 W/m/C. This compares well with the manufacturers value of 0.146 W/m/C for lexan alone. The difference is probably due to the addition of the liquid crystal surface and the adhesive transfer tape used to hold the assembly together. The uncertainty of the measurement is estimated to be 5%.

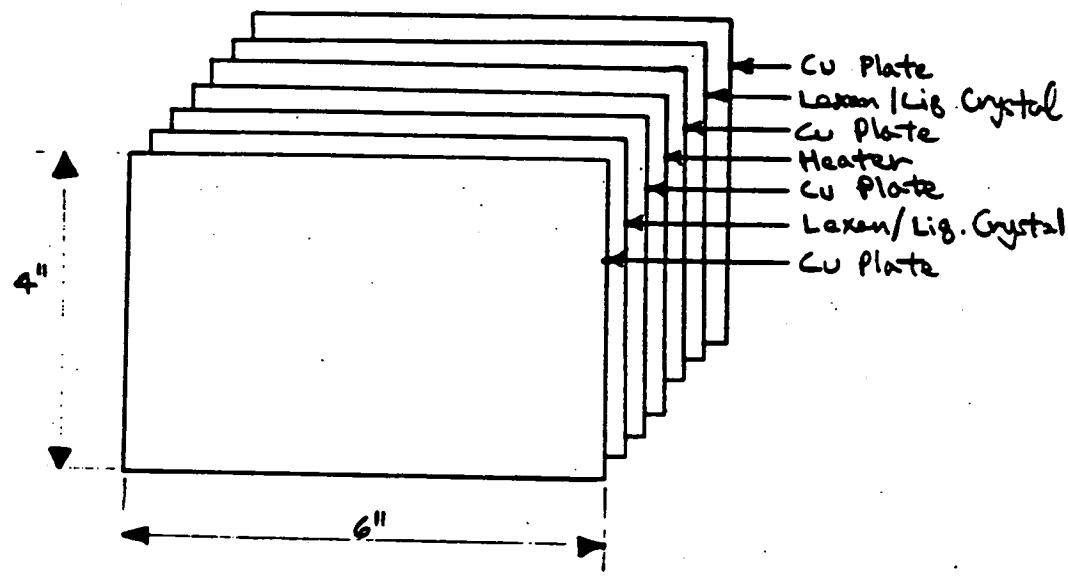

Figure A.2a–Composite wall construction.

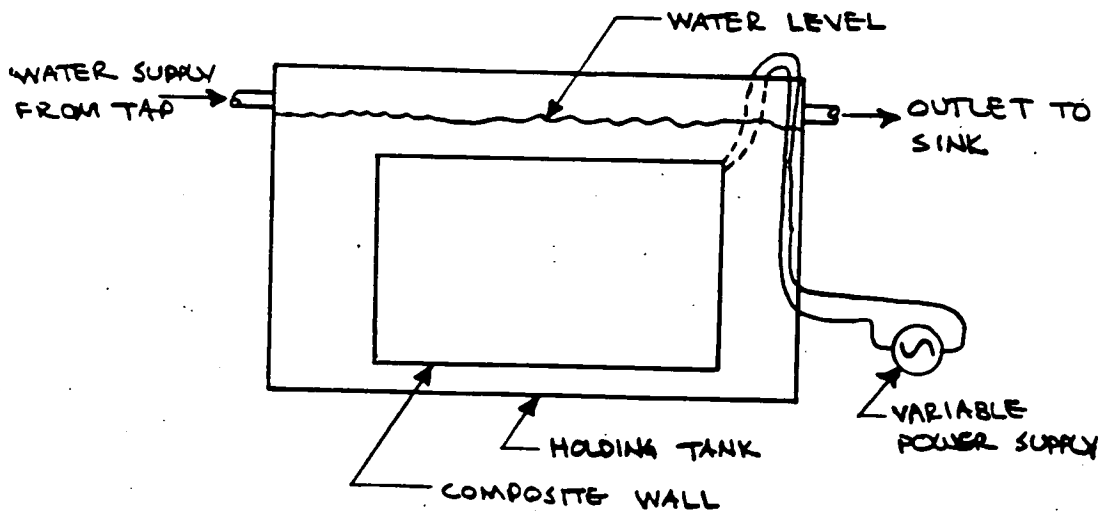

Figure A.2b–Experimental setup for conductivity measurement.

A3). Measurement of autocorrelation*

The autocorrelation gives information on the scales and evolution of a turbulent flow. It is similar to a frequency spectrum except that the information is presented in the time domain rather than in the frequency domain.

The autocorrelation is the correlation of the fluctuating velocity component, u' at two different times, $u'(t)u'(t+\tau)$. In a steady flow this is independent of time, t, but depends only on the time difference, τ. Also, in a steady flow the turbulent normal stresses are independent of time($u'^2(t)=u'^2(t+\tau)$=const.) This can be used to non-dimensionalize the autocorrelation as follows:

$$\rho(\tau)=\frac{\overline{u'(t)u'(t+\tau)}}{\overline{u'^2(t)}} \qquad \text{(A.3.1)}$$

This is known as the autocorrelation coefficient.

The autocorrelation is related to two important turbulence scales. The first is the integral scale, I. This scale is defined as the area under the autocorrelation coefficient curve. This time scale represents an average time over which u' correlates with itself. This scale is representative of the large scales in the turbulent flow. The second important scale is the Taylor microscale, λ. This scale is defined by the curvature of the autocorrelation coefficient at the origin, as follows:

---

*This section was originally written by Mr. Steve Russ. Small modifications have been made.

$$\left.\frac{d^2\rho}{d\tau^2}\right|_{\tau=0} = -\frac{2}{\lambda^2} \qquad \text{(A.3.2)}$$

This time scale represents the dissipating scales of the flow. Utilizing the fact that the turbulence is stationary, the following relationship can be derived (Tennekes and Lumley--1972):

$$\overline{\left(\frac{du'}{dt}\right)^2} = \frac{\overline{2u'^2}}{\lambda^2} \qquad \text{(A.3.3)}$$

Thus, the Taylor microscale can be used to estimate the turbulent dissipation (assuming small-scale isotropy). Both of these time scales can be converted to length scales by multiplying by the local convective velocity, U.

A simple set of data acquisition and reduction programs to process these measurements have been written by Mr. Steve Russ and the author. This set-up utilizes a hot-wire anemometer, a Norland Prowler digital oscilloscope and an HP lab computer. In this measurement the Norland is set to acquire several traces of data from the hot-wire anemometer bridge at fixed intervals. The velocity traces are stored on a disk for later data reduction. The data reduction program computes the autocorrelation coefficient function and the various time scales from the velocity traces. One set of data traces with a small acquisition time is required for the measurement of the Taylor microscale. The data acquisition rate must be rapid enough so that the curvature at the origin is apparent on the autocorrelation curve. A second set of data traces with a longer acquisition time is required for the measurement of the integral scale. The data acquisition rate must be slow enough so that the autocorrelation coefficient curve goes to zero for large τ. The measurement was accomplished by the following steps:

1. A normal hot-wire is placed in the flow and the anemometer is set to RUN.
2. The output from the anemometer is sent to the Norland.
3. The Norland is set to acquire data at the desired rate.
4. The high-pass filter is set to 1/2 the acquisition frequency to avoid aliasing.
5. The HP program "DATATRANS" is run. This will take the desired data traces.
6. The HP program "SCALRED" is run to compute the autocorrelation coefficient curve and the time and length scales.
7. The HP program "PLOTRHO" is used to graph the data.

It was found that at least eight velocity traces at both the high frequency and the low frequency were needed to obtain a smooth autocorrelation coefficient curve. The rates of data acquisition depend on the particular flow. A listing of the programs is attached.

```
10    !*******************************************
20    ! PROWLER-COMPUTER INTERFACING PROGRAM (DATATRANS)
30    !*******************************************
40    ! TRANSFER OF DATA
50    DIM A$[10000] BUFFER,C$[300],A1(2),A2(2),V(2),Vel(2)
60    DIM Factor(3),Offset(3),Volt(4095),Velc(4095)
70    REMOTE 715
80    !
90    !  HOT-WIRE INFORMATION GOES HERE
100   !
110   A=-1.60786
120   B=3.28453
130   Powerhw=.435
140   INPUT "INPUT TEMPERATURE OF FLOW",Temp
150   Sqrcf=SQR(225/(250-Temp))
160   INPUT "INPUT ATMOSPHERIC PRESSURE(In. Hg)",Press
170   Press=Press*25.4
180   INPUT "INPUT GAIN FROM SIGNAL CONDITIONER",Gainhw
190   INPUT "INPUT OFFSET FROM SIGNAL CONDITIONER",Offsethw
200   INPUT "INPUT OFFSET OF CHANNEL A (UNIT 715)",Offch1
210   INPUT "INPUT BASE FILE NAME",Bfile$
220   INPUT "INPUT NUMBER OF DATA SETS",Nmax
221   PRINT "DATA SET:"
230   !
240   FOR Jk=1 TO Nmax
241     PRINT Jk
250     File$=Bfile$&VAL$(Jk)
260   ! CREATE DATA FILES
270     ASSIGN @Prowler TO 715
280     ASSIGN @Buffa TO BUFFER A$
290   !
300   ! INITIATE DATA TRANSFER
310     OUTPUT 715 USING "#,K";"_KCGA"    ! SEND CONTENTS OF CH. A IN XFAST BIN
320     WAIT .1
330     TRANSFER @Prowler TO @Buffa;COUNT 8452
340     MASS STORAGE IS ":CS80,700,0"
350     WAIT 1.
360   !
370     OUTPUT 715 USING "#,K";"R"
380   !*******************************************
390   ! CONVERSION OF BINARY DATA TO DECIMAL VALUES
400   !
410   ! RESET BUFFER POINTERS:
420     CONTROL @Buffa,5;1
430     WAIT 1.
440   !
450   ! FIND FACTOR AND OFFSET:
460     FOR J=1 TO 2
470       ENTER @Buffa USING "#,2A";C$              ! ENTER EXPONENT
480       V(1)=IVAL(C$,16)! CONVERT FROM HEXADECIMAL TO DECIMAL
490       Exp=2^(V(1)-128)! COMPUTE EXPONENT
500       Su=.5
510       Power=4.
520       FOR K=1 TO 6
530         ENTER @Buffa USING "#,A";C$             ! ENTER FRACTIONAL VALUE
```

```
540         V(1)=IVAL(C$,16)! CONVERT TO DECIMAL
550         Tot=V(1)/2^Power
560         Power=Power+4.
570         Su=Su+Tot
580       NEXT K
590       IF J=1 THEN  ! COMPUTE FACTOR
600         Factor(1)=Su*Exp
610       ! PRINT "FACTOR";Nc;"= ";Factor(1 )
620       END IF
630       IF J=2 THEN  ! COMPUTE EXPONENT
640         Offset(1)=Su*Exp
650        !PRINT "OFFSET";Nc;"= ";Offset(1 )
660         PRINT
670       END IF
680     NEXT J
690   !
700   ! ENTER AND IGNORE REST OF HEADER:
710     ENTER @Buffa USING "#,240A";C$
720   !
730   ! CONVERSION OF DATA:
740     FOR J=1 TO 4096
750       ENTER @Buffa USING "#,B";A1(1)! ENTER ONE BYTE
760       ENTER @Buffa USING "#,B";A2(1)
770       V(1)=A2(1)*256.+A1(1)  ! TRANSPOSE ORDER OF BYTES
780       V(1)=V(1)-32768  ! OFFSET BY 8000 HEX
790       V(1)=V(1)*Factor(1)+Offset(1)     ! CALCULATE ACTUAL VOLTAGE
800       I=J-1
810     ! PRINT "I,V(";Nc;")= ";I;V(Nc)-OFFCH1
820       Volt(I)=V(1)-Offch1
830     !
840     !  LINEARIZE SIGNAL
850     !
860       Volt(I)=(Volt(I)/Gainhw+Offsethw)*Sqrcf
870       Velc(I)=(A+B*Volt(I)^2)^(1/Powerhw)
880       IF INT(I/100)=I/100 THEN DISP I,V(1)-Offch1,Velc(I)
890     NEXT J
900     BEEP
910   !*****************************************
920   !
930   ! STORE DATA IN DATA FILE
940     MASS STORAGE IS ":CS80,700,1"
950     CREATE BDAT File$,130
960     ASSIGN @Path TO File$
970     OUTPUT @Path;Velc(*)
980     MASS STORAGE IS ":CS80,700,0"
990   NEXT Jk
1000  !*****************************************
1010  !
1020  END
```

```
10    !*********************************************************************
20    !  THIS PROGRAM IS USED TO CALCULATE THE AUTOCORROLATION FROM
30    !  VELOCITY MATRICES TAKEN AT FREQUENCIES 2,000 AND 200 Hz (SCALRED)
40    !*********************************************************************
50    OPTION BASE 1
60    DIM Vel1(4095),Rho1(6,2),Rho2(101,2),Rho1ave(6,2),Rho2ave(101,2),Velh(4095
)
70    INPUT "INPUT NUMBER OF TRACES ",Nr
80    INPUT "INPUT HIGH/LOW FREQ. FILE BASE NAME",File$,File1$
90    INPUT "INPUT HIGH/LOW FREQUENCIES",Freqh,Freql
100   !
110   Rho1ave(6,2)=0
120   FOR K5=1 TO Nr
130     Numb$=VAL$(K5)
140     Nameh$=File$&Numb$
150     Name1$=File1$&Numb$
160     N=1
170     M=2
180     Rho1(1,1)=1.0
190     Rho2(1,1)=1.0
200     Rho1(1,2)=0.
210     Rho2(1,2)=0.
220     !
230     !  GET  HIGH FREQ. VELOCITY MATRIX FROM DISK
240     !
250     Th=1/Freqh
260     Tl=1/Freql
270     MASS STORAGE IS ":CS80,700,1"
280     ASSIGN @Path TO Nameh$
290     ENTER @Path;Velh(*)
300     MASS STORAGE IS ":CS80,700,0"
310     !
320     !  CALCULATE Ubar AND Urms FROM DATA
330     !
340     Sum1=0.
350     Sum2=0.
360     FOR I=1 TO 4095
370       Sum1=Sum1+Velh(I)
380       Sum2=Sum2+Velh(I)^2
390     NEXT I
400     Ubar1=Sum1/4095
410     Urms1=Sum2/4094-Sum1^2/4095/4094
420     !
430     !  CALCULATE CORRELATIONS AT Tau=1*T,Tau=2*t,Tau=3*T,TAU=4*T,TAU=5*T
440     !
450     Sum1=0.
460     Sum2=0.
470     Sum3=0.
480     Sum4=0.
490     Sum5=0.
500     FOR I=1 TO 4090
510       IF I/100=INT(I/100) THEN DISP I
520       Sum1=Sum1+(Ubar1-Velh(I))*(Ubar1-Velh(I+1))
530       Sum2=Sum2+(Ubar1-Velh(I))*(Ubar1-Velh(I+2))
540       Sum3=Sum3+(Ubar1-Velh(I))*(Ubar1-Velh(I+3))
```

```
550       Sum4=Sum4+(Ubar1-Velh(I))*(Ubar1-Velh(I+4))
560       Sum5=Sum5+(Ubar1-Velh(I))*(Ubar1-Velh(I+5))
570     NEXT I
580     Rho1(2,1)=Sum1/4090/Urms1
590     Rho1(3,1)=Sum2/4090/Urms1
600     Rho1(4,1)=Sum3/4090/Urms1
610     Rho1(5,1)=Sum4/4090/Urms1
620     Rho1(6,1)=Sum5/4090/Urms1
630     FOR I=1 TO 5
640       Rho1(I+1,2)=I*Th
650     NEXT I
660     !
670     Rho1ave(1,1)=1.
680     Rho1ave(1,2)=0.
690     FOR I=1 TO 5
700       Rho1ave(I+1,1)=Rho1ave(I+1,1)+Rho1(I+1,1)
710     NEXT I
720     !
730   !
740   !  GET LOWER FREQ. VELOCITY MATRIX FROM DISK
750   !
760     MASS STORAGE IS ":CS80,700,1"
770     ASSIGN @Path TO Name1$
780     ENTER @Path;Vel1(*)
790     MASS STORAGE IS ":CS80,700,0"
800     !
810     !  CALCULATE Urms AND Ubar
820     !
830     Sum1=0.
840     Sum2=0.
850     FOR I=1 TO 4095
860       Sum1=Sum1+Vel1(I)
870       Sum2=Sum2+Vel1(I)^2
880     NEXT I
890     Ubar2=Sum1/4095
900     Urms2=Sum2/4094-Sum1^2/4095/4094
910     !
920     !  CALCULATE CORRELATIONS
930     !
940     FOR I=1 TO 100
950       Sum1=0.
960       FOR J=1 TO 3995
970         Sum1=Sum1+(Ubar2-Vel1(J))*(Ubar2-Vel1(J+I))
980       NEXT J
990       Rho2(I+1,1)=Sum1/3995/Urms2
1000      Rho2(I+1,2)=I*T1
1010      DISP I
1020    NEXT I
1030    Rho2ave(1,1)=1.
1040    Rho2ave(1,2)=0.
1050    FOR I=1 TO 100
1060      Rho2ave(I+1,1)=Rho2ave(I+1,1)+Rho2(I+1,1)
1070    NEXT I
1080  NEXT K5
1090  FOR I=1 TO 5
```

```
1100    Rho1ave(I+1,1)=Rho1ave(I+1,1)/Nr
1110    Rho1ave(I+1,2)=Rho1(I+1,2)
1120  NEXT I
1130  FOR I=1 TO 100
1140    Rho2ave(I+1,1)=Rho2ave(I+1,1)/Nr
1150    Rho2ave(I+1,2)=Rho2(I+1,2)
1160  NEXT I
1170  !*********************************************************
1180  !
1190  !  LEAST SQUARES FIT PARABOLA TO THIS DATA TO GET MICROSCALE
1200  !
1210  Sum1=0.
1220  Sum2=0.
1230  Sum3=0.
1240  Sum4=0.
1250  FOR I=1 TO 6
1260    Y=Rho1ave(I,1)
1270    X=Rho1ave(I,2)^2
1280    Sum1=Sum1+X
1290    Sum2=Sum2+Y
1300    Sum3=Sum3+X*X
1310    Sum4=Sum4+X*Y
1320  NEXT I
1330  Slope=(6*Sum4-Sum1*Sum2)/(6*Sum3-Sum1*Sum1)
1340  Microt=SQR(-1.0/Slope)
1350  Micro1=Ubar1*Microt
1360  !
1370  !  CALCULATE INTEGRAL SCALES
1380  !
1390  Sum1=0.
1400  FOR I=2 TO 100 STEP 2
1410    Sum1=Sum1+(Rho2ave(I-1,1)+4.0*Rho2ave(I,1)+Rho2ave(I+1,1))*(Rho2ave(I+1,
2)-Rho2ave(I-1,2))/6
1420  NEXT I
1430  Itime=Sum1
1440  Ilength=Ubar2*Itime
1450  !
1460  !  PRINT OUT RESULTS
1470  INPUT "DO YOU WISH TO STORE DATA? (Y/N)",Sto$
1480  IF Sto$="Y" THEN
1490    INPUT "INPUT DATA FILE NAME",Stor$
1491    MASS STORAGE IS ":CS80,700,1"
1500    CREATE BDAT Stor$,7
1510    ASSIGN @Path TO Stor$
1520    OUTPUT @Path;Rho1ave(*),Rho2ave(*)
1521    MASS STORAGE IS ":CS80,700,0"
1530  END IF
1540  !
1550  INPUT "DO YOU WISH RESULTS PRINTED ON SCREEN OR PRINTER ? (S/P)",Pri$
1560  PRINTER IS 1
1570  IF Pri$="P" THEN PRINTER IS 701
1580  Ti2=SQR(Urms2)/Ubar2*100
1590  PRINT "AVERAGE VELOCITY  ",Ubar2
1600  PRINT "AVERAGE TURBULENCE INTENSITY  ",Ti2
1610  PRINT "INTEGRAL TIME SCALE(s)  ",Itime
```

```
1620  PRINT "INTEGRAL LENGTH SCALE (m)  ",Ilength
1630  PRINT "TAYLOR MICRO TIME SCALE (s)  ",Microt
1640  PRINT "TAYLOR MICRO LENGTH SCALE (m)  ",Microl
1650  PRINT "   TAU         RHO  "
1660  FOR I=1 TO 11
1670    PRINT Rho2((I-1)*10+1,2),Rho2((I-1)*10+1,1)
1680  NEXT I
1690  !
1700  PRINTER IS 1
1710  !
1711  !  CALCULATE LENGTH SCALES FROM TIME SCALES
1712  !
1713  INPUT "DO YOU WISH TO CHANGE TO LENGTH SCALES?",Inp$
1714  IF Inp$="Y" THEN
1715    FOR I=1 TO 101
1716      Rho2(I,2)=Rho2(I,2)*Ubar2
1717    NEXT I
1718    FOR I=1 TO 6
1719      Rho1(I,2)=Rho1(I,2)*Ubar1
1720    NEXT I
1722  !
1723  INPUT "DO YOU WISH TO STORE DATA? (Y/N)",Sto$
1728  IF Sto$="Y" THEN
1738    INPUT "INPUT DATA FILE NAME",Stor$
1739    MASS STORAGE IS ":CS80,700,1"
1748    CREATE BDAT Stor$,7
1758    ASSIGN @Path TO Stor$
1768    OUTPUT @Path;Rho1ave(*),Rho2ave(*)
1769    MASS STORAGE IS ':CS80,700,0"
1778  END IF
1788  !
1798  END IF
1808  !
1818  END
```

```
10    !*************************************************************************
20    ! THIS PROGRAM IS USED TO PLOT DATA EITHER MANUALLY OR THROUGH A DATA FILE
30    ! ON LINEAR-LINEAR AXES (PLOTRHO)
40    !*************************************************************************
50    OPTION BASE 1
60    DIM Xd(500),Yd(500),Title$[50],Labelx$[50],Labely$[50],Rho2(100,2),Rho1(6,
2)! ARRAY TO BE PLOTTED
70    GRAPHICS ON
80    GCLEAR
90    GINIT
100   LORG 5
110   DEG
120   !*************************************************************************
130   Title$=""                                          ! TITLE OF PLOT
140   Xmin=0.     ! MINIMUM VALUE OF X
150   Xmax=.02    ! MAXIMUM VALUE OF X
160   Ymin=-.2    ! MINIMUM VALUE OF Y
170   Ymax=1.     ! MAXIMUM VALUE OF Y
180   Xtic=.002    ! SMALL SCALE
190   Nxtic=2     ! HOW MANY SMALL SCALES IN LARGE SCALE
200   Ytic=.05
210   Nytic=4
220   Lab$="Y"   ! WANT LABEL
230   Labelx$="T [S]"                    ! X-AXIS LABEL
240   Labely$="RHO"                  ! Y-AXIS LABEL
310   !*************************************************************************
320   LDIR 0
330   CSIZE 6
340   LORG 5
350   FOR I=-.1 TO .3 STEP .1
360     MOVE 70+I,95
370     LABEL Title$
380   NEXT I
390   CSIZE 5
400   LORG 5
410   MOVE 69,5
420   LABEL Labelx$
430   LDIR 90
440   MOVE 6,52
450   LABEL Labely$
460   VIEWPORT 15,124,12,90
470   !*********************************************************
480   ! LINEAR-LINEAR AXES
490   WINDOW Xmin,Xmax,Ymin,Ymax
500   AXES Xtic,Ytic,Xmin,Ymin,Nxtic,Nytic,5
510   AXES Xtic,Ytic,Xmax,Ymax,Nxtic,Nytic,5
520   IF Grid$="Y" THEN GRID Nxtic*Xtic,Nytic*Ytic,Xmax,Ymax
530   !
540   CLIP OFF
550   LDIR 0
560   IF Lab$="N" THEN GOTO 800
570   Ylab=(Ymax-Ymin)/20
580   FOR I=1 TO (Xmax-Xmin)/(Xtic*Nxtic)
590     X1=I*Xtic*Nxtic+Xmin
600     MOVE X1,Ymin
```

```
610     LORG 6
620     LABEL X1
630   NEXT I
640   !
650   Xlab=(Xmax-Xmin)/25
660   LDIR 90
670   FOR I=1 TO (Ymax-Ymin)/(Ytic*Nytic)+1
680     Y1=I*Ytic*Nytic+Ymin
690     MOVE -Xlab+Xmin,Y1
700     IF ABS(Y1)<1.E-10 THEN GOTO 720
710     LABEL Y1
720     IF ABS(Y1)<1.E-10 THEN LABEL "0"
730   NEXT I
740   LDIR 0
750   CLIP ON
760   MOVE 0,0
770   LINE TYPE 5
780   IDRAW 100,0
781   LINE TYPE 1
790   !*************************************************************************
800   ! PLOT DATA ENTERED MANUALLY
810   CLIP ON
820   LORG 5
830   CSIZE 1,.5
840   INPUT "INPUT DATA FILE NAME",File$
850   MASS STORAGE IS ":CS80,700,1"
860   ASSIGN @Path TO File$
870   ENTER @Path;Rho1(*),Rho2(*)
880   MASS STORAGE IS ":CS80,700,0"
890   FOR I=1 TO 100
900     MOVE Rho2(I,2),Rho2(I,1)
910     LABEL "+"
920   NEXT I
921   FOR I=1 TO 6
922     MOVE Rho1(I,2),Rho1(I,1)
923     LABEL "+"
924   NEXT I
930   !*************************************************************************
940   INPUT "DO YOU WISH A HARD COPY? (Y OR N)",A$
950   IF A$="N" THEN 1040
960   INPUT "EXPANDED MODE? (Y/N)",Expand$
970   IF Expand$="Y" THEN
980     DUMP DEVICE IS 701,EXPANDED
990     DUMP GRAPHICS
1000  END IF
1010  IF Expand$="N" THEN DUMP GRAPHICS 1 TO #701
1020 !OUTPUT 701;"

1030  OUTPUT 701;"

1040  GCLEAR
1050  END
```

NASA
National Aeronautics and Space Administration

Report Documentation Page

1. Report No.	2. Government Accession No.	3. Recipient's Catalog No.
NASA CR-187150		

4. Title and Subtitle
Free-Stream Turbulence and Concave Curvature Effects on Heated, Transitional Boundary Layers
Volume I-Final Report

5. Report Date
August 1991

6. Performing Organization Code

7. Author(s)
J. Kim and T.W. Simon

8. Performing Organization Report No.
None

10. Work Unit No.
505-62-52

9. Performing Organization Name and Address
Univeristy of Minnesota
Department of Mechanical Engineering
Minneapolis, Minnesota 55455

11. Contract or Grant No.
NAG3-881

13. Type of Report and Period Covered
Contractor Report
Final

12. Sponsoring Agency Name and Address
National Aeronautics and Space Administration
Lewis Research Center
Cleveland, Ohio 44135-3191

14. Sponsoring Agency Code

15. Supplementary Notes
Project Manager, Fred Simon, Internal Fluid Mechanics Division, NASA Lewis Research Center, (216) 433-5894.

16. Abstract

An experimental investigation of the transition process on flat-plate and concave curved-wall boundary layers for various free-stream turbulence levels was performed. Where possible, sampling according to the intermittency function was made. Such sampling allowe segregation of the signal into two types of behavior—laminar-like and turbulent-like. Results show that for transition on a flat-plate, the two forms of boundary layer behavior, identified as laminar-like and turbulent-like, cannot be thought of as separate Blasius and fully-turbulent profiles, respectively. Thus, simple transition models in which the desired quantity is assumed to be an average, weighted on intermittency, of the theoretical laminar and fully turbulent values is not expected to be successful. Deviation of the flow identified as laminar-like from theoretical laminar behavior is shown to be due to recovery after the passage of a turbulent spot, while deviation of the flow identified as turbulent-like from the fully-turbulent values is thought to be due to incomplete establishment of th fully-turbulent power spectral distribution. Turbulent Prandtl numbers for the transitional flow, computed from measured shear stress turbulent heat flux and mean velocity and temperature profiles, were less than unity. For the curved-wall case with low free-stream turbulence intensity, the existence of Görtler vortices on the concave wall within both laminar and turbulent flows was established using liquid crystal visualization and spanwise velocity and temperature traverses. Transition was found to occur via a vortex break-down mode. The vortex wavelength was quite irregular in both the laminar and turbulent flows, but the vortices were stable in time and space. The upwash was found to be more unstable, with higher levels of u′ and u′v′, and lower skin friction coefficients and shap factors. Turbulent Prandtl numbers, measured using a triple-wire probe, were found to be near unity for all post-transitional profiles, indicating no gross violation of Reynolds analogy. No evidence of streamwise vortices was seen in the high turbulence intensity case It is not known whether this is due to the high eddy viscosity over the entire flow which reduces the turbulent Görtler number to stabl values and causes the vortices to disappear, or whether it is due to an unstable vortex structure. Predictions based on two-dimensiona modelling of the flow over a concave wall with high free-stream turbulence levels, as on the pressure surface of a turbine blade, woul seem to be adequate. High levels of free-stream turbulence superimposed on a free-stream velocity gradient (which occurs within curved channels) was found to cause a cross-stream transport of momentum within the "potential core" of the flow. The total pressur within the "potential core" can thus rise to levels higher than that which occurs at the inlet to the test section. Documentation is presented in two volumes. Volume I contains the text of the report including figures and supporting appendices. Volume II contains data reduction program listings and tabulated data.

17. Key Words (Suggested by Author(s))
Boundary layer transition
Heat transfer
Flat plates
Curvature

18. Distribution Statement
Unclassified - Unlimited
Subject Category 34

19. Security Classif. (of the report)	20. Security Classif. (of this page)	21. No. of pages	22. Price*
Unclassified	Unclassified	188	A09

*For sale by the National Technical Information Service, Springfield, Virginia 22161